

UNIVERSITY OF STRATHCLYDE
DEPARTMENT OF PHYSICS

**Collective Charged Particle
Dynamics in Relativistically
Transparent Laser-Plasma
Interactions**



by

Bruno González-Izquierdo

in partial fulfilment of the requirements for the degree of Doctor of Philosophy
in Physics

2016

Copyright Declaration

This thesis is the result of the author's original research. It has been composed by the author and has not been previously submitted for examination which has led to the award of a degree.

The copyright of the thesis belongs to the author under the terms of the United Kingdom Copyright Act as qualified by University of Strathclyde Regulation 3.50. Due acknowledgement must always be made of the use of any material contained in, or derived from, this thesis.

Signed:

Date:

Nothing is so fatal to the progress of the human mind as to suppose that our views of science are ultimate; that there are no mysteries in nature; that our triumphs are complete, and that there are no new worlds to conquer.

Humphry Davy, 1810

Abstract

This thesis reports on experimental and numerical investigations of the collective response of electrons and ions to the interaction of ultra-intense (10^{20} Wcm $^{-2}$) laser with ultra-thin (nanometre scale) foils undergoing expansion and relativistic induced transparency. The onset of this relativistic mechanism is also characterised and studied in detail. This new insight into relativistic transparency is an important step towards optical control of charged particle dynamics in laser-driven dense plasma sources and in its potential applications; including ion and radiation source development.

The experimental and numerical investigations exploring the onset and the underpinning physics of the relativistic transparency have focused on its dependency on the target areal density, laser intensity and polarisation. The results show a maximum laser transmission for the thinnest targets investigated, which decreases exponentially with increasing target thickness. The same trend is obtained for linearly and circularly polarised laser light. However, for a given target thickness, the linear polarisation case exhibits a significantly higher transmission fraction, with respect to the circular polarisation case, due to additional electron heating and expansion. Moreover, it is shown that for the thinnest targets, once they become relativistically transparent, the transmitted light fraction increases rapidly as the laser intensity increases. The increasing rate is shown to be more pronounced in the thinnest targets investigated. This is diagnosed by measurement of both the fundamental and second harmonic wavelengths. An alternative approach, based on numerical measurement of the critical surface velocity, as a function of time, for various target thickness, and comparing it with corresponding analytical models is also proposed. The onset of relativistic induced

transparency is found to curb the radiation pressure efficiency of the charged particle acceleration mechanism.

Investigations of the collective response of electrons in ultra-thin foils undergoing transparency show that a ‘relativistic plasma aperture’ is generated by intense laser light in this regime, resulting in the fundamental optical phenomenon of diffraction. It is numerically found that the plasma electrons collectively respond to the resulting laser near-field diffraction pattern, resulting in a beam of energetic electrons with spatial-intensity distribution, related to this diffraction structure, which can be controlled by variation of the laser pulse parameters, and in turn the onset of relativistic transparency. Additionally, it is shown that static electron beam, and induced magnetic field, structures can be made to rotate at fixed or variable angular frequencies depending on the degree of ellipticity in the laser polarisation. The predicted electron beam distributions using the ‘relativistic plasma aperture’ concept are verified experimentally.

Understanding the collective response of plasma electrons to transparency and how this affects the subsequent acceleration of ions is highly important to the interpretation of experiments exploring ion acceleration employing ultra-thin foils. Control of this collective electron motion, and thus the resultant electrostatic fields, could enable unprecedented control over the spatial-intensity distribution of laser-driven ion acceleration. The results presented in this thesis show that in ultra-thin foils undergoing transparency the electron dynamics are mapped onto the beam of protons accelerated via strong charge-separation-induced electrostatic fields. It is demonstrated that the degree of ellipticity of the laser polarisation defines the spatial-intensity distribution of the proton beam profile and can therefore be used to control it. This demonstration of dynamic optical control of structures within the spatial-intensity distribution of the beam of laser-accelerated ions opens a new route to optimising the properties of these promising ion sources.

Acknowledgements

Until relatively recently science was typically restricted to solitary people, with brilliant minds or to high-born people with a particular intellectual curiosity. This was distinctly manifested in the fact that most scientific advances of these times were attributed to a single person. However, in the last years, most of the knowledge, gathered along all that preceding time, was bounded in mature theoretical models and opened up new ways of investigation, most of which required experimental validation. The level of complexity to most physics at present is so high that rigorous experiments, employing exceptionally precise and sophisticated devices, much of them requiring large facilities, are needed. This new style of research has particular challenges, which requires the collaboration of numerous scientists (of multi-disciplinaries) working together toward a common goal. In my opinion, this has demonstrated enormous efficiency with the materialisation, in only a few decades, of some of the most significant scientific discoveries performed to-date.

I feel immensely fortunate for having been part of one of these fascinating investigations, during my PhD, whose success would not have been possible without the close collaboration of many talent researchers. My PhD supervisor, Prof. Paul McKenna, has not only been the pillar of my thesis with his continuous support and encouragement, but also for his brilliant wisdom and wealth of his discussions regarding the investigations presented in this thesis. I believe he is a reference of a perfect supervisor, researcher and person. I will always be grateful for him believing in me and giving me this opportunity, which has been one of the most personally and professionally enriching experiences of my life.

I would also like to thank to Ross for all his support during the experiments

and analysis of the results presented within. For me he is one of the best laser-plasma physics experimentalists which I've ever met and had the privilege to work with. I will miss our philosophical conversations. I would also like to thank Martin for his continuous cooperation in obtaining the 3D PIC simulations presented in this thesis. I envy his outstanding ability in performing very complex simulations. Thanks to Remi for his very fruitful conversations about the theoretical concepts. I would like to transmit my sincere gratitude to Robbie for his unconditional help in the English-proof of this entire thesis. Thank you very much also to Haydn, David M., Harry, David C., Rachel, John, Adam, Nick for all the good times spent on experiments and for making me feel like one of the team. Thank you very much to Prof. David Neely for all your help, support and for your mind challenges which you always proposed to us during the experiments. I really enjoyed dealing with your challenge questions.

I owe to Prof. Jose Luis Ocaña Moreno a special gratitude for giving me the opportunity to participate in the *Laser Technology* Masters which immersed me in this fascinating and exciting world. I would also like to transmit him my sincerest gratitude for his continuous support during and after the Masters course. Beyond doubt, he is one of the people responsible that, today, I am writing these lines for my PhD thesis completion.

Se suele decir que lo mejor siempre se deja para el final, y en este caso puedo asegurar que no se trata de una excepción. Pese a que soy una persona a la que le cuesta bastante expresar sus sentimientos abiertamente, me gustaría agradecer de corazón a mis padres todo el apoyo y comprensión que me han mostrado siempre en las decisiones que he ido tomando a lo largo de mi vida, incluso en aquellas, como esta, que requerían irme lejos de allí. Gracias por todo, aunque no os lo diga con mucha frecuencia. También querría dar las gracias a mis hermano/as por su continuo ánimo y apoyo durante estos años. Ello me ha ayudado en gran parte a afrontar los retos profesionales que me he ido proponiendo en este tiempo y a intentar superarme a mí mismo en cada uno de ellos.

Role of Author

The analysis and interpretation of the experiment and simulation results presented in this thesis and the new understanding of the underlying physics introduced was performed by the author, under supervision of Prof Paul McKenna and cooperation with other group members. The author made significant contributions to the planning and successful delivery of the experiment described in this thesis. He made the measurements and analysed both the experiment and simulation results obtained. The success of the experiments would have not been possible without the leadership of Prof. Paul McKenna and Dr. Ross Gray, among other colleagues. The author also had a leading role in the interpretation and description of the research results with the cooperation of Prof. Paul McKenna, Dr. Ross Gray and Dr. Martin King. In addition, the author and Prof. Paul McKenna have led the conception of publications in which the investigation results presented in this thesis have been included.

Chapter 5: The diagnostics for measuring the transmitted and back reflected light were implemented by the author in each experimental campaign. The CCD cameras and beam configuration to record the transmitted light was designed by Dr. Ross Gray. All corresponding experimental data has been analysed by the author. The 1D PIC simulations were designed, performed and analysed by the author. 2D PIC simulations were also design, performed and analysed by the author with the collaboration of Dr. Ross Gray and Dr. Martin King.

Chapter 6 and Chapter 7: The author was responsible for the design and implementation of the diagnostic for measuring the spatial-intensity distribution of charged particles, with the collaboration of Dr. Ross Gray, Mr.

Robbie Wilson and Mr. John McCreadie. The author played a determinant contribution to developing the new concepts presented in these chapters, investigating the collective response of electrons and protons in relativistically transparent targets, with the close collaboration of Prof. Paul McKenna, Dr. Ross Gray and Dr. Martin King. All of the experimental data and 3D PIC simulations have been analysed by the author. Most of the 3D PIC simulations have been performed by Dr. Martin King and planned together with the author and Prof. Paul McKenna. The comparison of the helical magnetic fields, presented in **Chapter 6**, with astrophysical events has been formulated by Dr. Martin King with the collaboration of the author. The author had a leading role in the interpretation of all experimental and simulation results.

Publications

Publications directly resulting from the research included in this thesis

1. **Optically controlled dense current structures driven by relativistic plasma aperture-induced diffraction**

B. Gonzalez-Izquierdo, R. J. Gray, M. King, R. J. Dance, R. Wilson, J. McCreddie, N. M. H. Butler, R. Capdessus, S.J. Hawkes, J. S. Green, M. Borghesi, D. Neely and P. McKenna, *Nature Physics*, 12, 505-512, 2016.

2. **Optical polarization control of laser-driven proton acceleration in foils undergoing relativistic transparency**

B. Gonzalez-Izquierdo, M. King, R. J. Gray, R. Wilson, R. J. Dance, H. Powell, D. A. Maclellan, J. McCreddie, N. M. H. Butler, S. Hawkes, J. S. Green, C. D. Murphy, L. C. Stockhausen, D. C. Carroll, N. Booth, G. G. Scott, M. Borghesi, D. Neely and Paul McKenna, Under review, 2016.

3. **Influence of laser polarization on collective electron dynamics in ultraintense laser-foil interactions**

B. Gonzalez-Izquierdo, R. J. Gray, M. King, R. Wilson, R. J. Dance, H. Powell, D. A. Maclellan, J. McCreddie, N. M. H. Butler, S. Hawkes, J. S. Green, C. D. Murphy, L. C. Stockhausen, D. C. Carroll, N. Booth, G. G. Scott, M. Borghesi, D. Neely and Paul McKenna, Under review, 2016.

4. **Azimuthal asymmetry in collective electron dynamics in relativistically transparent laser–foil interactions**

R.J. Gray, D.A. MacLellan, **B. Gonzalez-Izquierdo**, H.W. Powell, D.C. Carroll, C.D. Murphy, L.C. Stockhausen, D.R. Rusby, G.G. Scott, R. Wilson, N. Booth, D.R. Symes, S.J. Hawkes, R. Torres, M. Borghesi, D. Neely and P. McKenna, *New Journal of Physics*, 16, 093027, 2014.

Additional publications resulting from related research performed during this PhD

1. **Intra-pulse transition between ion acceleration mechanisms in intense laser-foil interactions**

H. Padda, M. King, R.J. Gray, H.W. Powell, **B. Gonzalez-Izquierdo**, L.C. Stockhausen, R. Wilson, D.C. Carroll, R. J. Dance, D.A. MacLellan, X. Y. Yuan, N. M. H. Butler, R. Capdessus, R. Torres, M. Borghesi, D. Neely and P. McKenna, *Physics of Plasma*, 23, 063116, 2016.

2. **Ion acceleration and plasma jet formation in ultra-thin foils undergoing expansion and relativistic transparency**

M. King, R.J. Gray, H.W. Powell, D.A. MacLellan, **B. Gonzalez-Izquierdo**, L.C. Stockhausen, G.S. Hicks, N.P. Dover, D.R. Rusby, D.C. Carroll, H. Padda, R. Torres, S. Kar, R.J. Clarke, I.O. Musgrave, Z. Najmudin, M. Borghesi, D. Neely and P. McKenna, *Nuclear Instruments and Methods in Physics Research Section A*, 829, 163-166, 2016.

3. **Proton acceleration enhanced by a plasma jet in expanding foils undergoing relativistic transparency**

H. W. Powell, M. King, R. J. Gray, D. A. MacLellan, **B. Gonzalez-Izquierdo**, L. C. Stockhausen, G. Hicks, N. P. Dover, D. R. Rusby, D. C. Carroll, H. Padda, R. Torres, S. Kar, R. J. Clarke, I. O. Musgrave, Z. Najmudin, M. Borghesi, D. Neely and P. McKenna, *New Journal of Physics*, 17, 103033, 2015.

4. **Annular Fast Electron Transport in Silicon Arising from Low-Temperature Resistivity**

D.A. MacLellan, D.C. Carroll, R.J. Gray, N. Booth, M. Burza, M.P. Desjarlais, F. Du, **B. Gonzalez-Izquierdo**, D. Neely, H.W. Powell, A.P.L. Robinson, D.R. Rusby, G.G. Scott, X.H. Yuan, C.G. Wahlstrom, and P. McKenna, *Physical Review Letters*, 111, 9, 095001, 2013.

5. **Fast electron transport patterns in intense laser-irradiated solids diagnosed by modeling measured multi-MeV proton beams**

D.A. Maclellan, D.C. Carroll, R.J. Gray, N. Booth, **B. Gonzalez-Izquierdo**, H.W. Powell, G.G. Scott, D. Neely, and P. Mckenna, *Laser and Particle Beams*, 31, 3, 475-480, 2013.

Contents

Abstract	i
Acknowledgements	iii
Role of Author	v
Publications	vii
List of Figures	xiii
1 Introduction - From the unknown to plasma physics	1
1.1 Laser Plasma Physics	5
1.2 Thesis Outline	10
2 Fundamental Concepts of Laser-Plasma Interactions	12
2.1 What is a plasma?	18
2.2 Laser-induced ionisation processes	24
2.2.1 Multi-photon ionisation	24
2.2.2 Tunnelling ionisation	26
2.2.3 Barrier Suppression ionisation	27
2.3 When an ultra intense laser beam interacts with plasma	30
2.3.1 Propagation of laser pulse in plasma	30
2.3.2 Polarisation of plane waves	35
2.3.3 Plane waves interacting with plasma electrons	36
2.3.4 Laser absorption mechanisms in plasma	42
2.4 Laser-plasma charged particle acceleration mechanisms	47

3	Onset of Relativistic Induced Transparency	52
3.1	Introduction	52
3.2	Onset of RIT in thick targets	54
3.3	Onset of RIT in thin targets	58
3.4	Examining the effects of RIT on ion acceleration	61
3.5	Other potential applications of the onset of RIT	64
4	Methodology: Laser, Set-ups, Diagnostics & Simulations	67
4.1	Astra-Gemini Laser	67
4.2	Experimental set-up & Key diagnostics	70
4.2.1	Diagnostics	72
4.2.2	Additional devices used in the diagnostics	81
4.3	EPOCH-PIC Simulations	88
5	Deciphering the onset of relativistic induced transparency in foils using optical diagnostics	92
5.1	Relativistic transparency - Target thickness and laser polarisation dependency	92
5.1.1	Experimental Results & EPOCH-PIC Simulations	93
5.2	Relativistic transparency dependency on laser intensity	98
5.2.1	Experimental Results & EPOCH-PIC Simulations	99
5.3	Relativistic transparency curbs radiation pressure - Critical density velocity transition	102
5.3.1	EPOCH-PIC Simulations	104
5.3.2	Experimental Results	115
5.3.3	Discussion of results	117
5.4	Conclusions	120
6	Collective electron response to the onset of relativistic in- duced transparency in ultra-thin foils	122
6.1	Experimental Results	122
6.1.1	Target foils for which transparency does not occur	123

6.1.2	Ultra-thin target foils undergoing transparency	127
6.2	‘Relativistic Plasma Aperture’ in thin foils	128
6.2.1	Linear polarisation	130
6.2.2	Circular polarisation	137
6.2.3	Elliptical polarisation	143
6.2.4	Discussion of results	147
6.2.5	Focal spot size effect	148
6.3	Conclusions	156
7	Collective proton response to the onset of relativistic in-	
	duced transparency in ultra-thin foils	159
7.1	Experimental Results	160
7.1.1	Target foils for which transparency does not occur	160
7.1.2	Ultra-thin target foils undergoing transparency	162
7.2	Collective proton response to relativistic transparency and diffrac-	
	tion in thin foils	165
7.2.1	Hydrocarbon layer on both target surfaces	167
7.2.2	Hydrocarbon layer only on target rear	174
7.2.3	Hydrocarbon layer only on target front	176
7.2.4	Comparing the dynamics of protons sourced at each surface	
	of the target	177
7.2.5	Focal spot size effect	189
7.3	Conclusions	192
8	Conclusions & Future Work	195
8.1	Main research achievements	195
8.2	Future work	199
	Bibliography	202

List of Figures

2.1	Illustration of ionisation processes	25
2.2	Wave dispersion relation	31
2.3	Wave propagation in an underdense and overdense plasma	33
2.4	Normal and oblique incidence of an intense laser in plasma	34
2.5	Relativistic trajectory of an electron	39
2.6	Ponderomotive force effect on a charged particle	42
2.7	Resonant absorption mechanism	44
2.8	Vacuum heating absorption mechanism	45
2.9	$J \times B$ heating mechanism	47
2.10	TNSA and RPA particle acceleration mechanisms	49
3.1	Schematic of the RIT process phases	55
4.1	Astra-Gemini laser configuration	69
4.2	Flow diagram of the Astra-Gemini laser	69
4.3	Experimental target chamber layout	71
4.4	Experimental target chamber set-up	74
4.5	Experimental set-up of the transmitted light diagnostic	76
4.6	Illustration of the main components and quantum efficiency of a pixel from a chip of a CCD camera	77
4.7	Experimental set-up for the measurement of the transmitted light spectrum	77
4.8	Schematic of the Ocean Optics and Shamrock spectrometers	79
4.9	Experimental RCF and IP stack design	82

4.10 Representation of an IP film and its band diagram of absorption and emission	85
4.11 Illustration of RCF films	86
4.12 Representation of a RCF EBT-2 and HD-V2 film	87
4.13 Macro-particles and Yee grid in PIC simulations	89
4.14 PIC algorithm for the fields and fluid momenta evaluation	90
5.1 Experimental results of the transmitted light at 1ω	94
5.2 Experimental measurements of the transmitted light spectrum at 1ω	95
5.3 Experimental result of the transmitted light spectrum using an Andor Shamrock spectrometer	96
5.4 Experimental transmission as a function of target thickness	98
5.5 Experimental generated light in transmission at 2ω	99
5.6 Experimental transmission as a function of the laser intensity	100
5.7 Experimental 2ω light in transmission as a function of the laser intensity	101
5.8 Electron density and laser intensity from a 2D PIC simulation	105
5.9 2D PIC simulation electron density and velocities comparison	106
5.10 Time-space 2D PIC simulation of relativistic critical density veloc- ity	109
5.11 Analytical critical density velocities	111
5.12 Analysis of the relativistic conditions - 10 nm	112
5.13 Analysis of the relativistic conditions - 40 nm	114
5.14 Experimental results of the back-reflected light	117
5.15 Experiment and PIC simulation summary	118
6.1 Schematic configuration of the experimental set-up to measure the electron spatial-intensity distribution	123
6.2 Measured electron density distribution in thick targets and linear polarisation	124

6.3	Measured electron density distribution in thick targets and elliptical polarisation	125
6.4	Measured electron density distribution in thick targets and circular polarisation	126
6.5	Measured electron density distribution for a 10 nm target	127
6.6	Schematic of the Gaussian spatial-intensity distribution of an ultra-intense laser pulse	131
6.7	3D simulation profile of a linearly polarised laser in a predefined aperture with a fixed 3 μm -diameter	132
6.8	Intensity diffraction pattern induced by a fixed, predefined aperture	133
6.9	3D PIC simulations of laser diffraction and plasma electron density - linear polarisation	134
6.10	Electron density and the laser intensity - linear polarisation	135
6.11	Analytical model representation - linear polarisation	135
6.12	3D PIC simulations of laser diffraction and plasma electron density - circular polarisation	138
6.13	Electron density and the laser intensity - circular polarisation	139
6.14	Analytical model representation - circular polarisation	139
6.15	Combined plot showing the 3D laser intensity profile and the temporal evolution of the electron density distribution, overlaid with the laser intensity distribution	141
6.16	Magnetic field structure driven by circularly polarised light	142
6.17	3D PIC simulations of laser diffraction and plasma electron density - elliptical polarisation	144
6.18	Electron density and the laser intensity - elliptical polarisation	145
6.19	Analytical model representation - elliptical polarisation	146
6.20	3D PIC simulation results for the electron density distribution	147
6.21	3D simulation profiles for a 1.5 μ (FWHM) laser	149
6.22	3D EPOCH simulation with laser focal spot size equal to 1.5 μm	150
6.23	HVDT and 3d PIC simulation of a 1.5 μm -diameter aperture	151

6.24	3D simulation profiles for a 6μ (FWHM) laser	152
6.25	Analytical model and PIC simulation of the near-field diffraction pattern through a $6 \mu\text{m}$ -diameter aperture - linear polarisation	153
6.26	3D EPOCH simulation with laser focal spot size equal to $6 \mu\text{m}$	155
6.27	PIC simulation of the near-field diffraction pattern through a $6 \mu\text{m}$ -diameter aperture - circular polarisation	156
7.1	Schematic configuration of the experimental set-up used to mea- sure the proton spatial-intensity distribution	160
7.2	Experiment results for the proton density distribution in thick tar- gets and linear polarisation	161
7.3	Experiment results for proton density distribution in thick targets - elliptical and circular polarisation	162
7.4	Representative experiment results of the proton beam density dis- tributions in thin targets	163
7.5	Illustration of the 3D PIC simulation layout to investigate the pro- ton spatial-intensity distribution	168
7.6	3D-PIC simulation results showing the proton spatial-density dis- tribution for linear polarisation	169
7.7	3D-PIC simulation results showing the proton spatial-density dis- tribution for linear polarisation - projections	169
7.8	3D-PIC simulation results showing the proton spatial-density dis- tribution for elliptical polarisation	171
7.9	3D-PIC simulation results showing the proton spatial-density dis- tribution for elliptical polarisation - projections	172
7.10	3D-PIC simulation results showing the proton spatial-density dis- tribution for circular polarisation	173
7.11	3D-PIC simulation results showing the proton spatial-density dis- tribution for circular polarisation - projections	174
7.12	Comparison of spatial-density and kinetic energy distributions for only target rear surface accelerated protons	175

7.13 Comparison of spatial-density and kinetic energy distributions for only target front surface accelerated protons	177
7.14 Electrostatic field and particle density evolution with protons on both surfaces - linear polarisation	179
7.15 Front-only and rear-only proton sources - linear polarisation	180
7.16 Electrostatic field and particle density evolution with protons on both surfaces - elliptical polarisation	181
7.17 Front-only and rear-only proton sources - elliptical polarisation	183
7.18 Electrostatic field and particle density evolution with protons on both surfaces - circular polarisation	184
7.19 Front-only and rear-only proton sources - circular polarisation	185
7.20 Evolution of the maximum proton energy and rate of change in kinetic energy	187
7.21 Evolution of the maximum longitudinal electrostatic field . .	188
7.22 3D-PIC simulation of proton spatial-density for linear polarisation and 1.5 and 6 μm focal spot size	190
7.23 Electrostatic field and particle density evolution with hydrocarbon layers on both surfaces - 1.5 μm focal spot size	191
7.24 Electrostatic field and particle density evolution with hydrocarbon layers on both surfaces - 6 μm focal spot size	192

Chapter 1

Introduction - From the unknown to plasma physics

Curiosity and adaptability can be considered as some of the most important traits which have given humans an evolutionary advantage over other species. This curiosity has driven humans to feel a fascination and desire to explain the natural events which they can see and perceive around them, since early times. Although early civilisations, such as Greeks or Babylonians, were curious and sceptical, with the advent of authority figures, first approaches to interpret the world in the form of ‘revealed’ religions, and dogmatisms led humanity to predominantly accept the traditional interpretations. With the passage of time, this kind of thinking was left behind and thus, emerged different minds which defended a more critical contemplation of the world and which were not in conformity with the atavistic ideas of the time. This conception was elegantly described by Immanuel Kant, in 1784, when he wrote an essay about *What is Enlightenment?*:

Enlightenment is man’s emergence from his self-imposed immaturity. Immaturity is the inability to use one’s own understanding without guidance from another. This immaturity is self-imposed when its cause lies not in lack of understanding, but in indecision and lack of resolve and courage to use it without another’s guidance. Dare to

know! (*Sapere Aude!*).

This group of people quickly understood that with a ‘rational’ interpretation of every aspect of nature, not only could they reproduce, control and use it for new and fascinating applications, but could also improve on the existing. From that moment, reason would be one of the most powerful tools to describe and to justify the universe around us. This was the pillar for the emergence of the known *Scientific method*; the purpose of which is to find the explanation of phenomena based on empirical, measurable and reproducible evidence via the principles of reasoning. So, it is in the following very elegant and effective way that science works (most of the time). A phenomenon is observed, experiments are performed (if possible), a theoretical/simulation model which explain the observation is developed and new potentially observable phenomena are predicted. If these phenomena are not explained with the proposed theoretical/simulation model, this model is dropped and a new one is sought which can explain the observed phenomena in a more precise way.

One phenomenon which has always been both an object of fascination, and intrigue, for humanity, has been *light*. That strange visual sensation experienced in situations such as when the sun was higher than the horizon or when a fire was initiated. What was this mysterious and extraordinary phenomenon? Where did it come from? What was it made of?

To find the first documented evidence where human beings tried to search an answer to these questions about light, we have to go to the fifth century BCE (Before Common Era) in Ancient Greece, when Empedocles of Agrigentum wrote a poem, named *About Nature*, where he postulates the existence of four fundamental elements: earth, air, water and fire. Several others tried to solve this puzzle, such as Plato, Aristotle, Titus Lucretius Carus (who said that light was formed by tiny particles which travel through the air without impediment, pushed forwards by other subsequent particles), Claudius Ptolemy (who studied

the refraction effect observed when light travel from one medium to another), or Hero of Alexandria who proposed that light, travelling through the same medium, will follow the shortest path between two points (a predecessor to Fermat's principle). Furthermore, there is an exceptional testimony from the Arabic scientific community after the tenth century CE (Common Era) whose one of the most prestigious figure was Abu Sa'd al-'Ala' ibn Sahl. He demonstrated the *refraction law* using right triangles and the relation between legs and hypotenuses (now known as *Snell's law*). Another major Arabic scientific figure was Ibn al-Haytham, more known as Alhazen, who in the book *Opticae Thesaurus* included an extensive description of his idea about perception of light.

Although some of the aforementioned people also tried to explain the composition of light, they, instead, focused their efforts more to the end of delivering a description of how light is detected by our eyes, and of the behaviour exhibited by light as it interacts and travels through different media. They used a natural philosophy employing hypotheses without mathematics or any solid empirical base. In Europe, it was not until the Renaissance, that the free discussion of philosophical and scientific ideas grew. From that moment, and especially from Galileo Galilei, the conception of the nature of light would be found to be more sophisticated than previously thought, based on experiments and predictions. It was at this time that mathematics started to be used to interpret reality. In this period arose one of the most famous arguments in physics: *is light a wave or a particle?*

Rene Descartes was the first scientist to describe light as a wave (wave hypothesis) based on its similarity with sound waves. The velocity of both changes when they travel from one medium to another, which results in modification of wave propagation direction. On the other hand, Pierre Gassendi, like Lucretius several centuries before, proposed that light was composed of tiny particles, and he was also the first modern scientist to postulate the corpuscular hypothesis.

One of the most famous scientists who defended this corpuscular hypothesis was Isaac Newton. He conducted multiple experiments with light and in all of them he saw very sharp shadows but never observed diffraction effects. On the other side was Christiaan Huygens who developed a mathematical and coherent theory about the wave nature of light. Some years later Thomas Young carried out one of the most distinguished experiments about the intrinsic nature of light, commonly referred to as the *double-slit experiment*. In this experiment he demonstrated the diffraction of light travelling through two parallel narrow slits, resulting in producing an interference pattern. These results could only be explained with the wave hypothesis of the light. In addition, Augustin-Jean Fresnel, developed a mathematical theory about light waves [1], which predicted with high precision the experiments concerning interference and the diffraction of light. Moreover, with Michael Faraday's experiments and James Clark Maxwell's mathematical theory, it was clear that light was not only a wave but also an electromagnetic wave (see section 2). This electromagnetic wave hypothesis was experimentally demonstrated by Heinrich Rudolf Hertz, who was able to induce an electrical current in a circuit from another circuit placed at a distance to this first one. His experiments also demonstrated that there are more electromagnetic waves outside the range of visible light which are invisible to the human eye.

The wave theory of light seemed to explain most physical phenomena of light-matter interaction. However, this changed in 1905 when Albert Einstein published a paper where he presented an explanation of the photoelectric effect, which could not be explained by the wave theory of the light. Based on Planck's hypothesis, where the energy of a linked system, like an electron with an atom has discrete values (i.e. quantised), he proposed that any electromagnetic wave was also quantised in packets of energy, which he called *Lichtquant* (known today as *photons*). This new theory provided a very clear explanation of the experimental results, which led to the acceptance of the idea that light is both

a wave and a particle: commonly known as wave-particle duality. Depending on the experimental conditions light will demonstrate either a wave-like or a particle behaviour. A recent publication displays the simultaneous observation of this wave-particle duality of light for the first time [2]. Additionally, after Louis de Broglie we know that, as light, universally every known particle presents wave-particle duality depending on the environmental conditions.

During the first half of the twentieth century CE knowledge about the generation and propagation of light was encapsulated in a matured theory (improved with the quantum theory). In the earlier 1950s Charles H. Townes, and Nikolay Basov and Alexander Prokhorov working in parallel but independently to Townes, developed a new microwave source called *MASERs* (Microwave Amplification by Stimulated Emission of Radiation). The singularity of this new source was its high temporal/spatial coherence, monochromaticity, low divergence and high brightness. In 1958, Charles H. Townes published, together with his brother-in-law Arthur Schawlow, a work where they extended the maser idea to infrared and optical visible wavelengths [3]. Unfortunately, they did not have sufficient economic support and thus were unable to make it a reality. However, two years later, in 1960, the private Hughes Laboratories built the first optical maser, commonly referred to as a *LASER* (Light Amplification by Stimulated Emission of Radiation). The scientific community was fair awarding the Nobel's prize to Townes (together with Basov and Prokhorov) instead of to researchers from the Hughes Laboratories. This new light source opened the gates to a world more strange and wonderful than we could have imagined.

1.1 Laser Plasma Physics

Due to the advent of the first laser, in 1960, an enthusiastic run to use this new light source was initiated, not only in traditional experiments but also in

finding new potential applications. One of the most fascinating uses, out of the multiple applications that lasers currently have, is its use in plasma generation and laser-plasma interactions studies. Today, these studies are being focused in their potential use as an alternative to conventional particle accelerators, that are the standard for particle colliding, in inertial confinement fusion and for the generation of high energy charged particles for medical applications. However, numerous investigations and efforts still have to be made by the scientific community to obtain higher quality, controllability and stability of particle beams and energy spectrum, which could actually compete with the traditional techniques.

To achieve high particle energies, conventional accelerators are based on constructing huge structures, such as the LHC (Large Hadron Collider) at CERN, straddles the border between France and Switzerland. This is a circular ring with a 27 km circumference, which produces a few TeV proton energies. Although it was eventually cancelled due to economic issues, the construction of the Superconducting Super Collider (SSC) project was initiated in the 1980's in the United States. This would have been an ~ 87 km circular proton-antiproton collider, producing proton energies up to a few tens of TeV. However, purely increasing the radius of colliders in order to increase the maximum particle energy has the undesirable effect of critically increasing the levels of synchrotron radiation emitted, which prevents circular accelerators being used to accelerate lighter particles, i.e. electrons, beyond a few TeV. For example, a 1 TeV electron would radiate more than half its energy in just one rotation of a 16 km radius collider [4]. Due to this phenomenon, most current research efforts on electron accelerators focus on linear devices, as for example the SLAC National Accelerator. However, a circular or linear configuration, using conventional RF (Radio-Frequency) techniques applied to electron acceleration, have accelerating gradients of no more than a few tens of MVm^{-1} . This results in enormous

accelerator lengths to achieve high particle energies, as evidenced by the 3.2 km SLAC facility. A substantial increase in accelerating gradients is required in order to build charged particles accelerators of reasonable lengths, that can fit in universities or hospitals for cancer treatment by using protons and heavy ions beams [5,6]. Although this medical application needs lower particle energies than those obtained with the conventional accelerators, the large size required for its implementation make them not practical and economically non-viable.

One of the most promising techniques for achieving large magnitude acceleration gradients to accelerate charged particles, with a more compact size, is the laser-plasma accelerator scheme. First proposed by Tajima and Dawson in 1979 [7] (the production of plasma using laser pulses was proposed by Dawson earlier in 1964 [8]). Their key idea was to excite a large amplitude electron plasma waves by using a short pulse lasers in high density plasmas; which is commonly referred to as laser wakefield acceleration (LWFA). Unfortunately, at that time lasers with the required properties to test their mechanism were not available. In 1995 Nakajima *et al.* [9] were able to accelerate electrons up to 100 MeV using the LWFA method, after the development in 1985 of the Chirped Pulse Amplification (CPA) technique [10–12]. CPA enabled the generation of ultra-short and intense pulses while avoiding the damage threshold of solid state optics in the laser system. Another approach to electron acceleration has been to use the radiation pressure of an electromagnetic wave directly in gas and solid targets through the ponderomotive force [13,14]. At the time of writing this thesis, this method cannot reach the maximum electron energies obtained with the LWFA technique, but it has opened new directions for ion acceleration. Due to the fact that the laser intensities required to directly accelerate heavier ions are not feasible so far, the ions are accelerated due to high electrostatic fields generated from charge particle separation during the laser plasma interaction. The most promising technique involving laser pressure, known as Radiation Pressure Acceleration

(RPA) is described in more detail in the next chapter amongst other electron-ion acceleration methods.

With the current classes of laser-plasma accelerators it is possible to reach acceleration gradients in the range GVm^{-1} - TVm^{-1} . That means between 3 and 4 orders of magnitude higher than those achieved in the conventional RF accelerators. This is not only an important reason for using laser-plasma for particle acceleration; the issue of dielectric breakdown in RF cavities has also been overcome. To reach these large gradients implies the requirement of very high electric fields which may cause electrical breakdown in the accelerator walls or residual gas within the cavity. In a plasma, there is no such limitation since the material is already ionised. Furthermore, plasmas are able to propagate large electric fields in the form of electron plasma waves, orders of magnitude larger than the fields in conventional accelerators, enabling the charged particles to reach relativistic energies. Although laser plasma accelerators can overcome some of the limitations of conventional particle accelerators, in addition to reaching much higher acceleration gradients, there are still many challenges to overcome to be a real and competitive alternative, like a substantial increase in the maximum charged particle energies.

Another promising application of laser-plasma interaction is in inertial confinement fusion (ICF) where multiple high power laser beams interact simultaneously on a spherical capsule (or the inside of a hohlraum surrounding the capsule) filled with deuterium-tritium (D-T) to achieve fusion and generate a potential new source of energy. For a fusion power plant, gains (energy released compare to energy required to confine the plasma) above 100 are required due to relatively low driver and hydrodynamic efficiencies [15]. For these reasons, Tabak *et al.* proposed in 1994 the fast ignition as a higher gain approach compared to conventional central hot spot ignition [16]. In this scheme the ignition step is separated from the compression processes, by using a secondary ultra-intense

laser, which, by channelling [17, 18], is expected to penetrate as close as possible to the compressed core of the target. The expectation is that the compression and symmetry requirements will be reduced significantly. Around this concept, a variety of new approaches have been developed, such as using a re-entrant cone shell, designed to keep the propagation path of the secondary short-pulse laser free from the plasma that forms around the imploding shell; thus avoiding laser propagation issues [19, 20]. Others, however use charged particles for the ignition process, such as electron beams, instead of a secondary laser [21–23]. To achieve the implosion, petawatt laser pulses are required to generate MeV electrons. These deposit several tens of kilojoules in the compressed D-T core. In addition, the use of protons [24, 25] and heavy ions [24, 26, 27] configurations for the ignition step have also been proposed. In spite of the huge effort of the laser-plasma community in the last few decades, and the good results predicted by theoretical and simulation models, today key challenges still have to be overcome to achieve fusion by inertial confinement. This fact is due to the multiple issues arising around the actual experiments like the maximum energy achieved and coupled into the core, the filamentation [28] and the instabilities [29–31] (which might also reduce the energy coupling between the laser and plasma and the energy transported by the electron beam which is deposited into the compressed core) that arise during the intense laser plasma interaction.

Although the laser plasma field has been an active research field for some decades, due to the extremely high laser intensities required and the very short time and space scales where everything happens, we are far from having a ‘complete’ understanding. We have however, achieved a precise understanding of some aspects. Moreover, this is accentuated by the continuous improvement of the technology enabling us to go further and deeper into the underpinning physics.

This thesis addresses a fundamental relativistic effect - relativistic induced

transparency - driven by intense laser light interaction with dense plasma. It is focused on experimental and numerical (by Particle in Cell simulations) investigations for the characterisation of the onset of this transparency regime and its effect in the collective electron and ion response, whose new and original conclusions are described in detail in the following chapters.

1.2 Thesis Outline

This thesis is structured as follows:

- In **Chapter 2** a detailed description of the most significant background theory, which is essential to define and understand the underpinning physics involved in the physical processes included in the research chapters of this thesis, is presented. This chapter starts with the definition of the ‘plasma’ concept and continues with the description of laser-plasma generation and interaction. Finally, a brief introduction of the particular laser-plasma particle acceleration mechanisms are included.
- **Chapter 3** includes a precise review of the state of the art of the relativistic induced transparency due to it is one of the most important concepts presented in this thesis.
- Before the research work is presented, in **Chapter 4** the methods used to obtain the experiment and numerical data are introduced. This includes the laser, set-ups and diagnostics employed in the experiments. A description of the PIC code used for carrying out the simulations is also included.
- **Chapter 5** presents results from an investigation of the experimental characterisation of the onset of the relativistic induced transparency for different laser polarisations, laser intensities and target thicknesses. Results from 1D-2D PIC simulations are also included to interpret and explain

the experimental findings. In addition, by using 2D PIC simulations, and focused in the evolution of the front surface velocity of the target, for a range of thin target thicknesses, distinctive acceleration mechanisms are identified, demonstrating additionally that the onset of the relativistic transparency curbs the efficiency of the radiation pressure.

- In **Chapter 6** a novel approach to explain the electron-laser interaction with ultra-thin foils undergoing relativistic transparency is introduced and investigated in depth. This study has been performed numerically (by 3D PIC simulations) and experimentally for different laser polarisations and target thicknesses.
- Following on from the investigation of electron dynamics, in **Chapter 7** the investigation of the proton dynamics in ultra-thin foils undergoing relativistic transparency is presented experimentally and through 3D PIC simulations for different laser polarisations and target thicknesses.
- Finally, in **Chapter 8**, the conclusions of the most important research results of this thesis are briefly summarised. Potential future work and steps are also discussed.

Chapter 2

Fundamental Concepts of Laser-Plasma Interactions

Before introducing the fundamental concepts of laser-plasma physics relevant to this thesis, it is useful first to review some basic electromagnetic theory, including the four Maxwell's equations and the Lorentz's force equation. Thanks to these equations the global physics, behaviour and nature of plasma, as well as the interaction with light, can be described and explained. A thorough knowledge of these fundamental equations is therefore required to understand the underpinning plasma physics as a whole.

Maxwell's equations

Before the Scottish physicist James Clerk Maxwell published his *Electromagnetic Theory of Light* in 1864, electricity was known a rather long time. Scientists knew that a '*charged particle*' (the electron was not discovered until 1897 by J.J Thompson [32], and the proton until 1919 by Ernest Rutherford) created an electric force between other charged particles, and which was proportional to the product of the particle charges and inversely proportional to the square of the distance between them. One century earlier, this phenomenon was formulated by Charles-Augustin de Coulomb as a result of precise experiments to confirm the

inverse-square laws of electricity and magnetism, which were defined by Joseph Priestley and John Michell some years earlier. Moreover, in 1813, Karl Friedich Gauss formulated the relation between the electric field and the density of the charges that generated such a field (although it was Joseph Louis Lagrange who discovered this relation in 1762). Besides this, the scientific community knew that the motion of these particles through space was the origin of electric currents.

It was also known that several materials exhibited magnetic properties, and like charged particles (depending on their charge), could attract or repel each other. However, both concepts were completely independent. Hans Christian Oersted, in 1820, discovered that an electrical current produced a magnetic field, although he could never explain the physical reason behind this phenomenon. Nevertheless, it was a very important step linking these two concepts which were independent until that moment.

Another enigma in this era was *light*. There were different theories which described light like a wave and others like a particle (as presented in the Introduction of this thesis), but there wasn't a theory which could explain its generation and propagation.

In the 1830's, however, arose the genius of Michael Faraday. After many experiments on electricity and magnetism, Faraday proposed that one body could interact with another by means of electrical and magnetic forces through the existence of *lines of force*. He demonstrated the presence of an induction (electromotive force generated in a material which is exposed to a time varying magnetic field) between two electrical currents. He also demonstrated that in the inner region of a conductor in equilibrium the electromagnetic field is *zero* (known as the *Faraday cage*), and demonstrated that a magnetic field varying in time creates an electric field. These contributions alone would be enough to consider him as one of the most important experimental physicists who contributed to the formulation of the electromagnetism theory. However,

he went one step further and showed experimentally that linear polarised light changed its polarisation plane when travelling through a parallel magnetic field in a medium (a phenomenon later named the *Faraday's rotation*). This was the first experimental evidence about the relation of light and electromagnetic fields. Unfortunately, he did not have enough mathematics and physics knowledge to formulate a theory to explain his results.

The age of electromagnetism began in 1855, when Maxwell, being only 24 years old, presented his study *On Faraday's Lines of Force* [33] to the Cambridge Philosophical Society. In it, he established a theoretical analysis to explain the experimental observations of Faraday; explaining the relation and the influence between electric and magnetic fields using a total of **20 equations**. However, it was in 1861-1862, when Maxwell published a new version of his previous paper in four parts, *On Physical Lines of Force* [34], where he established the equations which describe the interaction between electric and magnetic fields using vectorial calculus and quaternion algebra (introduced by William Rowan Hamilton in 1843) combining the laws and theorem proposed by Coulomb, Faraday, Gauss and Ampere. Additionally, in this paper, Maxwell introduced for the first time the displacement current term of the Ampere's law; where an electrical field, varying in time, generated a magnetic field. This was his unique original contribution in these equations, but, as is often the case, merit is not only from creating but also combining dispersed concepts in a more elegant unified and compact theory.

Playing with these equations Maxwell noticed that in the *luminiferous ether* case (the existence of the ether was accepted from many years prior to this), where in the case when there is not any particle charges, not all these equations were zero. Combining the non-zero equations he got that both, the electric and magnetic fields were described as a mathematical *wave function*. Moreover, he saw that the term $1/\sqrt{\epsilon_0\mu_0}$ had units of velocity. In that moment, the values of ϵ_0 and μ_0 were approximately calculated. When Maxwell substituted these values in

he got a value for the velocity of the electrical and magnetic waves on the order of 31070000 m/s . This value was very close to the velocity of light obtained from experiments around this time. He concluded undoubtedly that light was constituted by electrical and magnetic waves, as stated in his *On Physical Lines of Force* [34]:

“We can scarcely avoid the inference that light consists in the transverse undulations of the same medium which is the cause of electric and magnetic phenomena.”

All these novel and revolutionary ideas were published in the aforementioned *Electromagnetic Theory of Light* paper in 1864. After this paper, and the experimental results of Faraday, concepts of electric fields, magnetic fields and light, completely independent until that moment, would not be separated again [35]. In fact it was Oliver Heaviside who some years later reduced the 20 Maxwell’s equations to the four equations recognised by scientists inside the physics community [36], and which in their differential form are:

Gauss’ Law for Electric field generation

$$\nabla \cdot \mathbf{E} = \frac{\rho}{\epsilon_0} \quad (2.1)$$

where \mathbf{E} is the electric field, ρ is the charge density and ϵ_0 is the vacuum permittivity.

Gauss’ Law for Magnetic field generation

$$\nabla \cdot \mathbf{B} = 0 \quad (2.2)$$

where \mathbf{B} is the magnetic flux density and commonly known as magnetic field.

Faraday-Maxwell equation (Electromagnetic Induction)

$$\nabla \times \mathbf{E} = -\frac{\partial \mathbf{B}}{\partial t} \quad (2.3)$$

Ampere-Maxwell equation

$$\nabla \times \mathbf{B} = \mu_0 \mathbf{J} + \mu_0 \epsilon_0 \frac{\partial \mathbf{E}}{\partial t} \quad (2.4)$$

where \mathbf{J} is the current density and μ_0 is the vacuum permeability.

The formulation of the electromagnetic theory was so important that the honoured physicist, Richard Feynman, declared in *The Feynman Lectures on Physics* [37]:

“From a long view of the history of mankind - seen from, say, ten thousand years from now - there can be little doubt that the most significant event of the 19th century will be judged as Maxwell’s discovery of the laws of electrodynamics. The American Civil War will pale into provincial insignificance in comparison with this important scientific event of the same decade.”

Lorentz’s equation

As it has been discussed in the previous paragraphs, the four Maxwell’s equations describe the properties of electric and magnetic fields and their sources, which are electric charges, electric currents (moving charges) and time varying electric and magnetic fields. That is, electric and magnetic fields have been examined as consequences, but what are the effects of these fields on matter?

According to the Maxwell’s equations a charge originates a field and this field affects other charges. This idea is very similar to Coulomb’s version where charges affect other charges. However, in Maxwell’s notation the second step is included, where the fields affect other charges, and these fields act as an intermediary of

the interaction between charges. This influence of the fields over matter (i.e. the exerted force of the fields over the charges) is not described by the Maxwell's equations, but by the *Lorentz's equation*.

J.J. Thompson was one of the first scientists who tried to formulate a mathematical expression to describe motion of charged particles by a magnetic field. In 1881 he obtained the following equation, from experimental data, of the magnetic force as a function of the charge q_e , its velocity \mathbf{v} and the magnetic field \mathbf{B} : " $F = \frac{1}{2}q_e\mathbf{v} \times \mathbf{B}$ ". This expression is correct except for the factor of $1/2$. Although the numeric value predicted by this equation is not correct, the behaviour of charged particles subject to the magnetic field was altogether qualitatively described by his equation. Studying this equation, we can see that any particle only feels the effect of a magnetic force if it has an electrical charge, q_e , it is inside of a magnetic field, \mathbf{B} , and it is moving with a velocity, \mathbf{v} . This last assertion is quite interesting since if an immense charge, q_e , inside an enormous magnetic field, \mathbf{B} , is not moving, the charge will not experience any magnetic force. Summarising, only moving charges generate a magnetic field (Ampere-Maxwell equation (2.4)) and only moving charges can experience a magnetic force (Lorentz's equation (2.6)). Moreover, because of the inclusion on the cross product ($\mathbf{v} \times \mathbf{B}$), in this equation, the resulting force will always be perpendicular to the velocity and the magnetic field, respectively. This implies that a charged particle cannot gain or lose any kinetic energy in a magnetic field but only change its direction.

In relation to the factor of $\frac{1}{2}$, it was Oliver Heaviside (who re-organised and reduced the Maxwell's equations) who, in 1889, formulated the correct equation of the magnetic force:

$$F = q_e\mathbf{v} \times \mathbf{B} \tag{2.5}$$

At this point, it was only necessary to include the effect of the electric field in the previous equation in order to find a complete expression of the electromagnetic

force over a charged particle. This honour was achieved by Hendrik Antoon Lorentz, who, in 1892, published such an equation, including the effect of both the electric and magnetic fields:

$$\mathbf{F} = q_e(\mathbf{E} + \mathbf{v} \times \mathbf{B}) \quad (2.6)$$

Unlike the magnetic force, a particle will feel the effect of an electric force if it has a charge e and if there is an electric field \mathbf{E} :

$$\mathbf{F} = q_e \mathbf{E} \quad (2.7)$$

In this case the charged particle does not have to move, i.e. have a velocity, to experience an electric force. In addition, the electric force will be in the direction of the charged particle sign and in the electric field plane (unlike the magnetic case where the force is perpendicular to the field). The electric force in an electron ($q_e = -e$) will be thus opposite to the electric field direction, and in the same direction for positive charged particles ($q_e = Ze$). Because of this fact, a charged particle can gain or lose kinetic energy in an electric field, on the contrary to the case of a magnetic field.

With the four Maxwell's equation, and the Lorentz's equation we have all the necessary formalisation to understand the generation of electromagnetic fields and the resultant interactions it has with matter.

2.1 What is a plasma?

The latest models and cosmological observations [38] indicate that from the total mass-energy of the universe the $\sim 68\%$ is in form of dark energy, $\sim 27\%$ is in form of dark matter and only $\sim 5\%$ is in form of baryonic matter. Although it is thought that 90% of the baryonic matter is in the plasma state, it was not until

the last period of the 19th century that the plasma state of matter was created in the laboratory environment. The first documented experiment of this was carried out by William Crookes, who in 1879, and using a Crookes tube (named in his honour), was able to ionise residual gas remaining in the tube with a very high electrical potential between an anode and cathode (producing a plasma), and generating ‘cathode rays’ (electron beams). However, the term ‘plasma’ composed of similar number of ions and electrons, was not used until 1928, when Irving Langmuir published a paper [39] where he observed (and confirmed a previous work by *Penning* [40]), conducting experiments with mercury arcs, that near the electrodes a *sheath* was created containing a gas with approximately equal number of ions as electrons.

The origin of the name *plasma* as a reference to this ionised gas is well described by his colleague Harold M. Mott-Smith [41]:

“[...] Langmuir began to study mercury vapour discharges. [...] We noticed the similarity of the discharge structures they revealed. Langmuir pointed out the importance and [...] We struggled to find a name for it. [...] one day Langmuir came in triumphantly and said he had it. He pointed out that the ‘equilibrium’ part of the discharge acted as a sort of sub-stratum carrying particles of special kinds, like high-velocity electrons from thermionic filaments, molecules and ions of gas impurities. This reminds him of the way blood plasma carries around red and white corpuscles and germs. So he proposed to call our ‘uniform discharge’ a ‘plasma’.”

However, not all ionised gases are considered as plasmas. Unlike ordinary air where the motion of a neutral molecule is controlled by the eventual collisions with other neighbouring molecules, in a plasma, which consists of positive and negative charged particles, the situation is notably different. Due to the movement of these charged particles, they generate locally positive and negative regions originating

electric fields. Moreover, because of this movement of charged particles (an electrical current), magnetic fields are generated; as discussed previously. These fields decrease with distance but are able to affect the motion of particles situated at “large distances”. Because of this, the motion of a particle not only depends on local conditions but also on the electromagnetic fields generated by other particles not situated relatively close to it. This representative effect in plasmas is known as *collective behaviour*, arising as a consequence of the following characteristics which are necessary to be satisfied in order to distinguish a plasma from a neutral gas, or a partially ionised gas [42, 43]:

- Quasi-neutrality: Starting with a neutral ionised gas ($Zn_i = n_e$), if, for example, a new positive test particle is included, a charge imbalance will be created. However, this charge imbalance will be quickly neutralised by a ‘cloud’ of electrons which will be attracted to the new additional positive charge. Imagine a situation where the plasma is relatively cold and there is no thermal motion, there would be the same amount of negative charges in the cloud than positive in the test particle. In this scenario the shielding would be perfect, and there would not be an electric field present outside the cloud. However, in a more realistic situation, plasma particles have thermal motion, and the electrons at the edge of the cloud have enough energy to escape from the electrostatic potential created by the test particle.

Peter Debye and Erich Huckel were the first scientists who in 1923 [44] in the context of *electrolytic* theory, pointed out that the field due to any charge imbalance is shielded and its influence is effectively restricted to within a finite range.

From the scalar potential ϕ created by the test particle in 1-dimension we can obtain an approximate thickness of the charge cloud around it, required

for shielding. Using Gauss's Law (2.1) we obtain:

$$\frac{d^2\phi}{dx^2} = \frac{-e(n_i - n_e)}{\epsilon_0} \quad (Z = 1) \quad (2.8)$$

where $\mathbf{E} = -d\phi/dx \hat{x}$ was assumed. Moreover, if we ignore the ion motion and the plasma is thermally in equilibrium, we can assume that the number density of the electron cloud n_e is given by a Boltzmann distribution of the form:

$$n_e = n \cdot \exp\left(\frac{e\phi}{k_B T_e}\right) \quad (2.9)$$

where k_B is the Boltzmann constant and T_e the electron temperature.

Now, substituting equation (2.9) into (2.8) and assuming that the ion density is $n_i = n$ in a region far from the electron cloud, we find:

$$\frac{d^2\phi}{dx^2} = \frac{en}{\epsilon_0} \cdot \left[\exp\left(\frac{e\phi}{k_B T_e}\right) - 1 \right] \quad (2.10)$$

If the last equation is expanded in a Taylor's series in the first order around 0, by assuming a potential energy much lower than the electron temperature, it is found:

$$\frac{d^2\phi}{dx^2} = \frac{e^2 n}{\epsilon_0 k_B T_e} \phi \quad (2.11)$$

Finally, solving this differential equation, the scalar potential created by the test particle in 1-dimension is:

$$\phi = \phi_0 \exp\left(\frac{-|x|}{\lambda_D}\right) \quad (2.12)$$

where the parameter:

$$\lambda_D = \sqrt{\frac{\epsilon_0 k_B T_e}{e^2 n}} \quad (2.13)$$

is known as *Debye length* and defines the shielding distance beyond which the plasma remains effectively neutral. For this reason, outside the sheath the potential will be very weak, creating a small charge imbalance and generating a ‘quasi-neutral’ plasma, but neutral enough to consider $Zn_i \approx n_e$.

Therefore, quasi-neutrality suggests a plasma can be interpreted as neutral overall, but electrically charged locally. The scale beyond which the plasma can be considered as neutral is defined by the Debye length. For distances smaller than this value the plasma will be electrically charged and the motion of each individual charged particle will be determined by the electromagnetic influence of surrounding charged particles.

- The previous effect is only true if λ_D is much smaller than the dimensions of the plasma L ($\lambda_D \ll L$). If this criterion is satisfied, whenever local concentrations of charge arise or external potentials are introduced into the plasma, these will be shielded out in a distance short compared to L , leaving the bulk of the plasma free of large electric potentials or fields.
- Moreover, as shown in equation (2.13), λ_D decreases when the plasma density n increases. Therefore, in order to satisfy the previous points, it is required that a large number of electrons, N_D , be present within a region of space commonly referred to as the Debye sphere, i.e. $N_D \gg 1$, which is the region of the charged cloud inside of a sphere with a radius equal to λ_D .

Langmuir also introduced the concept of electron oscillations inside a plasma [39]. However, the equation to describe these oscillations (also known as Langmuir waves) was derived by Tonks and Langmuir [45] in 1929. They used Gauss’s law of electric field generation (2.1), which in one dimension can be approximated as:

$$E = \frac{en_e}{\epsilon_0} x \quad (2.14)$$

Additionally, electron dynamics will be governed by the Lorentz's Force, which in the case of sufficiently small oscillation the term $\mathbf{v} \times \mathbf{B}$ can be neglected (as explained in more detail in the section 2.3.3):

$$\mathbf{F} = -e\mathbf{E} \longrightarrow m_e \frac{d^2x}{dt^2} = -e\mathbf{E} \quad (2.15)$$

Combining (2.14) and (2.15) and rearranging, the equation of the motion of electrons in a plasma is described as:

$$\frac{d^2x}{dt^2} + \frac{e^2 n_e}{\epsilon_0 m_e} x = 0 \quad (2.16)$$

The equation (2.16) clearly shows that electrons will oscillate around their rest position with simple harmonic motion, at a naturally frequency equal to:

$$\omega_p = \sqrt{\frac{e^2 n_e}{\epsilon_0 m_e}} \quad (2.17)$$

where $e = |-e|$ is the absolute value of the electron charge, n_e is the electron density, ϵ_0 is the vacuum permittivity, and m_e is the electron mass. This frequency is known as the *plasma frequency*.

The electron density, n_e , depending on the material, can be obtained as:

$$n_e = Z \cdot N_A \cdot \frac{\rho}{M} \quad (2.18)$$

where Z is the ionisation state (corresponding to the atomic number at full ionisation), N_A is Avogadro's constant, ρ is the material density and M its molar mass.

2.2 Laser-induced ionisation processes

In the previous section the state of matter known as plasma has been introduced. Continuing with the chapter thread, in this section, the mechanisms behind the generation of plasma during an ultra intense laser-solid interaction as well as its interaction with the charged particles within the plasma is examined.

As a consequence of the photo-electric effect, in order to directly photo-ionise an atom (extract one or more electrons) it is necessary that the incident photon has energy at least the same as the binding energy of that electron to the atom. Although the binding energies depend on the element, even the weakest energies are greater than a few to tens of eV [46,47]. The laser used to obtain the research presented in this thesis has a central wavelength of 800 nm (for more details see Section 4.1). At such a wavelength each photon is ~ 1.3 eV in energy terms (from $E = h\nu$), and therefore it is not possible to achieve direct ionisation via single photon absorption. However, ionisation processes can emerge as a consequence of non-linear effects when intense laser beams interact with matter. Depending on the particular parameters of the laser, diverse ionisation processes can be distinguished. Some of the most relevant are presented in the following sections.

2.2.1 Multi-photon ionisation

The multi-photon ionisation process was theoretically predicted, in terms of two photon transitions, by M. Goeppert-Mayer in 1931 [48]. However, because of the high photon densities and energies required to experimentally reproduce this process, the scientific community had to wait almost thirty years, until 1960, when the first laser was discovered, to validate and demonstrate it. In this process each electron has to absorb more than one photon, in a relatively short time-scale, in order to overcome the Coulomb potential of the nucleus. This potential acts like a barrier which binds the electrons into the atomic nuclei. In the case of the

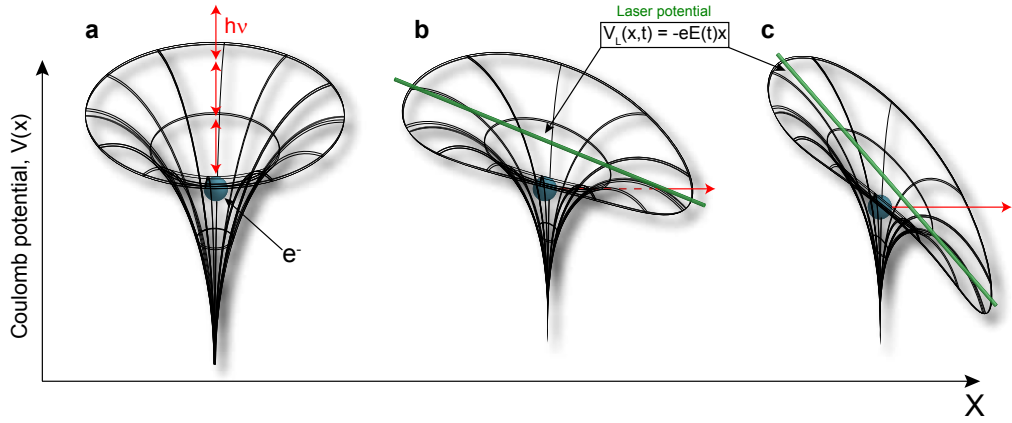


Figure 2.1: Illustration of the three ionisation processes discussed in this section. **a**, Multi-photon, where every red arrow represents a photon absorbed; **b**, tunnelling and **c** barrier suppression. The mesh grid represents the Coulomb potential barrier.

hydrogen atom (with a binding energy of 13.6 eV) it would be necessary for its electron to absorb at least 11 photons (of 800 nm light). Figure 2.1a shows a sketch of this process.

The N-photon ionisation rate (where N is the number of photons absorbed) of an atom varies as $\sigma_N I^N$; where σ_N is a generalised N-photon ionisation cross section and I the laser intensity. As σ_N decreases when the non-linear order N increases, an N-photon ionisation process can be observed at any order N if a high enough intensity is used. Increasing the laser intensity, the photon density (photons/cm³) is increased. When the photons density is higher than the atomic density, more than one photon can interact with each atom. The higher laser intensity, the higher photon density, and therefore higher ionisation rate. One example can be found in [49] where a 11-photon ionisation of Xe at intensities of 10^{14} - 10^{15} is reported. It can be intuitive that further increase of the laser intensity more electrons will be ionised from their atoms. However, when the electrical potential from the laser has values in the order of, or higher, than the Coulomb potential of the electrons (when partnered to the parent atoms), others non-linear ionisation processes can emerge, which are discussed below.

2.2.2 Tunnelling ionisation

The Coulomb potential from an atom can be analytically described as:

$$V(x) = -\frac{1}{4\pi\epsilon_0} \frac{Ze^2}{|x|} \quad (2.19)$$

where Z is the atomic number, e the electron charge and x the distance from the charged particle.

Likewise, the electric potential generated by a laser field is defined as:

$$V_L(x, t) = -eE(t)x \quad (2.20)$$

where $E(t)$ is the time evolving electric field of the laser.

When a photon from the laser interacts with an electron in an atom, both the Coulomb potential of the electron, $V(x)$, and the electric potential from the photon, $V_L(x, t)$, are superposed modifying the Coulomb potential and forming a potential barrier:

$$V(x) = -\frac{1}{4\pi\epsilon_0} \frac{Ze^2}{|x|} - eE(t)x \quad (2.21)$$

Although in a classical perspective it is not possible for the electron to overcome the barrier, in a quantum context, the electron will have a probability to pass through the potential barrier (known as the *tunnelling effect*). This effect is dependent upon the height of the barrier compared to the energy of the electron and the width of the barrier.

Frequently, a value known as *Keldysh* parameter, γ , is used to distinguish quantitatively the tunnelling regime from the multi-photon ionisation process [50]. This parameter compares the ionisation energy, E_{ion} , with the classical

ponderomotive potential, ϕ_{pond} :

$$\gamma = \sqrt{\frac{E_{ion}}{2\phi_{pond}}} \quad (2.22)$$

ϕ_{pond} is described as:

$$\phi_{pond} = \frac{e^2 E^2}{4m_e \omega_L^2} \quad (2.23)$$

Qualitatively these two ionisation processes can be differentiated with low ionisation energies and high electric fields (or $\gamma \leq 1$) for the tunnelling effect to dominate, and with high ionisation energies and low electric fields (or $\gamma > 1$) for the multi-photon ionisation to be the dominate process.

2.2.3 Barrier Suppression ionisation

When the intensity of laser light is increased even further, there will be a moment when the total potential formed by the Coulomb potential of the electrons and the electric potential from the incoming photons will exceed the ionisation potential of the atom, and the electrons will be directly ionised without tunnelling. This process is commonly referred to as *barrier suppression ionisation*.

From equation (2.21) the laser intensity needed to ionise an atom by barrier suppression can be calculated as:

$$\frac{dV}{dx} = 0 \Rightarrow \frac{dV}{dx} = \frac{1}{4\pi\epsilon_0} \frac{Ze^2}{x^2} - eE = 0 \quad (2.24)$$

$$\Rightarrow \frac{1}{4\pi\epsilon_0} \frac{Ze^2}{x^2} = eE \quad (2.25)$$

$$\Rightarrow x_{max} = \sqrt{\frac{Ze}{4\pi\epsilon_0 E}} \quad (2.26)$$

$$\Rightarrow V(x_{max}) = \sqrt{\frac{Ze^3}{\pi\epsilon_0} E} \quad (2.27)$$

If $|V(x_{max})|$ is greater than the ionisation potential then:

$$\sqrt{\frac{Ze^3}{\pi\epsilon_0} E} = E_{ion} \Rightarrow E = \pi\epsilon_0 \frac{E_{ion}^2}{Ze^3} \Rightarrow I = \frac{c\pi^2\epsilon_0^3}{2Z^2e^6} E_{ion}^4 \quad (2.28)$$

As an example, the ionisation potential of the electron from an hydrogen atom is 13.6 eV. From (2.28), it is found that a laser intensity of $1.4 \times 10^{14} \text{ Wcm}^{-2}$ is required to ionise an electron through barrier suppression. This intensity is several orders of magnitude lower than the laser intensity used to obtain the experimental results and simulations included in this thesis ($\sim 10^{20}$ - 10^{21} Wcm^{-2}). This means that for an ideal laser pulse, with an excellent contrast, the beginning of the rising edge of the laser pulse has sufficient intensity to fully (or partially) ionise a target by barrier suppression, even the atoms with the strongest bound electrons. Laser pulse contrast is defined as the relationship between the intensity of the main peak and the preceding undesirable signals. These signals could appear in distinct sectors of the ultra intense pulses generation process, such as the Amplified Spontaneous Emission (ASE) pedestal or the uncompensated dispersion at the rising edge of the pulse (formed when parts of the pulse are not compressed properly). An excellent contrast is when none of those signals are preceding or after the main pulse, or their intensity is significantly lower than the main peak of the laser.

For an actual ultra-intense laser pulse the contrast has a finite value on the order of 10^8 - 10^{10} . With these values the ASE has sufficient intensity to ionise the front side of a solid target by multi-photon or tunnelling process creating a pre-plasma before the main pulse arrives. Moreover, collisional ionisation processes play an important role in the generation of pre-plasma. This is because when an electron escapes from the Coulomb potential of its host atom by multi-photon

process, for example, its energy is relatively low, increasing its probability of a collision (known as collision cross section) with atoms in its vicinity. These collisions are then able to ionise other atoms. As the laser intensity increases, and ionised electrons gain more energy, their collision efficiency decreases. At this point, the plasma exhibits collisionless behaviour due to Coulomb collisions. This effect is a consequence of the decreasing cross section of electron-ion interactions when the plasma temperature is high enough (\sim electron temperature), thus the degree of collisions is proportional to $T^{-3/2}$ [51]. Moreover, for a plasma with collisionless dynamics, the mean free path between collisions is much larger than the ‘macroscopic’ length scale over which the plasma varies. In addition, the collision frequency is much smaller than the usual frequency at which the plasma varies (typically the plasma frequency).

Due to the considerable electron temperatures reached at the beginning of the laser interaction, the resultant plasma exhibits very high internal thermal pressures which cause it to expand. This expansion creates a decreasing electron density which is usually assumed to follow an exponential profile:

$$n_e = n_{e0} \cdot e^{-x/L} \quad (2.29)$$

where n_{e0} is the solid electron density of the material surface, x the distance from the target and L the scale length of the plasma. This last parameter is used as a measurement of the plasma length and its value corresponds to the distance over which the electron density decreases to $1/e$ of its maximum (e being the Euler’s number). The scale length has a key role in defining the predominant laser-plasma absorption processes, which are discussed in the next section 2.3.4. For short laser pulses, the density scale length is given by the product of the pulse duration and the ion acoustic speed, as is discussed, for instance, in references [52, 53].

2.3 When an ultra intense laser beam interacts with plasma

2.3.1 Propagation of laser pulse in plasma

The propagation of laser light through the plasma will be governed by the dispersion relation (which can be derived, as shown above, from the Maxwell's equation or from the energy conservation law):

$$\omega^2 = k^2 c^2 + \omega_p^2 \quad (2.30)$$

where k is the wavenumber of the incoming beam.

The solution to this equation is plotted in figure 2.2a. From the equation (2.30), distinct parameters can be defined, as the group velocity of a 1D electromagnetic wave:

$$v_g = \frac{d\omega}{dk} = \frac{kc^2}{(k^2c^2 + \omega_p^2)^{1/2}} \quad (2.31)$$

which exhibits an asymptotic tendency of the group velocity to the speed of light in vacuum c (as shown in figure 2.2a):

$$\lim_{k \rightarrow +\infty} \frac{kc^2}{(k^2c^2 + \omega_p^2)^{1/2}} = c \quad (2.32)$$

Figure 2.2a also shows that for laser frequencies smaller than the plasma frequency, ω_p , the wave will not be able to propagate through the plasma and will be reflected. In a physical interpretation of this phenomenon in the context of laser-solid interaction, for normal incidence, the incoming laser pulse will propagate within the preformed plasma up to the known *electron critical density*, n_c . This is defined as the electron density when the plasma frequency is equal to

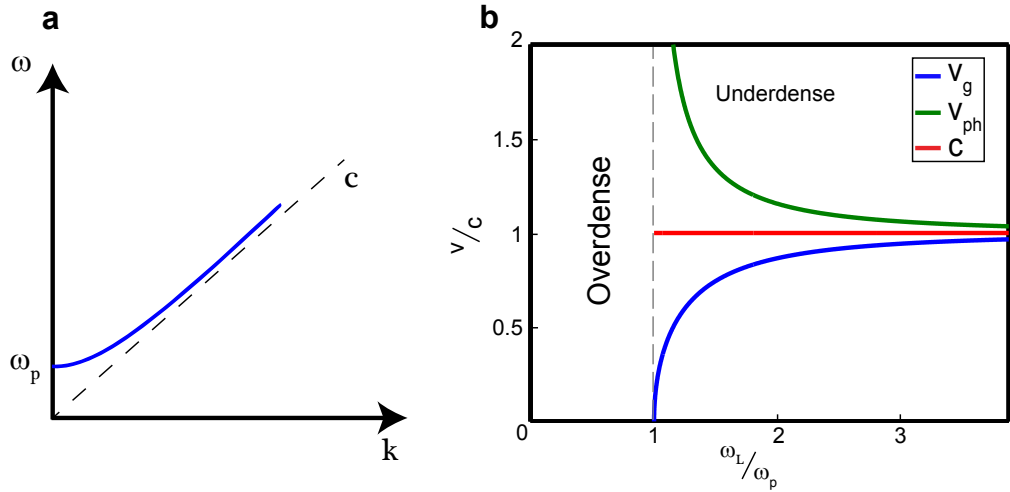


Figure 2.2: **a**, Wave dispersion relation; a wave only presents a real solution and thus, may propagate through plasma if its frequency, ω_L , is higher than the plasma frequency ω_p . **b**, Group and phase velocity of a wave propagating through plasma as a function of its frequency normalised to the plasma frequency. For $\omega_L/\omega_p > 1$ the plasma is *underdense*; instead, if $\omega_L/\omega_p < 1$ the plasma is *overdense*; in the interface between these two regions, the group velocity tends to 0 whereas the phase velocity tends to infinity. This is consistent as long as the condition $v_{ph}v_g = c^2$ is satisfied.

the laser frequency:

$$n_c = \frac{m_e \epsilon_0 \omega_L^2}{e^2} \quad (2.33)$$

The region with an electron density below n_c is known as *underdense* plasma. In this region, the group velocity of the laser pulse can be defined as $v_g = c(1 - \omega_p^2/\omega_L^2)^{1/2}$ (from (2.31)) which tends to c when $\omega_L \gg \omega_p$, and vanishes to 0 when $\omega_L = \omega_p$. By definition, the product of v_g with the phase velocity, v_{ph} , is equal to c^2 . Therefore, $v_{ph} = c(1 - \omega_p^2/\omega_L^2)^{-1/2}$, which also tends to c when $\omega_L \gg \omega_p$, instead will tend to ∞ when $\omega_L = \omega_p$. See figure 2.2b for an illustration of these concepts.

On the other hand, when the electron-plasma density is high enough that $\omega_L < \omega_p$, the plasma electrons will oscillate at frequencies higher than the light oscillations. In that case, the electrons will act like a perfect screen for the incoming laser, which will be back reflected. The plasma region beyond this boundary is known as *overdense* plasma. Another way to understand this screening behaviour is through the refractive index of the plasma which can be

derived from (2.30) as:

$$1 = \left(\frac{kc}{\omega}\right)^2 + \frac{\omega_p^2}{\omega^2} \quad (2.34)$$

resulting, finally:

$$\eta(n_e) = \sqrt{1 - \frac{\omega_p^2}{\omega^2}} \quad (2.35)$$

Equation (2.35) shows us that for laser frequencies lower than the plasma frequency, the refractive index becomes imaginary, and then physically impossible for the light to continue propagating through the plasma. This situation is also observed if the plasma frequency is expressed as a function of the laser frequency:

$$\omega_p^2 = \frac{e^2 n_e}{\epsilon_0 m_e} \cdot \frac{n_c}{n_c} = \frac{e^2 n_c}{\epsilon_0 m_e} \cdot \frac{n_e}{n_c} = \omega^2 \cdot \frac{n_e}{n_c} \quad (2.36)$$

And then,

$$\eta(n_e) = \sqrt{1 - \frac{n_e}{n_c}} \quad (2.37)$$

For electron densities n_e higher than the critical density n_c , the refractive index becomes imaginary and a real solution to the wave equation does not exist beyond that point.

Therefore, if the laser is interacting with the overdense region, from its rest frame perspective this region acts as a relativistic mirror, reflecting, Doppler-shifting (red or blue depending if in the moment of the interaction the overdense region is expanding due to thermal pressure or is being compressed by the laser light pressure) and compressing the incident laser pulses. Additional details are discussed in section 2.4 and 5.3.

Solving the wave equation for overdense plasma, considering this fact, with the new boundary and initial conditions, a decreasing exponential wave (evanescence wave) is obtained instead of the sinusoidal solution characteristic of underdense

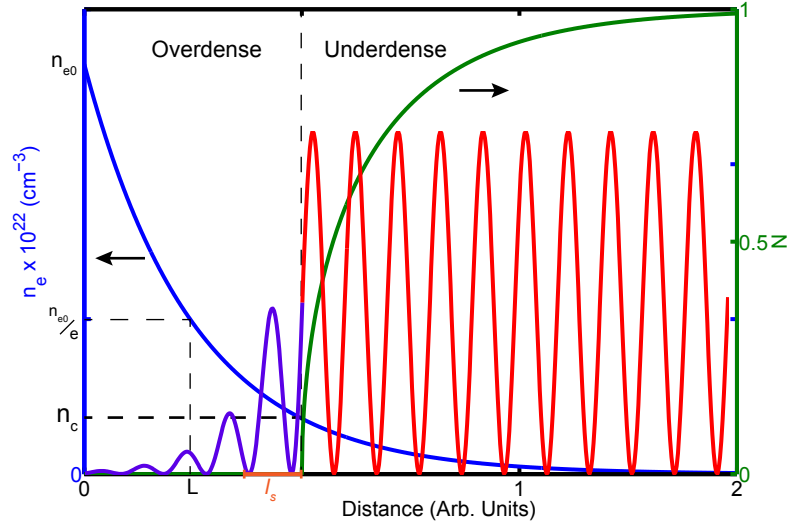


Figure 2.3: Illustration of wave propagation in an underdense and overdense plasma together with some of the most important plasma parameters, as critical density, n_c , scale length, L , or skin depth, l_s . Left axis shows the electron density expansion. Right axis shows the variation of the refractive index. The wave keeps its amplitude constant when propagating through underdense plasma and decreases exponentially as soon it reaches the overdense region.

regions. This evanescence wave can be expressed as:

$$E \sim \exp(ikx) \quad (2.38)$$

From the dispersion equation (2.30) the value of the imaginary k (assumed in an overdense region) is obtained:

$$k = \frac{(\omega^2 - \omega_p^2)^{1/2}}{c} = \pm i \frac{(\omega_p^2 - \omega^2)^{1/2}}{c} \quad (2.39)$$

Choosing the sign of k to match a physical solution, an expression for the evanescence wave is obtained as:

$$E \sim \exp(ikx) = \exp[-x(\omega_p^2 - \omega^2)^{1/2}/c] \quad (2.40)$$

This equation defines the parameter known as *skin depth*, $l_s = c/(\omega_p^2 - \omega^2)^{1/2}$, which is the depth at which the evanescence field can penetrate into the overdense plasma, and corresponding to a value of such a field equal to $1/e$ of its maximum.

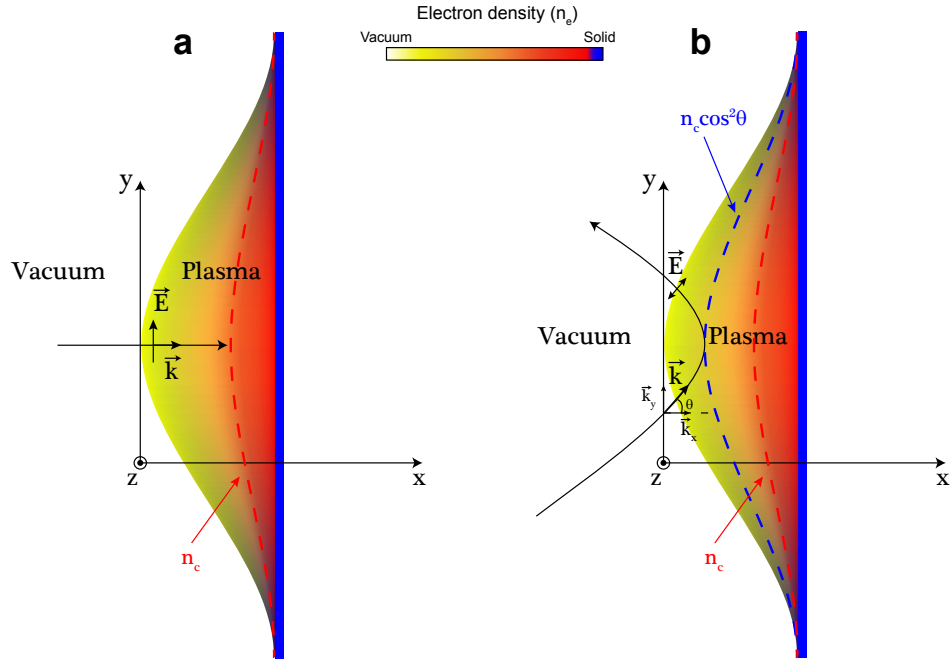


Figure 2.4: Schematic of an ultra intense laser-plasma interaction linearly polarised. **a**, normal incidence and **b**, oblique incidence. Whereas the wave is reflected at the critical density, n_c , in an oblique incidence it is reflected at the corrected critical density, $n_c \cos^2 \theta$, where θ is the angle of incidence.

All these concepts are summarised in Figure 2.3.

In the case of oblique incidence, where the k vector of the incoming laser forms a certain angle θ with the electron density gradient, the critical density has to be corrected according to the new situation. From the Figure 2.4b, where a scheme of the oblique incidence is shown, and supposing that the electric field is p polarised (contained in a plane parallel to Y-axis), the k vector has the components $[k_x, k_y, k_z] = [(\omega/c)\cos\theta, (\omega/c)\sin\theta, 0]$. Replacing the new k vector in the dispersion relation equation 2.30:

$$\omega^2 = (k_x^2 + k_y^2)c^2 + \omega_p^2 \quad (2.41)$$

Due to the fact that laser reflection occurs in a small region of the plasma it is valid to assume that the electron density only changes along the X-axis. In this scenario, the k vector along the Y-axis can be considered constant $(\omega/c)\sin\theta_0$. In addition, because the reflection takes place when the incoming electric field is

parallel to the X-axis and $\theta = 90^\circ$, the k_x component can be considered equal to 0. Including these concepts in the previous equation:

$$\omega^2 = k_y^2 c^2 + \omega_p^2 \Rightarrow \omega^2 = \frac{\omega^2}{c^2} \sin^2 \theta_0 \cdot c^2 + \omega_p^2 \quad (2.42)$$

Simplifying and rearranging:

$$\omega_p^2 = \omega^2 (1 - \sin^2 \theta_0) \Rightarrow \omega_p^2 = \omega^2 \cdot \cos^2 \theta_0 \quad (2.43)$$

Finally, replacing the laser plasma and the plasma frequency for their corresponding electron densities, the corrected critical density in an oblique incidence is described as $n_{co} = n_c \cdot \cos^2 \theta_0$, where n_c is the critical density in a normal incidence.

2.3.2 Polarisation of plane waves

One of the most important investigations presented in this thesis, is the effect of the laser polarisation in the electron and proton dynamics during ultra intense laser-solid interactions.

For a monochromatic wave, *polarisation* can be defined as the instantaneous oscillation of the electric field, \mathbf{E} , magnitude and phase, of such a wave in one determined direction along the three spatial components. If this oscillation changes between different directions (or planes) at each time, then it is said that the wave is *not polarised*. Instead, if the electric field of the wave oscillates along one specific direction during its propagation, the wave, can be called *polarised*. The total electric field, which defines an electromagnetic wave propagating in the x direction, can be obtained as the superposition of two orthogonal linear components, $E_y = E_{0y} \sin(\phi) \hat{y}$ and $E_z = E_{0z} \sin(\phi - \Delta\theta) \hat{z}$. If $E_{0z} = 0$ and the phase difference between both component is $\Delta\theta = 0$, the wave oscillates in one unique plane. The wave is then *linearly polarised*. If $E_{0y} = E_{0z}$ and

the phase difference between both component is $\Delta\theta = \pi/2$, the total electric field oscillates cutting multiple planes, along its propagation, following a circular trajectory. The wave is *circularly polarised*. Waves with any other variation, in magnitude or phase, are known as an *elliptical polarised* wave. For the linear polarisation case, usually, two particular classes are distinguished, *p-polarisation* and *s-polarisation*. In a p-polarised wave the electric field is oscillating parallel to the plane of incidence, which is defined by the propagation direction and a normal vector to the target surface or density gradient. The electric field is oscillating perpendicularly to such a plane in a s-polarised wave.

Although an electromagnetic wave is described with the following four basic fields: the electric field strength \mathbf{E} , the electric displacement density \mathbf{D} , the magnetic field strength \mathbf{H} and the magnetic field flux density \mathbf{B} , only the electric field \mathbf{E} is used to define the polarisation state of an electromagnetic wave. This is because when waves interact with matter the force exerted on the electrons by the electric field is much higher than the force respect to the magnetic field, in the non-relativistic case.

2.3.3 Plane waves interacting with plasma electrons

As it has already been mentioned, a semi-infinite plane wave propagating in the x direction can be defined through the total electric and magnetic field as [54, 55]:

$$\mathbf{E} = \mathbf{E}(x, t) = E_0 \hat{\epsilon} e^{i(\omega t - kx)} \quad (2.44)$$

$$\mathbf{B} = \mathbf{B}(x, t) = -\hat{x} \times \mathbf{E} \quad (2.45)$$

where $\hat{\epsilon}$ is the polarisation vector, being $\hat{\epsilon} = \hat{y}$ for linear polarisation along the y axis, and $\hat{\epsilon} = (\hat{y} \pm i\hat{z})/\sqrt{2}$ for circular polarisation.

When this plane wave interacts with a plasma, the dynamics of each individual

electron, i.e their velocity and position, is described by the Lorentz force equation (2.6):

$$\frac{d\mathbf{p}}{dt} = m_e \frac{d\mathbf{v}}{dt} = -e(\mathbf{E} + \mathbf{v} \times \mathbf{B}) \quad (2.46)$$

From Faraday's equation (2.3), the modulus of the electric and magnetic fields are related as $|\mathbf{E}| = c|\mathbf{B}|$. This relationship, together with the Lorentz's equation (2.6), reveal that for low laser intensities, when the electron oscillations by the electric field is non-relativistic, the contribution of the $\mathbf{v} \times \mathbf{B}$ term in their final motion can be considered negligible. In this scenario, and as an example, the electric field in a linear polarised wave can be expressed, from (2.44), as $\mathbf{E} = E_0 \sin(\omega t - kx) \hat{y}$. As it has already been included in the previous section 2.1 (when the plasma frequency was obtained), with this consideration and incorporating this electric field into the previous equation (2.46), the electron motion is described as:

$$\begin{cases} m_e \frac{dv}{dt} = -eE_0 \sin(\omega t - kx) \hat{y} \\ v(t) = \frac{eE_0}{m_e \omega} \cos(\omega t - kx) \hat{y} + v_0 \\ x(t) = \frac{eE_0}{m_e \omega^2} \sin(\omega t - kx) \hat{y} + x_0 \end{cases} \quad (2.47)$$

where the negative charge nature of the electrons has been considered. Electrons, then will oscillate following the electric field at out-of-phase velocities whose maximum value is $v_{max} = \frac{eE_0}{m_e \omega}$. This term, normalised to the speed of light, corresponds to the known normalised vector potential, \mathbf{a} :

$$\mathbf{a} = \frac{v_{max}}{c} = \frac{e|\mathbf{E}|}{m_e \omega c} \quad (2.48)$$

The peak value of this equation, $a_0 = \frac{eE_0}{m_e \omega c}$, is commonly used as a reference to define the laser-plasma regime since it includes the electron response to a given electric field and wavelength of an electromagnetic wave. For non-relativistic

interactions $a_0 < 1$.

If high laser fields are used, electron velocities will reach a significant fraction of the speed of light. In this regime relativistic effects, as the electron mass increase, will take place. It is thus necessary to correct the electron momentum by the Lorentz factor, $\gamma = 1/(1 - (v/c)^2)^{1/2}$, accordingly, $p = \gamma m_e c$. In addition, these relativistic velocities mean that the $\mathbf{v} \times \mathbf{B}$ term cannot be considered negligible any more. In this case, electrons experience simultaneously a perpendicular force due to the electric field and another force in the longitudinal direction due to the $\mathbf{v} \times \mathbf{B}$ term. These two velocities are included in the Lorentz's force equation as:

$$m_e \frac{d(v^{(1)} + v^{(2)})}{dt} = -e(\mathbf{E} + (v^{(1)} + v^{(2)}) \times \mathbf{B}) \quad (2.49)$$

Solving this equation, the velocities and the trajectories in the perpendicular and longitudinal plane are obtained as:

$$v^{(1)}(t) = a_0 c \cdot \sin(\omega t) \hat{y} \rightarrow y(t) = -a_0 \frac{c}{\omega} \cdot \cos(\omega t) \quad (2.50)$$

and

$$v^{(2)}(t) = \frac{a_0^2 c}{4} \cdot \cos(2\omega t) \hat{x} \rightarrow x(t) = -\frac{a_0^2 c}{8\omega} \cdot \sin(2\omega t) \quad (2.51)$$

These two equations illustrate that in a relativistic regime:

- The perpendicular velocity (and trajectory), $v^{(1)}$ is scaled with a_0 , whereas the longitudinal velocity, $v^{(2)}$ is scaled with a_0^2 .
- The perpendicular velocity (and trajectory), $v^{(1)}$ oscillates once per laser period ($\propto \omega$), whereas the longitudinal velocity, $v^{(2)}$ oscillates twice per laser frequency ($\propto 2\omega$).

For a circularly polarisation wave, the 2ω oscillation term vanished, due to $v^{(1)} \times \mathbf{B} = 0$. So, the electron still performs a circular trajectory due to the fact that

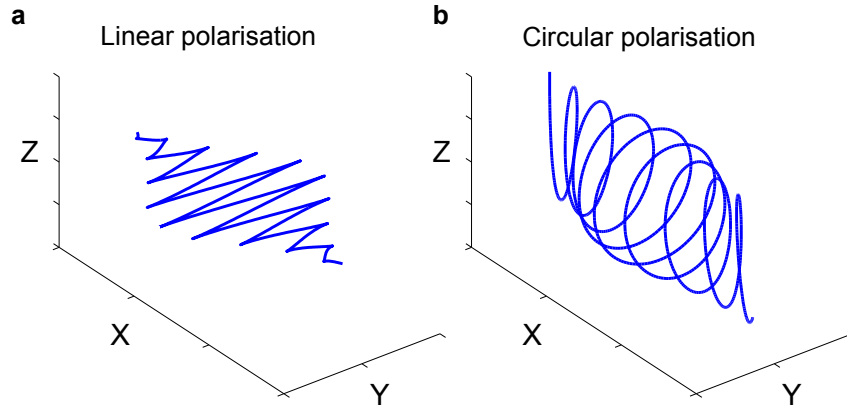


Figure 2.5: Relativistic trajectory of an electron for both **a** linear and **b** circular polarisation, in the laboratory frame, interacting with a time-finite Gaussian pulse.

it is not, on average, affected by magnetic force effects.

Figure 2.5 shows an example of the relativistic trajectory of an electron, for both, linear and circular polarisations, in the laboratory frame, interacting with a time-finite gaussian pulse. To calculate the trajectory for the circular polarisation case, the z component of the wave was also included [55].

For the relativistic regime $a_0 \gtrsim 1$. As shown in equation (2.48) this parameter is related to the electric field. However, frequently it is useful to work with this parameter in terms of the laser intensity. Intensity of an electromagnetic wave is defined as the time-average of the Poynting vector:

$$I = \langle \mathbf{S} \rangle = \left\langle \frac{1}{\mu_0} \mathbf{E} \times \mathbf{B} \right\rangle \quad (2.52)$$

where \mathbf{E} and \mathbf{B} are in the form of equations (2.44) and (2.45), respectively. The intensity can therefore be written for linear and circular polarisation in vacuum as:

$$I = \begin{cases} \frac{\epsilon_0 c E_0^2}{2} & \text{for linear polarisation} \\ \epsilon_0 c E_0^2 & \text{for circular polarisation} \end{cases} \quad (2.53)$$

where for the circular polarisation case the superposition of two perpendicular

linearly polarised waves:

$$I = \begin{cases} \mathbf{E} = \frac{E_0}{\sqrt{2}} \cos(\omega t - kx) \hat{y} + \frac{E_0}{\sqrt{2}} \sin(\omega t - kx) \hat{z} \\ \mathbf{B} = \frac{B_0}{\sqrt{2}} \cos(\omega t - kx) \hat{z} - \frac{B_0}{\sqrt{2}} \sin(\omega t - kx) \hat{y} \end{cases} \quad (2.54)$$

with peak amplitude of $E_0/\sqrt{2}$ (and $B_0/\sqrt{2}$), and a phase difference of $\pi/2$ have been used.

Therefore, including the electric field as a function of the wave intensity from the equation (2.53) in (2.48), the normalised vector potential is rewritten (normalised to 10^{18}) as:

$$a_0 \approx \begin{cases} \left(\frac{I \lambda_\mu^2}{1.37 \times 10^{18} \text{ W cm}^{-2}} \right)^{1/2} & \text{for linear polarisation} \\ \left(\frac{I \lambda_\mu^2}{2.74 \times 10^{18} \text{ W cm}^{-2}} \right)^{1/2} & \text{for circular polarisation} \end{cases} \quad (2.55)$$

where I is in W cm^{-2} and λ_μ is in microns.

The Lorentz factor, γ , averaged along a laser period, is usually also described in terms of a_0 as $\langle \gamma \rangle = (1 + \langle \mathbf{a}^2 \rangle)^{1/2}$ which is equal to $\langle \gamma \rangle = (1 + a_0^2/2)^{1/2}$ for linear polarisation and $\langle \gamma \rangle = (1 + a_0^2)^{1/2}$ for the circular case.

Ponderomotive force

In the previous section the effect of a plane wave on an electron was described. However, in a more realistic scenario, during a conventional laser-plasma experiment, the laser has finite spatial dimensions. The non-constant laser profile presents a spatial gradient which is going to produce a net gain in the energy of a charged particle, q . Unlike in the previous case, now the particle is not returning to its initial rest position after the interaction with the electromagnetic wave. In the non-relativistic case, i.e $a_0 < 1$, a charged particle oscillates around its centre position with a cycled-average oscillation energy described by the *ponderomotive*

potential, Φ_p [55–57]:

$$\Phi_p = \frac{m_e}{2} \langle v^2 \rangle = \frac{e^2}{2m_e \omega^2} \langle E^2 \rangle \quad (2.56)$$

The spatial gradient of this potential defines the known *ponderomotive force*, which describe the cycle-average of the position and velocity of the charged particle. Its usual non-relativistic form is:

$$f_p = -\nabla \Phi_p = -\frac{e^2}{2m_e \omega^2} \nabla \langle E^2 \rangle \quad (2.57)$$

This force is responsible for the secular component (perpendicular to the laser axis) of the oscillatory motion of the charged particles in an electromagnetic field. In addition, this force expels the particles from regions where the electric field (or intensity due to $I \propto E^2$) is higher. In figure 2.6a-c three time steps where a charged particle interact with a linear polarised wave are shown. In figure 2.6a the particle is placed in the centre of the wave, where the electric field is maximum. At that moment the particle will start to move, following the field direction. In figure 2.6b, a half cycle later, the electric field is pointing in the opposite direction, but because the wave presents a gradient in the strength of the electric field, now the particle feels a weaker field compared to the previous time step. The restoring movement is shorter as well. After a cycle is completed, the particle finally leaves the highest field regions, as is shown in figure 2.6c, and gaining a net energy in that process. Figure 2.6d illustrates the same *ponderomotive* effect on charged particles, but illustrating the effect of the wave intensity instead of the electric field. From this figure, it is clear that the charged particles will be forced to move away from the highest values and following the intensity directions.

This is valid for positively and negatively charged particles, since f_p is proportional to the charge squared. However, f_p also scales with the inverse of the particle mass, thus, for the laser intensities used in the research chapters

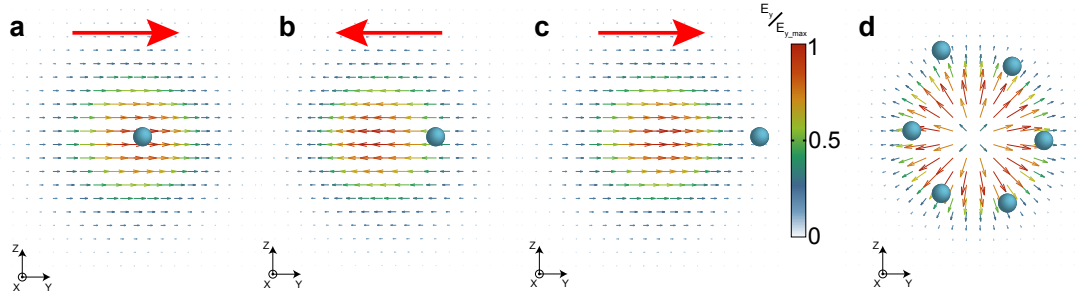


Figure 2.6: Illustration of the ponderomotive force effect on a charged particle (blue sphere) for a linearly polarised wave along the Y-axis. *a-c*, Electric field for three time steps representing a wave period. **a**, The charged particle, located at the highest electric field, moves on the right following the field direction (in case of a positive charged particle); **b**, the charged particle moves on the left following the field, but at that time, it is located in a lower field strength region so that it is not able to return to its original position; **c** the charged particle moves on the right following again the field direction. At that point, the charged particle is far from the electric field and it is not affected for such a field any more. The overall effect on the charged particle is displacement from higher to lower field values. The red arrow on the top of **a-c** represents the direction of the electric field for clarification. **d**, Wave intensity gradient direction. It shows the same response of charged particles than **a-c** which are displaced from higher to lower intensity values.

of this thesis, the ponderomotive effect on ions can be negligible in comparison with the effect on electrons.

In the relativistic regime, i.e $a_0 \gtrsim 1$, the ponderomotive force is defined as $f_p = -m_e c^2 \nabla \gamma$. From this equation the kinetic energy acquired for an electron after a laser cycle (i.e the ponderomotive potential) is derived as:

$$\Phi_p = m_e c^2 (\gamma - 1) \quad (2.58)$$

2.3.4 Laser absorption mechanisms in plasma

As has already been mentioned, an electron does not acquire a net gain when interacting with infinite plane electromagnetic waves (known as Lawson-Woodward theorem), and therefore they can not be accelerated by an electromagnetic field in vacuum. However, this theorem is not valid, for example, if, in a more realistic scenario, a focused laser beam with a finite temporal and spatial profile is used. In addition, in a plasma, where the electron density is

high, and depending on different parameters as laser intensity, angle of incidence and polarisation, diverse absorption mechanisms will arise predominantly in the regions near the overdense plasmas. It can be considered that a photon is absorbed if, during the interaction with plasma, it transfers its energy to any other particle and such energy is not transformed into a photon, with the same energy. The attained laser intensities and plasma temperatures in the research and experimental results presented in this thesis are high enough to consider only the known collisionless absorption mechanisms in the regions around the peak of the laser intensity. Although plasmas involve considerable degree of collisions, the dynamics and particle energy gain directly from the fields is more significant than from particle-particle interactions, in those regions. However, in the wings of the pulse, where a lower laser intensity is presented, significant collisional absorption may occur [58].

The most important collisionless absorption mechanisms in intense laser interactions are the resonance absorption, vacuum (Brunel) heating and the ponderomotive $\mathbf{J} \times \mathbf{B}$ heating [53, 59].

Resonance absorption mechanism

In the resonance absorption process when a p-polarised laser pulse is incident at some angle to the target normal, there will be a region of the interaction where the electric field of the laser beam will be parallel to the normal vector of the target surface. At that moment, the electric field will resonantly excite, at the critical density, an electron plasma wave at the laser frequency ($\omega_p = \omega_L$) (see Figure 2.7). In this way, energy is transferred from the electromagnetic wave into plasma waves. Because these waves are damped, energy will eventually be converted into thermal energy, and thus heat the plasma. Moreover, this process will be able to accelerate electrons in the direction of the target normal being more efficient when the plasma scale length, L , is much greater than the laser

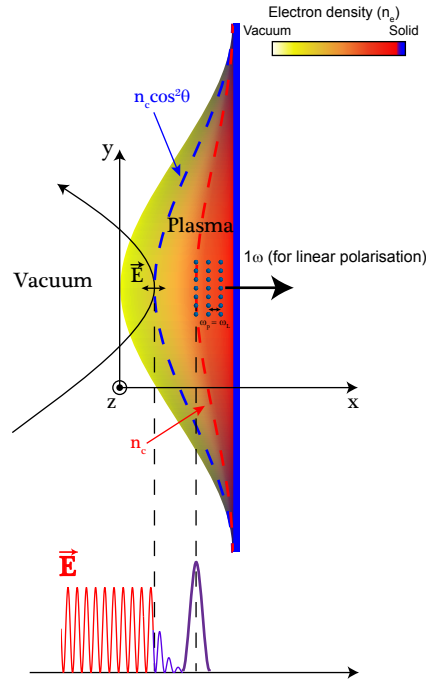


Figure 2.7: Illustration of the resonant absorption mechanism. A wave obliquely interacting with plasma is reflected in the corrected critical density surface, $n_c \cos^2 \theta$ (as was discussed in the section 2.3.1). The evanescent wave then resonates at the critical density surface, n_c , where $\omega_p = \omega_L$, producing electron plasma wave which are accelerated at this frequency.

wavelength. Resonant absorption will be dominant at laser irradiances in the range 10^{12} to 10^{17} Wcm^{-2} , occurring still at higher intensities (but no longer a dominant mechanism) [53, 56, 60–63].

Vacuum heating mechanism

A similar absorption mechanism, known as vacuum heating, not-so-resonant or Brunel effect [64], arises when a p-polarised laser pulse interacts with plasmas with $L \ll \lambda$ at an angle and with intensities $> 10^{18}$ Wcm^{-2} . If the scale length is sufficiently small (sharp density transition between plasma and vacuum), and the laser is sufficiently intense, the electric field, oscillating parallel to the normal vector of the target surface in the region of the angularly corrected critical density ($n_c \cos^2 \theta$), is able to pull the electrons out into vacuum in the first half period of the field (see figure 2.8a). In the second half period, the electric field, oscillating in the opposite direction, accelerates the electrons back into the overdense plasma,

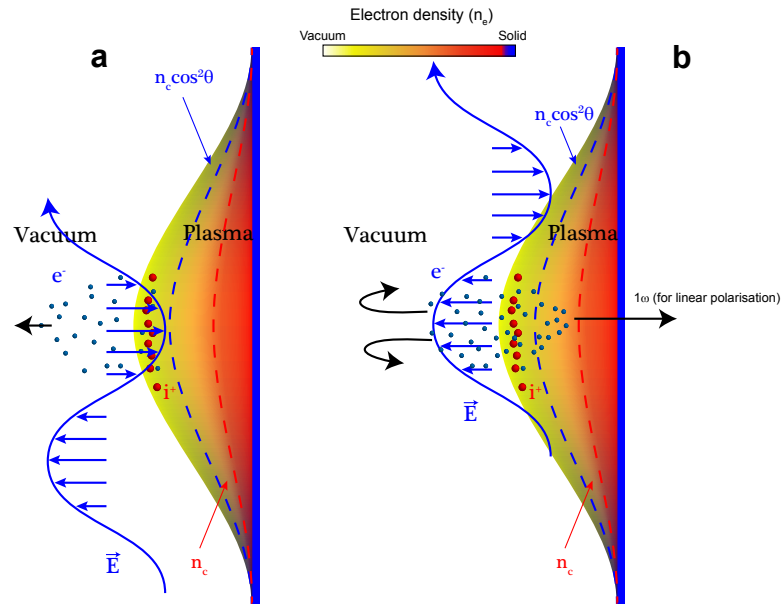


Figure 2.8: Schematic of the vacuum heating absorption mechanism. **a** For short density scale lengths, in the first half-period of a wave interacting obliquely with plasma, the electric field is able to expel electrons outside the plasma into the vacuum. **b**, In the second half-period, with an opposite direction, the field accelerates electrons beyond the corrected critical density surface, where the laser field decays evanescently resulting in a smaller restoring force and in an energy exchange from wave to electrons.

(see figure 2.8b), far from the angularly corrected critical density, where the laser field decays evanescently, resulting in a smaller restoring force and in an energy transfer from the laser to electrons in the plasma after each laser period. The velocity at which the electrons are accelerated through the plasma is, therefore, the oscillation velocity of the laser electric field, $v \simeq v_{osc} = eE/m_e\omega_L$.

Ponderomotive $J \times B$ heating

In the previous section, the *ponderomotive force* concept was introduced. That represents a particular solution in which the action of the electric field is higher than that due to the $\mathbf{v} \times \mathbf{B}$ term. However, for high laser intensities ($> 10^{18}$ Wcm $^{-2}$), the quiver energy of an electron exceeds its rest mass energy. In this situation, the $\mathbf{v} \times \mathbf{B}$ term presents values in the same order than the electric field component, and is therefore no longer negligible. This new term will create nonlinear oscillations in the electron motion. A general solution of

the *ponderomotive force* was proposed for first time by Kruer and Estabrook in 1985 [14]. They introduced the term $\mathbf{J} \times \mathbf{B}$ heating mechanism to the effect of the $\mathbf{v} \times \mathbf{B}$ term into the *ponderomotive force*. It is usually defined as [14, 55–57]:

$$F(r) = -\frac{e^2}{4m_e\omega^2} \nabla \langle E^2 \rangle \left(1 + \frac{1 - \epsilon^2}{1 + \epsilon^2} \cos(2\omega t) \right) \hat{r} \quad (2.59)$$

where ϵ ($0 < \epsilon < 1$) is the laser ellipticity.

This equation has two distinct terms. The first term is easily recognisable with the *ponderomotive force* which drives the electron forward, and expels them from the highest electric field values, at a constant push (0ω). The second term is responsible for driving the electrons forward at the same time that makes them oscillate back and forward, in the propagation direction, at twice the laser frequency (2ω). This second term is actually the $\mathbf{J} \times \mathbf{B}$ heating mechanism because when the electrons are oscillating longitudinally, there will be one moment that they will be beyond the critical density, where the laser field decays evanescently, producing a net energy transfer from the laser photons to the electrons. A schematic illustration of this mechanism is shown in the figure 2.9a.

For linearly polarised pulses $\epsilon = 0$, which makes the heating component, in the equation (2.59) maximum. On the contrary, for circular polarisations, $\epsilon = 1$ which causes the heating term to vanish. For a laser ellipticity just between linear and circular, i.e $\epsilon = 0.5$, the ellipticity factor of the heating component is equal to 0.6. That means that for such ellipticity the heating component of the ponderomotive force is closer to the linear polarisation than to circular. All this is illustrated in the figure 2.9b. These specific laser ellipticities are the same than the used in the experiments reported in chapters 6 and 7.

The $\mathbf{J} \times \mathbf{B}$ absorption mechanism is thus optimised for high laser intensities, linear polarisations and normal incidences. Because of that, this is the absorption

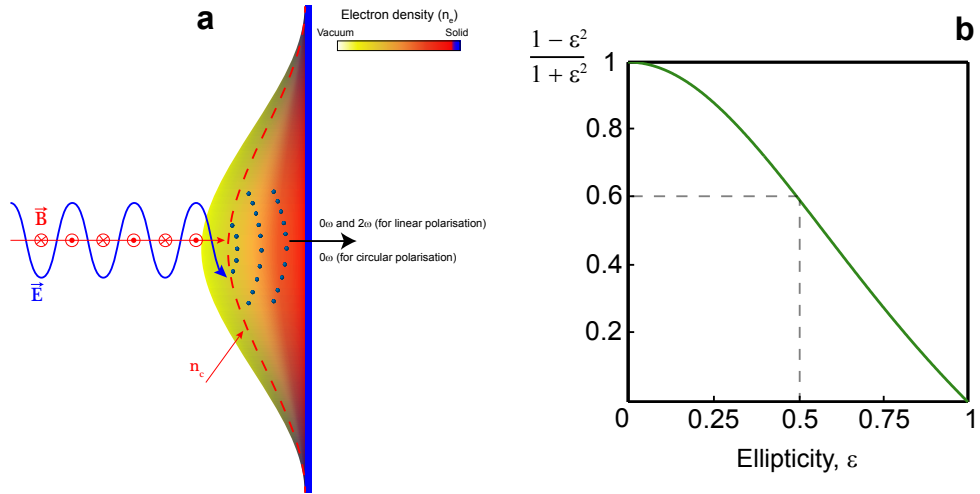


Figure 2.9: **a** Illustration of the $\mathbf{J} \times \mathbf{B}$ heating mechanism. For linearly polarised waves two accelerated electron populations are generated; one at a constant push (0ω) from the first term of the equation (2.59); a second oscillating at twice the laser frequency in their propagation, from the second term of the equation (2.59). For circular polarisation the second term vanishes, and then only one electron population is generated with a constant drive. **b** Second term in equation (2.59) as a function of the wave ellipticity. It shows that for an elliptically polarised wave equal to 0.5 (just between linear and circular), $\mathbf{J} \times \mathbf{B}$ heating is closer to the linear case than to the circular.

mechanism predominant in the experiments and simulations presented in this thesis.

2.4 Laser-plasma charged particle acceleration mechanisms

In the Introduction section (1.1) the concept of laser-driven particle acceleration has already been alluded to. Here the main processes are described, which are accepted by the scientific community for the explanation of the charge particle acceleration during an ultra intense laser plasma interaction.

During the collisionless processes, the plasma electrons will absorb a significant fraction of the laser pulse energy and will be pushed by the fields into the overdense plasma beyond the restoring influence of the laser, creating a relativistic acceleration of the electron population directed into the target, driving indirectly ion acceleration as well.

Since 2001, when Wilks *et al.* [65], introduced the Target Normal Sheath Acceleration (TNSA) scheme as a high power laser-driven technique for the generation of multi-MeV ions, it has become the most widely accepted mechanism for the energetic proton acceleration measured at the rear of thin (micron scale) foil targets irradiated by ultra-intense laser pulses ($> 10^{20}$ Wcm $^{-2}$). This mechanism involves the acceleration of ions by the extremely strong electric field (\sim TV/m) created at the rear side of the target by the relativistic electrons generated at the laser focus (front side) and transported through the target (see figure 2.10a).

In the last few years a new acceleration mechanism has been proposed, known as Radiation Pressure Acceleration (RPA), which will dominate in the interaction with thin (micro-nanometre scale) targets at ultra high intensities ($> 10^{21}$ Wcm $^{-2}$) [66–69]. From Maxwell we know that an electromagnetic wave exerts a pressure on a reflected surface ($P_{rad} = 2R\frac{I}{c}$, with the reflectivity $R = 1$ for a perfect reflection) resulting in direct acceleration. Since the photons from the ultra-intense pulse carry momentum, the final velocity of the accelerated surface, $\beta = v/c$, can be calculated from the momentum conservation or by the conservation of the number of photons, N , of the incident and reflected wave from the surface. Each photon has an energy equal to $\hbar\omega$, therefore the total energy of the incident wave is $N\hbar\omega$. Since the moving surface velocity, $V = \beta c$ in the laboratory frame, reaches relativistic values at the intensities considered, the reflected wave is going to experience a relativistic Doppler effect down-shifting its frequency, and then its energy, according to the relation $N\hbar\omega(1 - \beta)/(1 + \beta)$. The difference in both the incident and reflected waves transfer a total energy of $[2\beta/(1 + \beta)]N\hbar\omega$ to the surface. From the last expression, it can be appreciated that almost all of the energy of each reflected photon is delivered to the target, producing a total conversion of the wave energy into mechanical energy, in the limit $\beta \rightarrow 1$, and assuming that the number of photons is conserved for a perfect

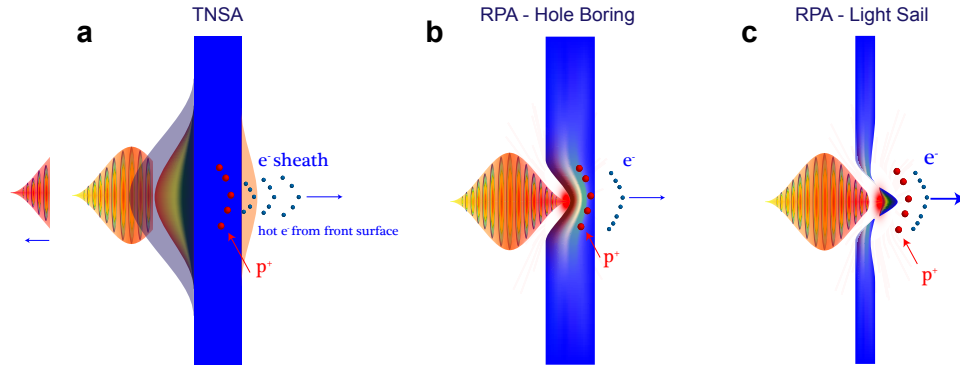


Figure 2.10: Schematic picture of the three main acceleration mechanisms in laser-solid interaction. **a**, TNSA, **b**, RPA - Hole Boring and **c**, RPA - Light Sail.

mirror. Electrons at the critical density surface, thus will be driven forward into the overdense plasma by this laser pressure, producing a charge separation layer and creating an electrostatic field that in turn accelerates the ions. For a typical Gaussian-shaped laser focus, the radiation pressure will bend the plasma critical surface inward following the Gaussian-shape of the beam, enabling the laser pulse to penetrate deeply into the target. This process is illustrated in figure 2.10b and it is commonly named *hole boring* when target thickness is of the order of μm (or higher). The recession velocity of the plasma critical surface due to the radiation pressure is known as *hole boring velocity* and was derived for first time by Wilks et al. [70]. This velocity was estimated by balance between the photon and the particle momentum flux, resulting in the following expression:

$$\frac{v_{hb}}{c} = \left(\frac{n_c}{n_e} \frac{I \lambda^2}{2.74 \cdot 10^{18} A m_p} \frac{Z m_e}{A m_p} \right)^{1/2} \quad (2.60)$$

where n_c is the electron critical density, n_e is the electron density, I is the intensity of the laser pulse, λ is the wavelength, Z is the ionisation state, A the mass number, and m_e and m_p the electron and proton mass, respectively.

This equation describes the hole boring velocity for non-relativistic case. However, for relativistic intensities, this equation predicts hole boring velocities greater than the speed of light. It is therefore necessary to relativistically correct

this equation. This new corrected equation can be found for example in [71] or [72]:

$$B = a_0 \sqrt{\frac{Z}{A} \frac{m_e}{m_p \cdot n_e/n_c}} \quad (2.61)$$

where

$$\frac{v_{hb}}{c} = \frac{B}{1+B} \quad (2.62)$$

Another mode of radiation pressure, distinct from pure *hole boring*, is known as *Light Sail* [68, 73], which is shown in figure 2.10c. Unlike the hole boring regime, this mode occurs when the laser pressure is able to push all of the target plasma-electrons (in the regions where the intensity is maximum) as a whole. This mode of RPA is expected to dominate over the hole boring mode for higher intensities and target thickness in the scales of nanometres. This scenario is similar to the idea of a laser driven space vehicle capable to interstellar travel at relativistic velocities proposed by Marx in 1966 [74] (which was conceptually and numerically corrected 27 years later [75]), and based on [76]. As in the *hole boring* regime, the reflected surface is pushed by an electromagnetic wave with intensity I and an angular frequency ω . The evolution of the velocity of this surface can be obtained from momentum conservation or by considering the Doppler shift of the reflected wave and the conservation of the total number of photons. In the *light sail* model the surface density $\sigma = \rho l$ (where ρ is the mass density and l the target thickness) is a significant parameter since the target is accelerated altogether. Another important parameter is the pulse energy per unit surface, or pulse fluence, F :

$$F = \int_0^t I(t) dt \quad (2.63)$$

where, for a top-hat profile laser $F = I_0 t$.

The *light sail velocity* is defined as:

$$\frac{v_{hb}}{c} = \beta(t) = \frac{[1 + \epsilon(t)]^2 - 1}{[1 + \epsilon(t)]^2 + 1} \quad (2.64)$$

where

$$\epsilon(t) = \frac{2F(t)}{\rho l c^2} = \frac{2It}{\rho l c^2} \quad (2.65)$$

and where $\rho = m_i n_i = m_p n_p + m_e n_e = \frac{A}{Z} m_p n_e + m_e n_e$ (the term $m_e n_e$ is negligible compared to the first term and then usually it does not appear in the final equations).

Due to the radiation pressure implemented by the ponderomotive force, the maximum *hole boring* and *light sail velocities* of the plasma-particles are optimised for circularly polarised laser pulses. As described in section 2.3.3, for circularly polarised waves the longitudinal electron heating component along the density gradient due to the $\mathbf{J} \times \mathbf{B}$ mechanism, at 2ω , vanishes. This condition is particularly important to prevent the foil expansion due to the ‘thermal’ pressure of electrons, obtaining the maximum efficiency in the electron (and ions) acceleration from the front surface of the target, in the *hole boring* regime, and to allow the acceleration of the target as a single object in the *light sail* case. For any other laser ellipticity the heating component of this force decreases that maximum velocity.

Chapter 3

Onset of Relativistic Induced Transparency

3.1 Introduction

The theory of electromagnetic wave propagation in plasmas was a notably mature research field in the first half of the last century. The basis of these theories demonstrated that an electromagnetic wave with a frequency, lower than the plasma frequency could not propagate through such a plasma due to its refractive index being imaginary (as described in the section 2.3.1 of the Chapter 2). With the advent of lasers, intense electromagnetic waves were able to experimentally be produced. Around these strong electromagnetic waves new analytical investigations were developed. These new studies focused in the relativistic motion of the plasma electrons [77, 78], where their velocity was comparable to the speed of light when a highly intense laser beam interacts with them. Only the non-relativistic case was achievable until that moment [79]. This theory predicts that a laser beam of given frequency is able to propagate through an overdense plasma if the laser intensity is higher than a calculated threshold. This behaviour was implicitly attributed to the decrease in the effective plasma density (n_e/n_c) when the electron mass was relativistically

corrected at these relatively high velocities. Due to the extreme intensities required, it was not until two decades later, in the final years of the 1990's, when the first experimental evidence confirmed the transmission of ultra intense laser pulses through overdense plasmas due to relativistic effects [80, 81]. In order to interpret and understand the experimental results sophisticated PIC simulations were required. Because of the challenging computational requirement to solve the complex physics of high dense plasmas, the first PIC simulations were not developed until a few years earlier [82, 83], when suitable computer technology and codes were available. Since these first experiments, few new studies about the propagation of laser beams in large overdense plasmas were published [84, 85]. The main conclusions of laser propagation in overdense plasmas, at that moment, can be summarised as: (1) There exists a threshold intensity for laser propagation [86]; (2) an overdense plasma reflects the incident laser pulse, for intensities lower than this threshold, with the formation of a nonlinear skin-layer structure at the plasma-vacuum boundary; (3) for higher intensities, the onset of relativistic transparency enables laser beam propagation in relativistically underdense (but still classically overdense) plasma, forming nonlinear travelling plane waves [77, 78], solitary waves with specific properties [87], standing waves [88] or, the most extended interpretation, by the relativistic correction of the plasma frequency [89]. The latter is commonly referred to today as the *Relativistic Induced Transparency* (RIT) regime.

In 2006, however the conception of this regime was radically changed. In that year, two papers [90, 91] showed, experimentally, a significant increase in the maximum proton energies accelerated from thin foil targets (at nanometre scales) and at lower laser intensities than previous proton acceleration experiments utilising thicker targets (at micrometre scales) [92, 93] (among many others). These results were possible thanks to the employment, for the first time, of very high laser temporal intensity contrasts which allow for laser-target interaction

without target destruction by shocks caused by any pre-pulses, inherent to high-intensity short-pulse lasers. This new scenario motivated Yin *et al.* to perform high resolution PIC simulations of ultra intense short pulses interacting with thin (nanometre) carbon targets [94]. With these simulations they not only confirmed the ion energy enhancement, measured in the experiments [90,91], but also presented a new laser-driven ion acceleration mechanism as an explanation of such an enhancement. This mechanism, called *Laser Break-out Afterburner* (BOA), is enabled when the target becomes relativistically transparent (explained in more detail in the next section 3.4). From that moment, the relativistic regime has been the focus of a significant part of science community due to its potential applications (such as those included in section 3.5) in addition to the aforementioned ion energy increase. Another motivated study is related to the predicted curb of efficiency of the RPA Light Sail mechanism (see section 2.4) in thin foils when this regime emerges.

3.2 Onset of RIT in thick targets

As previously mentioned, a laser beam can propagate through an overdense plasma when the electron velocity reach relativistic magnitudes. At this point, the electron mass are relativistically increased by the Lorentz factor, γ , making them heavier than in the classical description. Consequently, the plasma critical density (2.33) has to be corrected accordingly:

$$n'_c = \frac{\gamma m_e \epsilon_0 \omega_L^2}{e^2} = \gamma n_c \quad (3.1)$$

As presented in Chapter 2.3.1, an overdense plasma is characterised as one in which the plasma frequency is higher than the laser frequency. In terms of target and critical densities this can be rewritten as $n_e > n'_c$. Due to the Lorentz factor depends on the electron kinetic energy adjusted by the laser intensity,

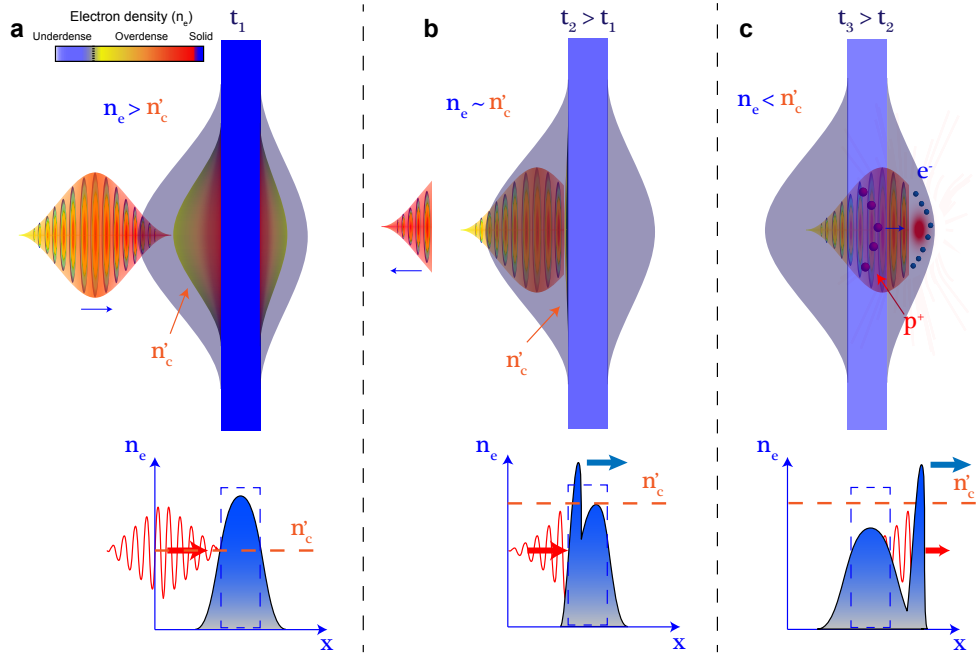


Figure 3.1: Schematic of the Relativistic Induced Transparency process phases. **a**, The first part of the rising edge heats the plasma electrons which tend to expand. **b**, The highest laser intensities ponderomotively drive electrons forward in the region of the relativistically corrected critical density surface. At this point, although the critical density is increased, the electron density just in front of the laser are also increased. **c**, A continuous decreasing electron density, because of plasma expansion, and increasing critical density, because of γ factor, make the plasma relativistically transparent when $n_e < n'_c$ is satisfied. At this moment, the laser can interact volumetrically with the plasma electrons.

if the laser intensity is high enough there will be a specific value which will satisfy $n_e < n'_c$. At that moment, the overdense plasma will be converted to relativistically underdense allowing for laser propagation through the plasma. Taking a solid aluminium target, for example, being irradiated with an 800 nm laser, becomes relativistically transparent at an intensity of $\sim 8 \times 10^{23} \text{ Wcm}^{-2}$, approximately 2-3 order of magnitude greater than that provided by the current state of the art laser systems. Because of this, today, $n_e < n'_c$ is experimentally satisfied by the combination of the relativistic effect, increasing the critical density by the γ factor, and by target expansion driven by electron heating (decreasing the plasma density, n_e) during the laser-target interaction. Figure 3.1 shows a schematic of this process. The main steps are:

1. When the rising edge of an ultra-intense laser pulse interacts with a solid

target, it will quickly ionise the material and generate plasma. The heated plasma expands due to thermal pressure creating an exponentially decreasing plasma density at the front surface of the target (see section 2.2 for a detailed explanation). Although the laser is able to propagate through the peripheral underdense regions, most of the plasma is of the condition $n_e > n'_c$ and will remain overdense during this first stage of the interaction. This scenario is illustrated in figure 3.1a.

2. A fraction of the rising edge of the pulse will be back reflected at the plasma density $n_e = n'_c$, however the rest of the laser pulse has a large enough intensity to exert a significant radiation pressure on the plasma electrons, causing them to pile up and create a very high electron density region localised around that electron density surface. This creates, in addition, a charge depletion layer region whose extension is determined by a balance between electrostatic and ponderomotive forces. At this moment of the interaction, the electron kinetic energies reach relativistic values with a corresponding increase in the γ factor. However, because the electron density is also increased, the condition $n_e < n'_c$ is not satisfied at this stage of the interaction (see figure 3.1b).
3. A continuous increase of the γ factor will take place until the laser pulse intensity peak interacts with the plasma and, together with the plasma expansion, enables the condition $n_e < n'_c$ to be satisfied at some point during the interaction. Thus, the remaining part of the laser pulse, is able to propagate through the relativistically underdense plasma, interacting with the electrons and conforming and modulating their dynamics in its path (see figure 3.1c).

This behaviour is the most widely accepted explanation of the relativistic transparency regime for circularly polarised light and thick solid targets;

considered targets with thickness greater than the laser wavelength and larger than the plasma collisionless skin depth. Although this behaviour is also accepted for linearly polarised light, some authors have reported that a more complex underlying behaviour may be contributing [77,89]. Unlike the circular polarisation case where the oscillatory part of the $\mathbf{v} \times \mathbf{B}$ term of the Lorentz's equation (2.6) vanishes, in the linear case this term plays a key role in electron heating and has to be balanced by the electrostatic field term to facilitate the propagation of the laser along the overdense plasma. The authors [77,89] derived a transparency condition in the case of linear polarisation and high intensity laser waves as $\omega^2 > 4\omega_p^2/\pi a_0$; where a_0 is the normalised vector potential (see section 2.3.3 for more details about this parameter).

The propagation velocity of the laser when travelling through a relativistically transparent plasma is another topic of interest. Initially, its velocity should be described by its group velocity, from the dispersion relation (see section 2.3.1 for more details). However, PIC simulations have found a significant deviation from the velocity value predicted for the dispersion properties when relativistic intensities are used, and assuming immobile background ions [95,96]. The authors estimated this corrected velocity as $v_{prop}/c = \exp\left(-\frac{n_{ph}}{n'_c}\right) v_g = \exp\left(-\frac{n_{ph}}{n'_c}\right) \left(1 - \frac{n_e}{n'_c}\right)^{1/2}$, where n_{ph} is the electron density peak formed just before the laser front. First studies exploring this modification of the propagation velocity interpreted it as an *anomalous penetration* stemming from electron oscillations at the front of the laser beam [83]. These new simulations [95,96], however, revealed that this modification in the propagation velocity can be explained by energy balance between the electron kinetic energy, incident and reflected laser field energy, and an efficient reflection (ratio of the reflected wave intensity to the incident intensity) of the laser beam propagating through the relativistically transparent plasma.

3.3 Onset of RIT in thin targets

Unlike the previous case, thin targets are usually considered as those with a thickness smaller than the laser wavelength and/or on the order of the plasma collisionless skin depth. One of the conditions, for which relativistic transparency in these targets can occur, is via laser radiation-driven compression of the target electron layer to a thickness less than the skin depth. The skin depth in this scenario has to be corrected following the electron density increasing during the radiation compression. This results in an increase in the plasma frequency (according to eq. (2.17)), which, in turn, reduces the skin depth value (equation (2.40)).

Although the condition of relativistic transparency presented in the previous section, for relatively thick targets, could also be assumed as an overall interpretation for thin targets, theoretical models revealed additional complex phenomena for the transparency condition when sub-wavelength thick targets are employed. A simple 1D model was derived by Vshivkov *et al.* [97], to initially explain the complex phenomena occurring in this regime. Assuming a Dirac delta-like density profile for the target and by the analytical calculation of the nonlinear transmission and reflection coefficients, they obtained a transparency threshold for thin foils and ultra intense ($a_0 \gg 1$) laser pulses as:

$$a_0 > \pi \frac{n_e l}{n_c \lambda} = \zeta \quad (3.2)$$

where l is the target thickness. As n_c and λ are intrinsic parameters of the laser the actual parameter which controls the onset of the relativistic transparency for thin targets is simply the areal density $n_e l$.

Supported in this base, in the last few years, some other authors have published similar analytical studies on the relativistic transparency threshold in

thin targets [55, 73, 98]. Additionally, they initialised their analysis with sharp target boundaries and Dirac delta profiles. For simplification they assumed a monochromatic circular laser polarisation so that electrons oscillate only in the plane perpendicular to the propagation axis (X-axis) and at $X = 0$. From these initial conditions, and by solving the equations of the incoming wave interacting normally with the sharp profiled target, they derived approximate (and for $\zeta > 1$) reflection (R) coefficients (assuming no laser absorption, A, and thus $T + R = 1$, where T is the transmission coefficient) as:

$$R = \begin{cases} \zeta^2/(1 + \zeta^2) & \text{for } a_0 < \sqrt{\zeta^2 - \zeta^{-2}} \\ (\zeta^2 - 1)/a_0^2 & \text{for } a_0 > \sqrt{\zeta^2 - \zeta^{-2}} \end{cases} \quad (3.3)$$

This relation shows that when $a_0 \gg 1$ the reflection coefficient decreases to low values, which in turn translates to a higher transmission (following the expression $T + R = 1$). As such, the condition $a_0 \gtrsim \zeta$ can be adopted as a threshold to estimate the onset of the relativistic transparency in thin foils. This expression is in agreement with that obtained in other work [97].

A brief study to test this transparency condition experimentally is presented. The thinnest target thickness employed was 10 nm and the utilised laser had an 800 nm wavelength. The solid electron density of aluminium (the used target material) is $n_e/n_c = 447$, for this wavelength. These experimental parameters result in $\zeta \sim 17.5$. Likewise, the maximum laser intensity achieved was $\sim I = 6 \times 10^{20} \text{ Wcm}^{-2}$, corresponding to $a_0 \sim 11.8$ (for circular polarisation case presented in equation (2.55)). In ideal conditions, our experimental research would be slightly below the transparency threshold condition predicted by the analytical studies of thin foils and circularly polarised light, due to $a_0 < \zeta$. Moreover, for $\zeta \sim 17.5$, equation (3.3) estimates a target reflectivity of $\sim 99 \%$, corresponding to a transmission of only $\sim 1 \%$; which is far from the actual $\sim 12 \%$ transmission

obtained in our experiments (see section 5.1). Therefore, although this analytical model can be used as a good approximation to calculate the onset of transparency in thin foils in idealised scenarios, it would not be correct to use it for analysing and estimating a more realistic scenario due to simplifying assumptions made in models. For example:

- The model assumes a constant a_0 , i.e. constant intensity, throughout the interaction. However, in a real experiment the laser intensity present a Gaussian-like profile in time. This changes the intensity from low to high to low values during the interaction, and in turn, a_0 also changes.
- The model assumes a perfectly sharp density profile target during the entire interaction. However, it is known that in a real scenario the target experiences expansion in the initial stage of the interaction and bending when radiation pressure overcomes this expansion during the period of high laser intensities.
- The model assumes a constant electron density during the full interaction. However, in a real laser-plasma interaction the electron density will decrease during the expansion phase, and increase abruptly when radiation pressure effects dominates over thermal pressure.
- The model is one-dimensional, which does not take into account any volumetric effects (as volume is a three dimensional parameter), of key importance to the transparency regime, and thus overestimates the threshold value for the onset of RIT.

Due to analytical models becoming extremely complex to describe and interpret this relativistic regime in thin foils for more realistic conditions, today, with help of high performance computer clusters, high-resolution PIC simulations (see section 4.3) are routinely implemented. Thanks to these simulations a solid and

accurate understanding of the underpinning physics of this regime, under distinct laser and target conditions, can be acquired. Using this form of simulation, together with experimental results, the onset of RIT has been demonstrated to depend significantly on the initial target thickness/density and, laser intensity and polarisation. These results correspond to the first research study presented in the Chapter 5 of this thesis.

3.4 Examining the effects of RIT on ion acceleration

Despite the onset of the RIT limiting the energy attainable via radiation pressure acceleration, as has been introduced in the first section of this chapter, experiments carried out in the last few years [90, 91] and [99] have shown a significant enhancement of the maximum proton energies, occurring in the relativistic transparent regime. In these works, the energy transfer from the electric field of the laser beam to the ions is attributed to a significant volumetric heating of the electrons, when the target becomes relativistically transparent during the interaction, originating strong longitudinal electrostatic fields. Several numerical and theoretical investigations have predicted this enhance of ion acceleration using ultra-intense and high-contrast lasers in targets with thicknesses in a nanometre scale [100–102]. One of the proposed mechanisms responsible for this ion acceleration enhancement is the aforementioned BOA mechanism, which has resulted from extensive analytical and numerical studies [94, 103, 104]. This mechanism would emerge when a thin target (of the order of the skin depth) becomes transparent to the incoming laser. At that moment, the laser propagates through the relativistic underdense plasma volumetrically interacting with the hot plasma electrons and ponderomotively accelerating them to relativistic velocities. Due to the considerable difference between the

drift velocity of electrons and ions, the relativistic underdense plasma can be susceptible to Buneman instabilities [105], which rapidly grow resulting in a reduction in the relative drift velocity between electrons and ions, resulting on electron-ion two stream instability. The low phase velocity of these instabilities eventually resonates with the ions, and can result in ion acceleration as a result of a large longitudinal electrostatic field generated during this process, which co-moves with them. This energy transfer from laser-to-electrons and electrons to ions via streaming is potentially preserved until an energy balance is achieved (saturation). Simulations have predicted that the highest ion acceleration efficiencies, via BOA mechanism, are obtained when the target becomes relativistically transparent, $n_e < n'_c$, before the peak of the laser pulse, and classically transparent (non-relativistically), $n_e < n_c$ at the end of the interaction [106].

A recent experiment [107] demonstrated the presence of a new mechanism for ion acceleration enhancement in ultra intense laser interactions with thin (nanometre scale) targets. This work revealed that, together with protons accelerated by TNSA (sheath fields) and RPA (laser radiation pressure) mechanism, a high energy proton component is also produced only when the target becomes relativistically transparent. Using 2D and 3D PIC simulations, Powell *et al.* [107] found that, under these conditions, a plasma jet is formed at the target rear. A self-generated azimuthal magnetic field confines this plasma jet and guides it into the expanded layer of sheath-accelerated protons. The portion of the laser pulse, which is relativistically transmitted through the target, directly accelerates electrons trapped within this jet to very high energies (tens of MeV). Finally, the resulting streaming of electrons into the ion layers is able to enhance the energy of protons in the vicinity of the jet. A similar feature has also been reported in reference [108]. One common characteristic of BOA and this new ion acceleration mechanism is that in both cases the ion acceleration

enhancement is produced when ultra-thin targets (\sim tens of nanometres) became entirely transparent, along the laser path, during the intense laser interaction.

Another ion acceleration mechanism which is reported to occur during the onset of relativistic transparency is known as *relativistically induced transparency acceleration* (RITA) [109]. Unlike the aforementioned mechanisms, in the RITA scheme, the ion acceleration enhancement is optimised for heavy and thicker targets (\sim micrometers) when they become relativistically transparent in a finite region of the expanded pre-plasma at the target front side. This means that the target becomes transparent only in the regions preceding the laser front, but is not entirely transparent during the interaction. The key to this scheme, assuming an immobile heavy ions background, is to generate an incremental transparency, in time, in which the rising edge of the laser ponderomotively drives the relativistically underdense electrons and builds them up in local high density region just beyond the instantaneous corrected critical density surface. This is described as a ‘snowplow’ effect in which the plow is the laser pulse and the ‘snow’ is the electrons. The charge separation between heavy ions and electrons in the region depleted of electrons creates an electrostatic potential which propagates following the ‘snowplow’. This strong electrostatic field would produce quasi-monoenergetic ion bunches, whose peak energy could be adjusted by controlling the laser rise time and the front surface plasma density gradient. In addition, the authors [109] estimate that the electron ‘snowplow’ would not be formed if its velocity is greater than the group velocity of the laser; which occurs for laser pulses with rising edges too short or for plasma density gradients which are too long. In those circumstances, the target would not exhibit an incrementally induced transparency, curbing the efficiency of this ion acceleration mechanism.

3.5 Other potential applications of the onset of RIT

Although the most interesting applications of the RIT process in relation to the topic of this thesis are those surrounding charged particle dynamics, there are other potential applications which are worth exploring.

Relativistic plasma shutter

As discussed previously, RIT regime occurs when $n_e < n'_c$ is satisfied for a given target material. This relation depends on the Lorentz's factor, γ , which, in turn, depends on the laser intensity (see section 2.3.3). For an ideal top-hat intensity profile laser pulse with constant intensity, the target would be relativistically transparent or presents classical opacity for the entire pulse duration. However, a more realistic laser pulse exhibits a Gaussian-like profile, where its intensity varies from low values to a maximum value during its duration. Additionally, in a real experimental environment these pulses present a finite contrast where a significant ASE signal prior to, and after, the main pulse is presented. With this pulse profile the RIT condition will only be satisfied for the highest intensity regions of the pulse, whereas the lowest intensity regions will be absorbed or reflected at the front surface of the target [110]. This enables not only the generation of clean ultra intense laser pulses in time, but also in space, since the radial low intensities from the pulse edges will be also reflected. The basis of this mechanism is directly comparable with that of a plasma mirror [111], although with some distinctive differences. A plasma mirror provides clean laser pulses in reflection, from a material whose reflectivity depends on the laser intensity. Such a material transmits the low intensity light preceding the main pulse, but reflects both the main pulse and the ASE after it, through the generation of an overcritical reflective surface on the rising edge of the pulse. On the other hand, a relativistic

plasma shutter provides clean laser pulses in transmission, when a classical opaque target becomes relativistically transparent for the highest laser intensities of the pulse, discarding both the prior and the after ASE signal. Consequently, relativistic plasma shutters could permit the generation of much cleaner intense laser pulses than those generated by plasma mirrors. However, today it is still in a conceptual phase due to numerous issues in a realistic experiment, as the target deformation (expansion and compression) effects during the intense laser interaction. In addition, the transmission fraction is low compared with reflective plasma optics. Whereas the latter presents an intensity-dependant reflectivity peaking at $\sim 80\text{-}90\%$, the transmission fraction, for example, for the thinnest target included in this thesis is ‘only’ of $\sim 35\%$ (see section 5.1).

Shortened laser pulses

As a consequence of the relativistic plasma shutter, for an ideal Gaussian profile some region of the rising edge of the pulse does not have a high enough intensity to satisfy the transparency condition, $n_e < n'_c$, and thus this region is reflected whereas the remainder of the pulse is transmitted. This produces, in transmission, a shorter laser pulse, which could be as short as a quasi-single-cycle [112]. It has been experimentally demonstrated that the temporally shortening laser pulse concept is plausible by ultra intense laser-interaction with initial thin overdense foils, and by relatively long laser pulses (\sim hundreds of fs) [113].

Facilitating Fast Ignition

As has already been discussed in the Introduction, the fast ignition concept was conceived as an alternative to central hot-spot ignition to enable efficient fusion by inertial confinement. One of the key requirements of this approach is to get as much energy from the ignition laser pulse as possible coupled to the compressed fuel. Using an ultra-intense ignition laser, RIT, together with cone-guiding [19,

20], channelling [17, 18] and hole boring [114, 115] could play a very important role in the fast ignition scheme [115]. This is due to the significant fraction of laser light which may propagate deeper into the classically overdense plasma, depositing its energy at a higher compressed density and thus making the inertial confinement fusion approach more accessible.

Chapter 4

Methodology: Laser, Set-ups, Diagnostics & Simulations

In this chapter, the laser system, the experiment arrangements and diagnostics used for the generation, measurement and collection of the experimental results presented in this thesis are defined and described in detail. In addition, the chosen PIC code to simulate the experimental data is also presented.

4.1 Astra-Gemini Laser

The Astra-Gemini laser system is located at the Central Laser Facility within the Rutherford Appleton Laboratory in Oxfordshire (United Kingdom). This laser is a chirped-pulse amplification (CPA) system [10, 11] providing up to 40 J in two beams (20 J in each beam), with pulses duration of 40 fs (Figure 4.1). An F/2 off-axis parabola focuses the incoming beam to form a focal spot on the order of 3 μm in diameter at Full-Width at Half-Maximum (FWHM), reaching intensities on the order of 10^{20} - 10^{21} Wcm^{-2} . The system is optimised to deliver one shot every 20 seconds. The front end main oscillator, in the Astra area, is a Ti:Sapphire (TiS) and as such operates at a central wavelength of 800 nm (bandwidth 40 nm). The output seed is formed of ultra-short pulses of 12 fs

with few milijoules in energy and high-quality wavefront profile. Before the main amplification step, the seed is stretched up to 7 ps and amplified to milijoules. A Pockels cell together a linear polariser is used after this first pre-amplification step in order to select individual pulses, from a train of pulses with a repetition rate of 10 Hz. These individual pulses are then sent to the principal stretcher, created using a wavelength-dependent delay line based on diffraction gratings, obtaining pulses of duration 1060 ps. Once the seed is stretched in time, in order to reduce its power and thus avoid the damage threshold of the optical components during the amplification and minimise pulse distortion, three amplification phases are implemented. In the first phase the seed pulse is sent four times through a 10 mm thick and 10 mm diameter TiS crystal, which is pumped on both sides with a frequency-doubled Q-switched Nd:YAG laser. After this, the pulse reaches a maximum output energy of 4 mJ. Before the second phase the beam is expanded to 6 mm diameter, again this is necessary to avoid optic damage. As in the first phase, this second energy amplification phase is formed by a TiS crystal, pumped with a frequency-doubled Q-switched Nd:YAG laser, in a ‘bow-tie’ configuration, in which the seed pulse passes through the crystal four times. At the end of this phase the pulse is expanded to 18 mm containing around 120 mJ of energy. The final amplification phase involves the pulses passing through a TiS crystal four times. However, in this case the crystal is 24 mm in diameter, 12 mm thick and pumped by four, frequency-doubled, Q-switched Nd:YAG lasers. The pulse energy at the end of this third amplification phase is of 1.2 J. A scheme of the Astra configuration is shown in figure 4.1a.

The output Astra pulse (1.2 J, 1060 ps) is then guided to the Gemini area (see figure 4.1b). The Gemini seed is, first, split in the two main beams. Each beam is expanded to ~ 50 mm in diameter before they are amplified in a 4-pass TiS amplifiers. The amplifier crystals are slightly bigger than in the Astra area with 90 mm in diameter and 25 mm in length, due the larger beam diameters.

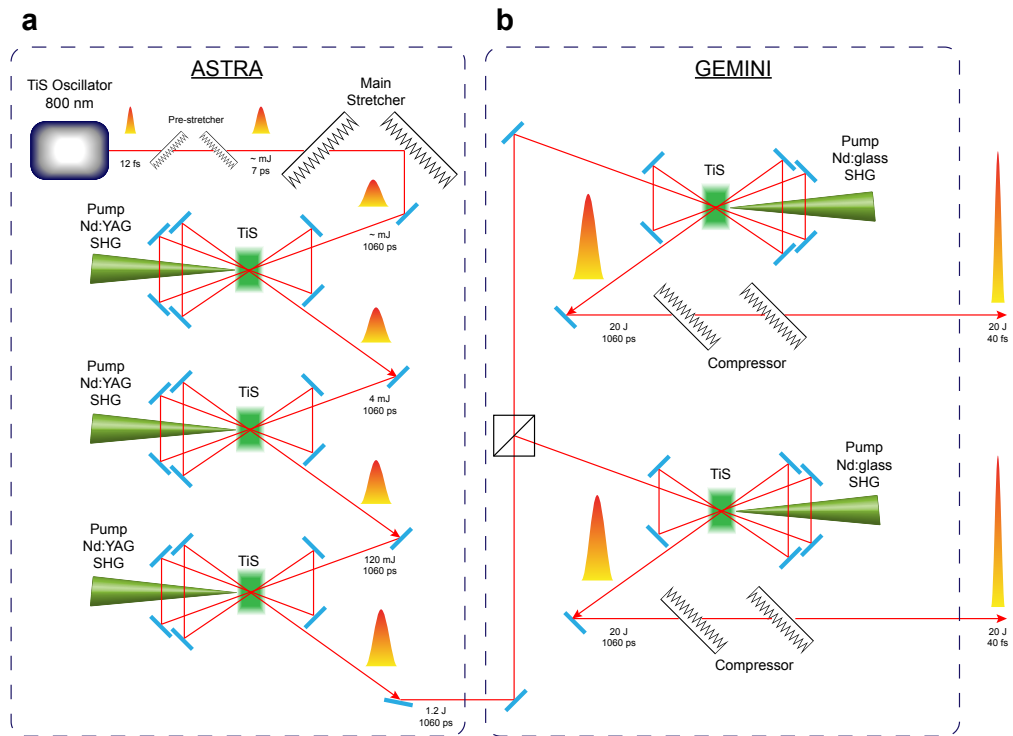


Figure 4.1: Schematic configuration of the Astra-Gemini laser. **a**, corresponds to Astra area while **b**, corresponds to Gemini area.

Each TiS crystal is pumped from both sides by two frequency-doubled Nd:glass beams. The output of the amplifiers are then expanded to 150 mm in diameter and compressed in a grating compressors giving an output of pulses of 20 J in energy and 40 fs in duration. In figure 4.2 a flow diagram of the Astra-Gemini laser is presented.

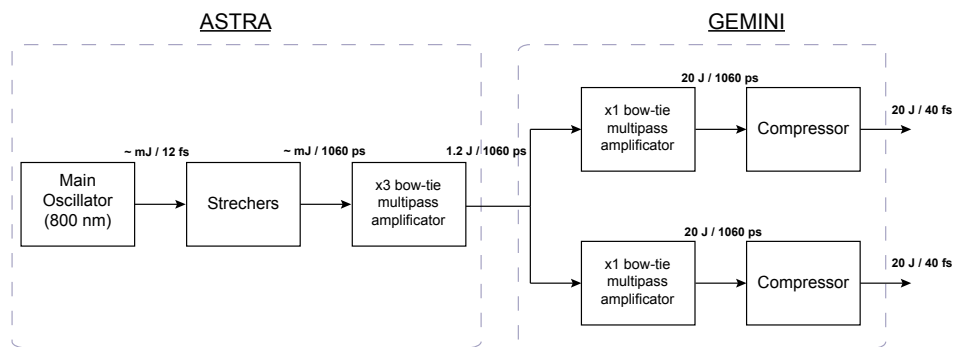


Figure 4.2: Flow diagram of the Astra-Gemini laser.

4.2 Experimental set-up & Key diagnostics

The experimental set-up used to obtain the results presented in this thesis is shown in figure 4.3a. In this configuration, the incoming beam is first passed through a double plasma mirror [111, 116] in order to increase the pulse contrast (where the reflectivity of each is $\sim 80\%$). With this system contrast of $\sim 10^8$ at 5 ps and $\sim 10^{11}$ at 1 ns is obtained (as it has been discussed in the section 2.2, e.g. 10^8 means that the peak intensity of the laser is 8 order of magnitude greater than the preceding undesirable signals, appearing in distinct sectors of the ultra intense pulses generation process, such as the ASE pedestal or the rising uncompensated dispersion). This corresponds to an enhancement of 4 order of magnitude in the pulse contrast using the double plasma mirror configuration. After the plasma mirrors, an adaptive optics (AO) mirror was used to minimise the effect of laser wavefront distortions (not included in figure 4.3a). This device consists of a reflecting surface which is able to selectively deform itself, and thus can compensate the distortion and correcting thus the deformations of the incoming wavefront. Therefore, the aim of the AO is get a laser wavefront as much flattened as possible, and thus a high quality focal spot can be formed by the parabola on the target. Due to the fact that the target thickness used in the experiments was tens of nanometres, both, plasma mirrors and AO, are crucial elements to avoid an over heating and expansion of the target prior to the main pulse interacts with the target and to achieve an interaction that as homogeneous and uniform as possible.

As a key part of the research presented in this thesis addresses the integration of nanometre targets under various degrees of laser polarisation it is necessary to control this parameter using wave plates; in particular a $\lambda/4$ wave plate was used. With this device we were able to switch the polarisation of the incoming beam between linear (default polarisation of the beam), elliptical and circular. Finally,

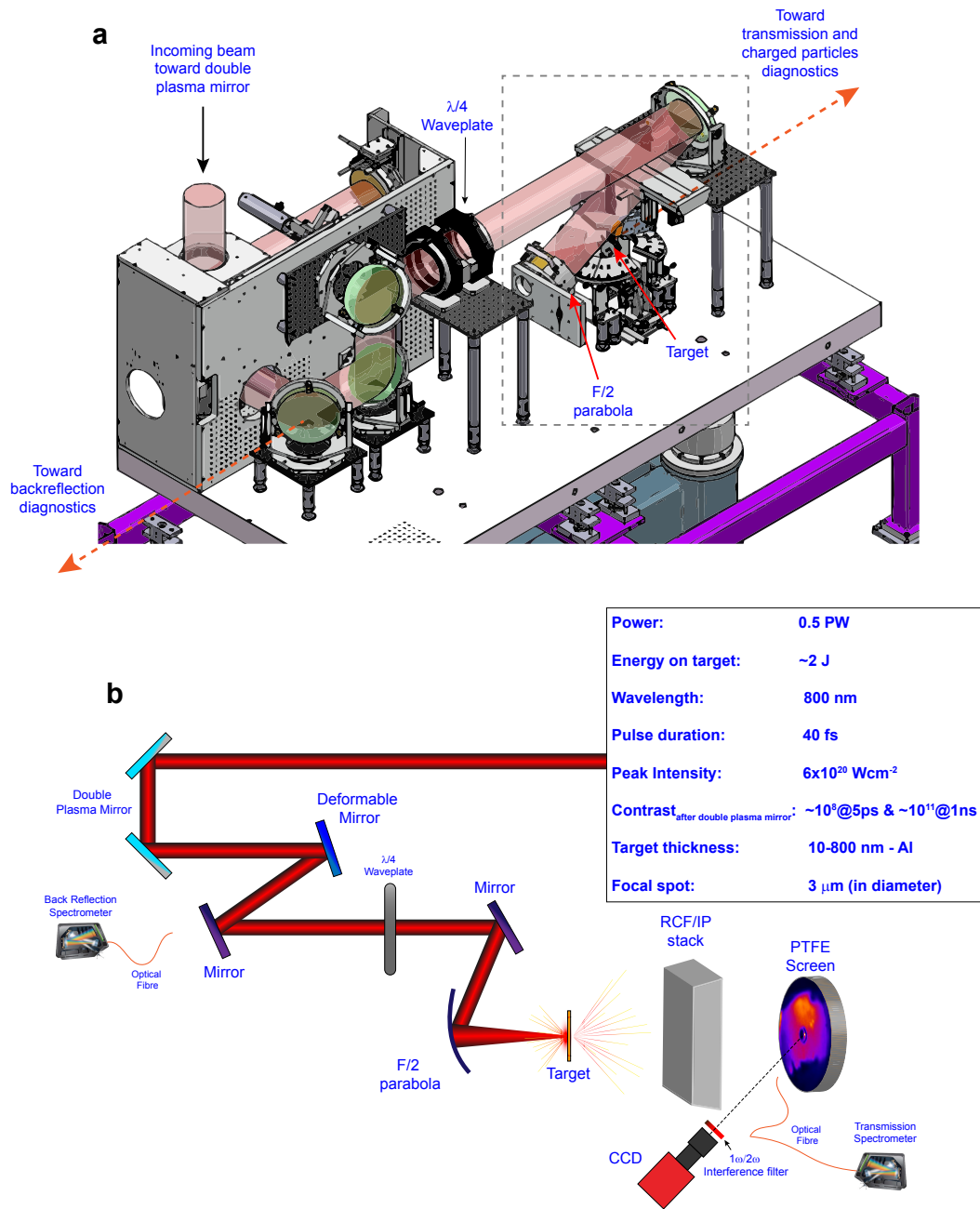


Figure 4.3: **a**, Experimental target chamber layout including the main systems for conforming and guiding the incoming laser pulse to the target. **b**, Schematic target chamber-layout including the main diagnostics for back-reflection, transmission, and spatial distribution measurement of the accelerated charged particles.

using a F/2 parabola, the pulse, with 2 J of energy (on target), was focused along target normal onto the front surface of aluminium foils with a focal spot size of 3 μm , in diameter. These parameter values provided a calculated peak intensity of $6 \times 10^{20} \text{ Wcm}^{-2}$. Target thickness between 10 and 800 nm were employed.

It should be noted that the actual energy reaching the target is lower than the nominal energy at the output of the final compressor. This occurs because of the limitations on reflectivity of the multiple optical components with which the pulse interacts after leaving the compressor.

The main measurements made using the set-up for the research data presented in this thesis were:

- Measurement and characterisation of the transmitted light density and its wavelength spectrum.
- Measurement and characterisation of the back reflected light spectrum.
- Measurement and characterisation of the accelerated electron and proton spatial distributions.

Figure 4.3b displays a schematic of the set-up together with the main diagnostics in relation to transmission, back-reflection and charged particles characterisation. A more detailed description of these diagnostics together with the most relevant components in each, is included in the following sections.

4.2.1 Diagnostics

In this section, the configuration of each individual diagnostic is presented and described in detail.

Spatial and spectral measurement of transmitted light

In figure 4.4a the experimental configuration, used inside the target chamber, to measure the spatial distribution and density of the light fraction transmitted

through the interaction solid target is presented (this chamber section corresponds to the dashed square in figure 4.3a). The incoming laser beam (in red) comes from the top-left, just after the waveplate. A mirror then guides the beam to the F/2 parabola which focuses the beam onto the target. The transmitted light (in green) is scattered from a diffuse screen placed just behind the target at ~ 18 cm. The selected diffuse screen for this purpose was Polytetrafluoroethylene (PTFE), commonly known as *Teflon*. This screen works in a similar way to a Lambertian surface which scatters the incident light in the same amount in all directions making its apparent brightness independent of the observer's viewing angle.

Scattered light from this screen is directed outside the chamber to the detection system. Figure 4.4b shows the same configuration, as in figure 4.4a, but zoomed in to show the main elements of the transmitted light detection system.

Outside the chamber, the transmitted light was guided to a box containing two CCD (Charge-Coupled Device) cameras in order to record the spatial distribution and photon density of this transmitted light. This configuration is shown in figure 4.5a. A more detailed view of this configuration is illustrated in figure 4.5b. First, an objective lens is used to control the focus and magnification of the scatter screen inside to the chamber. After the objective a beam splitter distributes the beam in two separated paths, where at the end of each path a CCD camera is located. By selection of the appropriate interferometric filter, each camera records light corresponding to the first and the second harmonic, respectively. These filters were located separately in front of each camera together with neutral density (ND) filters to attenuate the amount of incoming light in order to avoid saturation and damage to the CCD chips. The cameras used in this diagnostic were the commercial Stingray CCD cameras, capable 16-bit image capture. Although this kind of camera is popular in the astrophysics field, in the last few years it has been widely used to record the light in distinct paths as well

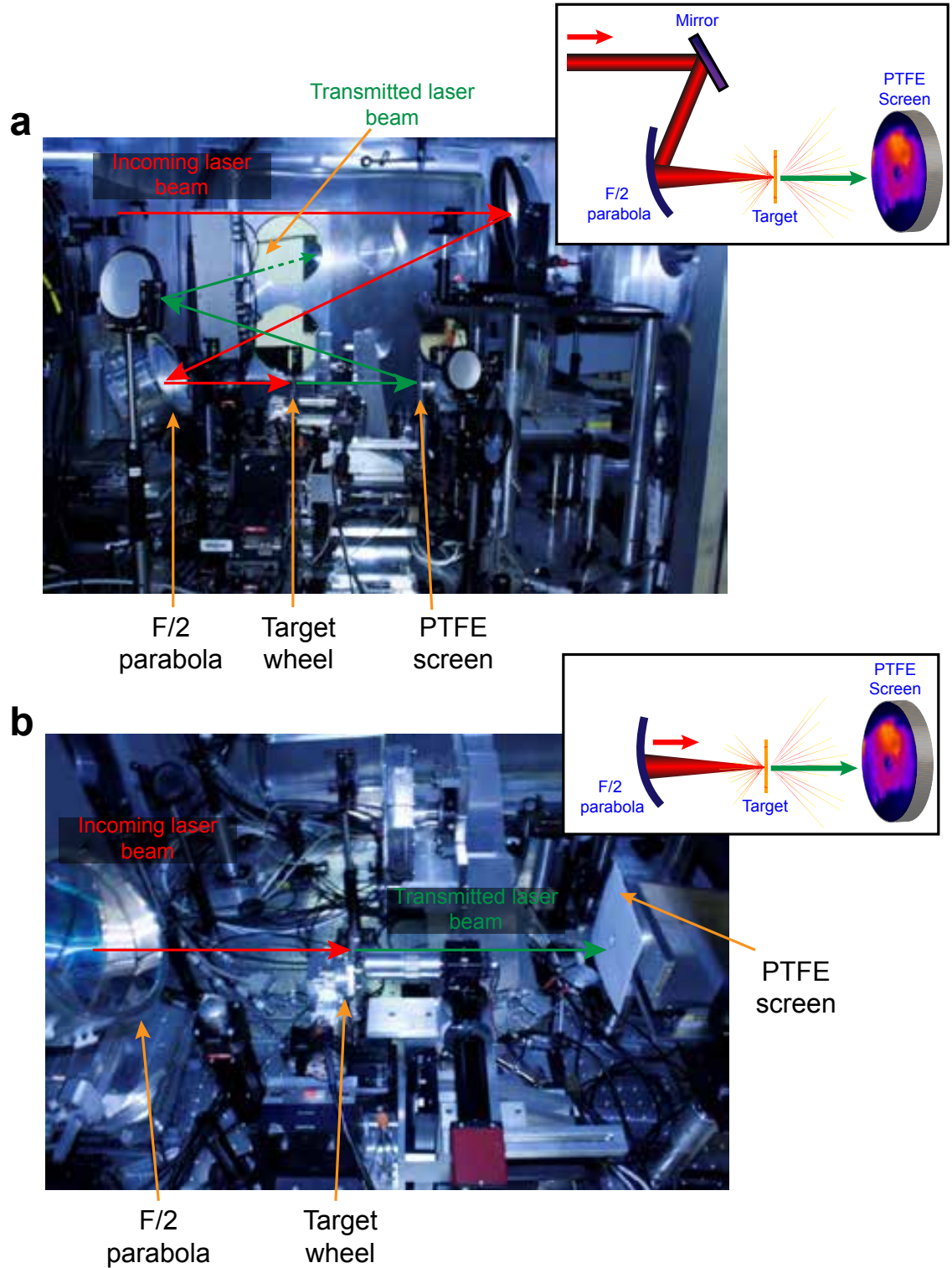


Figure 4.4: **a**, Experimental target chamber set-up illustrating the main systems around the target. Incoming laser beam (in red) and transmitted laser beam (in green). Top-right box illustrates a schematic configuration of the experimental set-up in **a**. **b**, Zoom in from **a** in order to identify more clearly the target and the systems around. Top-right box illustrates a schematic configuration of the experimental set-up in **b**.

as the X-ray generated in laser plasma experiments.

These cameras are formed by capacitors, with a MIS (Metal Insulator Semiconductor) structure (scheme illustrated in figure 4.6a), which act like individual pixel, collecting the incoming photons (usually a silicon photo active layer) and converting them into electrons which, in turn, are converted into ‘counts’, i.e. a measure of the intensity of light on that pixel. The total number of counts depends on the quantum efficiency (photo-electron generated for each incoming photon) of the CCD chip, which can be higher than 90% in the most sophisticated models. An important feature, for the experiments presented in this thesis, is its dependency on the incoming photon wavelength. Instead of having a homogeneous response, usually this camera has a quantum efficiency which changes appreciably as a function of wavelength, from a peak at some wavelengths to relatively lower values at others. Figure 4.6b shows the quantum efficiency of the cameras used in the experiments. It reveals an efficiency just above 10% for the first harmonic of the laser (i.e at 800 nm) to $\sim 23\%$ at the second (i.e at 400 nm). This change was taken into account when the transmission measurement, for both harmonics, were analysed.

In order to calibrate the photon density scattered on the diffuse screen, the screen was illuminated using the laser without a target in place. The pictures taken in this shot were used as reference and enable us to convert pixel values during normal shots, into laser energy transmitted through the target.

The spectrum of transmitted light was measured using an optical spectrometer, also placed outside the target chamber. An optical fibre was then connected to this spectrometer and pointed at the diffuse screen, inside the chamber. Figure 4.7 shows the experimental configuration of this set-up.

For many years optical spectrometers have been used to measure the intensity (photons number) of light as a function of its wavelength (or frequency). As for most optical devices its main application, in its beginning, was in astronomy and

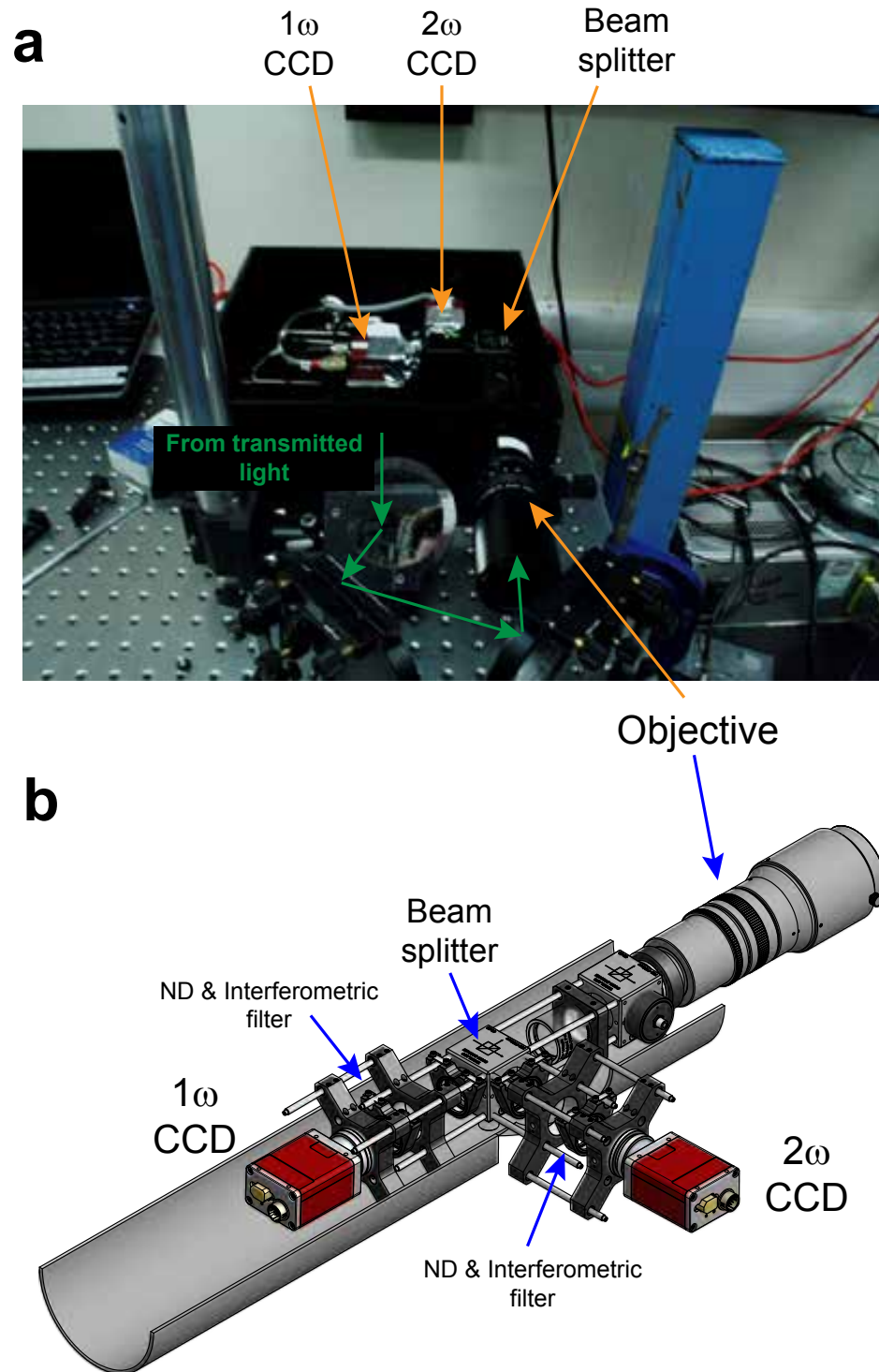


Figure 4.5: **a**, Experimental set-up of the transmitted light diagnostic placed outside the target chamber. The transmitted light coming from the chamber (green arrows) is guided into the black box where, after a beam splitter, is recorded in two independent CCD cameras to measure the total transmitted light at 1ω and 2ω , respectively. Interferometric filters placed in front of each camera enable the selection of each frequency. Convenient ND filters were also placed to avoid saturation and possible damages in the camera chips. **b**, Layout of the transmitted light diagnostic design.

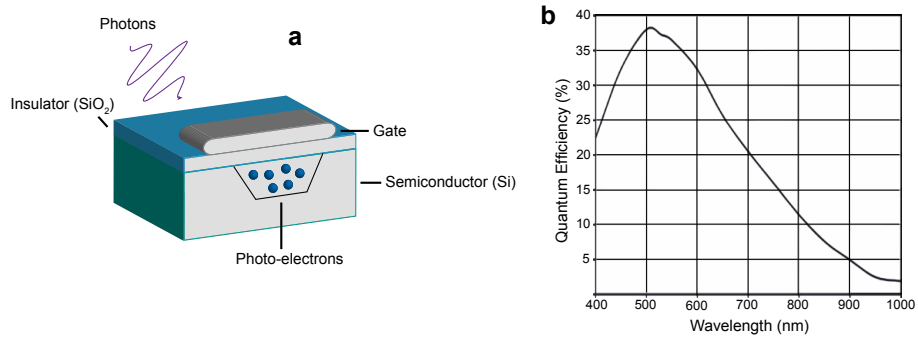


Figure 4.6: **a**, Illustration of the main components of a pixel from a chip of a CCD camera. **b**, Quantum efficiency as a function of wavelength of the CCD cameras used in the transmission diagnostic. It presents a much higher efficiency at the 2ω (400 nm) than at 1ω (800 nm). These values have to be considered for a correct calibration of the cameras response.

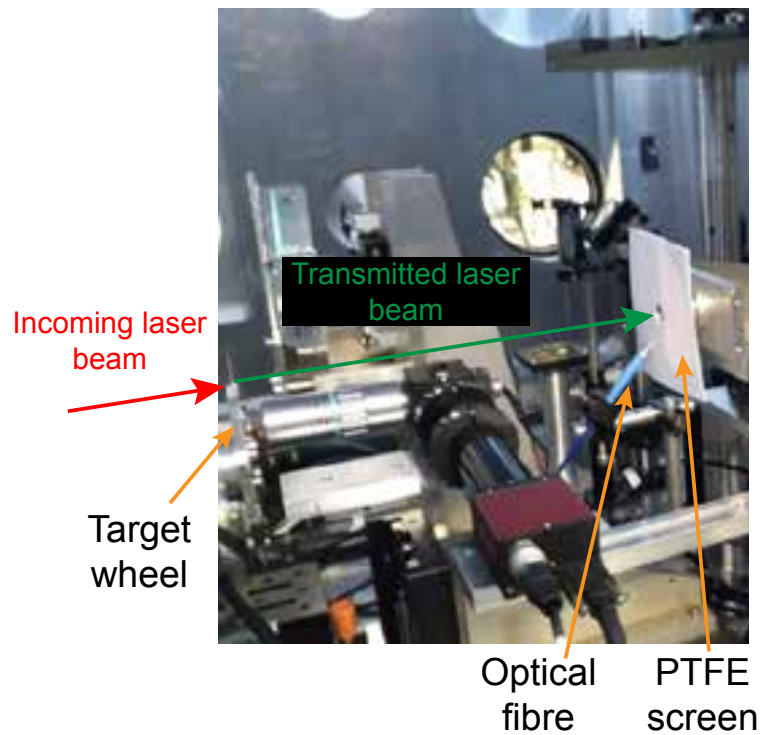


Figure 4.7: Experimental set-up for the measurement of the transmitted light spectrum. An optical fibre, connected to an optical spectrometer, was placed pointing at a diffuse screen which was located just in front of the rear surface of the target.

also in chemistry research. An optical spectrometer is typically composed of a dispersive section to spatially separate each individual wavelength, and a photosensible detector to record the final spectrum. Prisms and diffraction gratings are the most common dispersive mechanisms used in the current spectrometers. The most popular detectors currently are CCD cameras (as described previously) due to their high quantum efficiency and spectral resolution. In this thesis a commercial Ocean Optics spectrometer has been used to measure the spectrum of the transmitted beam during the laser plasma interaction. Figure 4.8a displays a schematic of the main components of such a spectrometer. The incoming beam from an optical fibre is first passed through a rectangular slit to regulate the amount of light entering the spectrometer in order to control the spectral resolution, figure 4.8a (label 2). At the same point a bandpass filter is used to select the range of wavelength to be measured, figure 4.8a (label 3). Before the light is separated into different wavelengths using a diffraction grating, figure 4.8a (label 5), first the beam must be collimated, figure 4.8a (label 4), in order to have uniform dispersion along the grating. Finally, a mirror, figure 4.8a (label 6), focuses the dispersed light from the grating onto a 2D CCD detector, figure 4.8a (label 8). The spectrometer used in the experiments, whose results are presented in Chapter 5, had a detection wavelength range of 900 nm (from 200 to 1100 nm, to encompass the first and second laser harmonics) and a 0.5 nm of spectral resolution.

As in the case on calibrating the energy response of the scatter screen, a shot without a target was carried out in order to calibrate both the energy contained within the spectrum and the central wavelength of the transmitted light. Comparing this reference shot with any transmitted spectrum during normal target shots made it possible to measure any spectral shift due to the laser plasma interaction. Besides this, the wavelength measured for any spectrometer has to be internally calibrated. For this purpose, a Hg-Ar calibration light source

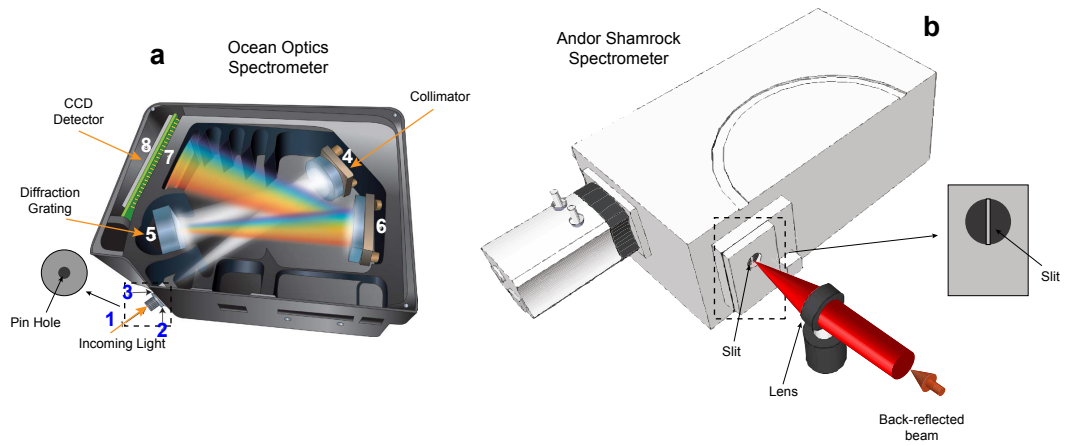


Figure 4.8: **a**, Schematic of the Ocean Optics spectrometer used in the transmission and back-reflection diagnostics. The light input of this class of spectrometer can be consider like a pin-hole. **b**, Schematic of the Shamrock spectrometer used in the back-reflection diagnostic. Unlike **a**, this kind of spectrometer present a slit in the incoming light path. This slit enables the measurement of the spatial spectrum of the incoming light along one radial direction.

was employed. This source emits a very known and stable wavelength spectrum. The spectrum measured by the spectrometer is then calibrated when the Hg-Ar lamp is connected to the spectrometer and the wavelength measured by the spectrometer and the known wavelength emitted by the lamp are cross-calibrated.

The experimental data obtained with this diagnostic conforms part of the research study included in the Chapter 5.

Spectral measurement of back-reflected light

In order to measure the spectrum of light reflected from the interaction target, the same class of optical spectrometer as in the transmitted light spectra diagnostic was used (figure 4.8a). In this case the optical fibre was positioned outside the chamber, in the path of the light reflected backward from the plasma generated when the laser interacts with the target. A schematic of this configuration is shown in figure 4.3b. Measuring the spectral shift of back-reflected light means it is possible to calculate the velocity and direction of movement of the target critical surface during the interaction. To measure such a shift, the spectrum recorded in the same shot as in the transmission diagnostic without any target in

the laser path, was used as a reference. Knowing the spectrum of laser light in this condition enables us to know what effect the plasma plays to the back-reflected light during shots involving targets.

A second configuration to measure the back-reflected spectrum was also employed. In the previous configuration the total light collected by the spectrometer was limited to the numerical aperture of the optical fibre used, i.e. a single pin hole. This limits the measurement of the spectrum to a spatially small area of the back reflected beam. In this second configuration, a different spectrometer was included (an Andor Shamrock). This spectrometer has the advantage in that it is able to measure the spectrum of an incoming beam spatially along one line with the incorporation of a narrow slit ($\sim 50 \mu\text{m}$) in front of the input port of the device. In order to guide the back-reflected light into the slit, a converging lens and some mirrors were utilised (see figure 4.8b for a schematic of this configuration). This set-up was placed outside the target chamber and just in the back-reflected beam path. With this second configuration it is therefore possible to measure and characterise the spectrum of the back-reflected light along a specific radial direction instead of an unique small area like in the previous configuration.

The experimental data obtained with this diagnostic forms part of the research study included in the Chapter 5.

Spatial distribution and energy measurement of accelerated electron and proton beams

To measure the spatial distribution of the beams of accelerated electrons and protons during the laser target interaction, Imaging plates (IP) and Radiochromic films (RCF) were used, respectively (see section 4.2.2 for more details about these films). Both kinds of films were packed together in a stack configuration as shown in figure 4.9a. In front of the stack a thin aluminium layer ($\sim 13 \mu\text{m}$) was included

to avoid any damage from transmitted light to the films inside the stack and to prevent heavy ion contribution in the final measurements. Due to their much higher mass, these heavy ions are mostly absorbed by this aluminium foil.

Several RCF layers interwoven with Mylar layers, with increasing thickness were used in a stack configuration, to obtain multiple proton distributions filtered in energy. Two stack configurations were distinctively used. One including only HD-V2; and the other HD-V2 and EBT-2 RCF designs were simultaneously used to properly resolve and visualise the spatial-intensity distribution of both the low energy-high density and the high energy-low density proton beams, respectively. For electrons, a similar configuration was used, but in this case with iron layers, of increasing thickness, interwoven with several IP layers in order to measure the spatial distribution of the electron beam for different energies (see figure 4.9b). RCF layers were placed first in stage and then the IP at back. This distribution is due to the particular energy deposition of protons and electrons on the layers. If the IP layers were placed preceding the RCF layers, the proton measurement would not be possible. The stack was located 3.4 cm downstream from the rear surface of the target, taking in account the electron and proton beams divergence in order to resolve properly their angular distribution.

The experimental data obtained with this diagnostic forms all the research included in the Chapter 6 and 7.

4.2.2 Additional devices used in the diagnostics

Waveplate - Controlling the polarisation of the laser beam

Although the waveplate did not form directly part of any diagnostic, it is a highly important component of the experimental set-up and to the data presented in this thesis.

A waveplate (or as it is commonly mention in the literature, *optical retarder*)

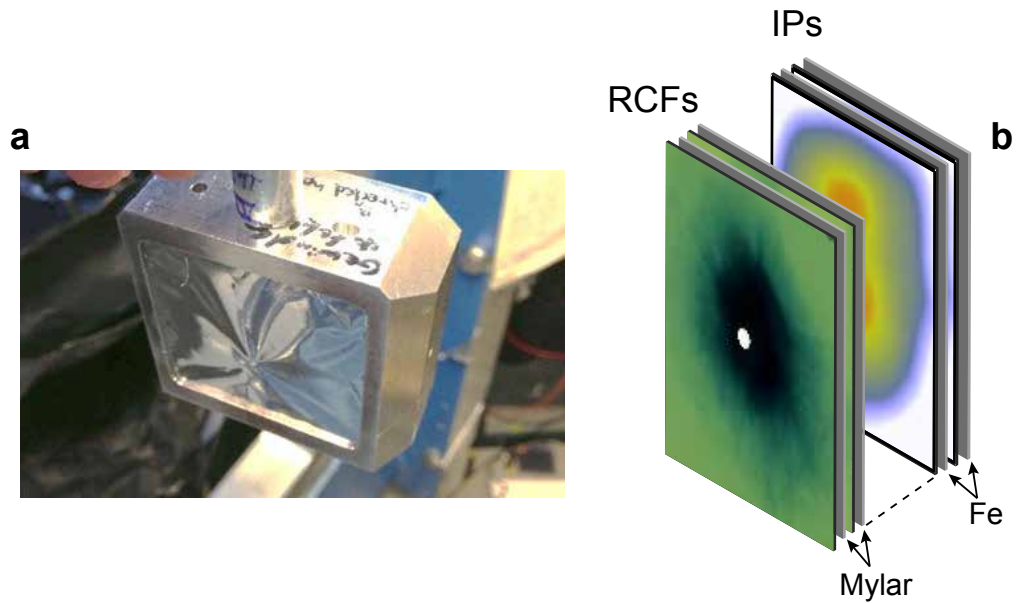


Figure 4.9: **a**, Experimental stack design, placed in front of the rear surface of the target. Inside the stack are included RCFs and IPs films to measure the spatial distribution of both beams, the accelerated protons and electrons, respectively, as it is shown in **b**. Mylar and Fe layers were interwoven with the RCFs and IPs, respectively, to classify the beams in discrete energies. An aluminium foil was placed in front of the stack to prevent any damage in the films from the transmitted light, and avoid heavier ions contribution in them.

is an optical device which introduces a relative phase shift between the two specific orthogonally polarised components of an electromagnetic wave. Although ideally the relative amplitude of the incident wave is not affected when it travels through the device [117], in a more realistic scenario, waveplates present a slight attenuation accentuated by multiple reflections between the inner surfaces of the plates. In each kind of waveplate there is always two directions or axes, a fast axis and a slow axis. If the electric field component of the incident wave is oscillating parallel to the slow axis it is retarded in phase relative to the electric component oscillating parallel to the fast axis when the wave travels through the waveplate. Depending on the relative retardation between the two axes, the waveplate can be classified as a quarter-waveplate ($\lambda/4$) when the relative retardation is $\pi/2$, or half-waveplate ($\lambda/2$) when is π . The waveplate used in the experiments presented in this thesis, and to switch between linear, circular and elliptical polarisation, was a quarter-waveplate. A half-waveplate was also used to switch between p and

s linear polarisations.

One of the most important mechanisms to produce a relative retardation in the two orthogonal linear components is by propagating the wave through a linearly birefringent medium. The basic principle of operation of these waveplates is based on an uniaxially anisotropic crystal whose optic axis is parallel to the end faces of the plate. Then, one of the two orthogonal components of the wave will be parallel and the other perpendicular to the optic axis (assuming perpendicular incidence of the wave with the waveplate). This crystal is built in a way that presents different refractive indices along the parallel (ordinary, n_o) and perpendicular (extraordinary, n_e) direction of the optic axis. The component parallel to the optic axis, therefore, is propagated through the crystal at a velocity equal to c/n_o and the perpendicular to c/n_e (where c is the speed of light in the vacuum). If the thickness of the crystal is d , the velocity difference between the two components leads to a cumulative phase shift equal to $(2\pi d/\lambda)(n_o - n_e)$ (where λ is the free-space wavelength of the incoming beam). Using this simplified equation (the multiple reflections between parallel faces of the crystal are not included), the crystal thickness required to produce any phase-shift given a material with a known birefringence ($n_o - n_e$) is calculated. Due to the presence of birefringence, if the slow and fast axes of the waveplate are rotated around the optical axis it is possible to change the polarisation of the incoming wave between different polarisation states. In our experiments, the quarter-waveplate was rotated to 0 , $\pi/4$, $\pi/8$ radians to switch the laser polarisation from linear, circular and elliptical, respectively. Those rotation angles induced a phase difference between the two orthogonal components of the incoming beam in $\Delta\theta = 0$ for linear, $\Delta\theta = \pi/2$ for circular and $\Delta\theta = \pi/4$ for the elliptical polarisation case. In all shots during the experiments, the incoming laser pulse was linear polarised (more precisely, p-polarised) with respect to the target.

In spite of there are several common material used for the crystals, such as

quartz or calcite, the quarter waveplate used in the experiments presented in this thesis was made from a mica crystal. Although mica is actually biaxially anisotropic, because they are parallel to each other and to the crystal, it behaves as an uniaxial crystal.

Imaging Plates - Spatial distribution measurement of electron beams

Although Imaging Plates (IPs) were designed as an alternative to the screen-film X-ray detectors used for medical and biological applications [118], currently they are also widely utilised in laser-plasma experiments as a X-ray [119], γ -rays, electron [120], proton and neutron detectors, due to its extremely high sensitivity, linear response over a large dynamic range, high spatial resolution, and the potential to use it multiple times due to its reusable nature. In the results presented in this thesis, IPs have been used to experimentally measure the two-dimensional spatial electron density distributions produced during the laser matter interactions.

Each IP is composed of a photostimulable phosphor layer [$BaFBr : Eu^{2+}$], supported by a flexible metal substrate (Figure 4.10a), which, when excited by ionising radiation, it is able to store the energy absorbed and re-emitting it when it is illuminated by a visible or infra-red radiation source. This process is known as photostimulated luminescence (PSL).

More precisely, when ionising radiation is absorbed by the photostimulable layer, some of the Eu^{2+} ions are further ionised to Eu^{3+} , exciting the new liberated electrons to the higher energy conduction band of the phosphor crystals. Although some of those generated electron-hole pairs directly recombine and scintillate, others are trapped in the Br^- and F^- vacancies (called F^+ centres), and which were introduced in the phosphor crystals during the manufacturing process. This idea is schematically showed in figure 4.10b.

In order to recover the information stored in the excited plates, visible light (\sim

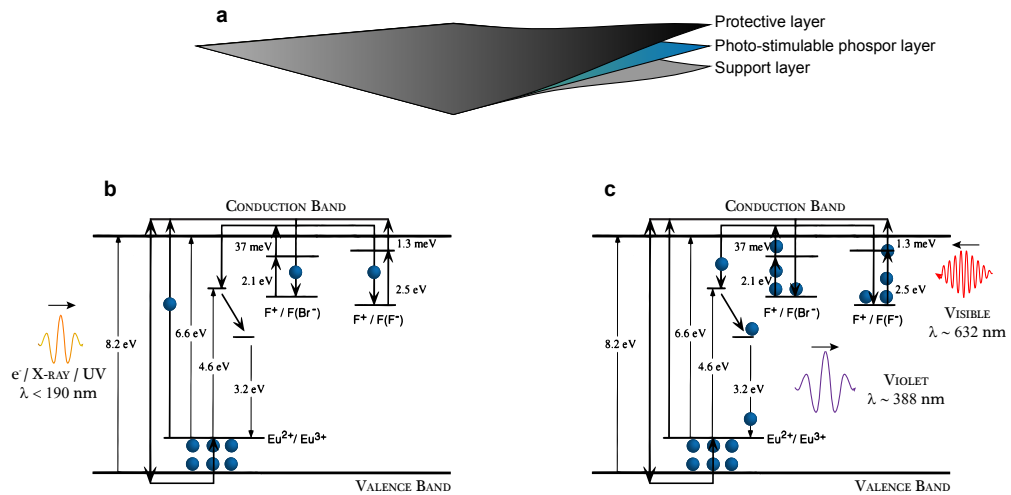


Figure 4.10: **a**, Representation of an IP film illustrating the individual layers which compose it. **b**, Band diagram of the absorption process of an incoming particle which excites an electron from the valence band and trapped in the F^+ centres. **c**, An external visible light (~ 632 nm) excites the electrons trapped in the F^+ centres, which relax to the lower energy levels, converting the Eu^{3+} ions in Eu^{2+} and emitting a photon in the process (~ 388 nm).

632 nm) from a laser is used. This light has enough energy to release the trapped electrons from the F^+ centers back to the conduction band, and from there they decay to the lower energy level, where are the Eu^{3+} ions, converting them again in Eu^{2+} and emitting a photon in the ultraviolet range (~ 388 nm). This idea is schematically shown in figure 4.10c.

A more detailed explanation of this mechanism can be found, for example, in [121] or [122].

Radiochromic Films - Spatial distribution measurement of proton beams

In order to experimentally measure the two-dimensional spatial proton density distribution presented in the research chapters of the thesis, RadioChromic Films (RCF) have been used [123, 124]. RCF consists typically of a single or double active layer sensitive to ionising radiation. The active layer is made of organic microcrystal monomers which are polymerised when exposed to radiation. Depending on the total absorption (proton dose) of the polymer

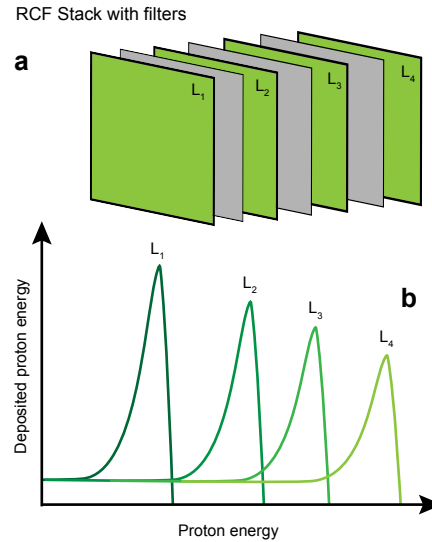


Figure 4.11: **a**, Illustration of RCF films in a stack. **b**, Bragg curves of the absorbed dose in each individual RCF film. These curves present the characteristic Bragg peaks of protons. Protons with highest energies are deposited in the latter films.

molecules, the active layer exhibits distinct coloured areas proportional to such absorption. Using an optical scanner, in transmission, the parameter to quantify the differences in colours (dose) is known as the Optical Density (OD) of the film (defined as $OD = \log_{10}(I/I_0)$), which can be described as the reduction in the intensity of light, from the scanner, when it is transmitted through the film (I) compared to the maximum light intensity, from the scanner, without film (I_0). To convert the measured optical density into proton dose, a RCF film was scanned, using the same technique, after its exposition to a known proton dose from a characterised conventional RF proton accelerator [125, 126].

When a certain number of RCF films are formed in a stack configuration, the energy spectrum of the accelerated protons can be measured; resolved in both, energy and spatial distribution. A stack composed of these films presents a limited maximum energy resolution of ~ 1 MeV due to the thickness of each film. Interweaving metallic or plastic filters with the RCF films can be also obtained distinct proton energy resolutions above ~ 1 MeV. Protons absorption present a distinctive response, in the form of a Bragg peak, when they travel through the RCF films (or matter). This pronounced peak is explained by the increasing of

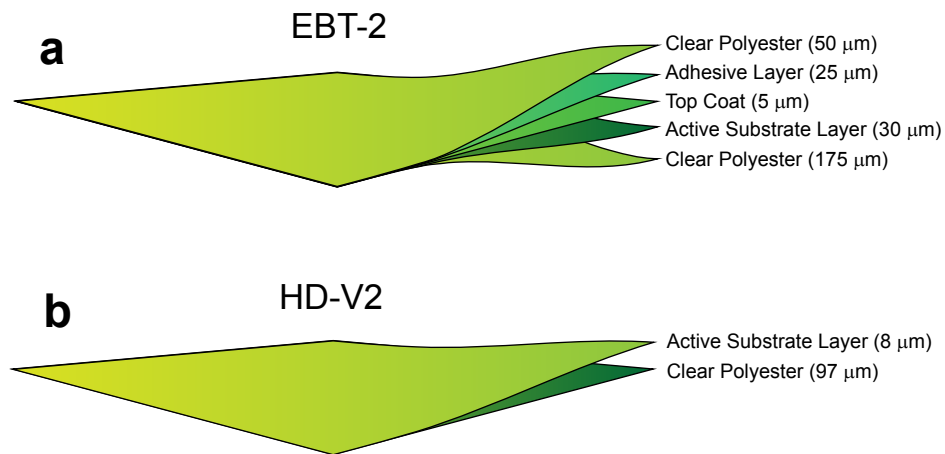


Figure 4.12: **a**, Representation of a RCF EBT-2 film illustrating the individual layers which compose it. **b**, Same for a RCF HD-V2 film.

the interaction cross section, between protons and the RCF films, as the energy of the protons decreases. In addition, this absorption is inversely proportional to the square of the proton kinetic energy. Because of that, protons with the highest energies are absorbed in last films of the stack. A schematic of this absorption process is illustrated in figure 4.11. Moreover, protons deposit a fraction of their energy in all layers penetrating through before being stopped, so the measured total deposited energy in a specific film is the convolution of the energy spectrum with the response function of the RCF itself.

This characteristic absorption process of protons in the RCF films also provides a precise measurement of the spatial distribution of proton beams, corresponding to a transversal section of the beam, for specific energies (by filtering). This, together with the distance between the target and the stack, allows to determine the divergence of the proton beam as a function of energy.

For the experimental results presented in this thesis, HD-V2 and EBT-2 RCF designs have been used (Figure 4.12). The most significant difference between both designs is that EBT-2 is much more sensitive to lower proton fluxes, being more suitable to imaging the spatial proton density distributions.

4.3 EPOCH-PIC Simulations

In intense laser solid interactions there are many processes which occur on the femtosecond and picosecond time scales, fundamental to the underlying physics. Many of these processes are unable to be resolved experimentally at present. In addition, currently with the available lasers there is a big limitation in terms of experimental repetition in order to validate and confirm previous results. These limitations are concerned mainly in the thermal processes appearing in the pump laser, amplification steps and in the stretcher and compressor gratings which have to be cooled down between shots. Nevertheless, a more important limitation for shots repetition is related to solid target alignment before each shot. In the last years, with the availability of high performance computers, simulations have been an advantageous tool to complement the analysis of experimental results. Simulations are based on the design of a real system model, which by using strategic simplifications, enables the understanding and interpretation of the studied system behaviour. In addition, this model is able to predict or anticipate results under different initial conditions on the system.

For this thesis Particle-in-Cell (PIC) simulations have been employed. Simulations of this kind have been broadly used in plasma physics [127] in order to simulate the full kinetics of a plasma and its interaction with the generated self-consistent electromagnetic fields, providing a very fundamental model of the dynamics of an ideal plasma. In the relativistic regime of short pulse laser-plasma interactions, where collisions are not dominant, PIC codes are particularly well suited for predicting the evolution and behaviour of the system. However, PIC codes also have limitations which must be considered. Trying to simulate laser interactions with highly overdense plasmas and/or high temporal/spatial resolution PIC codes becomes extremely expensive and requiring big computer clusters to run them. Because the scheme is explicit in these codes, they

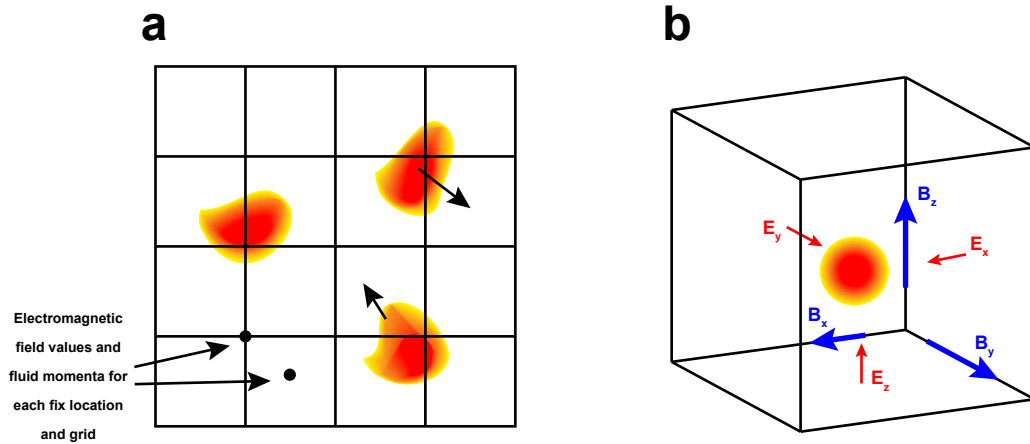


Figure 4.13: **a**, Macro-particles of finite size moving freely in space under the action of electromagnetic fields; **b**, Yee grid showing the geometry of the spatial discretization scheme for the electromagnetic field quantities.

must resolve the plasma frequency, skin depth and the Debye's length. For 3D simulations, the simultaneous refinement of the grid and time steps in all dimensions by a factor n leads to the computational effort increase by the factor n^4 .

One way to overcome these limitations (in the ps regime) is the use of hybrid PIC codes. This type of PIC code is based on a hydrodynamic description of the high-density background plasma considering the plasma particle interactions and its evolution as a fluid. These codes have much lower time resolution, because they suppose the background plasma to be quasi-neutral, and thus eliminate the fastest plasma oscillations at the Langmuir frequency. This enables the possibility to run simulations with very large plasma regions of high density. However, these codes do not consider some of the underlying physics and therefore, it is necessary to check if this omitted physics is important or not for each particular problem.

Although there are numerous PIC codes, all the simulations included in this thesis have been conducted using the EPOCH-PIC code [128, 129]. In this code a bunch of charged particle is considered like a macro-particle, which represent many real particles. Given that this code does not included collisions, the macro-particles are free to move through each other. Since they represent a 'cloud' of

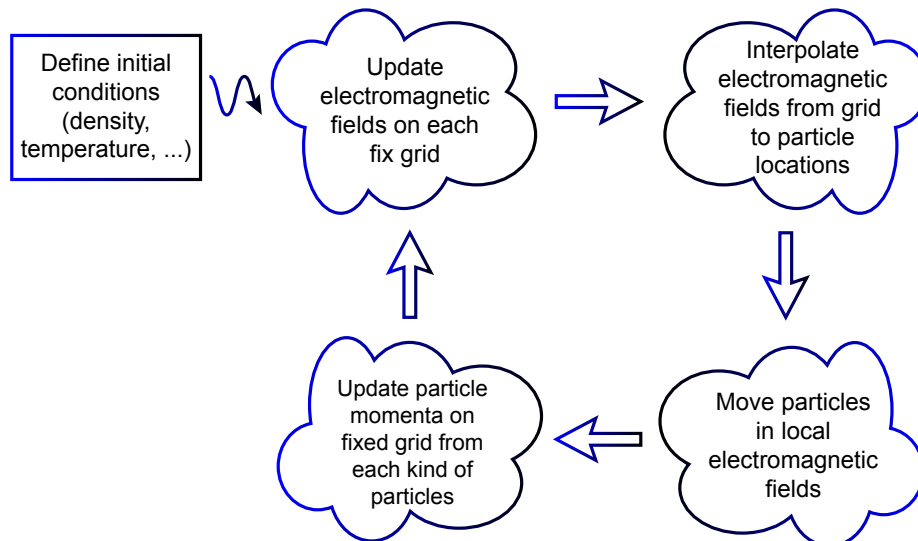


Figure 4.14: PIC algorithm for the fields and fluid momenta evaluation. From defined initial conditions it solves the Maxwell equations for each cell and then move accordingly the particles at time that updates their distinctive values. This process is repeated until the end of the simulation.

real particles they are going to occupy a finite volume and have a shape, which is not going to change under normal motion. These macro-particles do not rotate or have any internal degrees of freedom either. Before this code is run it is necessary to define initial conditions; such as electron/ion densities, temperature and centre of mass motion for each species (i.e. the particle momenta). Each individual macro-particle is then moved freely under the action of the Lorentz force (2.6) where their density and velocity as well as the electromagnetic field variables (Faraday-Maxwell (2.3) and Ampere-Maxwell (2.4) equations) are calculated only on a fixed grid (Figure 4.13a). In a 3D simulation the electromagnetic variables are defined on a Yee grid to centre all derivatives (Figure 4.13b). In a more general view, first it is necessary to update the electromagnetic fields on each fixed grid, from which it is required to know the initial conditions. The previous step is followed for an interpolation of the fields from the grid depending on the particle locations. Once the electromagnetic fields are determined the particles are moved following these fields. Finally, the fluid momenta (density, temperature,...) of each particle are updated and the process is started again (Figure 4.14). The

values of each variable are taken at each time-step and moved forward in time by a fixed time-step.

Chapter 5

Deciphering the onset of relativistic induced transparency in foils using optical diagnostics

This Chapter presents the first new research results included in this thesis. A detailed, experimental and PIC simulations investigation of the onset of RIT is presented. This study spans investigation of the onset of this process, as a function of target thickness and laser polarisation and intensity, to how it is responsible for limiting the maximum electron velocities and acceleration predicted by corresponding models and theories.

5.1 Relativistic transparency - Target thickness and laser polarisation dependency

Firstly, experimental results from an investigation of RIT dependency on target thickness is presented. These results reveal a strong change in the degree of transmitted light beyond a threshold target thickness. The transmitted light increases exponentially as the thickness decreases. In addition, a clear dependency

on the laser polarisation is concluded. A detailed description of results, together with PIC simulations, are included throughout this section.

5.1.1 Experimental Results & EPOCH-PIC Simulations

The experimental set-up used to measure and characterise laser transmission through nanometre scale targets due to the onset of RIT, is described in detail in the section 4.2.1 corresponding to the Methodology chapter. As is mentioned in that section, the main diagnostics employed were an optical spectrometer and two CCD cameras to record the transmitted light at the fundamental laser wavelength, and the second harmonic of this wavelength, as generated during the laser-plasma interaction. The laser intensity for every shot presented in this section was kept to its maximum attainable value of $(6\pm 1)\times 10^{20}$ Wcm⁻².

Figure 5.1 shows the raw images of the transmitted light at the fundamental wavelength for both linear and circular laser polarisations and various target thicknesses; from 10 to 100 nm. All the pixel counts are normalised to the maximum counts in the image obtained in the 10 nm case. In both, the linear and circular polarisation cases, it is clear that the maximum transmission is obtained using the thinnest target, decreasing rapidly when the target thickness is increased.

Figure 5.2a and b, shows the measurements of the transmitted light at 1ω , for linear and circular polarisation respectively, using an optical spectrometer. As with the CCD results, these results clearly show a much higher transmission for the thinnest target, of 10 nm, and being the signal negligible for the thickest targets. For the linear polarisation case, displayed in figure 5.2a, a reference spectrum profile of the incoming beam without a target in place, is included together with the wavelength spectrum for 10, 20, 40 and 100 nm target interactions. In Chapter 3, it was mentioned that one effect of RIT is the production of shorter laser pulses which, in turn, translates to a broader

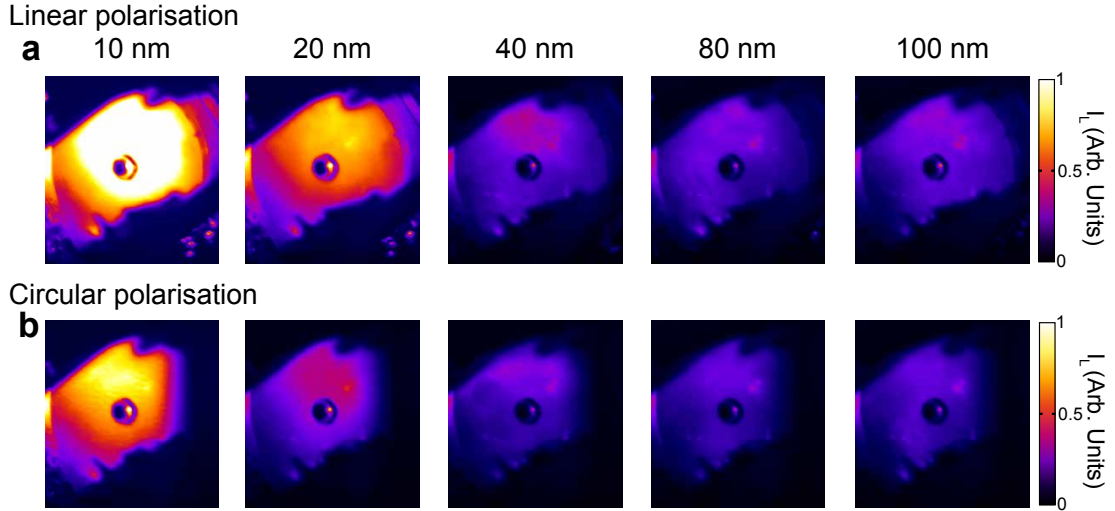


Figure 5.1: Measurements of the transmitted light, at 1ω , recorded with a CCD camera from a diffuse screen placed in front of the rear surface of the target, for given target thickness and for **a** linear and **b** circular polarisation cases.

wavelength spectrum (as experimentally shown in [113] or [130]). However, figure 5.2a shows that when the target becomes transparent for 10 and 20 nm targets, the spectrum is slightly narrowed when compared to the incoming laser pulse spectrum. In order to verify these results, the same transmitted light measurement was performed in an independent experiment utilising the same set-up, but with the spectrometer replaced with a different model. An Andor Shamrock [with no slit] was used, instead of the previous Ocean Optics spectrometer, to record the transmitted light wavelength spectrum. The results are presented in figure 5.3. As in the initial experiment (figure 5.2), they exhibit a wavelength narrowing compared to the spectrum of incoming light, which has not interacted with a target.

These results suggest that when a laser pulse propagates through a relativistically underdense plasma, it may be affected by nonlinear processes (such as self-phase modulation or group velocity dispersion), resulting in the transmitted pulse stretched in time (and narrowed in wavelength spectrum). Another plausible interpretation for this spectrum narrowing is in the fact that, as shown in figure 4.7 (from Chapter 4), the optical fibre used to collect the

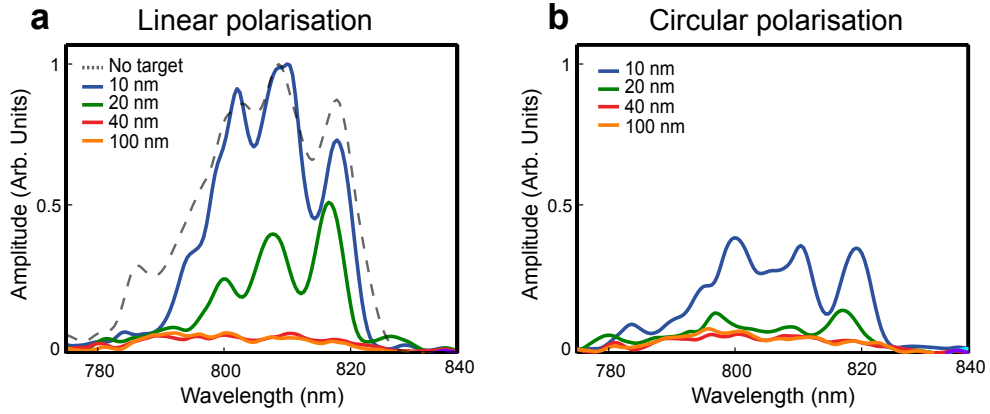


Figure 5.2: Experimental results of the transmitted light spectrum, at 1ω , measured with an Ocean Optics optical spectrometer; where the coupled optical fibre was pointing at a diffuse screen in the direction of transmitted light, for different target thickness and for both, **a**, linear and, **b**, circular polarisation cases.

transmitted spectrum was placed pointing at a region some distance from the centre of the transmitted light. It is possible that these regions could present distinctly characteristics compared to the central region of transmission (in a similar way that the back-reflected spectrum, studied in the next section and illustrated in the figure 5.14, can show a spatial variation in its spectral content). Potential future work could be undertaken, to confirm this wavelength narrowing of the transmitted light during RIT. To achieve this, one could simply guide all transmitted light into a spectrometer possessing an entrance slit, in order to measure the spatially-resolved transmitted spectrum along a radial direction of such a beam. This would determine whether the spectrum shows different bandwidths from the centre to the edges of the transmitted beam. Another possible option to obtain a similar result would be to collect all the transmitted light and guide it into an autocorrelator to evaluate the transmitted pulse duration in situ. Finally one further suggestion would be to make pin-holes in the diffuse screen, that collects the transmitted light, at strategic positions, including the centre and edges. An optical fibre could then be attached at each pin-hole in order to characterise the spectrum of transmitted light at those positions.

Regardless of the presence of wavelength narrowing, these results show an

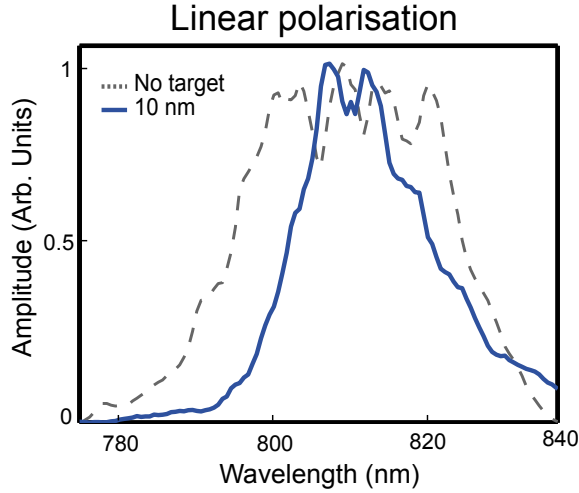


Figure 5.3: Measurement of the transmitted light spectrum, at 1ω , using a Shamrock optical spectrometer together with an optical fibre pointing a diffuse screen placed in front of the rear surface of the target, for linear polarisation and 10 nm target thickness. The spectrum of the incoming light (no target) is also included for comparison.

unambiguous dependency of the onset of RIT on target thickness. In the thickest targets investigated (> 40 nm) the condition $n_e < n'_c$ is not satisfied at any point during the laser interaction. In addition, these results also show an evident dependency with the laser polarisation. In the circular case, the $\mathbf{J} \times \mathbf{B}$ heating component of the ponderomotive force vanishes (as described in section 2.3.4). Consequently, most of the laser energy is used pushing the plasma electrons instead of heating them. On the other hand, in the linear polarisation case, the $\mathbf{J} \times \mathbf{B}$ component is maximised, significantly heating the plasma electrons and favouring their expansion, enabling thus the $n_e < n'_c$ condition to be satisfied much earlier than in the circular polarisation case.

From the aforementioned results, and after pixel counts to energy calibration for both CCD cameras and optical spectrometer, the percentage of total transmitted light can be calculated. These values are shown in figure 5.4a and b, for linear and circular polarisation respectively. They show an exponential decreasing transmission with increasing target thickness. The results shown in figure 5.4 correspond to those obtained with the optical spectrometer. The results obtained using the CCD camera are not included in this figure, but show very

similar values for all target cases. However, as it is illustrated in figure 5.1, the shot for the thinnest target, 10 nm, presented an evident saturation, and due to this the actual value of the light transmission would be distorted.

In order to understand and interpret the experimental findings, 2D PIC simulations of the laser-foil interaction have been performed, using the EPOCH code (see 4.3 for details of the code). The target in the simulations was composed of a fully ionised and neutral Al^{13+} plasma (without any hydrocarbon layer) with thickness of either 10, 20 and 40 nm for the linear polarisation case, and 10 and 20 nm for the circular case. The simulation space was defined as a $2.2 \mu\text{m} \times 7 \mu\text{m}$ box with 550×1750 computational mesh cells. This corresponds to a spatial resolution of 4 nm in both dimensions. In the case of the 10 nm target, the spatial resolution was increased to 1 nm in order to fully resolve the target thickness during the interaction. In all cases, the laser wavelength was 800 nm with a Gaussian temporal profile of 40 fs width (FWHM) focused to a Gaussian intensity distribution of 3 μm FWHM. The peak laser intensity was $6 \times 10^{20} \text{ Wcm}^{-2}$. The simulations were run for a total duration of 80 fs to ensure full interaction of the pulse and target, with a temporal resolution of 0.667 fs. Initially there were 4 simulation particles per cell per species, in all cases.

The simulation results for the degree of transmitted light, are overlaid with the experimental results in figure 5.4. The general exponential tendency of the transmitted light is reproduced in these simulations for both investigated polarisation cases. However, for the thinnest target the simulations predict a higher transmission than that measured experimentally. This could be due to the fact that in a 2D simulation the plasma particles are confined to a plane, which may contribute to a higher electron expansion and therefore earlier RIT onset.

The experimental results concerning the second harmonic generated during the laser-plasma interaction are shown in figure 5.5. In this case only the CCD

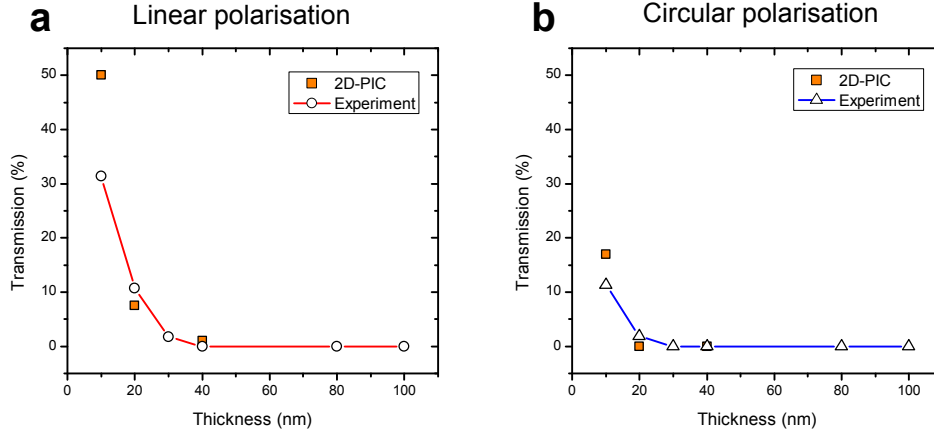


Figure 5.4: Experimental results, after pixel counts to energy conversion, of the transmitted light, at 1ω , overlaid with 2D PIC simulation values as a function of target thickness, for **a**, linear polarisation and **b**, circular polarisation.

camera results are included. Due to the intensity of this second harmonic being lower than the threshold sensitivity of the optical spectrometer employed, it did not record any second harmonic signal.

These results shows a very similar trend to the fundamental harmonic light transparency, for both laser polarisations. It is maximised in the thinnest targets and decreases exponentially with increasing target thickness. Besides this, the generated light at the second harmonic in the transmission path is significantly higher for linearly polarised light than in the circular case. Moreover, the overall values are significantly smaller than for the fundamental harmonic. This reveals that only a small fraction of the incoming laser energy is converted into the second harmonic in the transmission direction.

5.2 Relativistic transparency dependency on laser intensity

Whereas in the previous section the analysis of the onset of the RIT regime focused on target thickness and laser polarisation dependency, here a study of RIT in terms of laser intensity is presented.

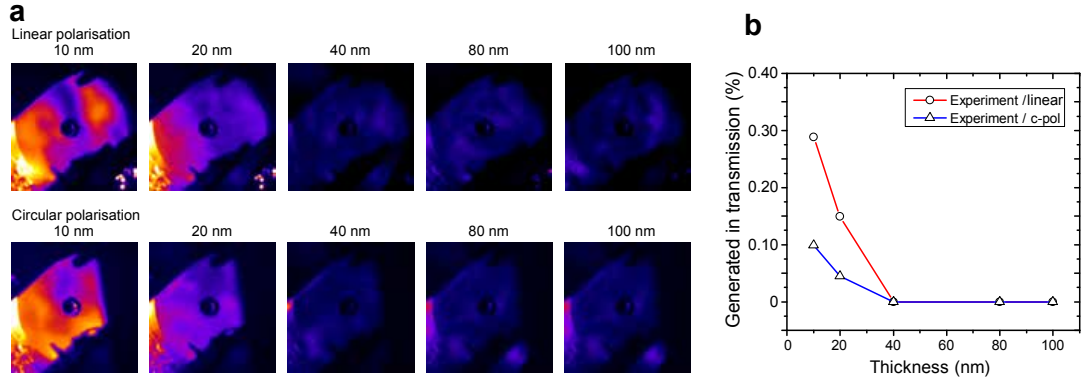


Figure 5.5: **a**, Measurements of the generated light at 2ω , in transmission recorded with a CCD camera imaging a diffuse screen placed at the rear surface of the target, for given target thicknesses and for both, linear and circular polarisation cases. **b**, Total 2ω light generated in transmission, after pixel counts to energy conversion, as a function of the target thickness for both linear and circular polarisation cases.

5.2.1 Experimental Results & EPOCH-PIC Simulations

For this study, the same experimental set-up as used in the previous section was employed. However, in this case in order to analyse and characterise the onset of RIT as a function of the laser intensity, the dependency of transmitted light for laser intensity values from 1×10^{20} to 7×10^{20} Wcm^{-2} were investigated. This intensity scan was conducted for target thickness, l , of 10, 20, 40 and 100 nm, and only linearly polarised light was used.

Due to a large number of simulations required for this study, in order to reduce the computational requirements 1D PIC simulations were performed. All the simulation parameters are the same as those in the previous section, for the 2D simulations, except the spatial dimensions which are reduced to one dimension in the present case. Although 1D simulations do not include the spatial behaviour of the plasma particles, for the study presented in this section they provide sufficient overall view and tendency to understand the transition to the RIT regime when the laser intensity is adjusted.

In figure 5.6a the experimental results of the transmitted light in target thickness, l , of 10, 20, 40 and 100 nm, for laser intensities between $\sim 1 \times 10^{20}$ - 7×10^{20} Wcm^{-2} are presented. This figure shows that for $l = 40$ nm and $l =$

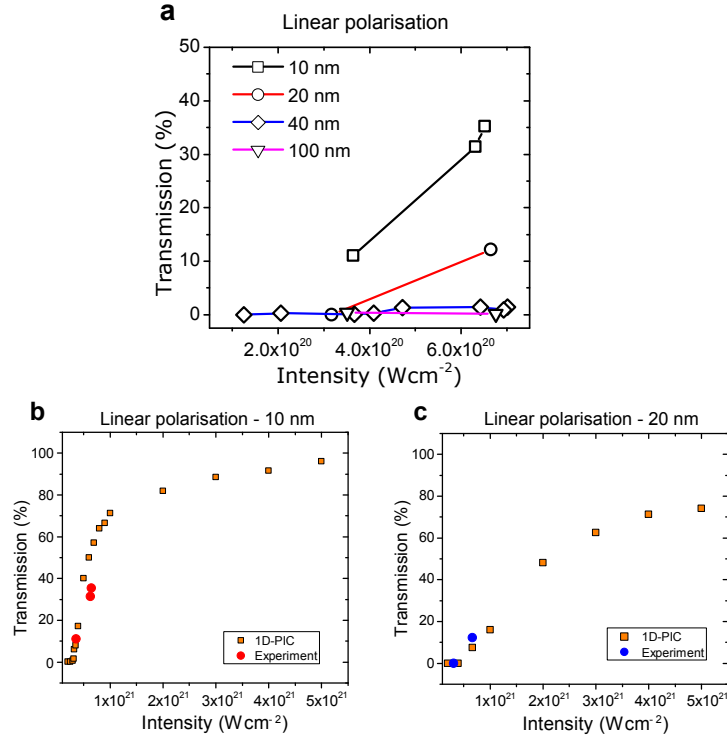


Figure 5.6: **a**, Experimental transmission data, at 1ω as a function of the laser intensity for given target thicknesses and linearly polarised light. **b**, Experimental transmission data as a function of the laser intensity for linearly polarised light and 10 nm target thickness, plotted together with 1D PIC simulation results. **c**, Same as **b**, but for 20 nm target thickness.

100 nm, the targets are opaque for all the intensities investigated. However, for the thinnest targets, $l = 20$ nm and $l = 10$ nm, the targets exhibit an increasing transparency effect from a certain threshold intensity. Both, this threshold intensity and the slope of the transmission increment for these two targets present different behaviour. The 10 nm case, for example, shows a smaller intensity threshold and steeper slope compare to the $l = 20$ nm target.

In figure 5.6b and c the 1D simulation results for the 10 and 20 nm cases, respectively, are displayed. The laser intensity was varied from 2×10^{20} to 5×10^{21} Wcm⁻². In both figures the corresponding experimental results are overlaid. The simulations for the 10 nm target, show that as soon as the target becomes transparent for a given threshold intensity, the transparency regime presents a quick predomination represented by a steep slope when the laser intensity is increased slightly. For the highest intensities, the total transmitted light tends

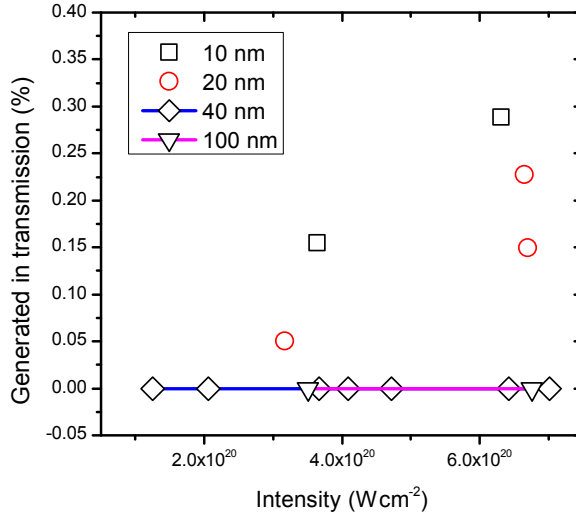


Figure 5.7: Measured 2ω light generated in transmission as a function of the laser intensity for various target thicknesses and linearly polarised light.

asymptotically to full transmission. For the 20 nm target, the threshold intensity is higher than for the 10 nm case, just as in the experimental results, by a factor of ~ 1.4 . In addition, for this thickness the slope of the transmission tendency is much smaller compared to the $l = 10$ nm target. Moreover, it also presents an asymptotically tendency toward full transmission, but at a rate much smaller than for the 10 nm case, being far from this point at the highest intensity investigated in this study.

Along the same lines, the laser intensity influence on the second harmonic generated in transmission has been experimentally investigated. The results of this are presented in figure 5.7. They show a similar tendency to that of the first harmonic case, that being zero for all the intensities studied and increasing with the intensity in the thinnest targets.

5.3 Relativistic transparency curbs radiation pressure - Critical density velocity transition

As was already mentioned in section 2.4, a reflective surface can be accelerated to relativistic velocities which is described by the *hole boring* and *light sail* models for thick (micrometre) and thin (nanometre) targets, respectively. If the target thickness is decreased to dimensions close to but higher than, the skin depth of the solid target, there will be a moment when the target becomes relativistically transparent thus limiting the radiation pressure of the laser pulse, and reducing its plasma-electron acceleration effectiveness.

Because of this, another approach to characterise the onset of RIT is to investigate the driving velocity of the critical density surface due to the laser pressure during the interaction. The purpose of this section is to present such a study using 2D EPOCH-PIC simulations and compare these with analytical models and experimental results.

In the case of the *Light Sail*, mode of RPA, equation (2.65) is obtained assuming a top-hat (in time) laser pulse. However, in a more realistic situation, the laser pulses in an experiment have instead a Gaussian-like temporal profile. In order to find a revised expression for the *Light Sail* velocity with this new profile, first it is necessary to recalculate the pulse fluence, F , from equation (2.63):

$$F(t) = \int_0^t I(t)dt = \int_0^t I_0 e^{-\left(\frac{t-t_0}{w}\right)^2} dt \quad (5.1)$$

Carrying out the integral, the pulse fluence for a Gaussian pulse is equal to:

$$F(t) = \frac{I_0}{2} \sqrt{\pi} w \left[\operatorname{erf} \left(\frac{t-t_0}{w} \right) + \operatorname{erf} \left(\frac{t_0}{w} \right) \right] \quad (5.2)$$

where $t_0 = FWHM$ (of the pulse duration), and $w = \frac{FWHM}{2\sqrt{\ln(2)}}$.

Replacing this new expression for the pulse fluence in (2.65), the *Light Sail* velocity for a Gaussian pulse is obtained.

As it was briefly mentioned in section 2.3.1, when an ultra intense laser is interacting with the critical density surface, this region acts as a relativistic mirror, reflecting, shifting and compressing the incident laser pulses. In addition, during this interaction high harmonics are generated. High harmonic generation, in an ultra intense laser-solid interaction, are usually associated with the relativistic oscillation of electrons across the steep plasma density gradient formed in the region of the critical density. This is known as the Relativistically Oscillating Mirror (ROM) mechanism [131,132]. This mechanism is generally presented to dominate at highly relativistic intensities and normal incidence in overdense plasmas, which are the same characteristics presented in the experiments reported in this chapter.

When the incoming laser beam propagates and interacts with the pre-expanded plasma, during the reflection at the critical density, its fundamental wavelength is subjected to nonlinear effects (such as self-phase modulation) which contribute to spectral broadening (or narrowing). These processes can mask effects purely due to reflection from the relativistic mirror. Working with the second harmonic (or any other higher), on the other hand, has the advantage of avoiding the effect of these nonlinearities since the high harmonics are generated only in a small area on the critical density surface and in a small temporal window centred around the peak of the incoming pulse.

In this relativistic mirror scenario, the frequency of the reflected pulse and high harmonics are shifted with respect to a stationary detector by the relativistic Doppler factor $(1 + \beta_0)/(1 - \beta_0) \simeq 4\gamma^2$, where $\gamma = (1 - \beta_0^2)^{-1/2}$ and $\beta_0 = v/c \lesssim 1$ is the velocity of the critical surface. Moreover, the reflected pulse experiences a temporal compression since the number of laser oscillations are kept constant during the frequency shift (frequency broadening).

Experimentally, the recession velocity of the critical surface has been measured through the analysis of the nominal wavelength shift from the second harmonic in the back reflection path.

5.3.1 EPOCH-PIC Simulations

In order to interpret the experimental results various 2D and 3D PIC simulations have been employed. The 2D simulations are the same as included in the previous section 5.1, but only for circularly polarised laser pulses, due to the maximum critical surface velocity being optimised for this polarisation (because of the absence of the electron heating term in the ponderomotive force), and for target thickness $l = 10 \rightarrow 500$ nm. Due to the high computational requirements, 3D simulations were only conducted for the $l = 10$ nm target case. A detailed description of this 3D simulation is included in Chapter 6.

Figure 5.8a-c shows results from a 2D simulation time step just when the thinnest target ($l = 10$ nm) undergoes RIT, for $l = 10, 40$ and 200 nm, respectively. For the three cases the laser intensity is overlaid with the electron density. From these representative figures it can be seen, as expected, that the laser radiation pressure is able to accelerate forward the plasma electrons. As the laser pulse has a Gaussian intensity profile (both temporal and spatially), the electron velocity is peaked where the laser intensity is highest. This creates an accelerated plasma structure where electron velocities decrease from laser axis to the edges of interaction.

In order to measure and characterise the evolution of the critical density surface velocity along the laser axis, a time-space configuration with the electron plasma density in this region was produced, as is shown in figure 5.9a-d and i-l, for various target thicknesses. A Matlab script was implemented to obtain the contour of the front surface of the relativistically corrected plasma density at which $n_e = n'_c$. The result of this calculation is illustrated as a gray-dashed

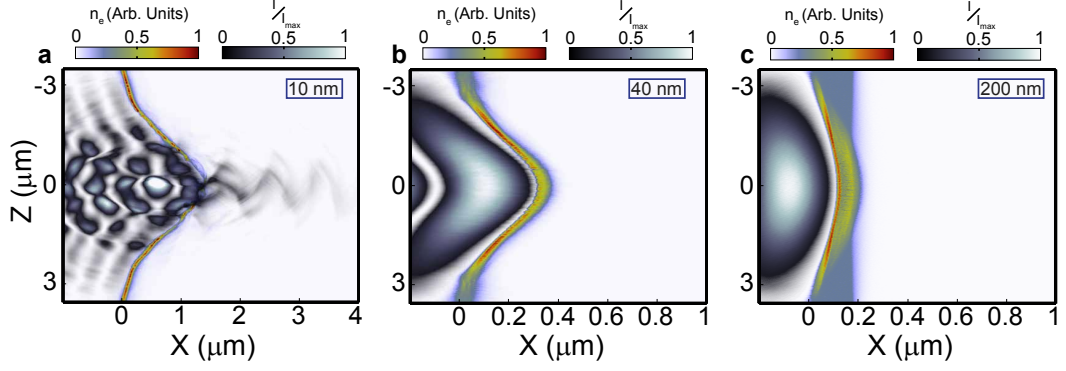


Figure 5.8: Electron density and laser intensity from a 2D PIC simulation, at X-Z plane, and circularly polarised light. **a**, $l = 10$ nm target thickness. **b**, $l = 40$ nm target thickness. **c**, $l = 200$ nm target thickness. All figures are at the same time step corresponding to the moment that the $l = 10$ nm target becomes relativistically transparent.

line overlaid in figures 5.9a-d and i-l. As such these figures show a time-space distribution, the velocity of the front corrected critical density surface is obtained directly from the gradient of such a contour. The velocity acquired from this method, as a function of time, is presented as a blue dot-dashed line in figures 5.9e-h and m-p, for each target thickness investigated. The predicted velocity of the critical density using the time-dependent hole boring model [equation (2.62) and solid green line], light sail model with a temporal top-hat intensity profile [equation (2.64) and orange dot-dashed line] and the new revised light sail model [equation (5.2)] with a temporal Gaussian intensity profile (solid red line) are included.

The main conclusions deduced from these figures are:

- In the case of the thickest target, $l = 500$ nm (Figures 5.9l and p), it can be seen that the velocity obtained from the 2D simulation matches very well with the hole boring model. In this context, the velocity is modulated by the laser intensity, increasing on the rising edge of the pulse up to a maximum value at the peak of the pulse, and decreasing during the falling edge of the pulse. This progression is well explained by the hole boring model because in it the velocity of the critical surface is directly proportional to the laser intensity. In the simulation, the rising part of

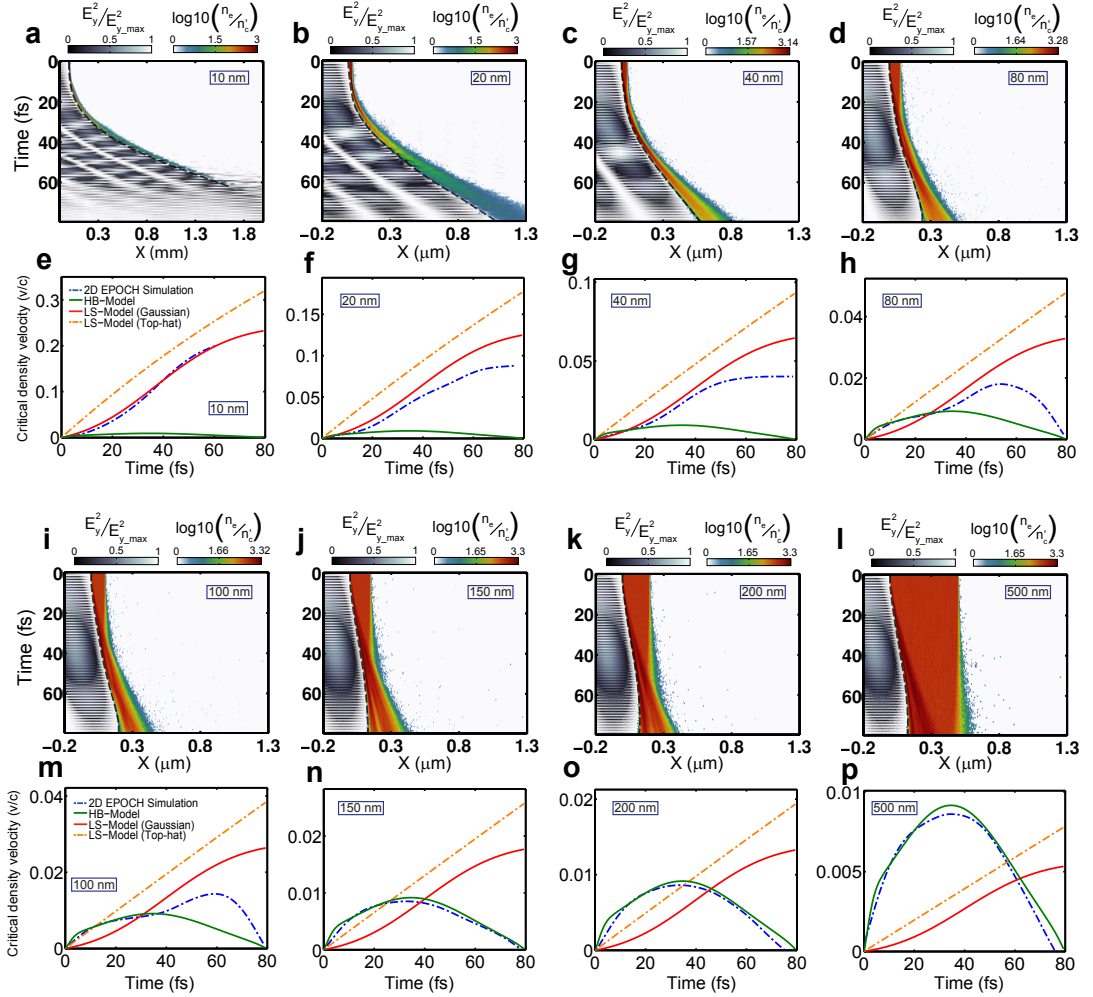


Figure 5.9: **a-d** and **i-l**, 2D PIC simulation time-space map of the electron density and laser electric field squared, E_y^2 , for given target thickness (inset), along the laser axis. **e-h** and **m-p**, Relativistic critical density velocity as a function of time (dotted-dashed blue line), from the EPOCH simulation results, corresponding to **a-d** and **i-l**, respectively. This velocity is calculated as the gradient of the gray dashed line in **a-d** and **i-l**, which delineates the relativistic critical density surface at each time. Time-dependent hole boring velocity from eq. (2.62) in solid green line; revised time-dependent light sail velocity from eq. (5.2) in solid red line; time-dependent light sail velocity from eq. (2.64) in dotted-dashed orange line.

the velocity is explained by the same reasoning. The decreasing velocity after the laser peak, however arises because at this point in the interaction the laser pressure is not able to compete with the heating expansion of the plasma in the critical density regions, and thus the velocity starts to decrease as the laser intensity decreases. This overall behaviour is explained by the fact that, to the laser, the target is infinitely thick, and therefore it is only able to push and accelerate the plasma electrons near the critical density region.

- The same scenario is reproduced for $l = 200$ and 150 nm (Figures 5.9k and o and 5.9j and n, respectively).
- However, for the $l = 100$ nm case, this behaviour starts to change, as it is shown in figure 5.9m. Whereas for the first part of the interaction the velocity obtained with the 2D simulation still follows the tendency of the hole boring model, when the peak of the pulse interacts with the target (~ 40 fs), and because the plasma density has decreased enough due to the heating expansion, the laser pressure is able to accelerate the plasma electrons beyond the velocity predicted by the hole boring model. This stage of the critical surface velocity shows, instead, a tendency closer to the new light sail model. Due to this behaviour occurs during the falling edge of the laser pulse, when the laser intensity has lower values, above ~ 60 fs, the velocity of the plasma also decreases rapidly.
- For the $l = 80$ nm target (Figures 5.9d and h) the velocity of the critical density presents similar behaviour to that in the $l = 100$ nm case. Nevertheless, now the velocity follows the new light sail model at an earlier time in the interaction.
- When the target thickness is decreased further, to $l = 40$ nm (Figures 5.9c and g), the velocity shows light sail behaviour from the beginning of

the interaction. However, during the falling edge of the pulse the laser pressure cannot continue accelerating the critical surface, thus keeping it at a constant velocity.

- For the $l = 20$ nm case, the plasma electrons are accelerated as a single block during the entire interaction. This is illustrated in figures 5.9b and f, where the velocity strongly follows the trend predicted by the new light sail model over the entire temporal window.
- For the laser intensity used in these simulations, and reducing the target thickness down to $l = 10$ nm, at ~ 60 fs the $n_e < n'_c$ is satisfied and the target becomes relativistically transparent to the incoming laser pulse. At that point the laser pressure becomes less efficient accelerating the plasma electrons as the percentage of transparency increases. Consequently, relativistic transparency limits the maximum velocity of the critical density movement predicted by the light sail model. This scenario is presented in Figures 5.9a and e. It can be seen that the velocity obtained from the 2D simulation is in very good agreement with that predicted by the new revised light sail model. However, at ~ 60 fs, the target becomes relativistically transparent and the electron acceleration due to radiation pressure is ceased. Example 3D simulations show that RIT occurs earlier in the interaction than in 2D, further limiting the maximum velocity of the critical density, as shown in figure 5.15 (this is discussed in more detail in section 5.3.3).

All the simulation results displayed in figure 5.9, as described above, correspond to the velocity of the critical density surface along the laser axis. In the next paragraphs, this study is extended not only to the velocity along the laser axis but also to the velocity of the critical surface at any point of the interaction. These results are included in figure 5.10 for all the target thicknesses used in this investigation. To generate this figure, a predominant electron momentum in the

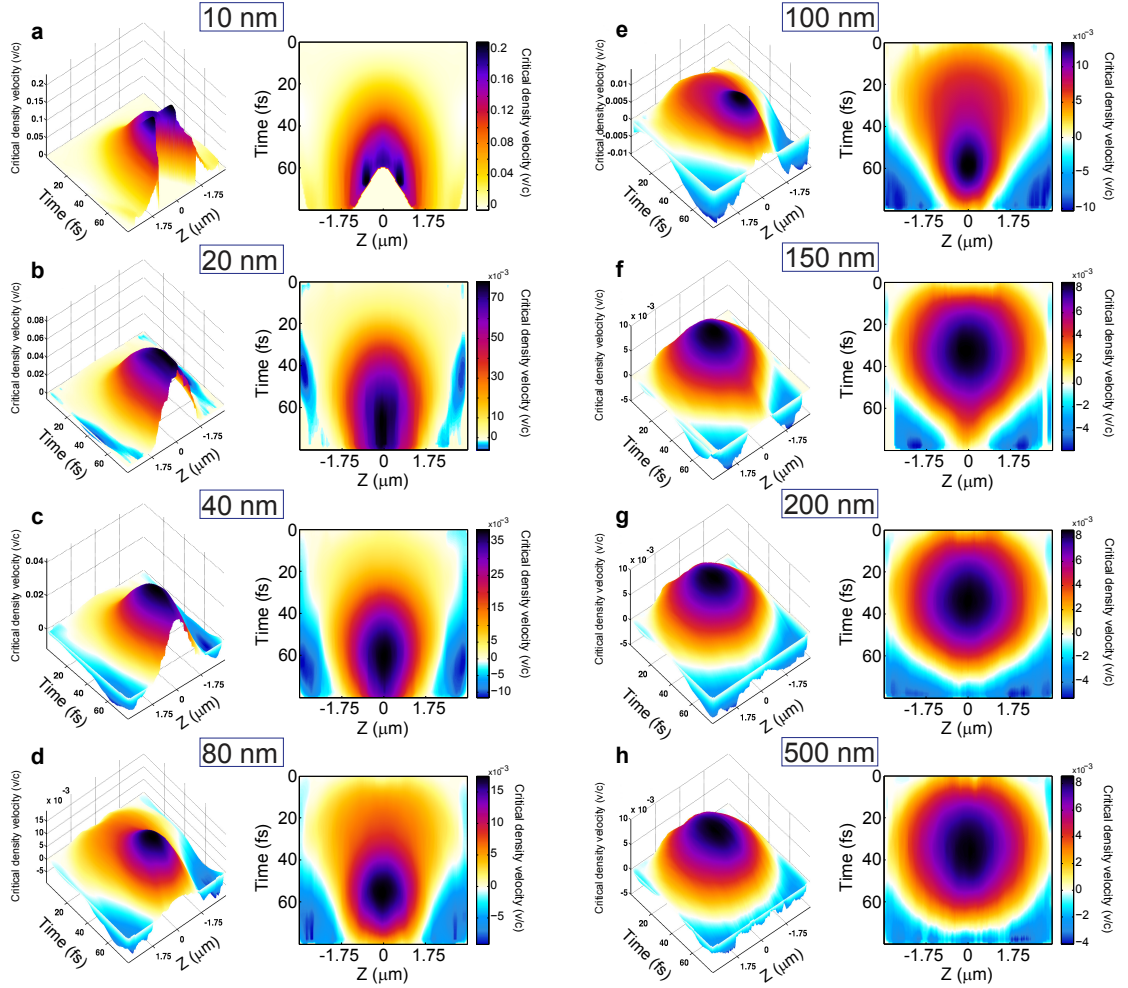


Figure 5.10: **a-h**, 2D PIC simulation of the relativistic critical density velocity as a function of time and position along the Z -axis, for given target thicknesses. The third dimension, with the colour scale, corresponds to the velocity of the critical density. These results show a clear change of the velocity, from a narrow region and highest values at latter times in the thinnest targets, to a broader region and highest values at the time that the laser intensity is maximum in the thicker targets.

X-axis (laser propagation axis) over the electron momentum in the perpendicular direction (Z-axis), was assumed during the laser interaction. This figure shows a clear dependency of the critical surface velocity on the target thickness. The key conclusions that can be made from this figure are:

- The thickest targets show that the highest velocities are extended in a broad distribution around the interaction region, being maximum when the laser intensity is highest.
- The critical density velocities in the thinnest targets are distributed in a narrow region around the laser axis, and at the end of the interaction during the falling edge of the pulse.
- Mid range target thicknesses, i.e. $l = 40\text{-}100$ nm, exhibit velocities in a distribution showing transitional characteristics of both previous scenarios.
- Figure 5.10a, which presents the thinnest target investigated, at $l = 10$ nm, shows how the maximum predicted velocities on axis, and around it, are curbed by the onset of RIT in these regions.

Figure 5.8a-c clearly shows that for the thinnest targets (figure 5.8a) the velocity of the critical density surface is significantly higher on axis and decreases rapidly for positions off-axis in the Z direction. However, in one of the thickest targets (figure 5.8c), the laser pressure is more uniform along the Z direction.

In figure 5.11a and b the velocity of the critical density surface, in time and space, along the Z direction, predicted by the revised light sail and hole boring models, respectively, is presented. These models match very well with the simulation results presented in figure 5.10; the revised light sail model exhibit a good agreement with the thinnest targets and the hole boring model with the corresponding thicker targets.

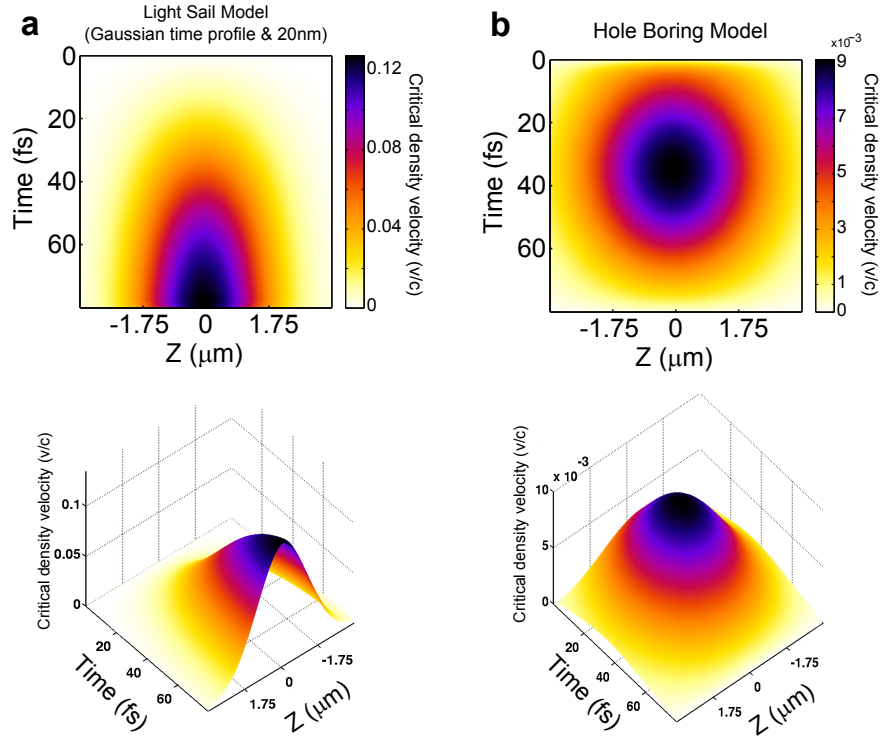


Figure 5.11: **a**, Analytical critical density velocity as a function of time and position along the Z-axis, using the revised light sail model from eq. (5.2). **b**, Same using the hole boring model from eq. (2.62).

Examining the relativistic transparency conditions

In the previous section, the most common relativistic transparency condition, $n_e < \gamma n_c$, has been assumed. However, in Chapter 3, other alternative conditions, for thin targets (10-20 nm), were discussed. One of this conditions is based on the reduction of the target thickness, due to laser radiation pressure, below the corrected skin depth. The other condition, derived from a 1D analytical model, defined relativistic transparency when $a_0 > \zeta$ is satisfied (see more details in the section 3.3).

Here, a detailed study of these conditions based on 2D PIC simulations included in the previous section, is presented. In order to compare thin and thick targets response, representative target thicknesses which become relativistically transparent or remain opaque during the laser interaction, have been selected; these are $l = 10$ nm and 40 nm, respectively.

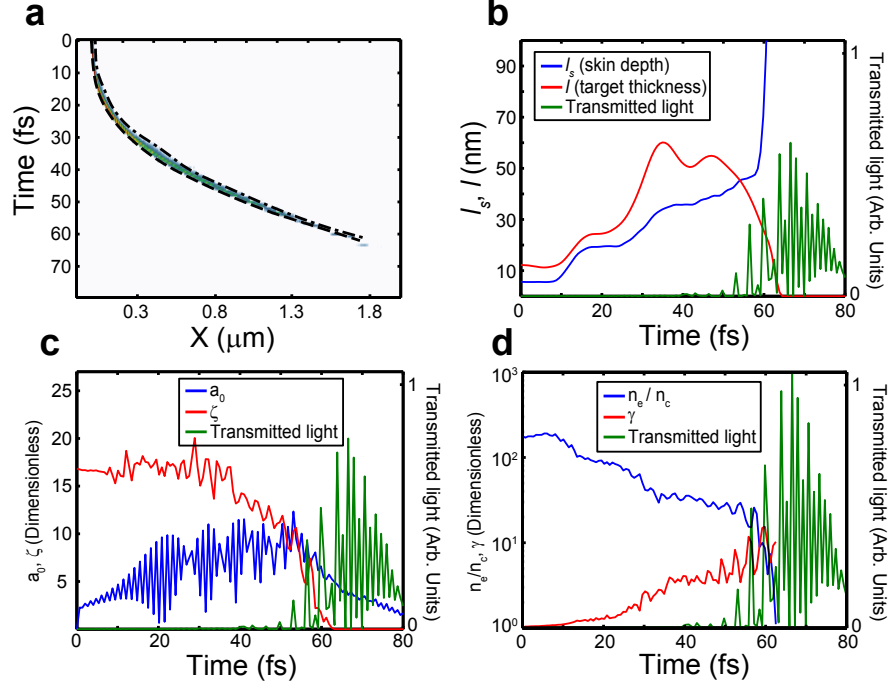


Figure 5.12: Analysis of the relativistic conditions for the 10 nm target case. **a**, Time-space electron density map along the laser axis with two dashed lines delimiting the front and rear critical density surfaces; **b**, Corrected skin depth from eq. (2.40) represented by the solid blue line, target thickness in the solid red line and transmitted intensity in the solid green line, as a function of time; **c**, normalised vector potential, a_0 in the solid blue line, ζ parameter from eq. (3.2) in the solid red line and transmitted intensity in the solid green line, as a function of time; **d**, electron density normalised to the critical density in the solid blue line, γ factor (from electron kinetic energy) in the solid red line and transmitted intensity in the solid green line, as a function of time.

Figure 5.12 illustrates the examination of the three conditions for relativistic transparency in thin targets, discussed in the section 3.3, for a $l = 10$ nm target, as a function of time. The details of each condition are as follows.

1. Figure 5.12b - Skin depth comparable with target thickness [Transparency occurs if $l_s > l$ (target thickness)]:

- 1.1. The skin depth is obtained using equation (2.40). It is a function of plasma frequency [eq. (2.17)] and therefore also the electron density, n_e , and relativistically corrected electron mass, i.e. γm_e . Besides this, the electron density is updated accordingly, at each time step, due to compression and expansion effects. The final skin depth is calculated taking the average value along the target thickness for each time step.

- 1.2. The target thickness is obtained, for each time step, as the distance from the front n'_c surface to the rear n'_c surface, represented by the two dashed lines in figure 5.12a.
- 1.3. The transmitted light is evaluated as the average of the total intensity from the rear surface, at each time step.
2. Figure 5.12c - Comparison of parameters a_0 and ζ parameter [Transparency occurs if $a_0 > \zeta$]:
 - 2.1. The normalised vector potential, a_0 (eq. (2.55)), corresponds to its maximum value at each time step.
 - 2.2. The ζ parameter is obtained using equation (3.2). The target thickness and the normalised electron density are those calculated in figure 5.12b and figure 5.12d, respectively, at each time step.
 - 2.3. The transmitted light is evaluated, as in the previous case, as the average of the total intensity from the rear surface, at each time step.
3. Figure 5.12d - Comparison of the Lorentz factor, γ , and the ratio n_e/n_c [Transparency occurs if $\gamma > n_e/n_c$]:
 - 3.1. The electron density, n_e , normalised to the critical density (eq. 2.33), n_c , is obtained from its average value at each time step.
 - 3.2. The γ factor is calculated from the electron kinetic energy average at each time step using equation (2.58).
 - 3.3. The transmitted light is evaluated, as in the previous cases, as the average of the total intensity of light emerging from the rear surface, at each time step.

Additionally, the same calculated parameters for a target which does not undergo transparency, $l = 40$ nm, is presented in figure 5.13. Analysis and comparison of these two sets of plots leads to the following conclusions:

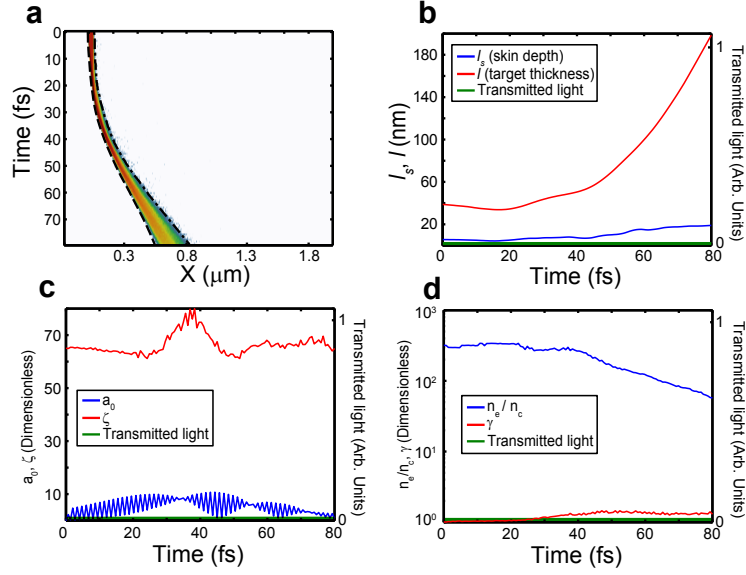


Figure 5.13: Analysis of the relativistic conditions for the 40 nm target case. **a**, Time-space electron density map along the laser axis with two dashed lines delimiting the front and rear critical density surfaces; **b**, Corrected skin depth from eq. (2.40) represented by the solid blue line, target thickness in the solid red line and transmitted intensity in the solid green line, as a function of time; **c**, normalised vector potential, a_0 in the solid blue line, ζ parameter from eq. (3.2) in the solid red line and transmitted intensity in the solid green line, as a function of time; **d**, electron density normalised to the critical density in the solid blue line, γ factor (from electron kinetic energy) in the solid red line and transmitted intensity in the solid green line, as a function of time.

1. Figure 5.12b. For the thinnest target, $l = 10$ nm, the transmitted light is ~ 0 at times where $l_s < l$. At around 53 fs this condition is inverted, when the target thickness starts to decrease (as is shown in figure 5.12a), and thus the skin depth increases due to the electron density reduction. At this time the amount of transmitted light increases.
2. Figure 5.12c. The amount of transmitted light remains around zero for times where $a_0 < \zeta$. Surprisingly, as in the previous transparency condition, at around 53 fs this condition is inverted as a combination of increasing a_0 and decreasing ζ due to the target thickness and electron density decreasing. Again, at this time in the interaction the first transmitted light signal appears.
3. Figure 5.12d. Although the transmitted light is zero for times where $n_e/n_c > \gamma$, at ~ 53 fs the target begins to be transparent while this condition

is still satisfied. Finally, this condition is inverted at approximately 60 fs into the interaction, when the target presents a more pronounced transmitted light signal.

4. Figure 5.12b-d. These simulation results, for a Gaussian-like laser pulse, with a peak intensity value of $6 \times 10^{20} \text{ Wcm}^{-2}$, interacting with a 10 nm aluminium target, are consistent with all three transparency conditions. This suggests that these are effectively equivalent conditions for these target and laser parameters, although the conditions included in figure 5.12b and c occur slightly earlier in the interaction compared to the condition presented in figure 5.12d. In addition, because all the conditions are satisfied, it is not possible to accurately determinate which condition dominates over the others, at these laser and target parameters.
5. Figure 5.13b-d. For thicker target case, $l = 40 \text{ nm}$, none of these transparency conditions are satisfied during the laser interaction. Consequently, no transmission of light through the target occurs.

5.3.2 Experimental Results

In this section, results from two different experiments are presented in which the velocity of the critical density is investigated. In the first a single optical fibre connected to an optical spectrometer was used to measure the spectrum of frequency double laser light back-reflected from the target, whereas in the second an optical spectrometer with a narrow slit was employed. Unlike the first configuration where it is only possible to measure the spectrum of a single small area (determined by the numerical aperture of the fibre), with the incorporation of the slit the spectrum along one radial direction can be measured (further details about these two configurations are included in 4.2.1 of Chapter 4).

In order to obtain the critical density surface velocity, from the experimental

data, as introduced at the beginning of this chapter, the relativistic Doppler effect has been used:

$$\beta_0 = \frac{v}{c} = \frac{1/\lambda_0^2 - 1/\lambda^2}{1/\lambda_0^2 + 1/\lambda^2} \quad (5.3)$$

where λ_0 is the nominal wavelength of the second harmonic, and λ is the shifted wavelength. λ_0 was calculated as half of the first harmonic nominal wavelength value.

Figure 5.14a-c shows the measured spectrum of the second harmonic of representative examples for $l = 10, 40$ and 100 nm targets, using the optical spectrometer with the slit configuration. For the 10 nm case, the spectrum contains stripes (corresponding to maximal peaks) with a blue and red shift. In the back reflection path, a blue shift corresponds to target expansion at the beginning of the interaction. The red shift, however is a signature of the surface compression, being accelerated forward by the laser pressure, and then of the critical density surface velocity. Both blue and red shifts are present on the reflected spectra due to the fact that the measurements are time-integrated. This figure also shows that the highest red shift occurs in a smaller region compared to the lowest red shift stripes. This behaviour is in good concordance with simulations of the light sail regime, as described in the previous sections. For the 40 nm target the measured red shift is smaller and it is presented in wider radial regions, compared to 10 nm case. For the case of $l = 100$ nm the measured red shift is even lower, and presents wider radial regions, with respect to the 10 and 40 nm cases. For this thicker target, i.e. 100 nm, from figure 5.14c, it seems that no blue shift was measured in the spectrum. Actually, it was, but because its intensity was near to the noise level and significantly lower than the red shift peak, the blue shift is not perceived at the intensity scale used. Summarising, the results from the three targets investigated are in good agreement with the simulation predictions.

In figure 5.14d the measured spectrum of the second harmonic of

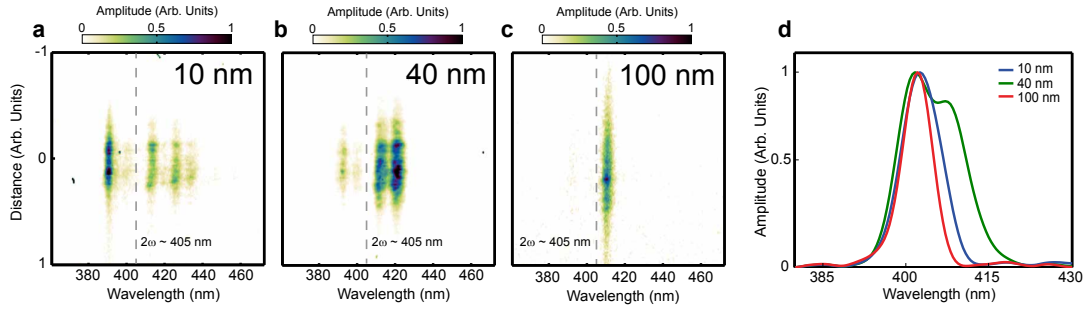


Figure 5.14: **a-c**, Example measurements of back-reflected light along a radial direction measured using a Shamrock optical spectrometer, for $l = 10, 40$ and 100 nm respectively. **d**, Same but measured using an Ocean Optics spectrometer, at a single position in the back-reflected beam.

representative examples for 10, 40 and 100 nm targets, using the optical spectrometer with a single optical fibre is presented. These results show that at 40 nm the maximum red shift is higher than for $l = 100$ nm. This is the same scenario seen in the previous set-up. However, surprisingly the 10 nm target thickness presents a maximum red shift lower than that for the $l = 40$ nm case, which is opposite to the simulation prediction and the measurement presented in Fig 5.14b. This can be explained by the fact that the optical fibre was aligned to only one region around the centre of the back reflected beam, in an undefined position. As it has been presented in the previous set-up, and in the simulations, at the thinnest target the maximum critical density velocities are located in a small region around the laser axis. Any small change in the position from this axis will result in a significant reduction of the maximum critical density velocity and thus the measured spectral shift.

5.3.3 Discussion of results

In this section a detailed study of the critical density surface velocity as a function of target thickness has been carried out. The results from two experiments using different configurations to measure spectral shifts and thus infer the critical surface velocity has been presented. 2D PIC simulations to interpret and understand the experimental results have also been included. In addition, two

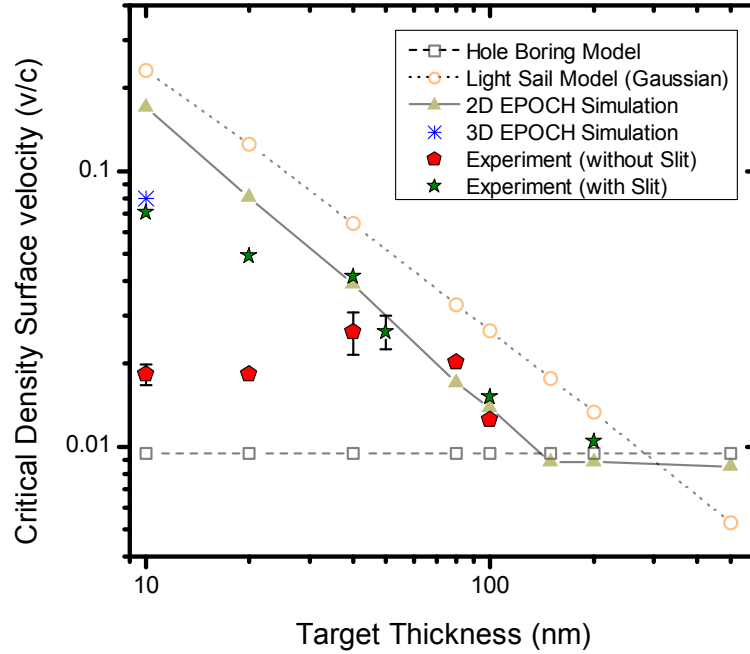


Figure 5.15: Summary of the most important results of the critical density surface velocity from experiments and PIC simulations, as a function of target thickness and for circularly polarised light.

theoretical models, the *hole boring* and a revised *light sail* model have been used to describe and classify the experimental results within these two models, depending on the target thickness employed. Figure 5.15 summarises all of the experimental and simulation results relating to the maximum critical surface velocity (on a logarithmic scale) for each target thickness investigated.

The main conclusions extracted from this figure are as follows:

- The velocity is essential independent of the target thickness in the *hole boring* model. (empty grey squares)
- The revised *light sail* model with a temporal Gaussian profile, presents a exponential tendency (linear in a logarithmic scale) of the velocity, which is maximised for the thinnest targets. (empty orange circles)
- The 2D PIC simulations show a constant velocity for the thickest targets whose values are very similar to those predicted by the *hole boring* model. However, for target thicknesed less than 150 nm the velocity starts to

increase as the target thickness decreases. Although they do not reach the values predicted by the revised *light sail model* in this region, they present a very similar linear tendency with target thickness. As discussed earlier, in the case of thinnest target (10 nm), the 2D simulation also produces a value very similar to that predicted by the revised *light sail model*. However, it is lower due to the target becoming transparent before the critical surface has reached its maximum velocity, as shown in figure 5.9a. (filled green triangles)

- A 3D PIC simulation has been run for a 10 nm target case. It shows that the maximum critical density velocity decreases considerably compared to the 2D simulation for the same target. This is due to the fact that the target becomes transparent early in the interaction, thus not getting to the higher velocities displayed in slightly thicker targets (20 nm). This reveals that volumetric effects play a key role in the onset of RIT regime. Unlike the 2D simulations where the maximum critical density corresponds to an instantaneous value, due to the computational requirements involved in a 3D simulation the temporal resolution was 20 fs. As a result, the critical density velocity was calculated in this case as the average velocity between the first time step when the target becomes transparent and the time step previous to that. (blue asterisk)
- The experimental results carried out with the single optical fibre are in agreement with the 2D simulations for the 80 and 100 nm targets. However, for thinner targets, lower maximum velocities are inferred from the experiment, compared to the simulations. The difference between experiment and simulations is even more pronounced for the thinnest targets (10 and 20 nm). The reason for this disagreement has been explained at the end of the previous section 5.3.2. (filled red pentagons)

- On the other hand, the experimental results obtained using the narrow slit optical spectrometer, show a very good agreement with the 2D simulations in the region of thick targets, 200 nm thickness (where *hole boring* is predominant), and in thinner targets, 40, 50 and 100 nm (where the maximum velocity is adequately explained with the *light sail* description). The thinnest target, at 10 nm, presents a significantly lower maximum velocity than that found in the 2D simulation, but close to that obtained in the 3D case. As it was studied in the first section 5.1 of this chapter, the target experimentally becomes transparent, and additionally as the simulations show, the onset of RIT reduces the radiation pressure and thus the maximum velocity. (filled green stars)

5.4 Conclusions

In this chapter, experimental and numerical investigations, via PIC simulations, exploring the onset and the underpinning physics of relativistic induced transparency is presented. This study has focused on the dependency of RIT on the target areal density, laser intensity and polarisation using optical diagnostics such as CCD cameras and optical spectrometers. The results show that the laser transmission is maximised for the thinnest targets, i.e. $l = 10$ nm, and decreases exponentially with increasing target thickness. The same trend is obtained for linearly and circularly polarised laser light. However, for a given target thickness, the linear polarisation case exhibits a significantly higher transmission fraction, with respect to the circular polarisation case, due to additional electron heating and expansion. Moreover, it is shown that once the thinnest targets become relativistically transparent, the transmitted light fraction increases rapidly as the laser intensity increases. The increasing rate is shown to be more pronounced in the thinnest targets investigated. This is diagnosed by measurement of both the

fundamental and second harmonic wavelengths.

Additionally, an alternative diagnostic approach to characterise the onset of the relativistic transparency regime, based on numerical determination of the critical surface velocity, as a function of time, for various target thickness, and comparing it with corresponding analytical models has been proposed. These results are in good agreement with the values predicted by the *hole boring* model for the thickest targets, both the time evolution and the maximum critical surface velocity. On the contrary, the traditional *light sail* model predicts an evolution and maximum velocities significantly different to those obtained with the numerical results presented in this chapter. The main reason for this disagreement is due to the light sail model using a temporal top-hat laser intensity profile is assumed. However, in the present numerical investigation a temporal Gaussian-like has been employed, as used in the experiments. Because of this, a revised light sail model including a temporal Gaussian laser beam has been formulated. This revised model presents a more agreeable predictive capability for the time evolution and maximum critical surface velocity in the thinnest targets. The experimental results are also in good agreement with these investigation conclusions. Both, experimental and numerical measurements show that the onset of relativistic induced transparency curbs the radiation pressure efficiency of the charged particle acceleration mechanisms, resulting in a lower maximum critical surface velocity during the laser-plasma interaction.

Chapter 6

Collective electron response to the onset of relativistic induced transparency in ultra-thin foils

In the previous chapter the onset of RIT in ultra-intense laser interaction with ultra-thin solid targets has been examined. In this chapter a detailed experimental, analytical modelling and numerical investigation of the laser effect on the collective dynamics of the plasma electrons, when the target becomes relativistically transparent, is presented. This investigation is focused on the key role the laser polarisation plays, which produces distinctive plasma electrons response and dynamics depending on the ellipticity degree employed. The effect of the laser focal spot size on the final spatial-intensity distribution of the electron beam is also characterised.

6.1 Experimental Results

The set-up used to make the experimental measurements reported in this chapter is described in detail in Chapter 4 (sections 4.2 and 4.2.2). In particular, the electron spatial-intensity distribution, for a range of electron energies, was

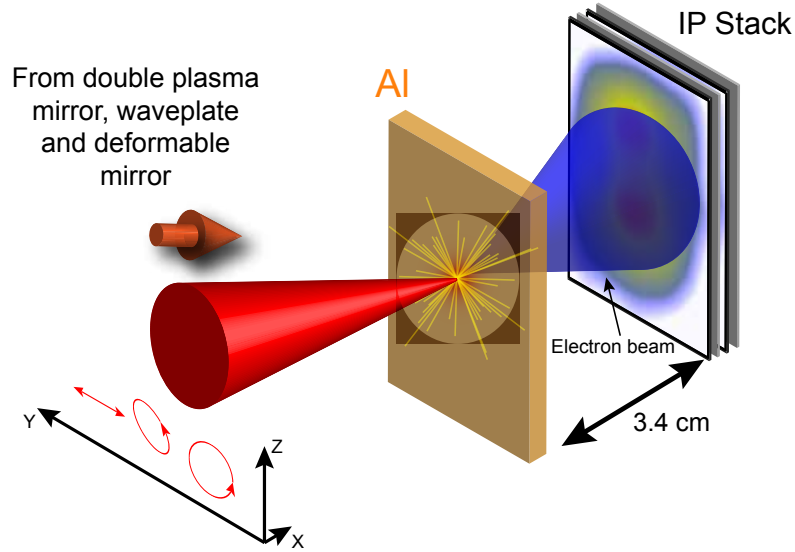


Figure 6.1: Schematic configuration of the experimental set-up to measure the electron spatial-intensity distribution for various target thickness and laser polarisations shown by the red arrows.

measured using an imaging plate (IP) stack placed at 3.4 cm from the target rear. The laser polarisation was controlled, using a $\lambda/4$ waveplate, between three particular cases: p-linear ($\Delta\theta = 0$), elliptical ($\Delta\theta = \pi/4$ and $\Delta\theta = -\pi/4$) and circular ($\Delta\theta = \pi/2$), where $\Delta\theta$ is the phase different between the two orthogonal electric field components of the laser beam. A $\lambda/2$ waveplate, for s-polarisation, was also employed. The laser intensity was $\sim 6 \times 10^{20} \text{ Wcm}^{-2}$ contained in a $\sim 3 \mu\text{m}$ focal spot (FWHM) diameter. Figure 6.1 illustrates a schematic of this configuration.

6.1.1 Target foils for which transparency does not occur

In this investigation, thick targets are considered which do not exhibit relativistic transparency during the laser-solid interaction, for laser intensity of $\sim 6 \times 10^{20} \text{ Wcm}^{-2}$. As characterised in Chapter 5, this corresponds to target thickness equal to or above 40 nm (for the linear polarisation case). Although the main investigation presented in this chapter concerns the electron response to the onset of relativistically induced transparency in thin targets, experimental results

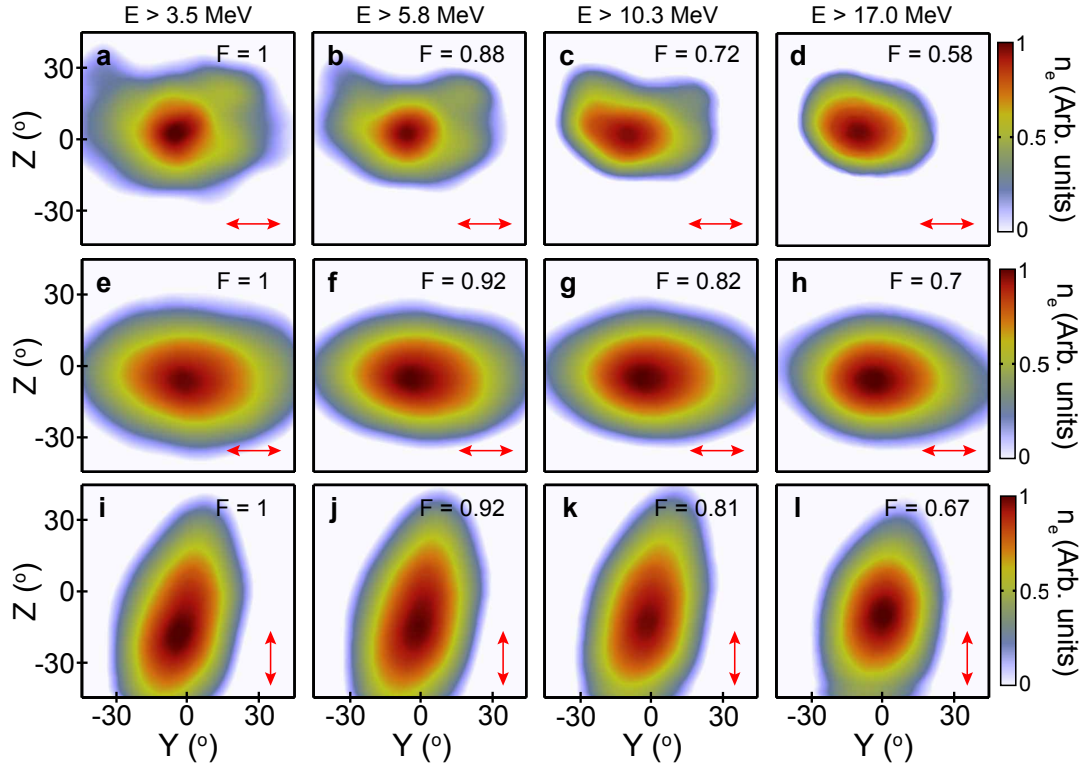


Figure 6.2: Measured electron density distribution. **a-d**, Electron density as measured using imaging plate for $l = 800$ nm, for electrons with energy greater than: **a**, 3.5 MeV; **b**, 5.8 MeV; **c**, 10.3 MeV; and **d**, 17.0 MeV; all for linear polarisation (Y-axis). **e-h**, Same for $l = 40$ nm and linear polarisation (Y-axis). **i-l**, Same for $l = 40$ nm and linear polarisation (Z-axis). The colour maps are scaled by the stated value F to clearly show the features of interest at each energy slice.

involving thick targets are first discussed in order to draw a comparison of the electron dynamics when the target remains opaque during the interaction. For this study, linear, elliptical and circular laser polarisations are considered.

Figure 6.2a-d shows the time-integrated measurements of the electron spatial-intensity distribution above given energy thresholds, measured in the Y-Z plane, for a target thickness $l = 800$ nm, and linearly polarised light along the Y-axis. The colour maps are scaled by the stated F value (this value defines the relative intensity of the electron density for each given energy; $F = 1$ refers to the highest electron density for each target thickness) to clearly show the features of interest at each energy slice. As described in Chapter 5, target thickness above ~ 200 nm can be considered infinitely thick for the laser parameters used in this thesis, for which induced transparency does not occur at any point during the laser

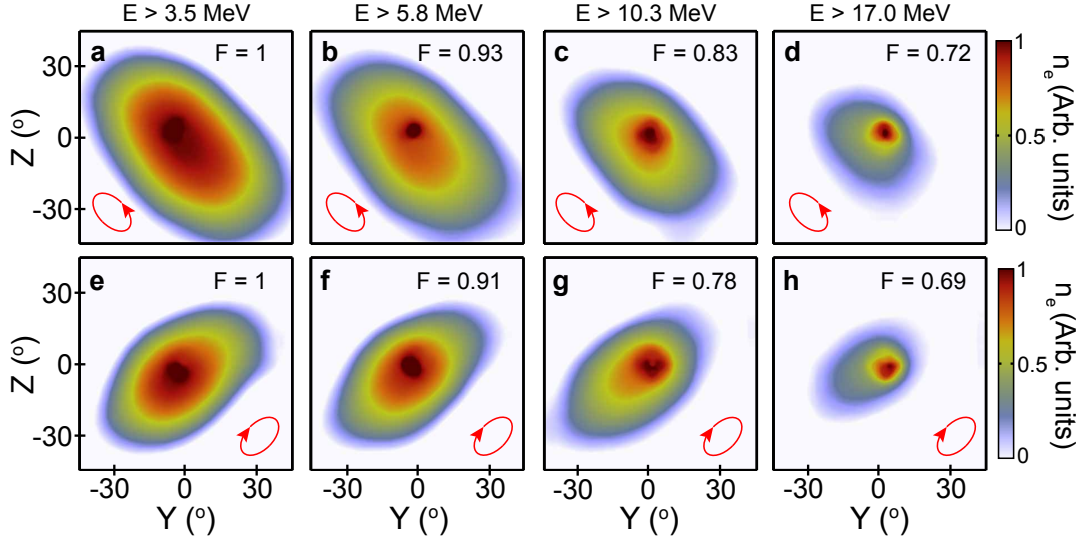


Figure 6.3: Measured electron density distribution. **a-d**, Electron density as measured using imaging plate for $l = 40$ nm, for electrons with energy greater than: **a**, 3.5 MeV; **b** 5.8 MeV; **c** 10.3 MeV; and **d**, 17.0 MeV; all for elliptical polarisation ($\Delta\theta = \pi/4$). **e-h**, Same for elliptical polarisation ($\Delta\theta = -\pi/4$). The colour maps are scaled by the stated value F to clearly show the features of interest at each energy slice.

interaction. Under these conditions the electrons are predominately accelerated by the hole boring mechanism, which is more efficient at higher intensities. For a laser spatial Gaussian-like profile peak intensities are along the laser axis. Figure 6.2a-d exhibits a predominantly circular electron beam (with a lower density halo) as expected from this electron acceleration mechanism.

For a target thickness of $l = 40$ nm, when the target still remains opaque but close to the transparency threshold, the electron beam presents a highly elliptical distribution at all the given energies with the major axis of this ellipse parallel to the laser polarisation, as is shown in figure 6.2e-h. For the same target thickness, $l = 40$ nm, but with linearly polarised light perpendicular to the previous one, i.e. along the Z -axis, the electron beam also exhibits an elliptical distribution, with the major axis parallel to the laser polarisation, as is shown in figure 6.2i-l. This polarisation-sensitive electron beam ellipticity indicates a strong electron interaction with the laser electric field, when the target thickness is opaque during all the laser interaction but, importantly, close to the relativistic transparency condition. It also highlights the potential to manipulate the collective electron

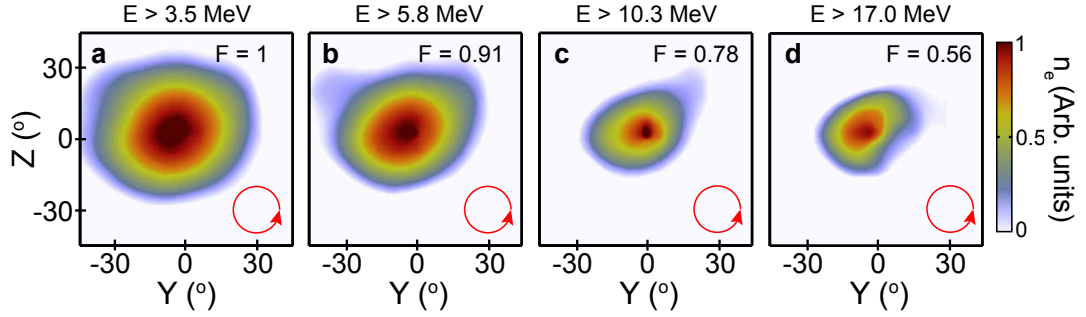


Figure 6.4: Measured electron density distribution. **a-d**, Electron density as measured using imaging plate for $l = 40$ nm and electrons with energy greater than: **a**, 3.5 MeV; **b**, 5.8 MeV; **c**, 10.3 MeV; and **d**, 17.0 MeV; all for circular polarisation. The colour maps are scaled by the stated value F to clearly show the features of interest at each energy slice.

motion in dense plasma.

In order to verify this strong electron interaction with the laser electric field for target thickness of $l = 40$ nm, electron beam measurements for elliptically polarised light was also performed. These results are presented in figure 6.3a-d (for $\Delta\theta = \pi/4$) and figure 6.3e-h (for $\Delta\theta = -\pi/4$). They also show a clear interaction with the laser electric field, where the electron beam exhibit in both cases an elliptical spatial-intensity distribution parallel to the ‘average’ polarisation axis.

On the other hand, for $l = 40$ nm target thickness, and employing circularly polarised light, the electron beam does not present an elliptical spatial distribution, but a circular distribution, with the highest electron density in the centre of the beam at all the given energies. This is also consistent with a strong electron interaction with the laser electric field and radiation pressure acceleration mechanisms. These results are shown in figure 6.4a-d.

All these results, employing $l = 40$ nm target, indicate that the plasma electrons are subjected to the laser field for longer than in the case for thicker targets and therefore, for all polarisation cases considered, the electrons are strongly affected by the laser E-field, being swept from side to side along the E-field direction.

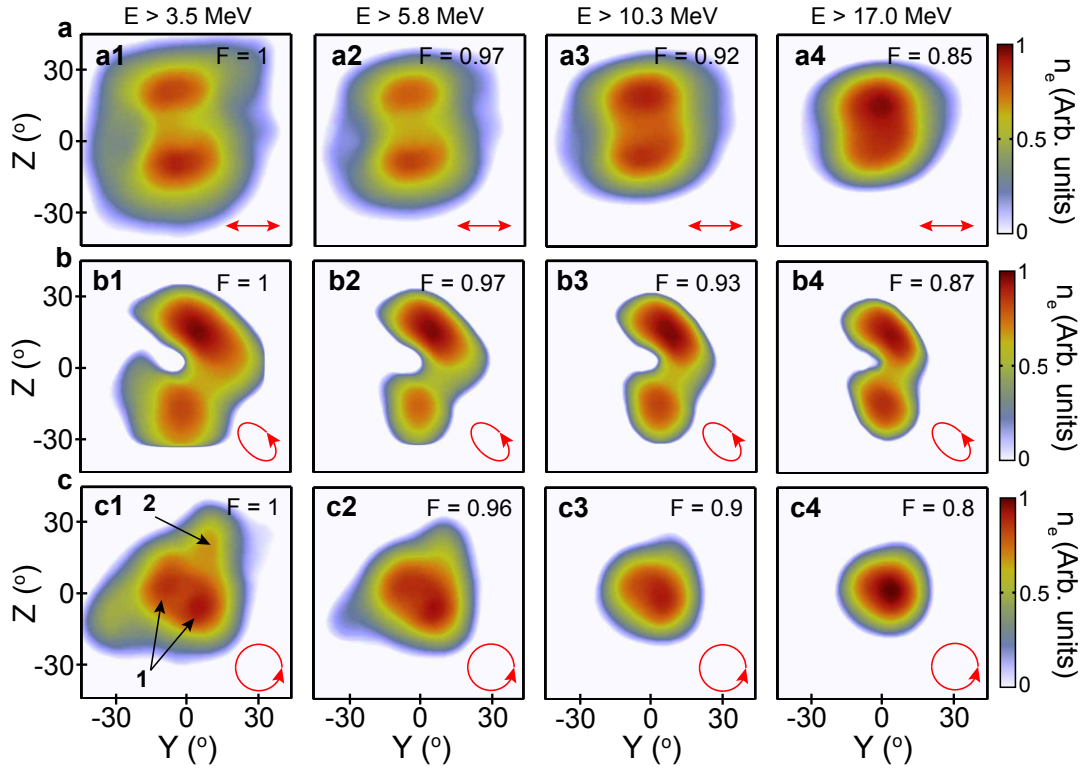


Figure 6.5: Measured electron density distribution for a $l = 10$ nm target. **a**, Electron density as measured using imaging plate for electrons with energy greater than: **a1**, 3.5 MeV; **a2**, 5.8 MeV; **a3**, 10.3 MeV; and **a4** 17.0 MeV; all for linear polarisation (Y-axis). **b**, Same for elliptical polarisation. **c**, Same for circular polarisation. The colour maps are scaled by the stated value F to clearly show the features of interest at each energy slice. The red arrows show the laser polarisation.

6.1.2 Ultra-thin target foils undergoing transparency

Unlike thick targets, in this investigation, thin targets are considered those which exhibit a significant relativistic transparency during the interaction for aluminium targets and a laser intensity of $\sim 6 \times 10^{20}$ Wcm $^{-2}$. As it was studied in Chapter 5, this corresponds to target thickness below $l = 40$ nm (for the linear polarisation case). Due to the most interesting results being found when there is a significant degree of relativistic induced transparency, this investigation focuses on the $l = 10$ nm case.

The salient features of the results are presented in figure 6.5, which shows example time-integrated measurements of the electron beam above given energy thresholds, measured in the Y-Z plane, for all three polarisation cases. As in

the previous figure the colour maps are scaled by the stated value F to clearly show the features of interest at each energy slice. A double-lobe electron density perpendicular to the laser polarisation axis is measured when linearly polarised light is used (figure 6.5a). A similar electron response is found for an elliptical laser polarisation, where a double-lobe electron density is produced perpendicular to the ‘average’ polarisation axis (figure 6.5b). The measurements for circularly polarised light, shown in figure 6.5c, exhibit a small-radius central ring with local maxima (labelled 1) and a lower density $\pi/2$ out-of-phase distributions at larger radii, (labelled 2) in figure 6.5c1, for electrons with energy greater than 3.5 MeV. This particular structure is adjusted to a circular distribution with the highest electron densities in the centre of the beam for energies above ~ 10 MeV, as shown in figure 6.5c4.

6.2 ‘Relativistic Plasma Aperture’ in thin foils

In order to explain the experimental results obtained using thin targets, a novel conception referring to laser-electron interaction in relativistically transparent plasmas is formulated. The concept introduced for the first time is that of a ‘relativistic plasma aperture’ produced in the ultra-thin foil by the ultra-intense laser. The remainder of the laser light transmitted through this self-formed aperture undergoes the fundamental optic process of diffraction. To understand and characterise this process as well as its implication on the electron dynamics in a laser-solid interaction subjected to relativistic transparency, numerous 3D PIC simulations have been performed. They show that the collective electron motion (including angular frequency of rotation) is determined by the resulting near-field diffraction pattern, which can also be controlled by varying the polarisation of the laser. In this section a detailed study of the electron response for each particular investigated laser polarisation is presented.

The 3D simulations were performed using the fully relativistic EPOCH PIC code [129]. The simulation space was defined as a $20 \mu\text{m} \times 20 \mu\text{m} \times 20 \mu\text{m}$ box with $1000 \times 720 \times 720$ computational mesh cells. The laser wavelength was 800 nm. The pulse has a Gaussian temporal profile with a FWHM width of 40 fs focused to a Gaussian intensity distribution of $3 \mu\text{m}$ at FWHM. The peak laser intensity was therefore $6 \times 10^{20} \text{ Wcm}^{-2}$ to match the experiments. Simulations are performed with the laser pulse polarised linearly (p-polarisation along the Y-axis), elliptically ($\pi/4$ phase difference) or circularly. The simulations were run for a total duration of 200 fs to ensure full propagation of the laser pulse through the simulation space. The target was representative of a solid 10 nm-thick Al^{13+} slab with 6 nm-thick C^{6+} and H^+ mixed hydrocarbon layers (with the form C_2H_6) on the front and rear surfaces, all fully ionised. The H and C ions, on the target surfaces, represent the hydrocarbon layers in the experiments. The smallest mesh cell size able to be used in these computationally intensive 3D simulations was 20 nm. The target was thus pre-expanded to a Gaussian profile (with 245 nm FWHM) in order to have a sufficient number of cells across it to avoid self-heating and other numerical artefacts. This results in reduced peak electron densities of $\sim 14.3n_c$, for the main target and $\sim 3.7n_c$ for the hydrocarbon layers. The ion density was initialised to neutralise the electrons using appropriate proportions of Al^{13+} , C^{6+} and H^+ ions. This approach is justified given that experimentally some degree of expansion, driven by electron heating early on the rising edge of the laser pulse, will occur in order to enable RIT to take place. The initial electron temperature was selected to 100 keV being low enough to avoid artificial thermal induced effects, but high enough to resolve the Debye length as closely as possible. Likewise, the initial ion temperature was selected to 1 keV. Simulations at increased temperatures fully resolving the Debye length do not significantly change the physics reported here but exhibit thermal instabilities on the target surface away from the interaction point, i.e. at the laser focus. Initially there

were ~ 22 simulation particles per cell per species (total of 3.11×10^9 simulation particles). This code assumes no binary collisions and the boundaries were defined as free-space. Although there was a degree of particle loss and charge build-up at the boundaries, this is acceptable as the region of interest is suitably far from any boundary effects given the overall simulation runtime.

6.2.1 Linear polarisation

The interference of waves which encounter a pinhole (or other obstacle) that is comparable in size to the waves's wavelength gives rise to diffraction phenomenon according to the Huygens-Fresnel principle [1, 133]. In the case of a thin foil target undergoing RIT, during the laser interaction, a localised region of the target near the peak of the focused intensity, at which $n_e < n'_c$ becomes relativistically underdense, as described in Chapter 3. We have named this effect the 'relativistic plasma aperture'. The diameter of this circular region, shown schematically in figure 6.6 for a Gaussian laser pulse, depends on the intensity profile of the focal spot and the plasma expansion characteristics. It will typically be on the order of the full width at half maximum of the laser focus, for linearly polarised light, and therefore ~ 2 -3 times the size of the laser wavelength for a tightly focused (near diffraction limited) beam. Thus, after formation of this aperture on the pulse rising edge, the conditions are ideal for strong diffraction of the remainder of the laser pulse propagating through it, as will be shown below.

Nevertheless, first an idealised case of a fixed aperture, i.e. without plasma evolution effects, is considered to evaluate the near-field diffraction pattern generated. The results of this ideal case will provide useful interpretation of the full 3D simulations concerning laser-plasma interactions. Figure 6.7 shows 3D PIC simulation results in which a laser pulse with focal spot FWHM diameter of $3 \mu\text{m}$ is passed through a fixed $3 \mu\text{m}$ diameter circular aperture. The laser is polarised along the Y-axis. The intensity distribution patterns in the Y-Z plane

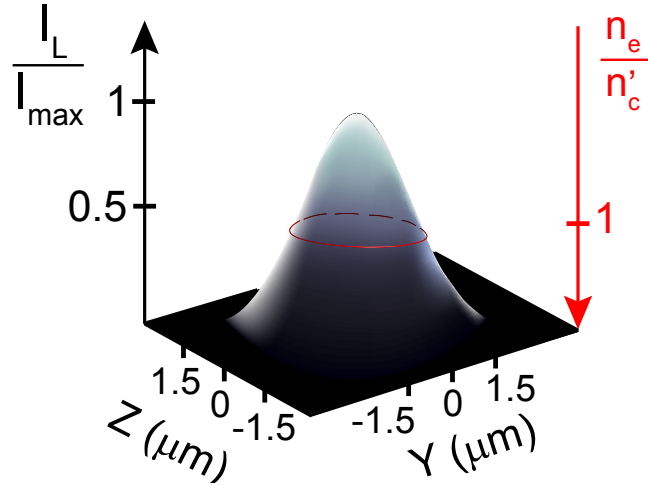


Figure 6.6: Schematic showing the Gaussian spatial-intensity distribution of an ultra-intense laser pulse with diameter (FWHM) equal to $3 \mu\text{m}$. For the case of near-critical, dense plasma, RIT occurs at intensities above those bounded by the red ring corresponding to the threshold condition ($n_e/n'_c = 1$), enabling this portion of the laser pulse to be transmitted.

at three example X positions are shown in figure 6.8a corresponding, from left to right, to 1', 2' and 3', respectively, in figure 6.7. The near-field pattern (i.e. at small X) is observed to vary strongly with position from an analogous even-IG₂₀ mode (Ince-Gaussian mode [134] with ellipticity 0.1) at $X = 0.4 \mu\text{m}$ to the odd-IG₁₁ mode at $X = 1.2 \mu\text{m}$. The pattern diffracts into an even-IG₀₀ mode in the far-field.

In order to confirm that these particular laser intensity distributions are fully described as diffraction patterns produced by a laser pulse passing through a circular aperture, a vectorial analysis using Hertz Vector Diffraction Theory (HVDT) [135] is employed. With this vectorial model, values for the electromagnetic field can be obtained not only in the plane of the aperture but also downstream. The near-field diffraction pattern, in the region of maximum interaction between the laser and the plasma electrons, is of particular interest in this investigation. Although other analytical models such as the scalar Rayleigh-Sommerfeld [136] or Fresnel-Kirchhoff [137] models can be used to study diffraction induced by an aperture, they work in the limit that the aperture radius is much bigger than the laser wavelength, that the electric field in the plane of the

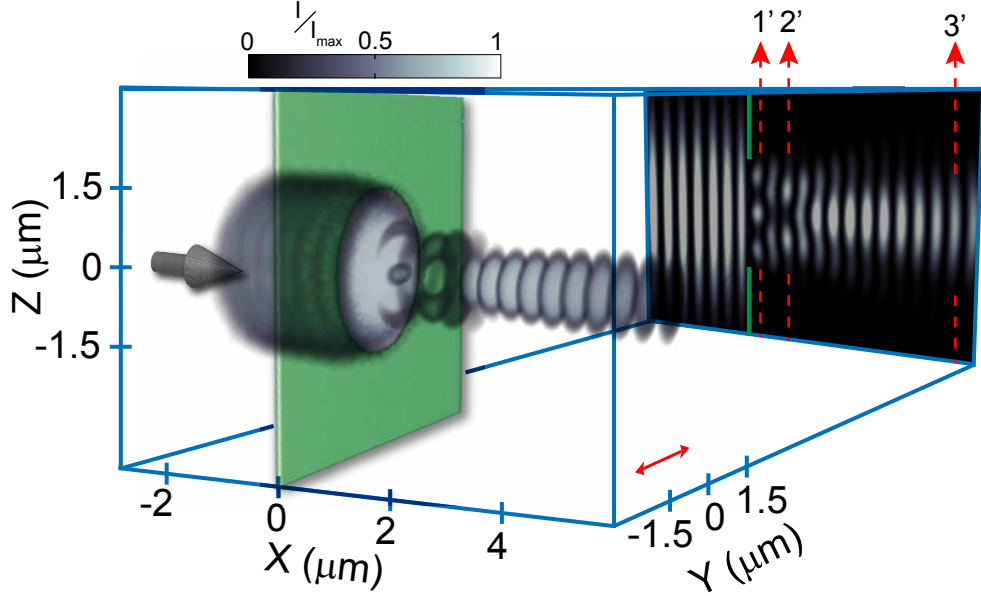


Figure 6.7: 3D simulation profile showing the spatial-intensity variation of the diffraction pattern of a linearly polarised (along Y-axis) laser pulse with $3 \mu\text{m}$ (FWHM) diameter passing through a fixed $3 \mu\text{m}$ -diameter aperture, and 2D (X-Z) cut-away in the $Y=0$ plane. 2D profile in the plane of the target at $X=0.4 \mu\text{m}$, $X=1.2 \mu\text{m}$ and $X=5.2 \mu\text{m}$ corresponding to the 1', 2' and 3' positions respectively are shown in figure 6.8a.

aperture is known and involve a scalar treatment of the diffracted light. Using the HVDT model these limitations are avoided. This model derives the electric field at any point from the aperture as:

$$E_y(x, y, z) = \frac{iE_0 p_1}{2\pi} \int_{-1}^1 \int_{-\sqrt{1-z_0^2}}^{\sqrt{1-z_0^2}} f_1 \left[(1 + s_1) - (1 + 3s_1) \frac{(y_1 - y_0)^2}{\rho_1^2} \right] dy_0 dz_0 \quad (6.1)$$

where

$$\rho_1 = \sqrt{(x_1 - x_0)^2 + (y_1 - y_0)^2 + p_1^2 z_0^2}; \quad f_1 = \frac{e^{-ip_1 \rho_1}}{\rho_1}; \quad s_1 = \frac{1}{ip_1 \rho_1} \left(1 + \frac{1}{ip_1 \rho_1} \right) \quad (6.2)$$

and $p_1 = 2\pi r/\lambda$, where r is the aperture radius and λ the laser wavelength. A more detailed description of each parameter is included in reference [135].

The evaluation of the previous equation for a Gaussian-like profile with $3 \mu\text{m}$ (FWHM) and 800 nm laser wavelength, and $3 \mu\text{m}$ aperture diameter is presented in figure 6.8b. These analytical results show a full description of the

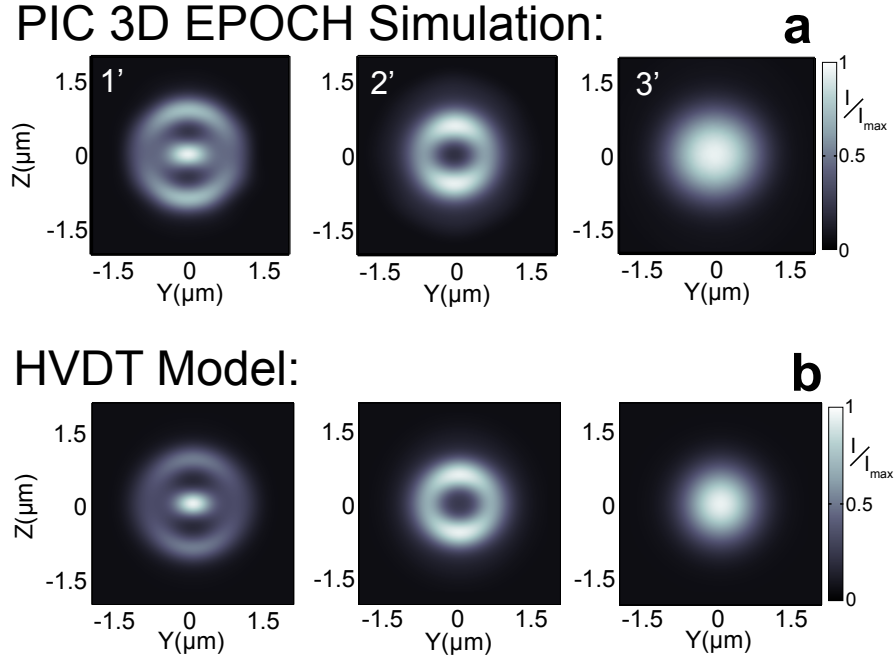


Figure 6.8: Intensity diffraction pattern induced by a fixed, predefined aperture. **a**, 2D profile in the plane of the target, from figure 6.7, at $X=0.4 \mu\text{m}$ (1'), $X=1.2 \mu\text{m}$ (2') and $X=5.2 \mu\text{m}$ (3'), exhibiting mode structures. **b**, Calculated diffraction patterns at the same three positions using Hertz vector diffraction theory (HVDT).

3D simulations for the same positions in X as observed when comparing figure 6.8a and 6.8b.

Once the ideal case is characterised, an investigation of the laser-generated relativistic plasma aperture in a uniform thin foil, the effect this has on the propagating laser light, and in turn how the evolving laser spatial profile influences the beam of fast electrons accelerated forward, is described. For this investigation full 3D PIC simulations (as described at the beginning of this section), using the same laser pulse and target parameters as the experiment discussed in the previous section, have been performed.

Figures 6.9a and b show an example simulation result for the laser intensity and electron density normalised to the corrected critical density just after RIT occurs, in a 3D perspective (figure 6.9a) and a perpendicular plane to the laser polarisation at $Y = 0$ (figure 6.9b), at time $T = 23 \text{ fs}$ (for the results in this chapter time is referred to the instant in which the laser peak interacts with the plasma,

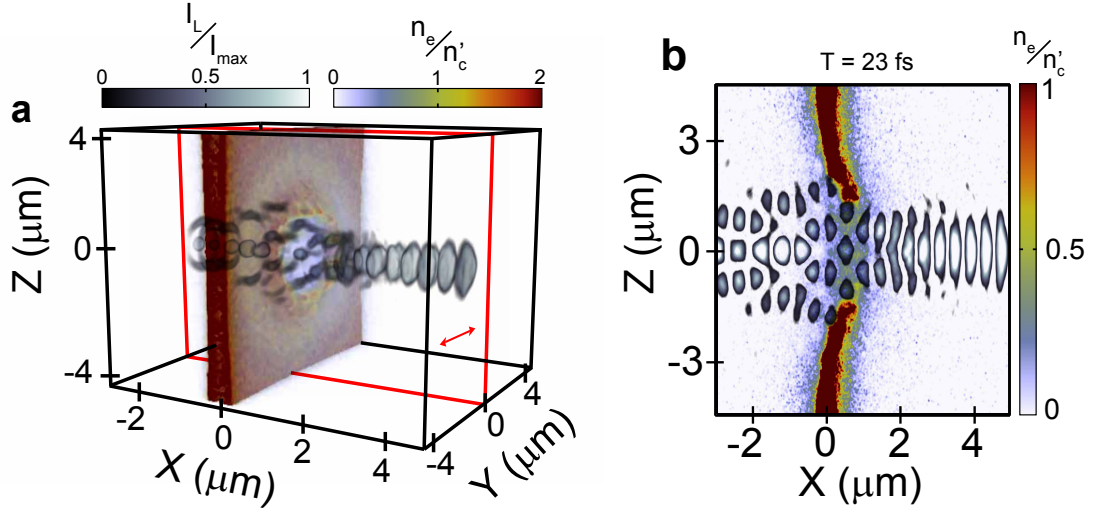


Figure 6.9: **a**, 3D PIC simulation result showing the laser diffraction and plasma electron density produced by the relativistic plasma aperture, in the linear polarisation case (along Y-axis), during a laser interaction with a planar foil and peak intensity of $6 \times 10^{20} \text{ Wcm}^{-2}$. The laser intensity, I_L , pattern overlapped with the plasma electron density normalised to n'_c are shown at 23 fs ($T = 0$ corresponds to the time at which the laser peak interacts with the plasma). The diffraction pattern is very similar to the fixed aperture case without plasma shown in figure 6.7. **b**, 2D (X-Z) cut-away in the $Y=0$ plane (red plane highlighted in **a**) showing the laser diffraction pattern (in grey scale) and the fast electron density distribution (colour scale).

which correspond to $T = 0$ fs). In order to obtain the corrected critical density, n'_c , the Lorentz factor, γ , was evaluated locally for each simulation cell considering the average electron momentum, for all figures included in this chapter. Interference between laser light which is reflected from the target before RIT occurs and the remaining incoming laser light results in a standing wave distribution with local nodes and anti-nodes at the target front ($X < 0 \mu\text{m}$). Despite local deformation of the target due to laser radiation pressure, during RIT the remainder of the laser pulse diffracts as it passes through the evolving plasma aperture. The resulting diffraction pattern at the target rear (shown in figure 6.9a and b) is very similar, in both the near and far fields, to the diffraction patterns shown in figure 6.7 and figure 6.8 obtained using the HVDT and the static aperture models.

An evolution of the aperture, including the rising edge and at relatively late times on the falling edge of the laser pulse, is shown in figure 6.10a-d. Just after RIT occurs, in figure 6.10b and c, the simulation clearly shows that the accelerated electrons respond to the diffracted laser intensity distribution. For a greater

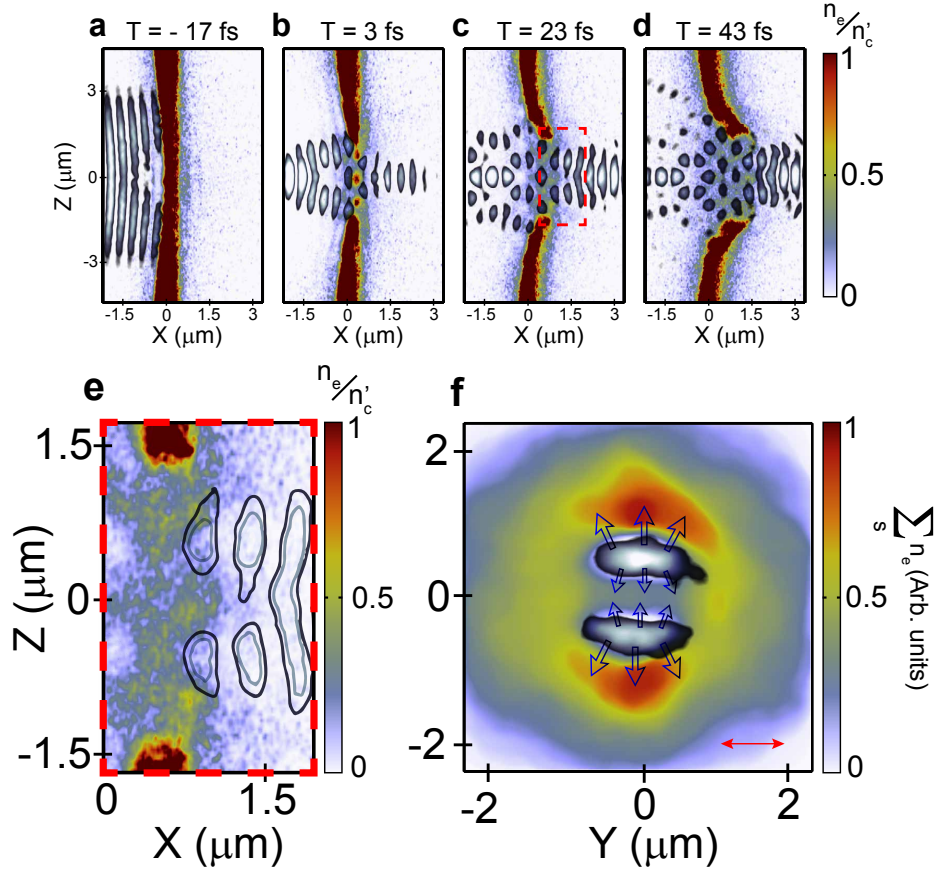


Figure 6.10: **a-d**, 2D (X-Z) slice in the $Y = 0$ plane (red plane highlighted in figure 6.9a) showing the electron density overlaid with the laser intensity at four example time steps ($T = 0$ corresponds to the time at which the laser peak interacts with the plasma). **e**, Same showing the region of interest bounded by the dashed rectangle in **c**. **f**, 2D (Y-Z) plane showing laser light intensity and electron density integrated over $X=0.7-1.5$ μm (corresponding to one laser wavelength in the region of the high density of electrons that are accelerated forward). The hollow arrows illustrate the direction of the ponderomotive force arising from the gradients in laser intensity.

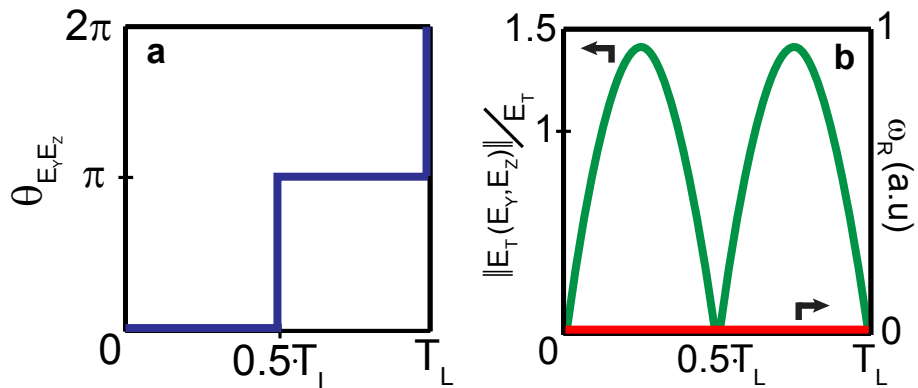


Figure 6.11: Analytical model representation of: **a**, angle of the polarisation vector with respect to the $+Y$ axis; **b**, angular velocity of the polarisation vector rotation with respect to the $+Y$ axis and magnitude of the laser electric field, for linear polarisation over one laser period, T_L .

appreciation, in figure 6.10e a zoomed area corresponding to the dashed square in figure 6.10c is shown. In these two figures, at the X position at which the electron density is highest on axis ($X \sim 1 \mu\text{m}$), the laser profile has a double diffraction lobe distribution orientated perpendicular to the polarisation direction, similar to the distribution shown in figure 6.7, and an Airy disk distribution in the far field ($X > 4 \mu\text{m}$), again similar to the far-field pattern seen in figure 6.7. The electrons in the region of the double diffraction lobe are subject to a transverse ponderomotive force in the plane of the target, as shown by the hollow arrows (from field mapping) as displayed in figure 6.10f. This drives the electrons into a double lobe distribution, perpendicular to the laser polarisation direction. A smaller number of electrons are also trapped on-axis between the opposing ponderomotive forces of similar magnitude produced by the two laser diffraction nodes.

In order to explain this results, analytical calculations to describe the angular velocity of the polarisation vector and magnitude of the electric field have been performed. As introduced in section 2.3.2, an electromagnetic wave can be defined as the superposition of two orthogonal linear components:

$$\begin{cases} E_y = E_{0y} \sin(\phi) \hat{y} \\ E_z = E_{0z} \sin(\phi - \Delta\theta) \hat{z} \end{cases} \quad (6.3)$$

where for a linearly polarised wave $E_{0z} = 0$ and the phase difference between both components is $\Delta\theta = 0$. The rotational angular velocity with respect to the +Y axis is described as $\omega_R = d\theta_{E_y E_z} / dt$, where $\theta_{E_y E_z} = \tan^{-1}(\mathbf{E}_z / \mathbf{E}_y)$ corresponds to the angle with respect to the +Y axis. The magnitude of the total electric field is $\|\mathbf{E}_T(E_y, E_z)\| = \sqrt{\mathbf{E}_y^2 + \mathbf{E}_z^2}$.

In the linear polarisation case, the calculated angle with respect to the +Y axis, the angular velocity of the polarisation vector and the magnitude of the electric field, are shown in figure 6.11 for one laser period. In this case, these

results reveal that the laser electric field flips between the two lobes over each half-laser period, producing the angular asymmetry in the ponderomotive force discussed above. Besides this, once the relativistic plasma aperture has acquired its maximum diameter and because of the angular velocity of the polarisation vector remains 0 for each laser period, the two laser diffraction nodes will remain temporally static reinforcing the generation and propagation of electrons into a double lobe distribution.

6.2.2 Circular polarisation

Continuing with the investigation of the laser polarisation effect on the electron response in thin foil undergoing RIT, an example 3D simulation result for circularly polarised laser intensity and electron density, normalised to the corrected critical density, just after RIT occurs, at $T = 23$ fs, is shown in figure 6.12a. This simulation corresponds to a full laser-plasma interaction, i.e. without a predefined aperture. Using circularly polarised light results in significantly less electron heating and expansion, consequently more radiation-pressure-driven target deformation. RIT therefore occurs later in the interaction, resulting in a smaller aperture ($\sim 1.5 \mu\text{m}$ in diameter) compared to the linear polarisation case ($\sim 3 \mu\text{m}$ in diameter). As in the linear case interference between laser light which is reflected from the target before RIT occurs and the remaining incoming laser light results in a standing wave distribution at the target front side ($X < 0 \mu\text{m}$). However, in the circular case, the diffraction pattern resulting from laser light passing through the evolving relativistically transparent plasma aperture, exhibits a single lobe rotating in a helical-like structure. This behaviour will generate an unique response of the accelerated electron beams, which is investigated below in more detail.

In order to evaluate and interpret this particular near-field diffraction pattern, an idealised 3D simulation with a predefined static aperture, i.e. without plasma

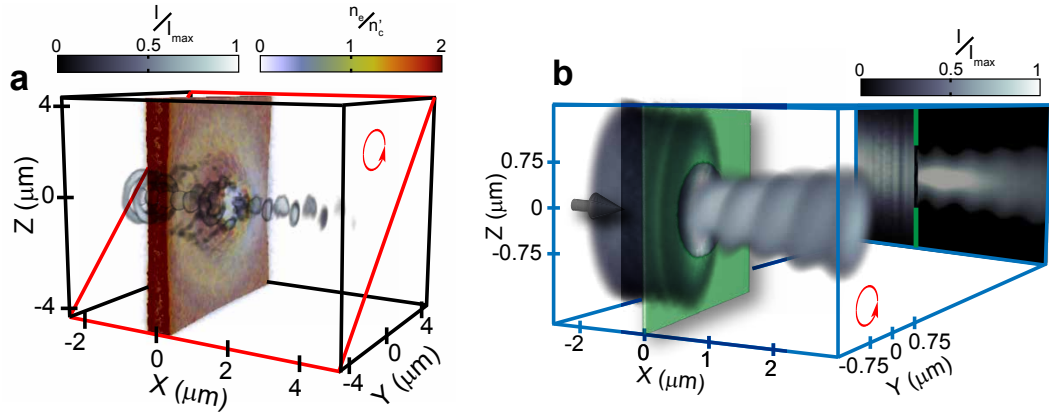


Figure 6.12: **a**, 3D PIC simulation result showing the laser diffraction and plasma electron density produced by the relativistic plasma aperture, in the circular polarisation case, during a laser interaction with a planar foil and peak intensity of $6 \times 10^{20} \text{ Wcm}^{-2}$. The laser intensity, I_L , pattern overlapped with the plasma electron density normalised to n'_c are shown at 23 fs ($T = 0$ corresponds to the time at which the laser peak interacts with the plasma). **b**, 3D simulation profile showing the spatial-intensity variation of the diffraction pattern of a circularly polarised laser pulse with $3 \mu\text{m}$ (FWHM) diameter passing through a predefined $1.5 \mu\text{m}$ -diameter aperture, and 2D cut-away in a 45° rotated plane around the laser propagation axis, as highlighted in a red square in **a**.

evolution effects, is performed. Figure 6.12b shows the result of this simulation in which a laser pulse with focal spot diameter of $3 \mu\text{m}$ (FWHM) is passed through a fixed $1.5 \mu\text{m}$ diameter circular aperture. It clearly shows that the circularly polarised laser acquires a single lobe diffraction pattern, which rotates in a helical-like structure when it propagates through the preformed circular aperture, confirming the results from the full 3D simulation included in figure 6.12a.

As in the linear polarisation case, a study of the evolution of the aperture has been performed. The results for given time-steps are displayed in figure 6.13a-d. As previously mentioned, in this polarisation case RIT occurs later in the laser interaction, with respect to linear polarisation, due to significantly less electron heating and expansion. When the target becomes relativistically transparent (figure 6.13c and d) the accelerated electrons ponderomotively respond to the diffracted laser intensity distribution generated. Figure 6.13e shows a zoomed in area corresponding to the dashed square in figure 6.13d, for more clarity. The rotating single-lobe diffraction pattern is expected to produce a ring-like

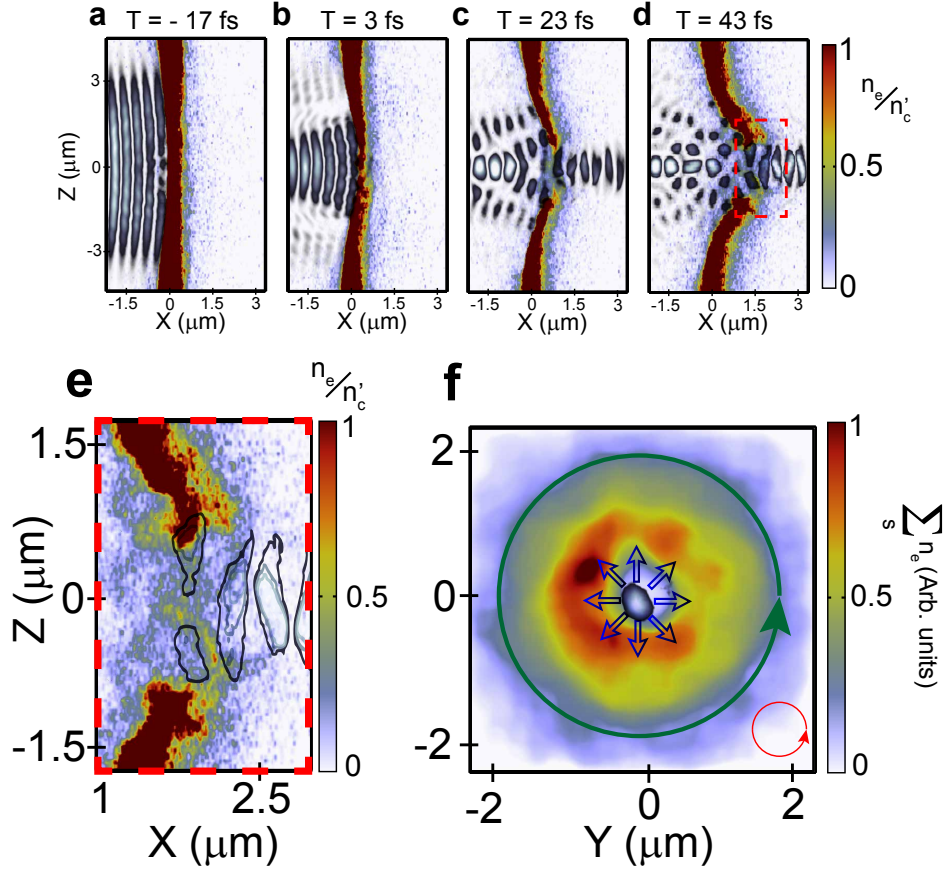


Figure 6.13: **a-d**, 2D (X-Z) slice in a 45° rotated plane around the laser propagation axis (red plane highlighted in figure 6.12a) showing the electron density overlaid with the laser intensity at four example time steps ($T = 0$ corresponds to the time at which the laser peak interacts with the plasma). **e**, Same showing the region of interest bounded by the dashed rectangle in **d**. **f**, 2D (Y-Z) plane showing laser light intensity and electron density integrated over $X=2-2.8$ μm (corresponding to one laser wavelength in the region of the high density of electrons that are accelerated forward). The hollow arrows illustrate the direction of the ponderomotive force arising from the gradients in laser intensity.

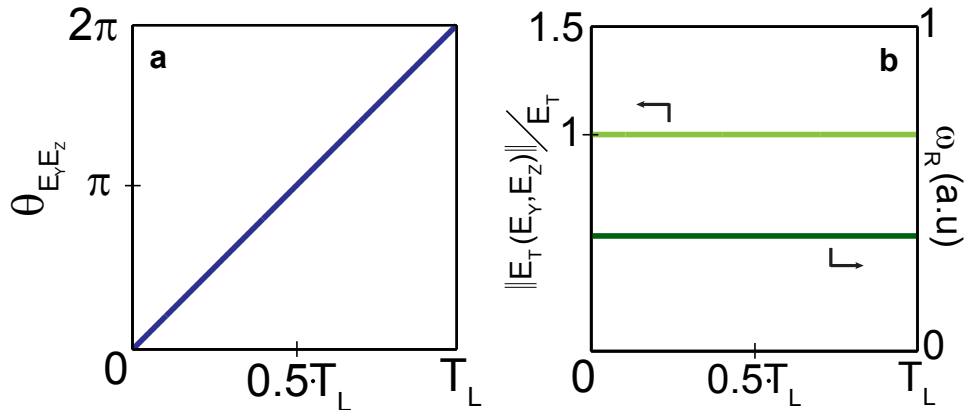


Figure 6.14: Analytical model representation of: **a**, angle of the polarisation vector with respect to the +Y axis; **b**, angular velocity of the polarisation vector rotation with respect to the +Y axis and magnitude of the laser electric field, for circular polarisation over one laser period, T_L .

electron distribution structure around it. These results can be explained with reference to the previous analytical model, equation (6.3), describing the angular velocity of the polarisation vector and magnitude of the electric field, as shown in figure 6.14 for one laser period. With circularly polarised light, with a phase difference equal to $\pi/2$ and $E_{0y} = E_{0z}$, the field components produce a dynamic intensity profile which makes a complete rotation, at constant angular velocity, around the laser propagation axis once per laser period. The instantaneous radial ponderomotive force is asymmetric, as shown in figure 6.13f, but when averaged over a laser period (or higher) a ring-like electron distribution centred on the laser propagation axis is produced.

An additional investigation of the generated diffraction pattern for circularly polarised laser, from these 3D simulations, is presented in figure 6.15. This figure shows the temporal evolution of the electron density distribution, overlaid with the laser intensity distribution, at $X=6 \mu\text{m}$, for the same time as figure 6.12a ($T = 23 \text{ fs}$). It is demonstrated that the rotating laser diffraction structure instigates an in-phase rotation of a structure in the plasma electron density (6.15b). This electron structure consists of a main high-energy component, rotating with a small radius of curvature about the propagation axis, and a lower density halo, of lower-energy electrons, $\pi/2$ out-of-phase, as shown in figure 6.15c and 6.15d.

This rotating diffraction-driven fast electron pattern can give rise to interesting and potentially useful magnetic field structures. The magnetic field driven by the collective electron response to diffraction of circularly polarised light is also helical in structure, tightly precessing at a radius close to that of the plasma aperture ($1.5 \mu\text{m}$ in diameter), as shown in figure 6.16a. When compared to the magnetic field generated by a lower intensity (but otherwise identical) circularly polarised laser, propagating through a comparable fixed circular aperture of $1.5 \mu\text{m}$ diameter (i.e. no plasma; figure 6.16b), it is clear that the diffraction effects play a key role in shaping the magnetic field structure, in the same way as the

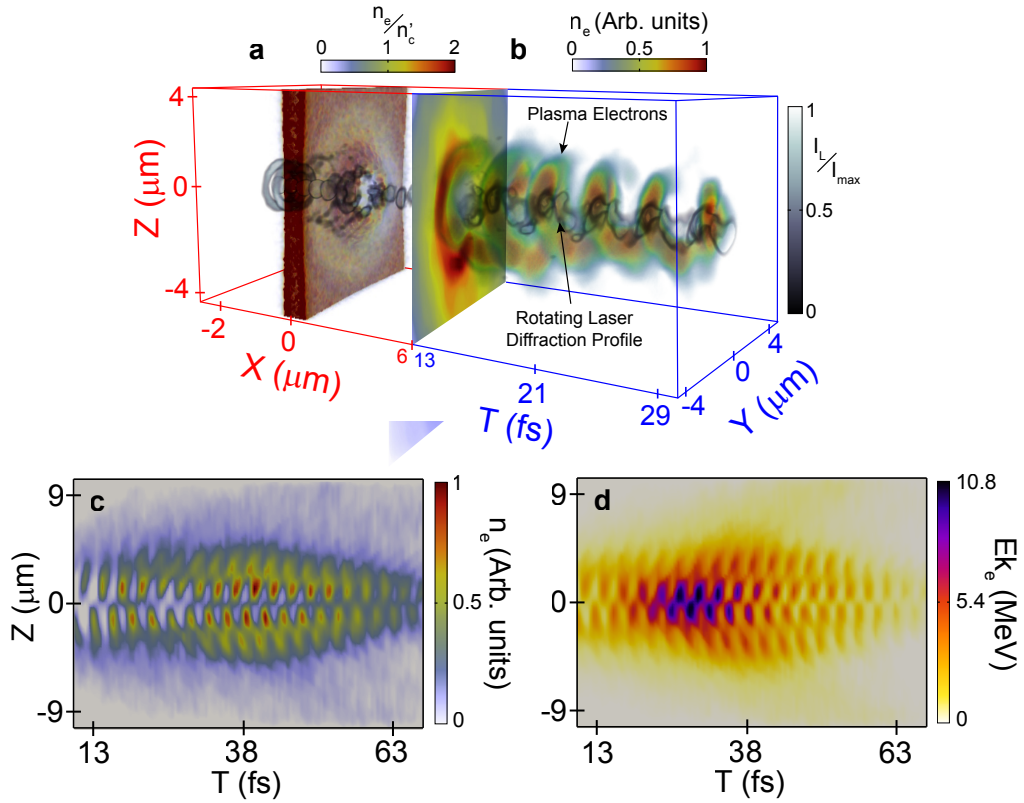


Figure 6.15: 3D PIC simulation results for circularly polarised light interacting with the relativistically induced plasma aperture. **a**, Combined plot showing the 3D laser intensity profile (up to $X=6$ μm) at 23 fs; **b** temporal evolution of the electron density distribution, overlaid with the laser intensity distribution, in the YZ plane at $X=6$ μm from 13 to 30 fs. **c**, Temporal evolution of the electron density along the Z -axis at $X=6$ μm and $Y=0$. **d**, Same for electron energy. The electron density and mean kinetic energy in each given cell of the simulation is plotted. The laser diffraction lobe pattern rotates once per laser cycle, driving an electron energy and density distribution which rotates in phase with it.

laser intensity structure is shaped. In both cases the magnetic field structure is shown 30 fs after the peak laser intensity has propagated through the aperture. The laser pulse propagating through the fixed aperture produces a magnetic field which is strongest close to the aperture, reducing as the beam expands. By contrast, in the relativistic plasma aperture case the magnetic field strength is relatively strong over a longer range and is more helical, suggesting that the field is modified by the induced plasma current structure. The underlying physics of the collective plasma effects on the magnetic field will be the subject of future investigation beyond the scope of this thesis.

The current and field structures produced in this way could be used to

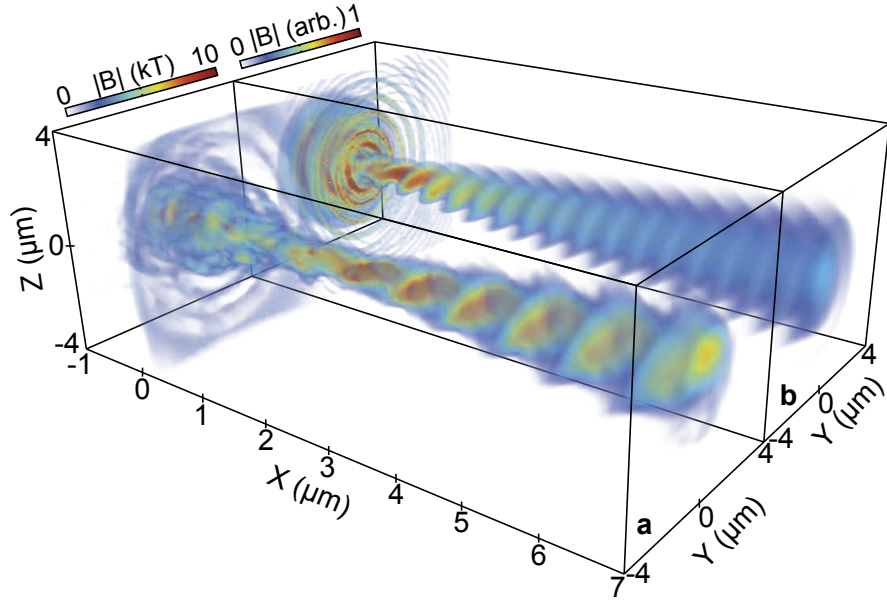


Figure 6.16: Magnetic field structure driven by circularly polarised light. **a**, Magnitude of the magnetic field driven by a circularly polarised laser pulse producing a relativistic plasma aperture in a 10-nm-thick Al target. A helical field structure is produced. **b**, Same for the case of a lower intensity laser pulse propagating through a fixed, predefined aperture of $1.5 \mu\text{m}$ diameter, that is, without plasma effects. The $3 \mu\text{m}$ (FWHM) laser focus is centred on $[X,Y,Z] = [0,0,0]$ in both cases and the field is sampled 30 fs after the peak of the laser intensity. Diffraction induced by the aperture results in a helical field profile in both cases. The structure is modified by the presence of the plasma in **a**.

generate laboratory analogues of astrophysical phenomena. Similar magnetic field structures have been detected in jets originating from active galactic nuclei (AGN), such as 3C 273 [138]. Such structures are commonly identified as being generated from the rotation of the accretion disk, whilst the analogous structures seen here arise from the rotation of the diffraction pattern. Further similarities to these jets can be observed in that the highest momentum component of the accelerated electrons occur along the central laser axis. Surrounding this region, the electron momentum reduces, as seen in figure 6.15d, resulting in an electron beam with properties similar to that of the spine-sheath jet morphology [139].

To test the scaling ratio of the two systems, it can be assumed that the length of the base of an AGN astrophysical jet is on the order of 1 pc [140]. Similarly, the diffraction-induced helical field is observed numerically over $15 \mu\text{m}$ after the target, giving a length scale ratio of $\sim 2 \times 10^{21}$ between the two systems. It can

also be assumed that the jet expands at a velocity close to c , resulting in a time scale of $\sim 1 \times 10^8$ s. As the laser-accelerated electrons expand at approximately the same velocity, the time scale ratio should correspond to that of the length scale ratio [141]. This would give an interaction time-scale of ~ 50 fs, which is very close to that of the laser pulse duration.

In the sub-parsec region of such astrophysical jets, the magnetic field strength is estimated to be on the order of 1×10^{-3} T [142] and the number density can be estimated at between 1×10^{10} and 1×10^{16} m^{-3} [143], giving $\omega_e/\Omega_e \sim 0.031\text{--}31.1$, where ω_e and Ω_e are the electron plasma frequency and cyclotron frequency, respectively. For the plasma aperture diffraction case using a circularly polarised pulse, it is found that $\omega_e/\Omega_e \sim 0.33$ (which would require $n_e \sim 1 \times 10^{12}$ m^{-3} for the astrophysical jet). The helical pitch in these simulations increases linearly from 15° to 55° over a distance of 15 μm from the target. Similarly, the magnetic field produced from these astrophysical jets has been observed to show evidence of an increase in pitch as it propagates further from the source [138]. These various estimates suggest that while there is a huge difference in scale between the two systems, there may be sufficient similarities that would allow future laboratory testing of the formation of helical magnetic field structures in astrophysical jets.

6.2.3 Elliptical polarisation

As a final investigation of the laser polarisation effect on the electron response in a thin foil undergoing relativistic transparency, an elliptically polarised laser intensity has been considered. The results of a full 3D PIC simulation with the laser intensity overlaid with the electron density, normalised to the corrected critical density, after RIT occurs at $T = 23$ fs, is shown in figure 6.17a. Because the $\mathbf{J} \times \mathbf{B}$ heating component is still significantly high for a phase difference equal to $\pi/4$ (corresponding to an ellipticity of 0.5), as discussed in section 2.3.4, the electrons are subject to a higher heating and expansion compare to the circular

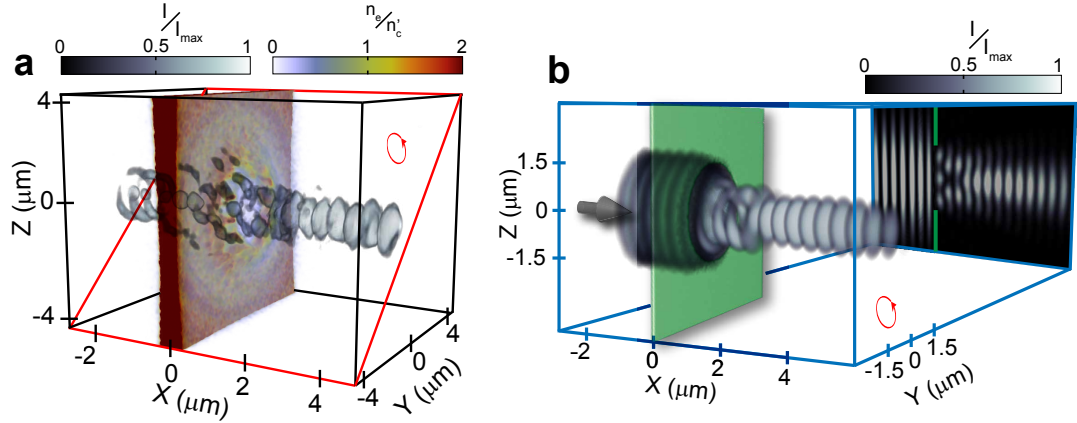


Figure 6.17: **a**, 3D PIC simulation result showing the laser diffraction and plasma electron density produced by the relativistic plasma aperture, in the elliptical polarisation case, during a laser interaction with a planar foil and peak intensity of $6 \times 10^{20} \text{ Wcm}^{-2}$. The laser intensity, I_L , pattern overlapped with the plasma electron density normalised to n'_c are shown at 23 fs ($T = 0$ corresponds to the time at which the laser peak interacts with the plasma). **b**, 3D simulation profile showing the spatial-intensity variation of the diffraction pattern of an elliptically polarised laser pulse with $3 \mu\text{m}$ (FWHM) diameter passing through a predefined $3 \mu\text{m}$ -diameter aperture, and 2D cut-away in a 45° rotated plane around the laser propagation axis, as highlighted in a red square in **a**.

case. This results in a relativistic plasma aperture with a diameter in the order of the linear polarisation case, approximately $3 \mu\text{m}$ in diameter. Because of this, a similar laser diffraction pattern is generated when the laser propagates through the relativistically transparent plasma, as shown in figure 6.17a. However, in this case, the laser diffraction pattern rotates with a particular velocity around the laser axis, as discussed below.

As in previous cases, an idealised 3D simulation with a predefined static aperture, i.e. without plasma evolution, is performed, in order to evaluate and interpret the near-field diffraction pattern generated. Figure 6.17b shows the result of this simulation in which a laser pulse with focal spot diameter of $3 \mu\text{m}$ (FWHM) is passed through a fixed $3 \mu\text{m}$ -diameter circular aperture. It shows that the elliptically polarised laser acquires the same diffraction pattern, as with linear polarisation, when it propagates through the preformed circular aperture. This is more obvious in the 2D X-Z plane in figure 6.17b (corresponding to a plane rotated 45° as the red square in figure 6.17a), where the near-field pattern (i.e. at small X) present an analogous even-IG₂₀ mode at $X = 0.4 \mu\text{m}$ an odd-

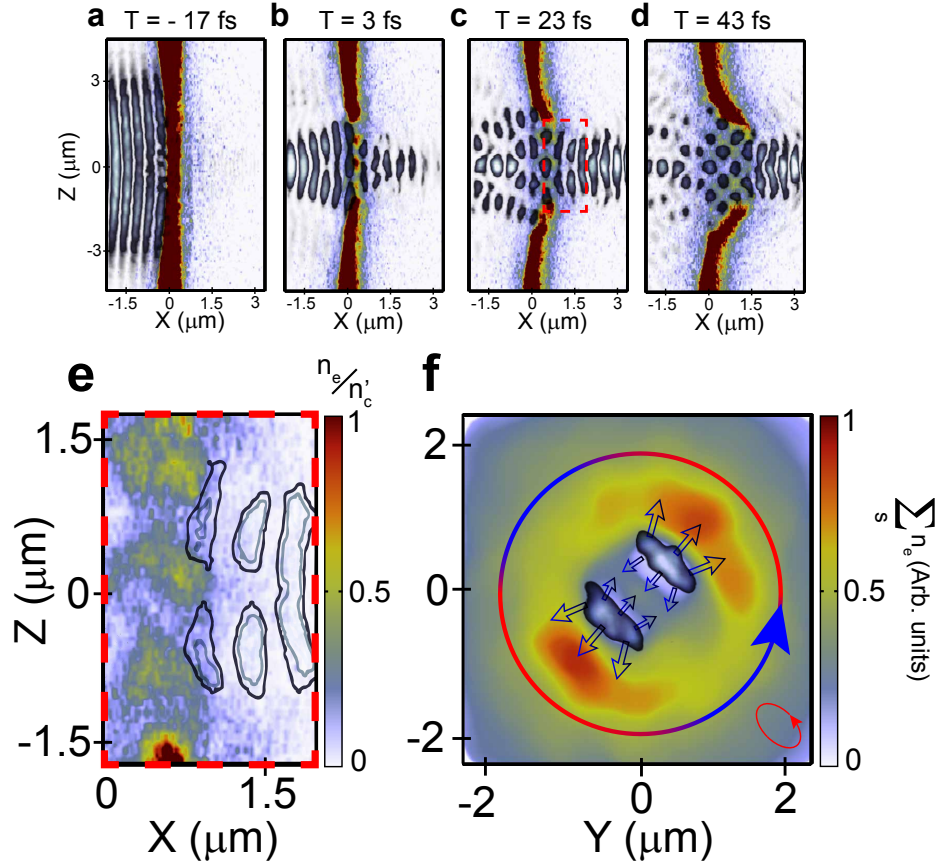


Figure 6.18: **a-d**, 2D (X-Z) cut-away in a 45° rotated plane around the laser propagation axis (red plane highlighted in figure 6.17a) showing the electron density overlaid with the laser intensity at four example time steps ($T = 0$ corresponds to the time at which the laser peak interacts with the plasma). **e**, Same showing the region of interest bounded by the dashed rectangle in **c**. **f**, 2D (Y-Z) plane showing laser light intensity and electron density integrated over $X=0.7-1.5 \mu\text{m}$ (corresponding to one laser wavelength in the region of the high density of electrons that are accelerated forward). The hollow black arrows illustrate the direction of the ponderomotive force arising from the gradients in laser intensity.

IG₁₁ mode at $X = 1.2 \mu\text{m}$ and an even-IG₀₀ mode in the far-field. This pattern is reproduced in the full 3D simulation results, as shown in figure 6.17a.

The generation of this particular diffraction pattern is shown in figure 6.18a-d, where the evolution of the aperture for given time-steps during the laser interaction is presented. As in the linear polarisation case, the simulations show that the accelerated electrons respond to the diffracted laser intensity distribution, just after RIT occurs, as shown in figure 6.18b and c. They demonstrate that, at the X position at which the electron density is highest on axis ($X \sim 1 \mu\text{m}$), the laser profile has also a double diffraction lobe distribution orientated

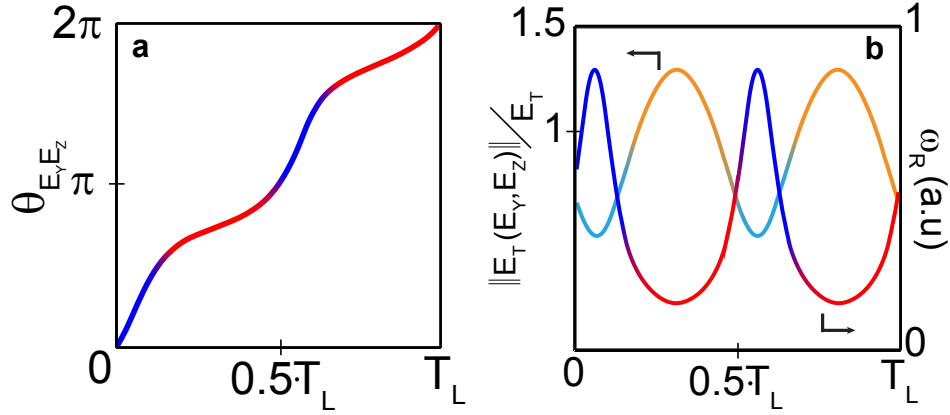


Figure 6.19: Analytical model representation of: **a**, angle of the polarisation vector with respect to the +Y axis; **b**, angular velocity of the polarisation vector rotation with respect to the +Y axis and magnitude of the laser electric field, for elliptical polarisation over one laser period, T_L .

perpendicular to the ‘average’ polarisation direction (very similar to figure 6.17b). A zoomed area corresponding to the dashed square in figure 6.18c is shown in figure 6.18e enabling a better appreciation of this double lobe structure. The electrons in this region are then subject to a transverse ponderomotive force as shown by the hollow arrows (from intensity gradient mapping) in figure 6.18f. A smaller number of electrons are also trapped on-axis between the opposing ponderomotive forces of similar magnitude produced by the two laser diffraction nodes.

This particular electron response can be also explained and understood by the analytical model described in equation (6.3), for a phase difference equal to $\pi/4$ and $E_{0y} = E_{0z}$. It shows that the polarisation vector rotates, but with an angular velocity which varies over the laser period. The magnitude of the laser electric field is highest during the part of the laser period where the polarisation vector rotates slowest, as seen when comparing the red and orange phases of the curves in figure 6.19. The plasma electrons thus respond to the angular variation in the radial ponderomotive force to produce a double lobe orientated perpendicular to the ‘average’ polarisation axis.

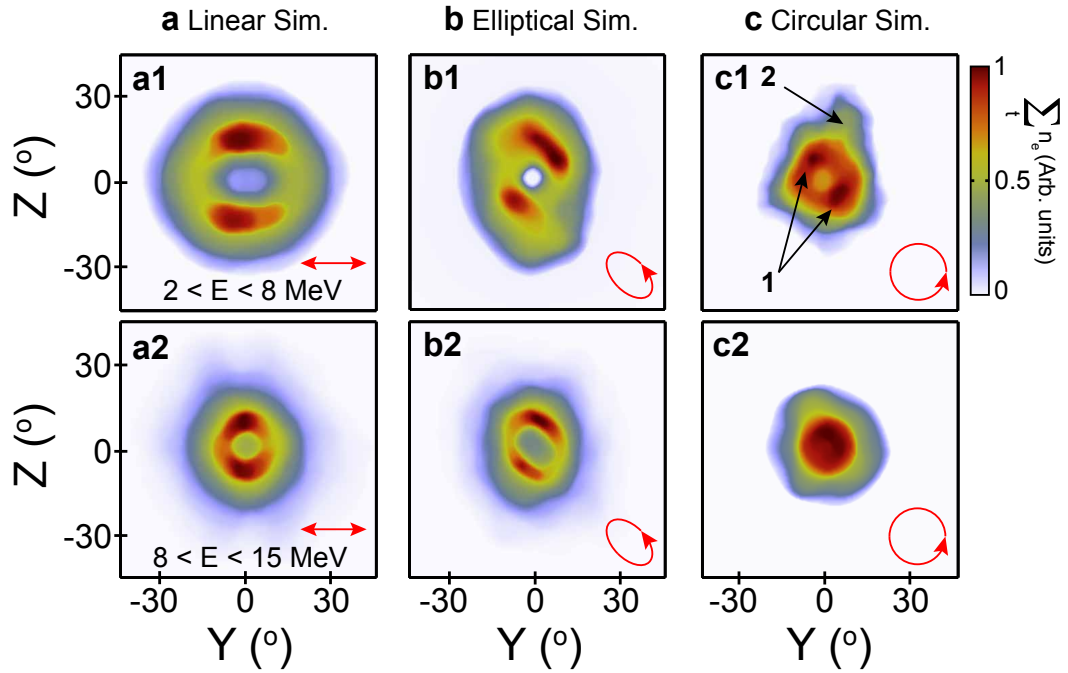


Figure 6.20: 3D PIC simulation results for the electron density distribution from $l = 10$ nm target undergoing RIT. **a**, Simulated time-integrated electron density in the plane Y-Z at $6 \mu\text{m}$ downstream from the rear side of the target, corresponding to linear polarisation for the two stated energy ranges: $2 < E < 8$ MeV (**a1**) and $8 < E < 15$ MeV (**a2**). **b**, Same for elliptical polarisation. **c**, Same for circular polarisation.

6.2.4 Discussion of results

In order to explain the electron spatial-intensity distribution in thin targets obtained in the experiments, for the three laser polarisations investigated (and included in figure 6.5), corresponding example results from the 3D EPOCH simulations, integrated over five laser cycles at the end of the pulse, are shown in figure 6.20a-c. As the experimental measurements are made 3.4 cm downstream from the target, the comparison is made in terms of electron angular deflection (as sampled at $X = 6 \mu\text{m}$ in the simulations). This comparison is focused on the shape of the distributions and how they vary with energy. It is this property that is sensitive to the near-field diffraction pattern of the transmitted light.

The simulation results reproduce reasonably well the behaviour observed in the experimental results for all three polarisation cases. The experimentally measured double-lobe electron density feature matches the simulation predictions

in terms of the angular separation of the lobes and their orientation with respect to the polarisation axes for both the linear and elliptical cases. The larger measured angular width of the lobes in the experiments may result from space-charge spreading of the beam as it propagates downstream towards the detector. From the discussion above, the circularly polarised case might be expected to produce an electron density ring owing to the constant rotational velocity of the electric field, as described by the analytical model shown in figure 6.14. However, the simulations show that there is in fact a slight distortion in the polarisation induced by the evolving plasma aperture, resulting in the ring-like distribution with localised maxima shown in figure 6.20c. The measurements for circularly polarised light reproduce both the small-radius central ring with local maxima (labelled 1) and the lower density $\pi/2$ out-of-phase distributions at larger radii (labelled 2) in figure 6.5c1 for electrons with energy greater than 3.5 MeV (corresponding to the same features in figure 6.20c1). The circular density profile for electrons with energies from 8 to 15 MeV (figure 6.20c2) is also reproduced experimentally for electron energies $\gtrsim 10$ MeV (figure 6.5c4).

This investigation of the sensitivity of the electron distribution to the drive laser polarisation, numerically and experimentally, reveals that the underpinning physics giving rise to the lobe features, in ultra intense laser interactions with thin targets, arises from diffraction. This is further confirmed by simulations discussed in the next section in which the relativistic plasma aperture diameter is varied, thus controlling transmitted light diffraction.

6.2.5 Focal spot size effect

Unlike the numerical investigations described in previous sections which were performed using the same laser focal spot size as in experiments, i.e. $3 \mu\text{m}$ (FWHM), here the effect of the laser focal spot size on the electron spatial distribution response is presented. The laser intensity of all the simulations

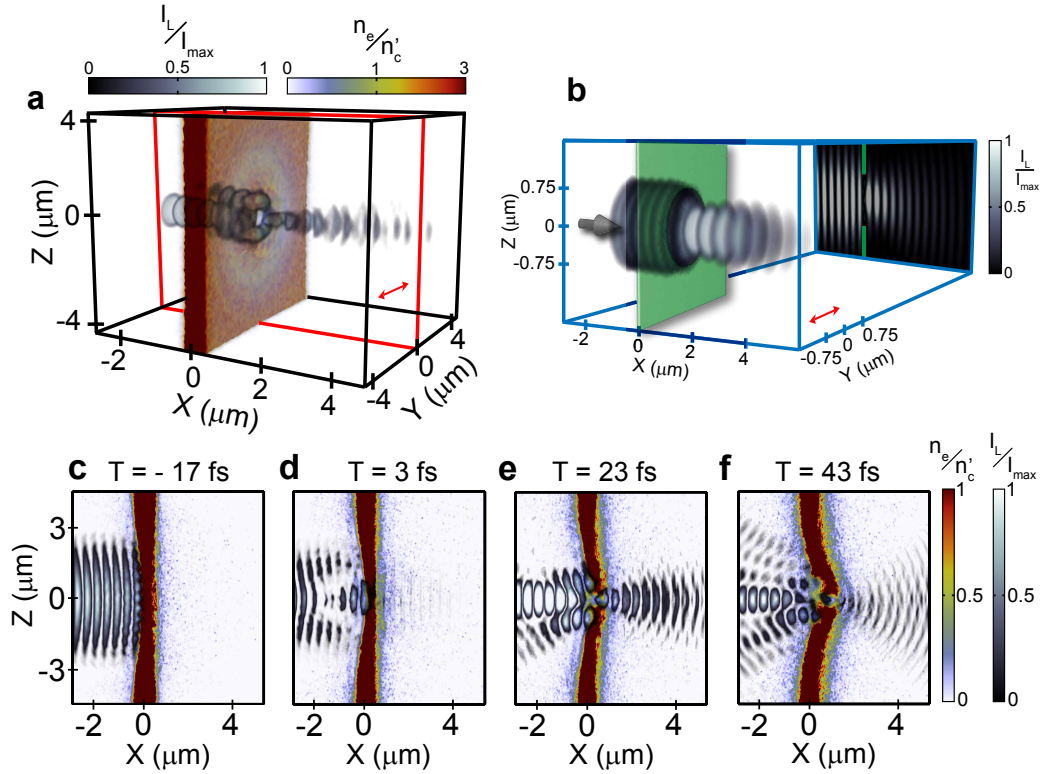


Figure 6.21: **a**, 3D PIC simulations of laser diffraction and plasma electron density produced by the relativistic plasma aperture showing the laser intensity, I_L , pattern overlapped with the plasma electron density normalised to n'_c , at 23 fs ($T = 0$ corresponds to the time at which the laser peak interacts with the plasma), for a linearly polarised laser. **b**, 3D simulation profile showing the spatial-intensity variation of the diffraction pattern of a linearly polarised laser pulse with $1.5 \mu\text{m}$ (FWHM) diameter passing through a predefined $1.5 \mu\text{m}$ -diameter aperture, and 2D cut-away in $Y=0$ plane. **c-f**, 2D (X - Z) cut-away in $Y=0$ plane (red plane highlighted in **b**) showing the electron density overlaid with the laser intensity at four example time steps from the same simulation as **a**.

presented in this section is the same as previous simulations, i.e. $6 \times 10^{20} \text{ Wcm}^{-2}$, adjusting the laser energy accordingly, for a linearly polarised light.

Electron spatial profile - $1.5 \mu\text{m}$ focal spot size

A full 3D PIC simulation reveals that as in the previous case, with a $3 \mu\text{m}$ focal spot size, a relativistic plasma aperture is generated with a diameter similar to the FWHM of the laser spot, in this case $1.5 \mu\text{m}$. However, because the ratio of the aperture radius to the laser wavelength is lower (and close in value), the diffraction pattern generated presents a single lobe when the laser propagates through the relativistic aperture. This is illustrated in figure 6.21a at a time $T =$

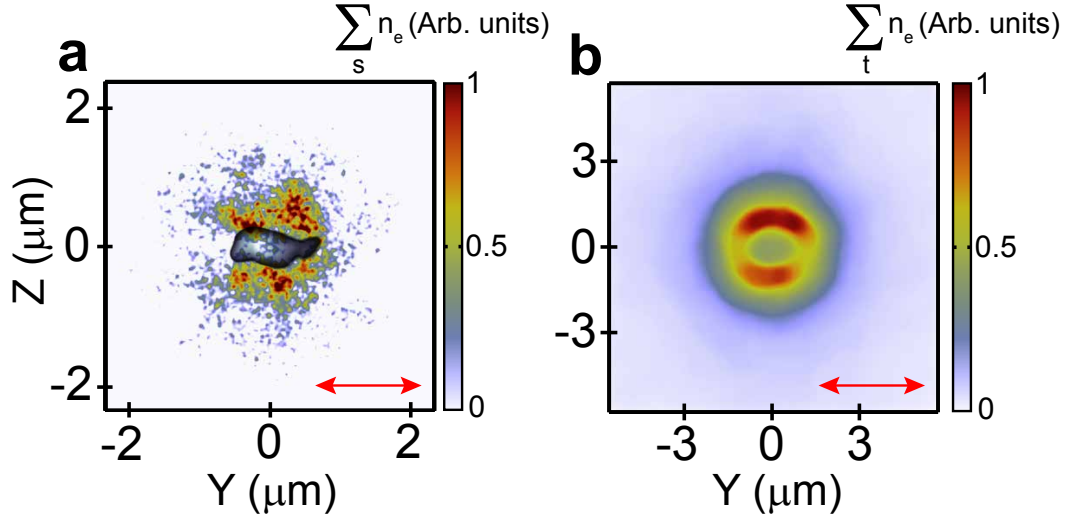


Figure 6.22: 3D EPOCH simulation result with laser focal spot size equal to $1.5 \mu\text{m}$ (FWHM). **a**, Laser intensity and electron density in the Y-Z plane (both spatially integrated over $X=0.7-1.5 \mu\text{m}$). **b**, Time-integrated electron density in the Y-Z plane at $X=6 \mu\text{m}$.

23 fs. It is worth mentioning that this diffraction structure is very similar to the circular polarisation case, with a $3 \mu\text{m}$ focal spot size (figure 6.13). However, in this case the diffraction pattern does not rotate, as expected from the previous investigation, and does not present any helical-like structure. Additionally, a study of the evolution of the relativistic aperture is presented in figure 6.21c-f. It shows that after the target becomes relativistically transparent, as illustrated in figure 6.21e and 6.21f, the laser exhibits a diffraction pattern characterised by a single lobe along the laser axis, which is maintained during the laser interaction. Besides this, this single lobe is stretched in the polarisation direction (Y-axis), which ponderomotively expels electrons preferentially in both directions in Z, producing a double-lobe electron density distribution, as shown in figure 6.22a. Unlike the $3 \mu\text{m}$ case, because a single laser node is produced on axis, no secondary low-density axial electron population is produced. A temporal integration of the electron density in the Y-Z plane, perpendicular to the laser polarisation, confirms that this double lobe in the electron structure predominates during the laser interaction, as shown in figure 6.22b.

An idealised 3D simulation with a predefined static aperture, i.e. without

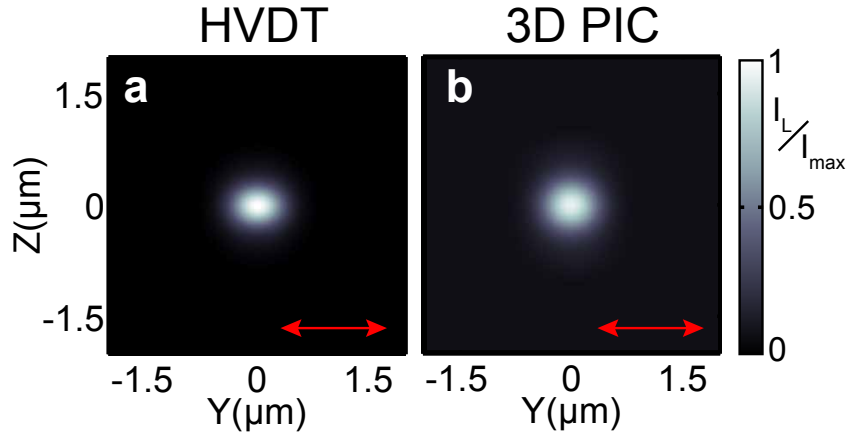


Figure 6.23: **a**, Laser intensity diffraction pattern at $X = 0.4 \mu\text{m}$, from the target, using the HVDT model assuming an aperture with $1.5 \mu\text{m}$ in diameter. **b**, Laser intensity diffraction pattern at $X = 0.4 \mu\text{m}$, from the target, using 3D PIC simulation with a laser focal spot size equal to $1.5 \mu\text{m}$ and a predefined aperture with $1.5 \mu\text{m}$ in diameter.

plasma evolution, has been also performed, in this case to confirm if this laser structure after the relativistic plasma aperture actually corresponds to a defined diffraction pattern. In this simulation an incident laser pulse with a focal spot size of $1.5 \mu\text{m}$ (FWHM) propagates through a fixed circular aperture of $1.5 \mu\text{m}$ in diameter, as is shown in figure 6.21b. This simulation produces a single lobe in the laser diffraction pattern just as the full 3D PIC simulation (figure 6.21a). Figure 6.23b shows a 2D Y-Z plane of the laser intensity at $X = 0.4 \mu\text{m}$ which presents this particular diffraction pattern in the form of a single lobe centred on the laser axis. The analysis, using the HVDT model with the same laser and aperture parameters, describes completely the simulation result, as shown in figure 6.23a.

Electron spatial profile - $6 \mu\text{m}$ focal spot size

The relativistic plasma aperture diameter is defined by the condition $n_e < n'_c$ and increases with peak laser intensity for a given target material and thickness. With increasing laser focal spot size to $6 \mu\text{m}$ (FWHM) the transparency condition is satisfied in a bigger area. Because of this, the number of maxima in the near-field diffraction in the vicinity of the electrons increases, as shown in figure 6.24a for a

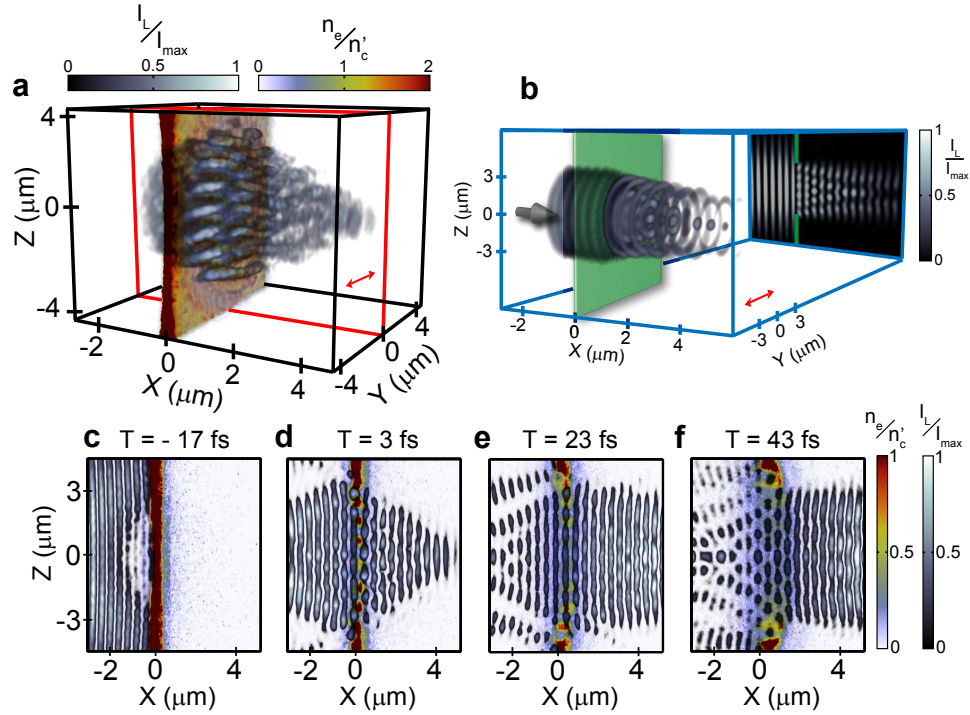


Figure 6.24: **a**, 3D PIC simulations of laser diffraction and plasma electron density produced by the relativistic plasma aperture showing the laser intensity, I_L , pattern overlapped with the plasma electron density normalised to n'_c , at 3 fs ($T = 0$ corresponds to the time at which the laser peak interacts with the plasma), for a linearly polarised laser. **b**, 3D simulation profile showing the spatial-intensity variation of the diffraction pattern of a linearly polarised laser pulse with $6 \mu\text{m}$ (FWHM) diameter passing through a predefined $6 \mu\text{m}$ -diameter aperture, and 2D cut-away in $Y=0$ plane. **c-f**, 2D (X - Z) cut-away in $Y=0$ plane (red plane highlighted in **b**) showing the electron density overlaid with the laser intensity at four example time steps from the same simulation as **a**.

full 3D PIC simulation at a time $T = 3$ fs. This is reproduced by a 3D simulation using an predefined circular aperture (no plasma) with a $6 \mu\text{m}$ diameter, as presented in figure 6.24b.

In fact, the diffraction pattern evolves in time, and more fringes are produced due to the relativistic plasma aperture size increasing with laser intensity (the condition $n_e < n'_c$ is met over a larger area of the laser focal spot), as shown in figure 6.24c-f. Additional 3D simulations with predefined circular apertures of various diameters, as well as analysis using the HVDT model have been performed in order to explain and interpret the effect of the aperture size on intense laser light diffraction and resulting electron dynamics.

In figure 6.25a-c, HVDT modelling results are compared with results from 3D

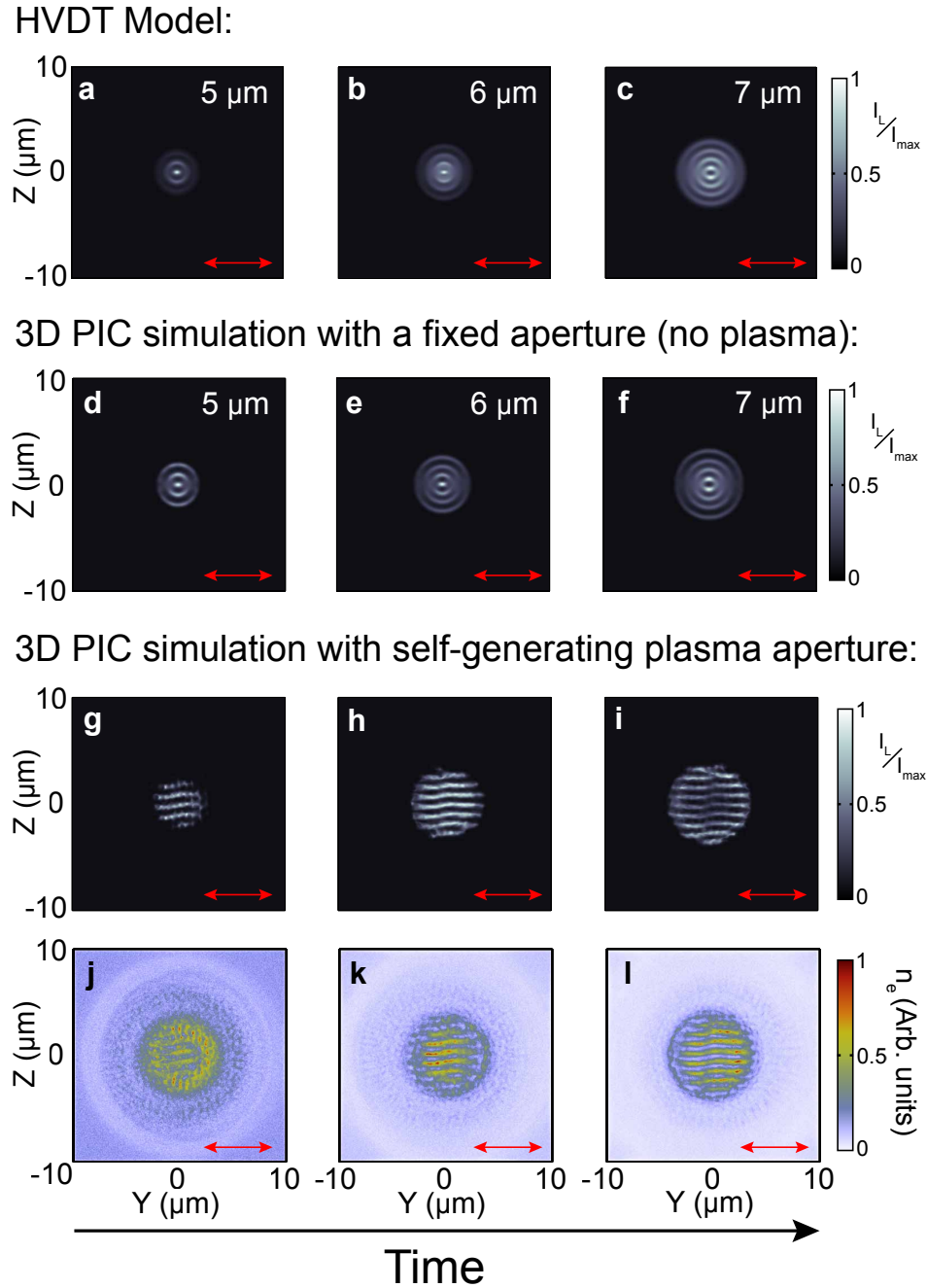


Figure 6.25: Analytical model and PIC simulation of the near-field diffraction pattern through a $6 \mu\text{m}$ -diameter aperture and linearly polarised laser. **a-c**, Calculated diffraction patterns at $X = 0.4 \mu\text{m}$ for a fixed circular aperture of: **a**, $5 \mu\text{m}$; **b**, $6 \mu\text{m}$; and **c**, $7 \mu\text{m}$ in diameter, respectively, using the HVDT theory. The laser wavelength is 800 nm , it is linearly polarised along the Y -axis and the focal spot size (FWHM) is equal to the aperture diameter; **d-f**, Same, obtained from 3D PIC simulations with a fixed ideal circular aperture (i.e. with no plasma); **g-i**, Three temporal snapshots of the spatial-intensity distribution of the diffraction pattern, at $X = 0.4 \mu\text{m}$, produced with a full 3D PIC simulation investigating the effect of the self-generated relativistic plasma aperture (corresponding to the same simulation presented in figure 6.24 and 6.26). **g** corresponds to a time step just after the target becomes relativistically transparent; **j-l**, Temporal evolution of the electron density distribution at the same time and position as in **g-i**.

PIC simulations without plasma (figure 6.25d-f), for fixed circular apertures with diameters equal to 5, 6 and 7 μm . The laser is linearly polarised, along the Y-axis. These results, which are in good agreement, show that the number of fringes in the expected diffraction pattern increases as a function of aperture size. The laser intensity and electron density profiles from the 3D PIC simulation result of the effects of the relativistic plasma aperture reported in figure 6.26a, are shown in figure 6.25g-i and figure 6.25j-l, respectively, at three different snapshots in time. As these temporal snapshots show, the diffraction pattern evolves over time, resulting in more fringes. This occurs because the plasma aperture size increases as the intensity of the laser pulse rising edge increases, as already mentioned. The number of stripes observed in the PIC simulation at any given time agrees with that expected from diffraction through an aperture of the corresponding size.

In a linearly polarised laser, an anisotropy in the plasma electron response to the laser field, induced by the polarisation, affects the diffraction pattern. With increasing laser intensity, plasma electrons are swept from side to side along the axis of polarisation by the laser electric field [31, 144], giving rise to the striped pattern observed in figure 6.26b. This sweeping motion causes the diffraction lobes to become more striped than circular, as shown in figure 6.25g-i. The striped electron diffraction lobe distribution in turn then modifies the laser distributions to form stripes (figure 6.25g-i) interweaved with the electron stripes (figure 6.25j-l and figure 6.26a).

It is also noted that the stripes, shown in figure 6.25 and in figure 6.26, are observed to slightly curve from left to right. Examining the polarisation of the laser before and after RIT at different points along the X-axis, it is found that the linearly polarised beam becomes slightly elliptically polarised when transmitted through the relativistic plasma aperture during RIT, similar to the effect reported in reference [145]. The work in that reference shows, via 3D PIC simulations, that anisotropy induced in the heating of the target electrons by a linearly polarised

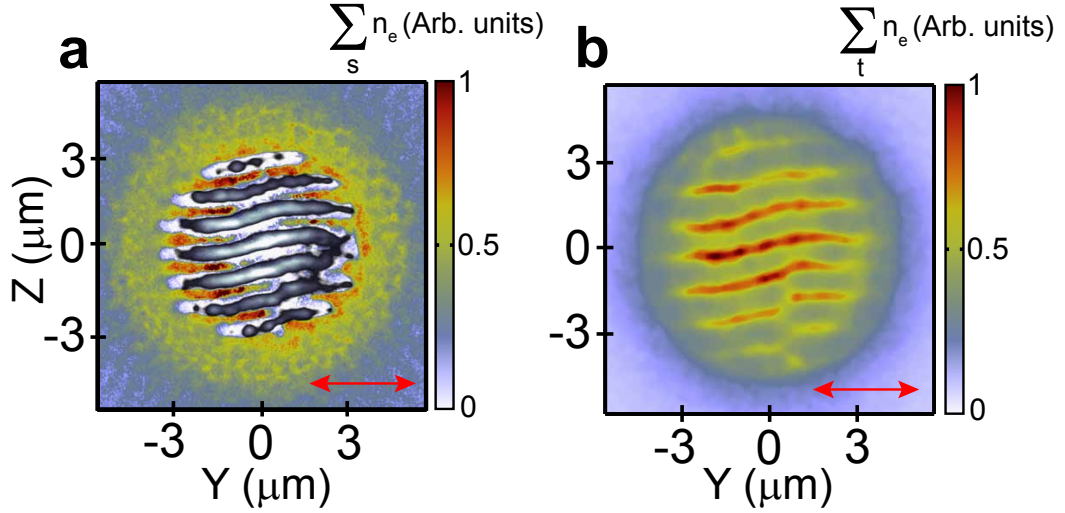


Figure 6.26: 3D EPOCH simulation result with laser focal spot size equal to $6 \mu\text{m}$ (FWHM). **a**, Laser intensity and electron density in the Y-Z plane (both spatially integrated over $X=0.7-1.5 \mu\text{m}$). **b**, Time-integrated electron density in the Y-Z plane at $X=6 \mu\text{m}$.

pulse can cause transient effects such as a difference in phase velocities in the two orthogonal directions, which can induce a degree of ellipticity in the polarisation. The PIC simulations presented in this section show that the degree of ellipticity of the laser polarisation changes with time. A measured average value of 4% deviation from linear polarisation (i.e. $e = \sqrt{(\mathbf{E}_y^2 - \mathbf{E}_z^2)/\mathbf{E}_y^2} = 0.96$; where $e = 0$ [$\mathbf{E}_z = \mathbf{E}_y$] corresponds to circular polarisation and $e = 1$ [$\mathbf{E}_z = 0$] corresponds to linear polarisation) accounts for the slight rotation effect observed in the stripes.

A similar investigation has been conducted using circularly polarised laser pulses. Good agreement is also observed as shown by the example PIC simulation results for circularly polarised laser light with focal spot size equal to $6 \mu\text{m}$, with (figure 6.27b) and without (figure 6.27a) plasma. The HVDT model assumes linear polarisation and hence is not applied in this circular polarisation case. However, the PIC simulation without plasma (figure 6.27a) shows the expected diffraction pattern (as verified by the agreement between the HVDT modelling (figure 6.25a-c) and with the 3D PIC simulation without plasma (figure 6.25d-f) for the linearly polarised case). Thus the spatial intensity profiles are shown to be attributed to diffraction via a self-generated, evolving relativistic plasma

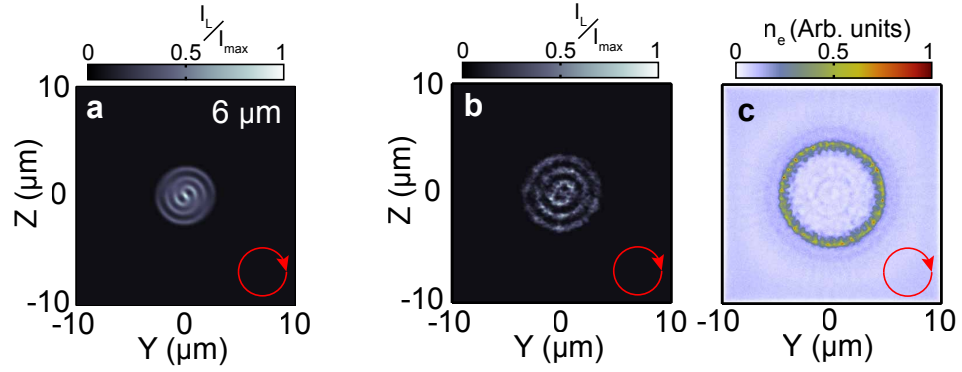


Figure 6.27: PIC simulation result of the near-field diffraction pattern through a $6 \mu\text{m}$ -diameter aperture and circularly polarised laser. **a**, 3D PIC simulation for an ideal $6 \mu\text{m}$ diameter fixed circular aperture (no plasma), at $X = 0.4 \mu\text{m}$; **b**, Same, from a full 3D PIC simulation of the plasma aperture with the same parameters as 6.25g-i, but with circular polarisation; **c**, Electron density profile at the same time and position as **b**.

aperture.

6.3 Conclusions

In this chapter a novel conception, and its demonstration by 3D PIC simulations, to explain and understand experimental results concerning the interaction of an ultra-intense laser pulse with thin solid targets is described and analysed in detail. The basis of this conception is that intense laser light can self-generate and be strongly diffracted by a relativistic plasma aperture produced in thin foils undergoing RIT. The plasma electrons collectively respond to the resulting near-field diffraction pattern. This is a new phenomenon in relativistic plasma optics and collective electron motion control. It is shown that, through suitable choice of laser drive parameters such as polarisation, the spatial-intensity distribution of a high-current beam of relativistic electrons can be controlled and modified as well as rotating structures induced. It is also shown that the angular rotational frequency can be varied by changing the degree of ellipticity in the laser polarisation. Additionally, it is shown that increasing and decreasing the laser focal spot size particular diffraction pattern are generated and mapped into the electron distribution. Although, at present their experimental

verification is not achievable, using higher energy pulses from new facilities proposed (as ELI [146, 147]) and employing diffraction limited focusing optics by elliptical plasma mirrors [148] testing these predictions will be experimentally feasible. Nevertheless, these results provide an important understanding of the underpinning physics of the electron response in relativistic plasmas.

This investigation opens up a new direction in spatial and temporal control of electron motion in dense plasmas and, by extension, the evolution of the high fields used to accelerate charged particles and produce high-energy radiation. In thin foils, including those undergoing RIT, the electric fields produced by displacement of electrons accelerate ions to multi-MeV energies. The spatial-intensity profile of the plasma electron beam is effectively mapped into the spatial-intensity profile of the ion beam. Thus, the techniques we introduce to change the profile of the plasma electron beam can also enable the spatial-intensity distribution of the ion beam to be controlled, the details of which are described and discussed in the next research chapter.

Besides this, there are a number of other ways in which one could envisage utilising the plasma aperture concept in particle and radiation source development. The simulations included in this chapter suggest that it could potentially be used to induce orbital angular momentum states at high laser intensity. A rotating diffraction lobe structure produced using circularly polarised light results in a helical structure of intense laser light with an optical vortex at the centre, on the beam axis. Such a structure can be used to trap plasma electrons on axis. A small population of electrons is observed to be trapped between the double-lobe structure by the inward directed ponderomotive forces in the linear polarisation simulations, as shown in figure 6.10. This effect could be optimised and used to induce an axial current filament in plasmas of relatively high density, with potential application to positron and ion acceleration (as positively charged particles are attracted towards the electron filament). It has

been shown in a recent theoretical and numerical study of wakefield acceleration in lower-density targets that helical light beams can be used to drive positron acceleration [149]. In addition, because the plasma electron motion is induced in phase with the drive laser, and this in turn can be synchronised to a second laser pulse (for example by splitting the laser beam), it may be possible to apply this scheme to enhance electron scattering processes in ultra-intense laser fields (such as nonlinear Compton or Thomson scattering). Thus, the results of this chapter are not only of fundamental importance to the understanding of relativistic transparency and the interpretation of experimental results involving transparency in ultra-thin foils, but could also profoundly affect the development of laser-driven particle and radiation sources involving dense laser-irradiated targets.

Chapter 7

Collective proton response to the onset of relativistic induced transparency in ultra-thin foils

In the previous chapter it was demonstrated that a relativistic plasma aperture produced in an ultra-thin foil at the focus of intense laser radiation can induce diffraction of transmitted light, enabling polarisation-based and focal spot size control of the collective motion of plasma electrons. In this chapter it is shown that in ultra-thin foils undergoing transparency these particular electron dynamics are mapped into the beam of protons accelerated via strong charge-separation-induced electrostatic fields. It is demonstrated experimentally and numerically (via 3D PIC simulations) that the degree of ellipticity of the laser polarisation defines the spatial-intensity distribution of the proton beam profile and can thereby be used to control it. Further, numerical investigations indicate that the laser focal spot size plays a key role in defining the spatial-intensity distribution of the beam of accelerated protons. This research is also focused on the influence of the collective electron dynamics on the protons, which are sourced from hydrocarbon layers, originating on the front and rear surfaces of the targets.

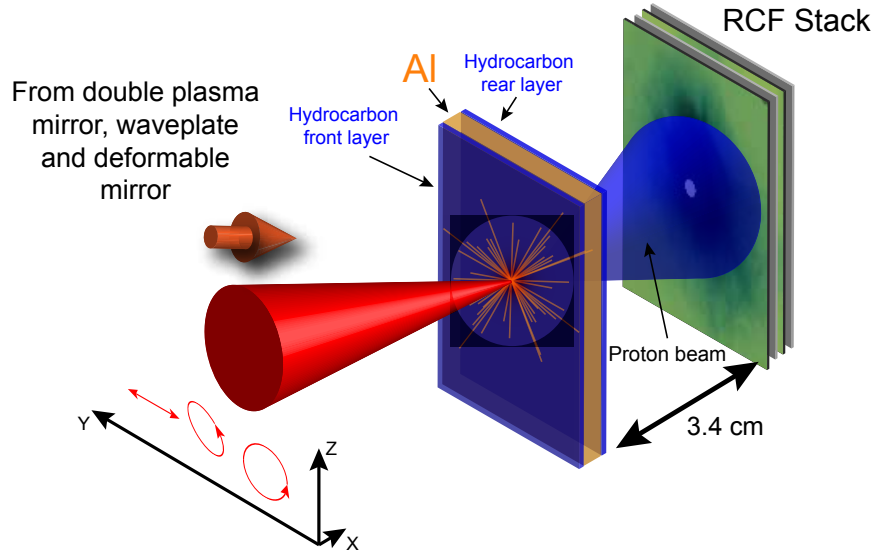


Figure 7.1: Schematic configuration of the experimental set-up used to measure the proton spatial-intensity distribution for various target thicknesses and laser polarisations.

7.1 Experimental Results

The experimental set-up used to measure the 2D spatial-intensity distribution of the beam of accelerated protons is the same set-up as employed in the previous chapter 6.1 (see also Chapter 4 [sections 4.2 and 4.2.2] for more details). However, in this case, a stacked dosimetry film (RCF) with mylar layers (for energy filtering), was used. Figure 7.1 illustrates a schematic of this configuration.

7.1.1 Target foils for which transparency does not occur

The main investigation of this chapter is focused on the collective proton dynamics in thin targets undergoing relativistic transparency. In order to compare, and have a reference, in this section an experimental investigation of the polarisation influence for defining particular spatial-intensity distributions of the accelerated proton beams is presented. In this investigation thick targets are considered, i.e. those that remain opaque during the laser interaction.

In figure 7.2a-c representative measurements of proton distributions, for given energies, in $l = 800$ nm (linear polarisation - Y axis), $l = 40$ nm (linear

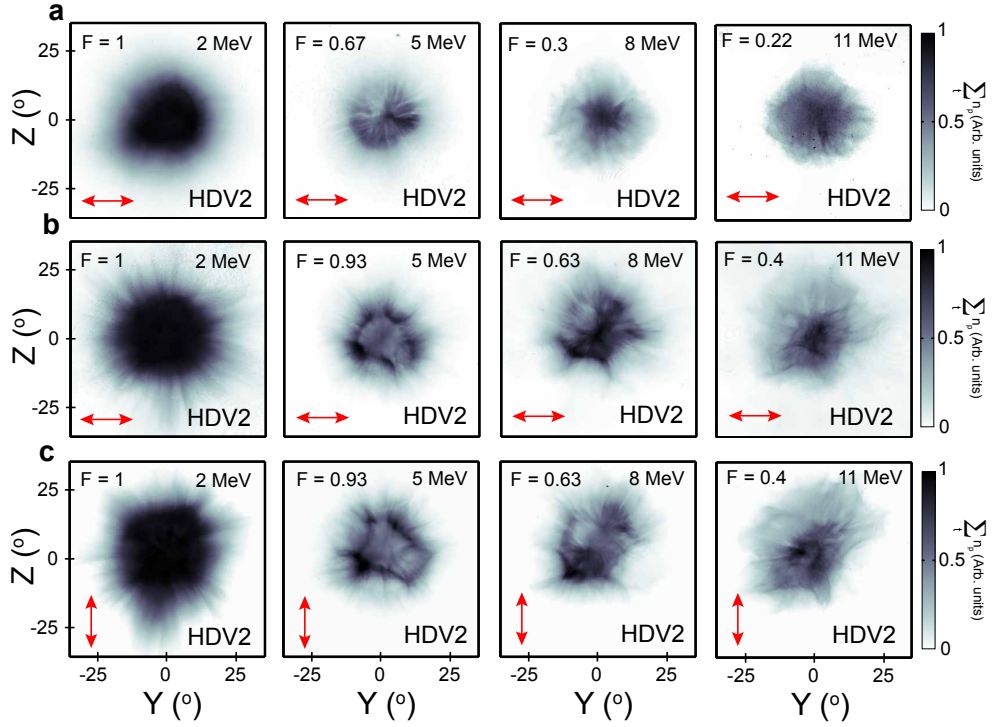


Figure 7.2: Experiment results for the proton density distribution. **a**, Proton density as measured using RCF films (HD-V2) for $l = 800$ nm and protons with energy, from left to right, greater than: 2 MeV, 5 MeV, 8 MeV and 11 MeV; all for linear polarisation (Y-axis). **b**, Same for $l = 40$ nm and linear polarisation (Y-axis). **c**, Same for $l = 40$ nm and linear polarisation (Z-axis). The grey-scale maps are scaled by the stated value F to clearly show the features of interest at each energy slice.

polarisation - Y axis) and $l = 40$ nm (s-polarisation) targets are displayed, respectively. The proton beams produced in these thick targets exhibit a divergence decreases with increasing energy, typical of proton beams produced by the TNSA mechanism [150]. Note that for $l = 40$ nm (linear polarisation - Y axis) and $l = 40$ nm (linear polarisation - Z axis) targets, the protons do not show as clear response as electrons to the laser polarisation, at this particular target thickness, as described in figures 6.2e-h and 6.2i-l.

In figure 7.3a-c representative measurements of proton distributions, for given energies, for $l = 40$ nm targets using elliptical (for $\Delta\theta = \pi/4$ and $\Delta\theta = -\pi/4$) and circular laser polarisation are shown respectively. As in the aforementioned linear polarisation case, for both elliptical cases investigated, protons exhibit a weak response to the emerging electric fields, which it is not as strong as the

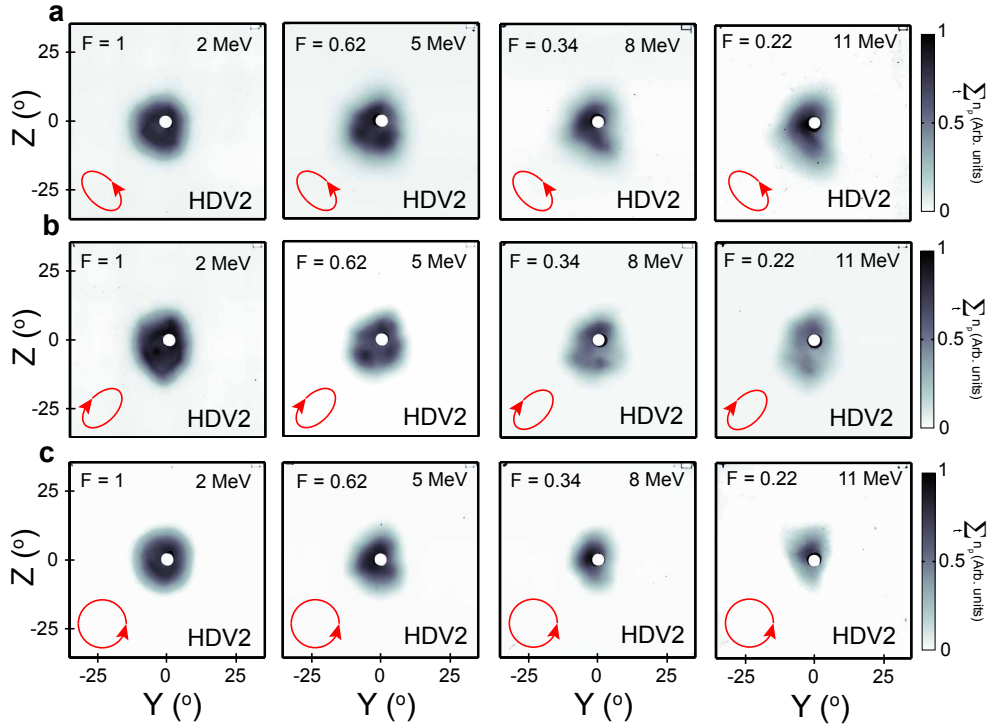


Figure 7.3: Experiment results for the proton density distribution for elliptical and circular polarisation. **a**, Proton density as measured using RCF films (HD-V2) for $l = 40$ nm and protons with energy, from left to right, greater than: 2 MeV, 5 MeV, 8 MeV and 11 MeV; all for elliptical polarisation ($\Delta\theta = \pi/4$). **b**, Same for elliptical polarisation ($\Delta\theta = -\pi/4$). **c**, Same for circular polarisation. The grey-scale maps are scaled by the stated value F to clearly show the features of interest at each energy slice.

electron response to the laser field at these same conditions, as displayed in figure 6.3. On the other hand, using a circularly polarised pulse, for $l = 40$ nm target, protons present a circular spatial-intensity distribution with the highest proton density located in the beam centre at all sampled energies, as seen in figure 7.3c. This particular structure is the same as displayed in the electron response for the same target thickness and laser polarisation, as shown in figure 6.4.

7.1.2 Ultra-thin target foils undergoing transparency

As in the previous chapter, the most interesting experiment results on the collective proton dynamics are found when there is a significant degree of relativistic induced transparency, which is the case for $l = 10$ nm targets. At this target thickness RIT occurs at the proper time in the interaction which

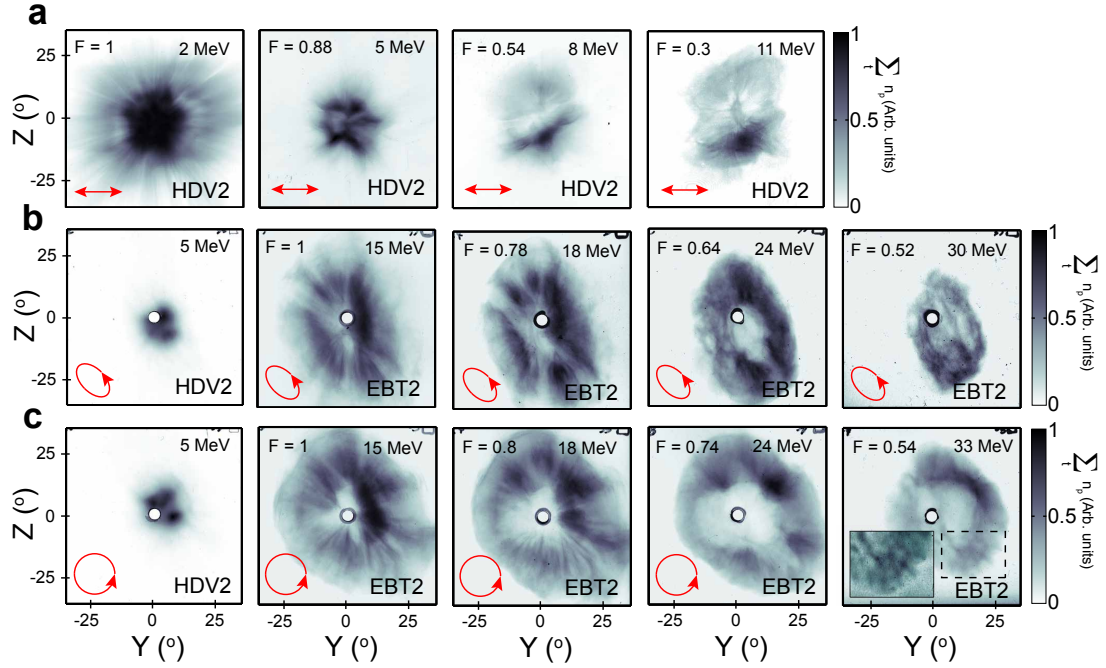


Figure 7.4: Representative experiment results of the proton beam density distributions at stated energies, as measured at $X=3.4$ cm and with $l = 10$ nm target, for **a** linear, **b** elliptical and **c** circularly polarised laser light, respectively. The densities are scaled by the stated value F to enable the features of interest at each energy slice to be clearly seen. The inset in **c** is further scaled to show the bubble-like density modulations present in the proton beam.

maximise the collective proton response. Figure 7.4a-c shows representative measurements of the spatial-intensity distribution of the beam of protons, for this target thickness, at given example proton energies, for linear, elliptical and circular polarisation, respectively. These example results clearly demonstrate that the proton beam profile is strongly affected by the laser polarisation and that the profiles change with proton energy.

The low energy (~ 5 MeV) distribution in the linear polarisation case exhibits a modulated annular distribution, with radial spoke-like features and higher densities along the Z -axis, at $Z = \pm 7^\circ$, i.e. at either side of the laser polarisation axis. At higher energies (~ 8 MeV and ~ 11 MeV) a spatially larger and lower density distribution is measured, exhibiting a double stripe or lobe pattern. The double-lobe pattern is not exactly perpendicular to the laser polarisation direction, as expected from the corresponding electron density distribution in figure 6.5a. They present a slight tilt in angle with respect to the polarization axis.

This rotation may result from changes to the laser polarisation occurring during RIT. As discussed by Stark *et al.* [145], a degree of ellipticity can be induced in a linearly polarised beam due to anisotropy in the heating of the target electrons. This could explain the slight rotation in the proton double-lobe structure, but the absence of this rotation in the electron pattern, suggest that in this case, proton structures could also be modified by self-magnetic fields generated within the target. In the elliptical and circular polarisation cases, the ring profiles produced at low energy are very small, whereas at higher energies (> 15 MeV) much larger annular density profiles with clear radial modulations are produced. The ring profiles are circular and elliptical for the respective polarisations and in the latter case the major axis is aligned at an angle similar to the major axis of polarisation in the Y-Z plane. For elliptical polarisation the proton pattern, at higher energies, also present a slight rotation respect to the major axis of the laser polarisation, which also suggests that they could be affected by self-magnetic fields when propagate through the plasma. The ring radial size decreases in both polarisation cases for increasing proton energies (e.g. ~ 30 - 33 MeV, as shown in figure 7.4b,c). For circular polarisation the radial profile is replaced by bubble-like modulations, similar to those reported in reference [151] and typically attributed to a Rayleigh-Taylor-like transverse instability [31, 151]. Note that the upper proton energy detection threshold was significantly higher for the circular and elliptical polarisation cases due to the use of a higher sensitivity dosimetry film in the high energy section (> 15 MeV) of the detector stack, i.e. EBT-2 instead of HD-V2.

These results demonstrate that the observed structures are produced only when relativistic transparency occurs, as shown when comparing with the measured proton distribution produced employing thicker targets discussed in the previous section (see Fig 7.2 and 7.3). Additionally, these particular proton structures are in good agreement with the experimental results of

electron dynamics described in figure 6.5 in the previous chapter. A detailed numerical study to describe and understand the generation and evolution of the collective dynamics of proton structures for this specific target thickness and laser polarisations is presented in the following sections.

7.2 Collective proton response to relativistic transparency and diffraction in thin foils

In this section the role of laser polarisation in defining and controlling the proton beam profile is investigated. As described in the previous section, the most interesting proton dynamics are found for the thinnest targets investigated, when the target becomes relativistically transparent during the laser interaction. Due to this, the present investigation is focused on these targets which correspond to $l = 10$ nm. A first detailed study, via 3D PIC simulations, including a hydrocarbon layer on both surfaces of the target, as the source of protons, is presented. Additionally, the influence of laser polarisation in the final proton beams structure when only a single hydrocarbon layer is included, is also investigated in detail. This study reveals that the collective proton dynamics depends upon whether a hydrocarbon layer is present on only one or both surfaces. A final numerical investigation indicates that the laser focal spot size additionally plays a key role in determining the spatial-intensity distribution of the accelerated protons. The characteristics and parameters of the 3D PIC simulations are the same as those included in the previous Chapter 6 (section 6.2).

Before the results of these investigations are presented it is worth describing the method used to obtain the electrostatic fields structures including throughout this section.

Electrostatic field calculation

One of the main parameters studied in this chapter is the electrostatic field, obtained using 3D PIC simulations, generated by charge separation between electrons and ions during the laser interaction. In these simulations electric fields appear indistinctly from the laser field and from the electrostatic field produced by charged particle separation. Because of this, the study of the dynamics and evolution of each individually without the undesired contribution of the other is not feasible. In order to obtain the pure electrostatic field generated by the charged particles in simulations, Poisson's equation for the scalar potential, $\nabla^2 V = \frac{\rho}{\epsilon_0}$, has been employed. The electrostatic field is calculated as $\mathbf{E} = -\nabla V$ (Gauss' law, eq. (2.1)). Poisson's equation is a second order, elliptic type, partial differential equation whose structure in 3-dimensional Cartesian coordinates, an using Dirichlet boundary conditions (where the solution V is known on the boundary), is:

$$\nabla^2 V = \nabla \cdot (\nabla V) = V_{xx} + V_{yy} + V_{zz} = \frac{\rho(x, y, z)}{\epsilon_0} \quad (7.1)$$

Due to the complexity of solving Poisson's equation analytically in 3-dimensions, a numerical (iterative) method has been used instead. In order to solve this equation numerically it is necessary first to replace the second order partial derivatives with second-order finite difference approximations on a grid structure, taking the form:

$$\frac{V_{i-1,j,k} - 2V_{i,j,k} + V_{i+1,j,k}}{\Delta x^2} + \frac{V_{i,j-1,k} - 2V_{i,j,k} + V_{i,j+1,k}}{\Delta y^2} + \frac{V_{i,j,k-1} - 2V_{i,j,k} + V_{i,j,k+1}}{\Delta z^2} = \frac{\rho_{i,j,k}}{\epsilon_0} \quad (7.2)$$

where i, j and k are the node numbers of each grid dimension, respectively, and $(i, j, k) \geq (2, 2, 2)$. Δx , Δy and Δz correspond to the spatial resolution in each

dimension.

Although there are several numerical methods to solve this type of equation, such as Gauss-Seidel [152] or Successive over-relaxation [153], the Jacobi method [154] was selected as it presents an easy implementation and provides an acceptable convergence after a reasonable number of iterations, for this particular study. Therefore, the Jacobi iterative solution of the equation (7.2) takes the form:

$$V_{i,j,k}^{(n+1)} = a_x \left(V_{i-1,j,k}^{(n)} + V_{i+1,j,k}^{(n)} \right) + a_y \left(V_{i,j-1,k}^{(n)} + V_{i,j+1,k}^{(n)} \right) + \quad (7.3)$$

$$a_z \left(V_{i,j,k-1}^{(n)} + V_{i,j,k+1}^{(n)} \right) = a_f \frac{\rho_{i,j,k}}{\epsilon_0}$$

where n is the iteration index and:

$$\begin{cases} a_x = \frac{\Delta y^2 \Delta z^2}{2(\Delta x^2 + \Delta y^2 + \Delta z^2)} \\ a_y = \frac{\Delta z^2 \Delta x^2}{2(\Delta x^2 + \Delta y^2 + \Delta z^2)} \\ a_z = \frac{\Delta x^2 \Delta y^2}{2(\Delta x^2 + \Delta y^2 + \Delta z^2)} \\ a_f = \frac{\Delta x^2 \Delta y^2 \Delta z^2}{2(\Delta x^2 + \Delta y^2 + \Delta z^2)} \end{cases} \quad (7.4)$$

This method is used for the generation of all the electrostatic fields described in this chapter.

7.2.1 Hydrocarbon layer on both target surfaces

Figure 7.5a shows a schematic representation of the laser-target interaction employed for the simulations of the present proton dynamics investigation. In these simulations, hydrocarbon layers are included on both surfaces of an aluminium target foil, which is representative of the target conditions in experiments (protons are sourced from hydrogen-containing layers which build up on the target surfaces at the vacuum chamber pressures typically used (\sim

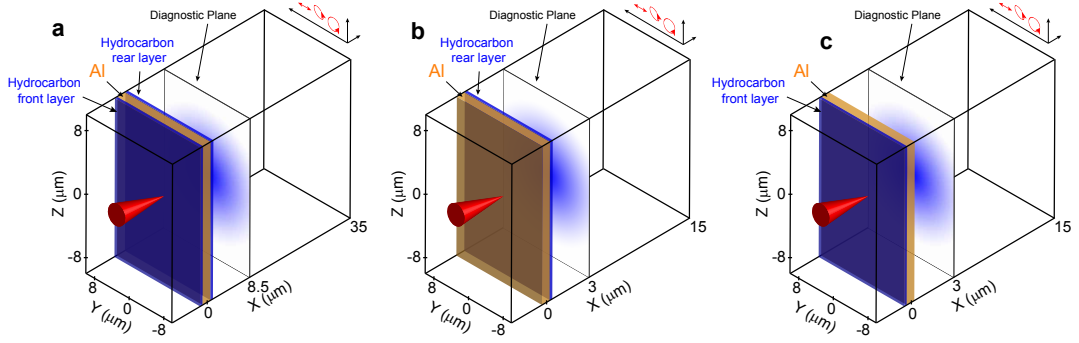


Figure 7.5: **a**, Illustration of the target and diagnostic plane employed in the 3D PIC simulations to investigate the proton spatial-intensity distribution for various laser polarisations including hydrocarbon layers in both target surfaces. The total simulation time is of 380 fs and $40 \mu\text{m} \times 20 \mu\text{m} \times 20 \mu\text{m}$ box size. **b**, Same as **a** but including a hydrocarbon layer only in the rear surface of the target. The total simulation time is of 160 fs and $20 \mu\text{m} \times 20 \mu\text{m} \times 20 \mu\text{m}$ box size. **c**, Same as **b** but including a hydrocarbon layer only in the front surface of the target.

10^{-5} mbar)). The total simulation time is of 380 fs to enable the propagation of the proton beam at longer distances. In order to investigate the origin of the two measured distinctive proton populations, i.e. the protons accelerated from the target front surface, as driven forward by laser radiation pressure (i.e. RPA), and the rear surface, as prominently produced by TNSA, have also been separately tracked. Both of these mechanisms are effective before the target becomes relativistically transparent, as described previously in Chapter 5.

Linear polarisation

Firstly, a linearly polarised laser pulse, along the Y-axis, is considered. The spatial-intensity profiles, and energy-resolved, of the proton populations, at $X=8.5 \mu\text{m}$, sourced at the front and rear sides of the target are seen to be distinctly different, as observed when comparing the combined plot in figure 7.6a and the separate plots in figure 7.6b,d and 7.6c,e. In figure 7.7a the integrated beam profile in the Y-Z plane (comprising protons sourced in both layers) at three example energy ranges extracted from the simulation box, integrated over $X = 8\text{-}35 \mu\text{m}$, is displayed.

In order to have a relative comparison with experimental results, figure 7.7b shows a projection of the same beam profiles to a distance of $X = 3.4 \text{ cm}$ (i.e. the

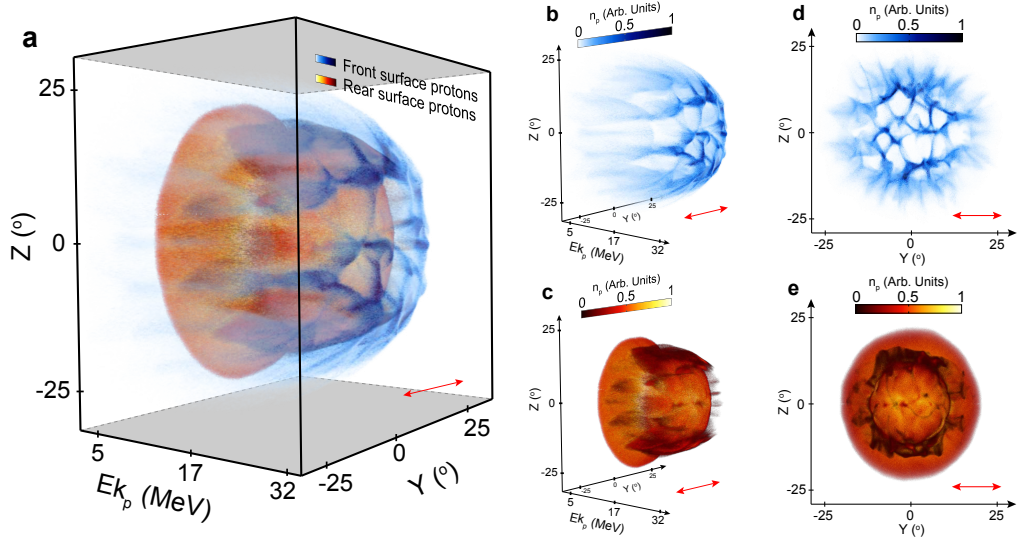


Figure 7.6: 3D-PIC simulation results showing the proton spatial-density distribution for a laser pulse of linear polarisation. **a**, Energy-resolved 2D proton density distribution at $X=8.5 \mu\text{m}$. The blue and red distributions correspond to protons originating at the target front and rear surfaces, respectively. The same two distributions are plotted separately in **b** and **c** for clarity. **d** and **e**, front view of **b** and **c**, respectively.

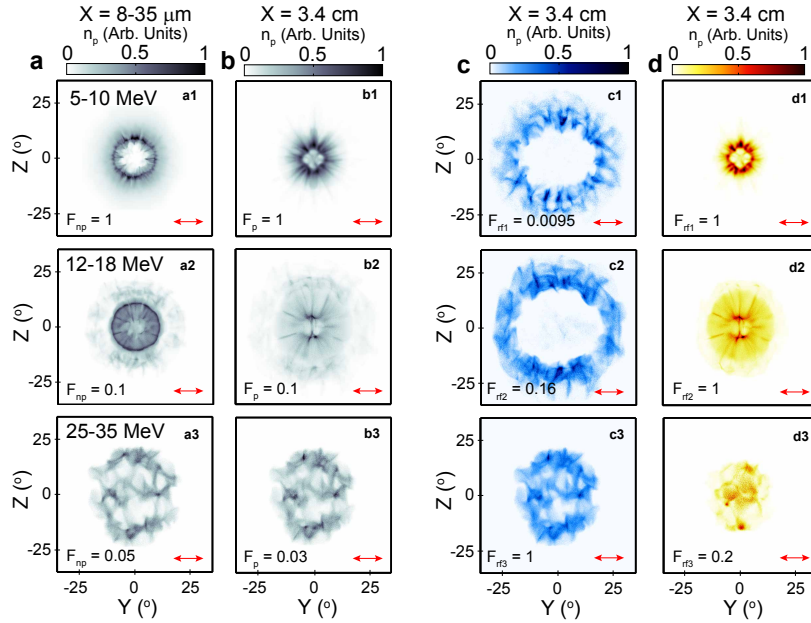


Figure 7.7: 3D-PIC simulation results showing the proton spatial-density distribution for linear polarisation along the Y-axis. **a**, Combined (front and rear sourced) proton spatial density distributions over the range $X=8-35 \mu\text{m}$, integrated over the stated energy ranges. **b**, Projection of the combined proton density to $X=3.4 \text{ cm}$ (for comparison with experiment). **c**, Proton distribution projected to $X=3.4 \text{ cm}$ arising only from protons sourced at the front side of the target foil. **d**, Proton distribution projected to $X=3.4 \text{ cm}$ arising only from protons sourced at the rear side of the target foil. The densities are scaled by the corresponding stated value F to enable the features of interest at each energy slice to be clearly observed and check from which surface are the predominant proton structures measured in the detector, in **c** and **d**. The results are sampled at $T = 303 \text{ fs}$ ($T = 0$ corresponds to the time at which the laser peak interacts with the plasma).

position at which the experimental measurements are made, presented in figure 7.1). This was calculated by using the proton momentum components in $[X,Y,Z]$ extracted from the simulation results. At relatively low energies (5-10 MeV), two distinct features in the proton beam are observed; a high-density, ring-like proton distribution with radial (spoke) features and a spatially larger, lower density halo feature. The ring has a radius of $\sim 9^\circ$ at $X=8-35 \mu\text{m}$, decreasing to $\sim 6^\circ$ at $X = 3.4 \text{ cm}$, indicating a small reduction in divergence. The density is higher at the top and bottom parts of the ring (i.e. along the Z -axis). The shape, size and radial distribution are all in good agreement with the experiment results shown in figure 7.4a. In the simulation result projected to $X = 3.4 \text{ cm}$ at the higher energy range, 12-18 MeV (figure 7.7b2), the ring collapses to form a double lobe distribution in Z , which has similar characteristics (spatially larger, lower density and doubled-lobed) to the experiment results at $\sim 11 \text{ MeV}$ in figure 7.4a. At even higher energies, $> 18 \text{ MeV}$, the beam is dominated by a distribution with modulated stripes. This pattern also presents a slight rotation respect to the laser polarisation direction in a similar way to the experimental results shown in figure 7.4a. A measurement at this high energy was not achieved in the linear polarisation case due to the use of lower sensitivity dosimetry film (HD-V2). Figure 7.7c and d shows the proton projection sourced at both the target front and rear surfaces, respectively. These two figures are directly comparable with the integrated (front and rear) results in figure 7.7b. In order to enable the features of interest, at each energy slice, to be clearly observed and check from which surface the predominant proton structures arise, the proton density in each figure is scaled by the maximum density for each given energy range. This scale is stated by the corresponding F value. From figure 7.7c and d it is clear that the low energy proton distributions, from 5 to 10 and 12 to 18 MeV, are produced by protons accelerated from the target rear surface. On the other hand, the high energy striped distribution and low density halo feature are clearly produced by

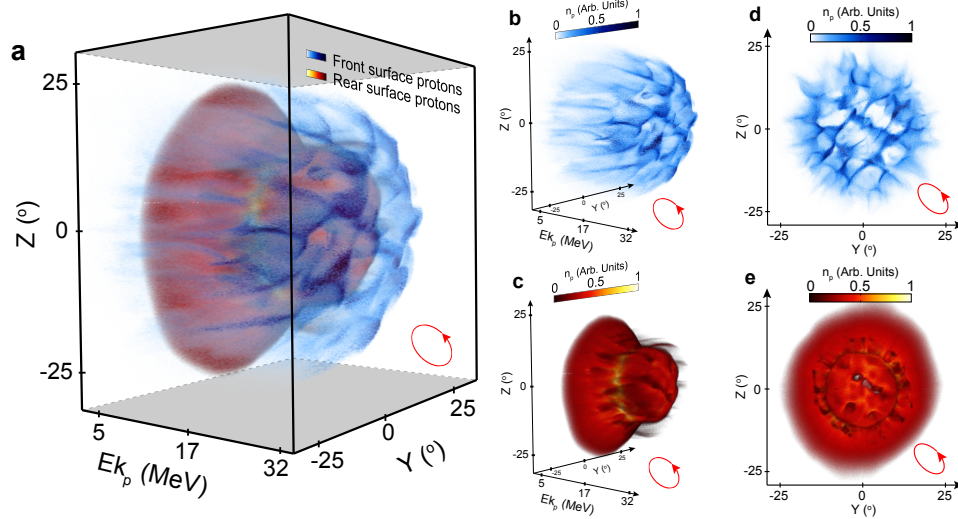


Figure 7.8: 3D-PIC simulation results showing the proton spatial-density distribution for elliptical polarisation. **a**, Energy-resolved 2D proton density distribution at $X=8.5 \mu\text{m}$. The blue and red distributions correspond to protons originating at the target front and rear surfaces, respectively. The same two distributions are plotted separately in **b** and **c** for clarity. **d** and **e**, front view of **b** and **c**, respectively.

protons accelerated from the target front surface.

Elliptical polarisation

The equivalent simulation results for elliptical polarisation are shown in figure 7.8 and figure 7.9. These results exhibit similar proton beam profiles to the linear case, but rotated by 45° , as defined by the orientation of the major axis of the ellipse (in the Y - Z plane). They also present clear differences between the spatial-intensity profiles of the proton populations sourced at the front and rear sides of the target. Both the high density ring at low proton energies and the striped population at higher energies are again produced. The increase in beam size between 5 and 18 MeV is very similar to that observed experimentally in figure 7.4b and in both cases a large ring is produced at ~ 18 MeV, which is orientated at an angle close to the major axis of the ellipse and has radial modulations. From the corresponding scale factor F in the projected proton distributions, described in figure 7.9c and d, it is also evident that the low energy proton distributions, from 5 to 10 and 12 to 18 MeV, are produced by protons accelerated from the

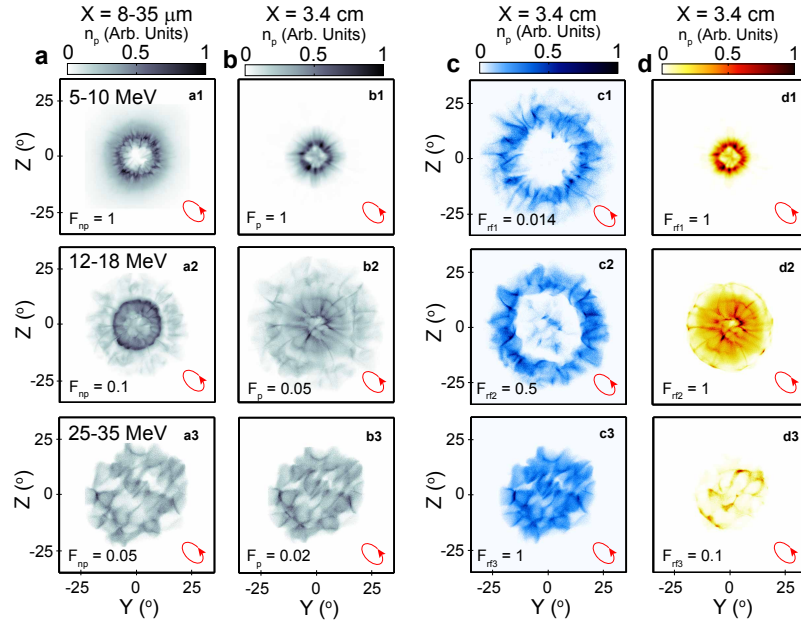


Figure 7.9: 3D-PIC simulation results showing the proton spatial-density distribution for elliptical polarisation. **a**, Combined (front and rear sourced) proton spatial density distributions over the range $X=8-35 \mu\text{m}$, integrated over the stated energy ranges. **b**, Projection of the combined proton density to $X=3.4 \text{ cm}$ (for comparison with experiment). **c**, Proton distribution projected to $X=3.4 \text{ cm}$ arising only from protons sourced at the front side of the target foil. **d**, Proton distribution projected to $X=3.4 \text{ cm}$ arising only from protons sourced at the rear side of the target foil. The densities are scaled by the corresponding stated value F to enable the features of interest at each energy slice to be clearly observed and check from which surface are the predominant proton structures measured in the detector, in **c** and **d**. The results are sampled at $T = 303 \text{ fs}$ ($T = 0$ corresponds to the time at which the laser peak interacts with the plasma).

target rear surface. High energy striped distribution are produced instead by protons sourced from the target front surface.

Circular polarisation

Finally, the proton spatial-intensity structures sourced from the front and rear surface of the target when employing circularly polarised laser pulse are shown in figures 7.10 and 7.11. These results also exhibit a small, high density ring at low energies of 5-10 MeV and a spatially larger, lower density ring at 14-20 MeV, both showing strong radial features and circular symmetry. This overall change in beam profile is similar to that experimentally measured, shown in figure 7.4c. With increasing energy (in the range of 22-35 MeV), the beam is modulated with bubble-like structures, which are circular and distinctly different from the stripe

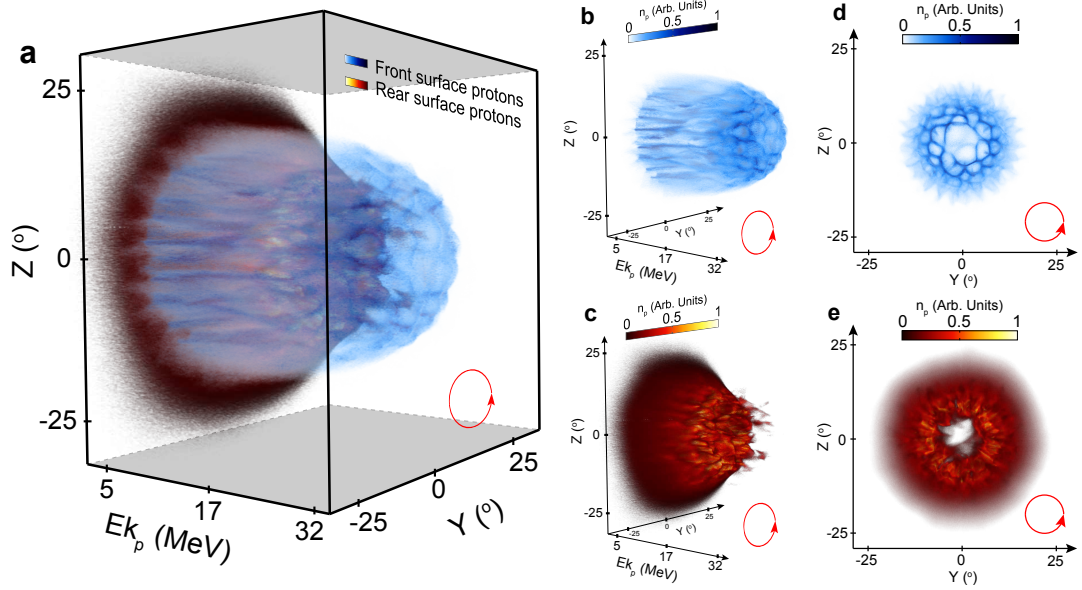


Figure 7.10: 3D-PIC simulation results showing the proton spatial-density distribution for circular polarisation. **a**, Energy-resolved 2D proton density distribution at $X=8.5 \mu\text{m}$. The blue and red distributions correspond to protons originating at the target front and rear surfaces, respectively. The same two distributions are plotted separately in **b** and **c** for clarity. **d** and **e**, front view of **b** and **c**, respectively.

patterns formed in the linear and elliptical polarisation cases. Similar bubble-like structures are also observed experimentally, as shown in the inset of figure 7.4c. These particular structures are described by Sgattoni *et al.* [31] as arising due to a laser-driven Rayleigh-Taylor instability (discussed in more detail in the next section). Compared to the linear and elliptical polarisation cases, a larger percentage of the protons produced by circularly polarised light originate from the target front (as observed in figure 7.11c and d comparing the corresponding scale factor F). This is consistent with previous results indicating more efficient RPA when using circular polarisation to reduce electron heating and thereby target expansion [67].

In conclusion, in all three polarisation cases characteristic features in the experimentally measured proton beam, including changes to the beam size and spatial-intensity structure as a function of energy, are observed in the simulation results projected to the plane used in the experiment (3.4 cm). The simulations further show that the proton beam distributions are strongly correlated to the

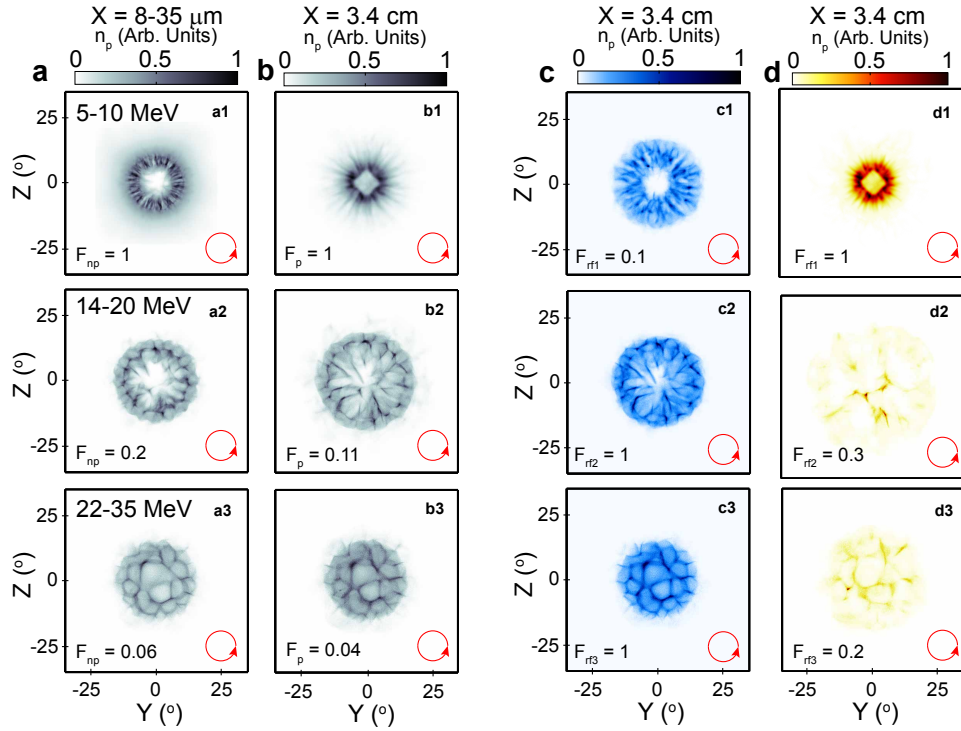


Figure 7.11: 3D-PIC simulation results showing the proton spatial-density distribution for circular polarisation. **a**, Combined (front and rear sourced) proton spatial density distributions over the range $X=8-35 \mu\text{m}$, integrated over the stated energy ranges. **b**, Projection of the combined proton density to $X=3.4 \text{ cm}$ (for comparison with experiment). **c**, Proton distribution projected to $X=3.4 \text{ cm}$ arising only from protons sourced at the front side of the target foil. **d**, Proton distribution projected to $X=3.4 \text{ cm}$ arising only from protons sourced at the rear side of the target foil. The densities are scaled by the corresponding stated value F to enable the features of interest at each energy slice to be clearly observed and check from which surface the protons contributing to the observed structures arise, in **c** and **d**. The results are sampled at $T = 303 \text{ fs}$ ($T = 0$ corresponds to the time at which the laser peak interacts with the plasma).

collective response of the plasma electrons to the near-field diffraction pattern of the intense laser light transmitted through the self-formed relativistic plasma aperture. The electron beam profile is mapped into the proton beam via modulation of the electrostatic acceleration field, as will be discussed in detail in the next section.

7.2.2 Hydrocarbon layer only on target rear

The previous results clearly demonstrate that different proton beam structures are produced in the populations accelerated from the front and rear sides of the target foil. To examine this aspect further, separate simulations with a single

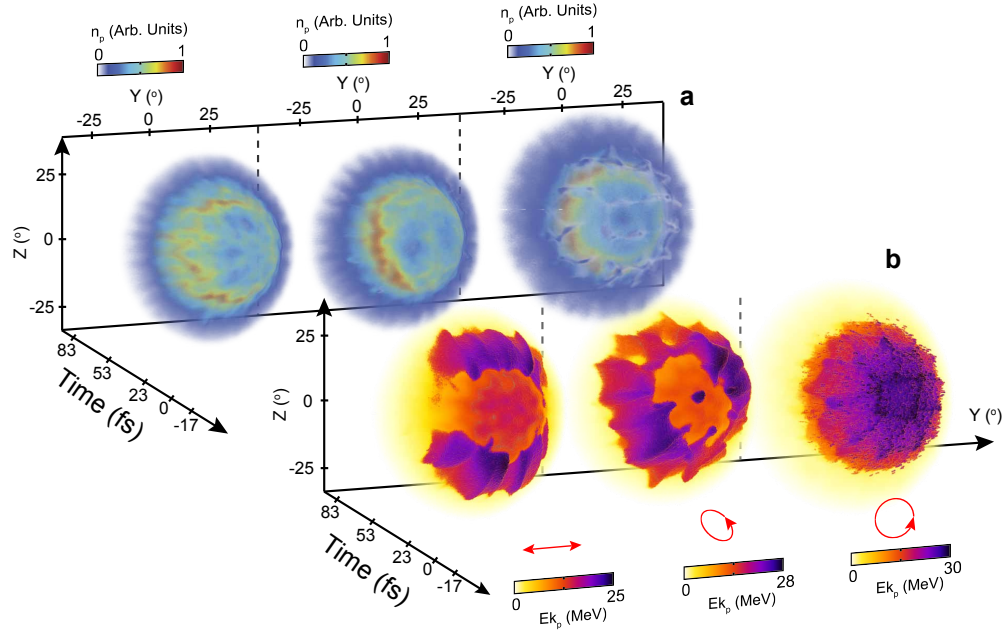


Figure 7.12: Comparison of spatial-density and kinetic energy distributions for only target rear surface accelerated protons. Time-resolved **a**, spatial-density distribution and **b**, kinetic energy distribution, at $X=3 \mu\text{m}$, for all three polarisation cases (as labelled with the red arrows).

hydrocarbon layer on either the target front or rear side, for all three polarisation cases have been performed. In this section, the investigation considering a hydrocarbon layer only on the rear surface of the target is presented. A schematic illustration of this configuration is shown in figure 7.5b.

The resulting proton density and kinetic energy distributions in the Y - Z plane, at $X=3 \mu\text{m}$, as a function of time are shown in figure 7.12. The total simulation time is of 160 fs. These simulation results show that protons accelerated from the target rear form a ring distribution in density. A close examination shows that the density at different points around the ring varies with polarisation. Importantly, it is clear that in the case of linear and elliptical polarisation the highest total proton densities and energies are produced perpendicular to the polarisation axis (or the major axis of polarisation in the latter case). With circularly polarised light the highest proton energies are observed in a radially modulated pattern within the ring. This modulation is produced by the protons closest to the rear surface of the target when they are accelerated and propagated through the remainder of

the hydrocarbon layer.

7.2.3 Hydrocarbon layer only on target front

Continuing with the investigation of the proton spatial-intensity structures, separate simulations with a single hydrocarbon layer placed at the front surface of the target have been performed. A schematic illustration of this configuration is shown in figure 7.5c. The resulting proton density and kinetic energy distributions in the Y-Z plane, at $X=3 \mu\text{m}$, as a function of time, are shown in figure 7.13. As in the previous case the total simulation time is of 160 fs. In this case the proton distribution accelerated from the front surface layer is heavily modulated in density. They present a striped pattern in the linear and elliptical polarisation cases along the laser polarisation axis in a similar way to that discussed in the previous section, with hydrocarbon layers included on both surfaces of the target. However, in this case the number of stripes is slightly higher. This is a result of the target becoming relativistically transparent earlier, and over a larger transverse area around the laser focal spot. On the other hand, the proton distribution is strongly modulated structure in the form of a bubble-like pattern in the circular polarisation case. Comparing this structure for circular polarisation with the corresponding structure when protons are only sourced at the target rear (figure 7.12a), shows that in both cases protons are subjected to instabilities. However, protons sourced at the front surface of the target clearly exhibit more significant instabilities. A more detailed study of these proton instabilities produced with circularly polarised light is presented in the next section.

Additionally, the proton energy distributions show evidence of the same modulation structures as the proton density for each laser polarisation, although the energy is more uniformly distributed about the proton beam front compared to the equivalent rear-surface case. These simulations results show that the highest energy protons are sourced at the front surface of the target, consistent

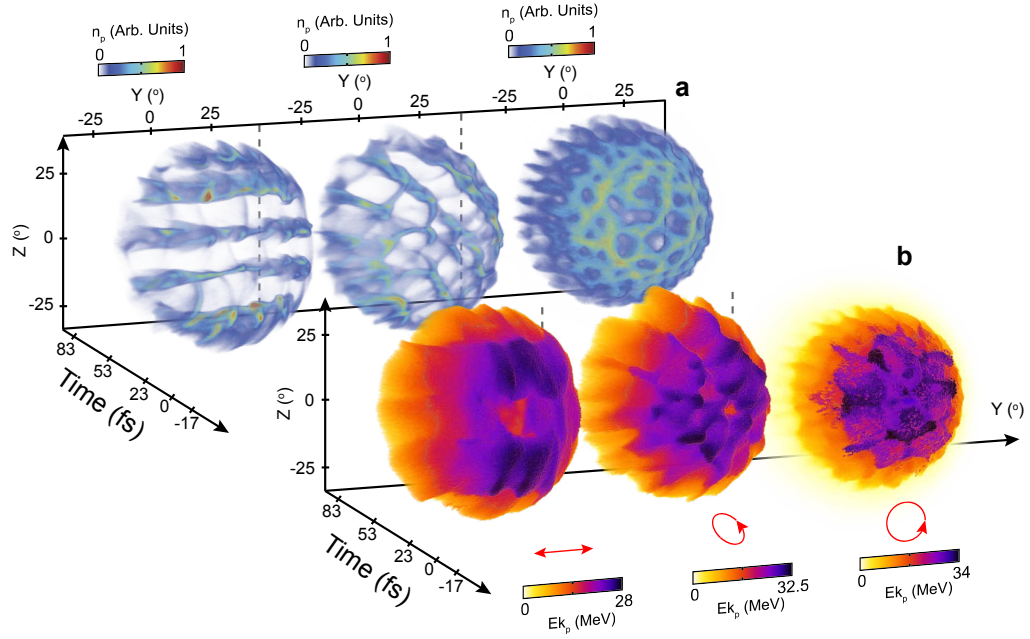


Figure 7.13: Comparison of spatial-density and kinetic energy distributions for only target front surface accelerated protons. Time-resolved **a**, spatial-density distribution and **b**, kinetic energy distribution, at $X=3 \mu\text{m}$, for all three polarisation cases (as labelled with the red arrows).

with the higher proton energies expected from the RPA mechanism, compared to rear-surface TNSA protons, for the laser pulse and target parameters investigated.

So far, the influence of the laser polarisation in defining particular proton spatial-intensity structures for the cases with hydrocarbon layers on either or both surfaces of the target have been investigated. In the following section a detailed study and discussion of the physics of the generation of these structures for each case is presented.

7.2.4 Comparing the dynamics of protons sourced at each surface of the target

The previous simulations and experimental results show that the individual proton beam distributions are strongly correlated to the collective response of the plasma electrons. The present investigation demonstrates that the electron beam profile is mapped into the proton beam via modulation of strong electrostatic acceleration fields originated from charge displacement. Electrons response to

the near-field diffraction pattern of the intense laser light transmitted through a self-formed relativistic plasma aperture, as described in the previous chapter 6.

In order to investigate the formation of the striped proton pattern, a linearly polarised laser, along the Y-axis, and hydrocarbon layers present on both surfaces of the target is considered. The dynamics of the two proton layers are explored by plotting the laser intensity contours, electron density, proton density and electrostatic field components in the X-Z plane at sample time steps in the interaction, before and after transparency has occurred. The results are presented in figure 7.14. Relativistic transparency occurs at $T = -5$ fs, i.e. 5 fs prior to the peak of the laser reaching the target. The temporal sequence in figure 7.14a shows compression of the target electron layer, formation of the relativistic plasma aperture and modulation of the plasma electron density (see figure 7.14a2) due to the near-field diffraction pattern of the intense laser light passing through the aperture. The longitudinal displacement of electrons arising from the transverse ponderomotive forces results in transverse modulations in the resulting longitudinal electrostatic field (see figure 7.14c3). An on-axis and two off-axis peaks in the electrostatic field are produced in the Z direction (at $Z = 0$ and $Z = \pm 1 \mu\text{m}$ in figure 7.14c3) by the transverse displacement of electrons (figure 7.14a3). These transverse field modulations seed regions of higher proton density in the Z direction (figure 7.14b3 and b4) when the proton distribution expands transversely to form a striped-like distribution downstream. The three dashed lines in figure 7.14 show how features in the laser near-field diffraction profile map into the electrostatic field components and subsequently into the beam of protons. This double hydrocarbon layer simulation reveals also that protons from the front side (in the region of the laser focus) are accelerated to higher energies than those from the rear and are driven through the sheath-accelerated rear surface population, as shown in the temporal sequence in figure 7.14b.

As indication, the maximum longitudinal electrostatic fields were found as

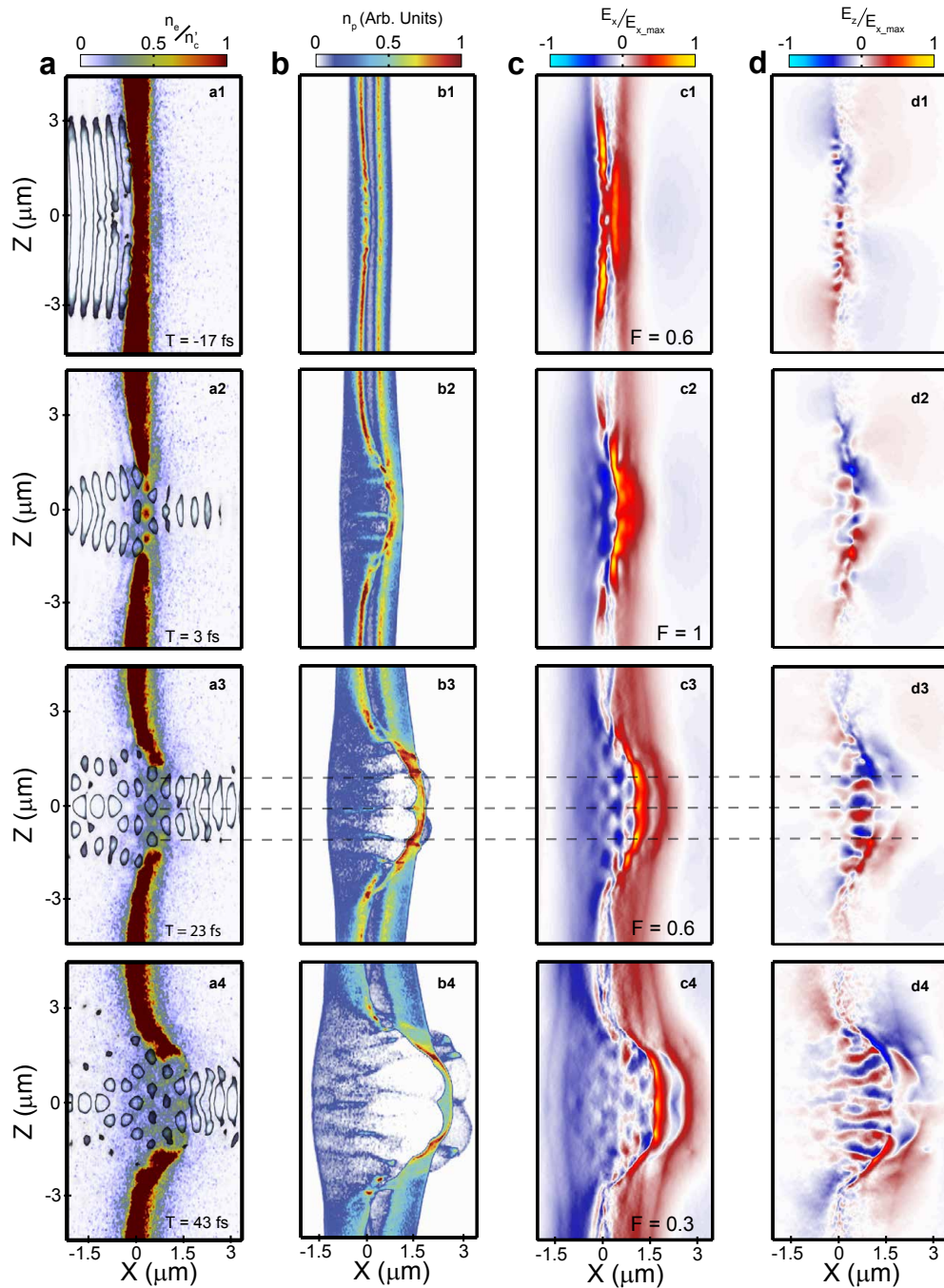


Figure 7.14: Electrostatic field and particle density evolution with protons on both surfaces. **a**, Laser intensity contours and electron density in the X-Z plane at $Y=0$ (same as figure 6.10a-d) at: **a1** $T=-17$ fs; **a2** $T=3$ fs; **a3** $T=23$ fs; and, **a4** $T=43$ fs; The onset of transparency and laser diffraction is observed. **b**, Same for proton density, showing the front surface protons being accelerated into the rear surface population. **c,d**, Same for the longitudinal and transverse electrostatic field components, resulting from charge separation, demonstrating the onset of transverse modulations. The simulation time sampled is stated in **a** and is the same in all four sub-plots. The laser is linearly polarised along the Y-axis. The dashed lines mark the positions in Z of high density electron lobes and are interleaved with maxima in the near-field laser diffraction pattern. The electrostatic field is strongly modulated at these Z positions, with maxima corresponding to regions of high electron density. The beam of accelerated protons thus forms stripes in the Z-axis.

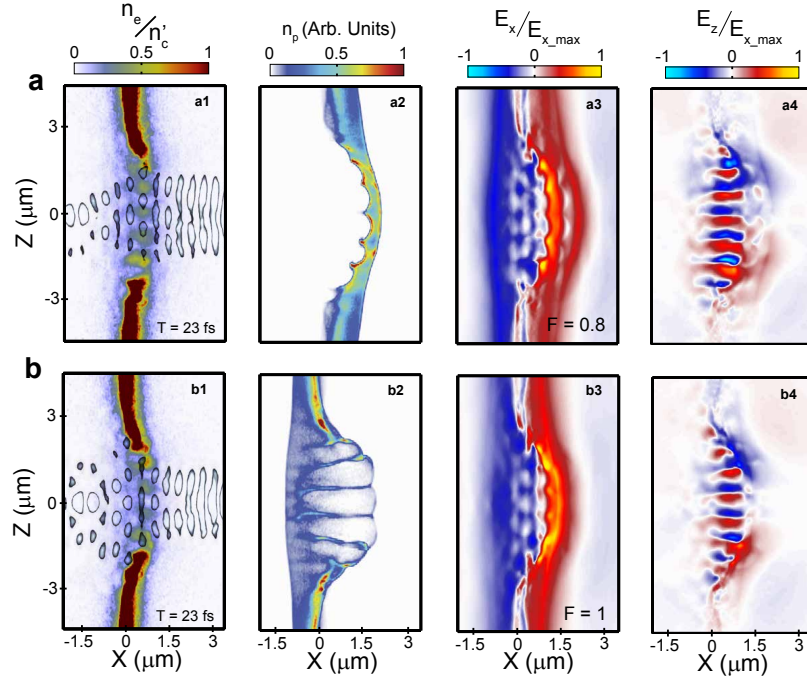


Figure 7.15: Comparison of electrostatic field and particle density distributions for front-only and rear-only proton sources and linearly polarised laser along Y-axis. **a-b**, From left to right (as in figure 7.14): laser intensity contours and electron density; proton density; and longitudinal and transverse electrostatic field components, in the X-Z plane at Y=0 for a hydrocarbon layer on the target **a**, rear surface and **b**, front surface. T=23 fs in both cases.

$E_x = 4.2 \times 10^{13} \text{ Vm}^{-1}$ for circular; $E_x = 3 \times 10^{13} \text{ Vm}^{-1}$ for linear and $E_x = 2.4 \times 10^{13} \text{ Vm}^{-1}$ for elliptical. For clarification, the electrostatic fields presented in all the figures included in this section have been normalised to these values correspondingly.

The cases for rear-surface-only and front-surface-only are presented in figure 7.15a and figure 7.15b, for which transparency occurs earlier in the interaction compared to the case with hydrocarbon layers on both surfaces of the target, at $T = -16 \text{ fs}$ and $T = -13 \text{ fs}$, respectively. A representative time step, $T = 23 \text{ fs}$, is included in these figures. Comparing these results with the case with protons on both surfaces of the target (figure 7.14), it is found that the plasma aperture formed in the target with protons on both surfaces is slightly smaller than the cases with protons on only one surface (either surface). Transparency, as mentioned, also occurs slightly later in the interaction because the effective target thickness is increased by $\sim 38\%$ by the presence of a second hydrocarbon layer,

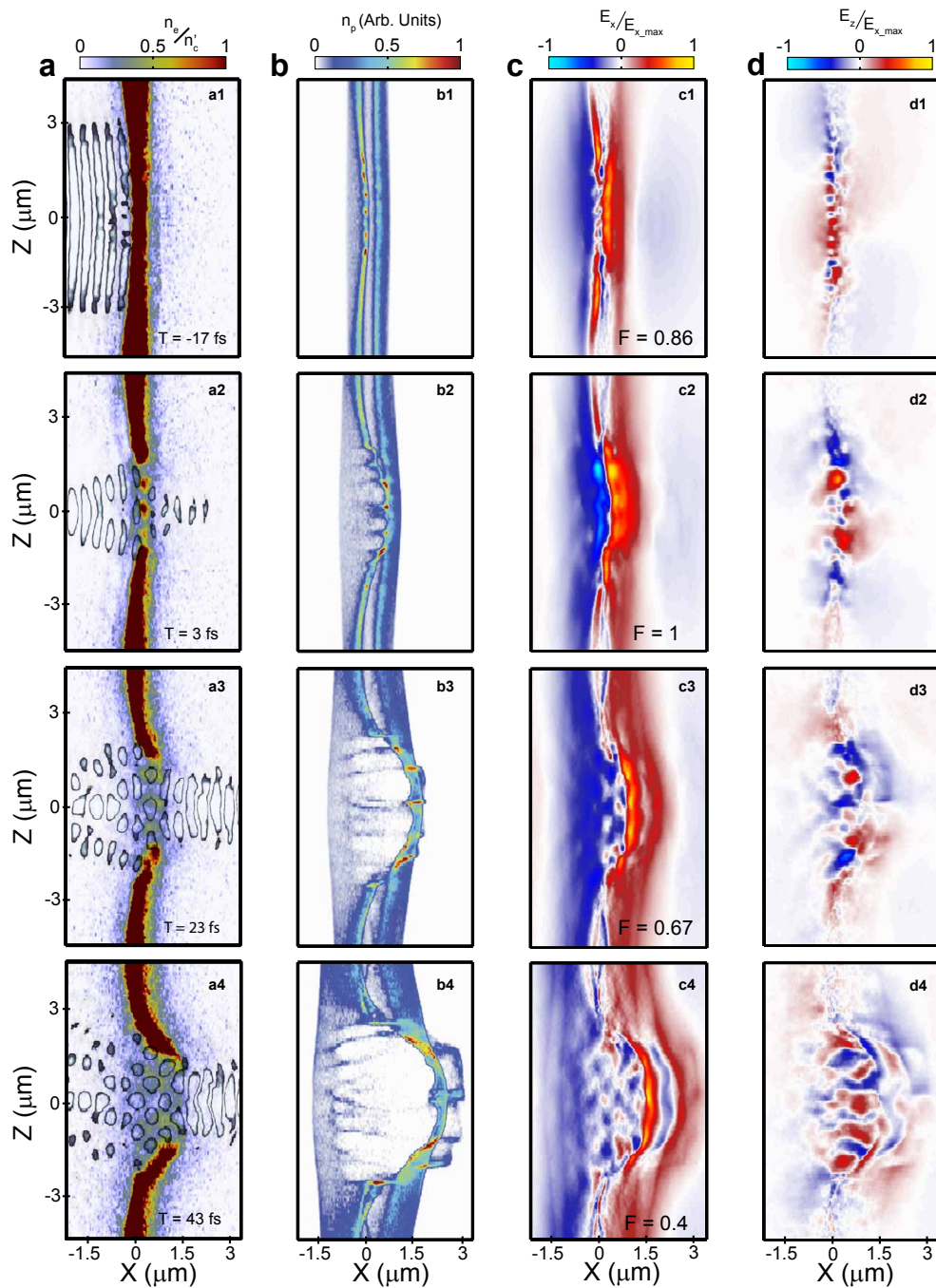


Figure 7.16: Electrostatic field and particle density evolution with protons on both surfaces. Same as figure 7.14 but for elliptically polarised laser. **a**, Laser intensity contours and electron density in a plane rotated 45° perpendicular to the major axis of the laser polarisation (same as figure 6.18a-d) at: **a1** $T=-17$ fs; **a2** $T=3$ fs; **a3** $T=23$ fs; and, **a4** $T=43$ fs; The onset of transparency and laser diffraction is observed. **b**, Same for proton density, showing the front surface protons being accelerated into the rear surface population. **c,d**, Same for the longitudinal and transverse electrostatic field components, resulting from charge separation.

The simulation time sampled is stated in **a** and is the same in all four sub-plots.

thus requiring the plasma electron population to expand further for RIT to occur. The difference in aperture size changes the number of diffraction lobes produced in the region of the highest electron density, as discussed in section 6.2.5 of the previous research chapter. Whereas two diffraction maxima (regions of intense laser light) are formed in the case with protons on both surfaces, as shown in figure 7.14a, four maxima are formed due to the larger aperture produced with protons on one surface only (either surface), as shown in figure 7.15. In this case, by electron displacement, the laser diffraction pattern generated from the larger aperture results in five peaks in the electrostatic field in the Z direction. The rear-surface-only simulation shows that the slowest protons at the back of the sheath-accelerated layer are subjected to the field modulations, resulting in the seeding of the density modulations displayed in figure 7.15a2. In the front-surface-only simulation the higher energy protons accelerated by radiation pressure propagate through the target and are strongly influenced by the transverse modulated electrostatic field. The fields in both the positive and negative X directions are modulated in the same way and hence the protons passing through this structure are deflected into a striped pattern. Figure 7.15b shows that the front surface proton contours coincide with the peaks in the modulated electrostatic field. This radiation-pressure-driven population is also more divergent than the rear surface TNSA protons (due to the transverse variation in radiation pressure).

The same numerical investigation has been performed using elliptically polarised laser pulse, for all three target conditions: (i) hydrocarbon layers on both surfaces of the target, (ii) hydrocarbon layer only on the rear surface and (iii) hydrocarbon layer only on the front surface. In all these cases the studied parameters present a very similar response as the linear polarisation scenario but rotated 45° perpendicular to the major axis of the laser polarisation and perpendicular to the formed proton stripes. The results are shown in figure 7.16 and figure 7.17, where the parameters are measured in a plane rotated at such a

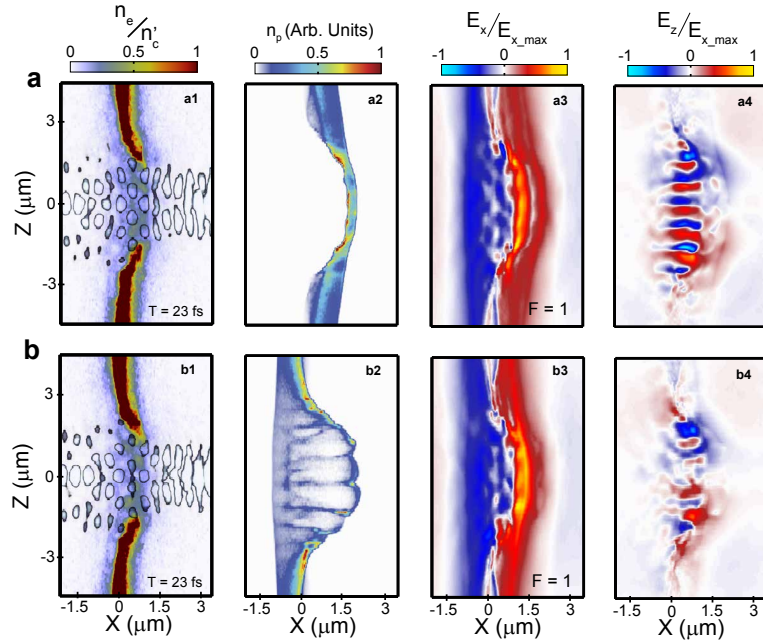


Figure 7.17: Comparison of electrostatic field and particle density distributions for front-only and rear-only proton sources with elliptically polarised laser. **a-b**, From left to right (as in figure 7.16): laser intensity contours and electron density; proton density; and longitudinal and transverse electrostatic field components, in a plane rotated 45° perpendicular to the major axis of the laser polarisation for hydrocarbon layer on the target **a**, rear surface and **b**, front surface. $T=23$ fs in both cases.

45° degree and perpendicular to the major axis of the laser polarisation. Because of this, the previous discussion using linearly polarised light is applicable for this elliptical polarisation case.

Figure 7.18 and figure 7.19 include the results of all the investigated parameters for circularly polarised light. In this case, the longitudinal electrostatic field is maximum along the laser axis for times before and during relativistic transparency. This results in the highest proton energy also being produced along the laser axis, as shown in figure 7.12b and 7.13b. Figure 7.18b and figure 7.19b2 show that the proton density from the front surface is strongly influenced by instabilities when travelling through the bulk of target in both cases. As mentioned, these proton instabilities are typically attributed to Rayleigh-Taylor process [31], between laser light and plasma electrons, which in turn modifies the proton structure. However, the protons originating at the target rear surface (i.e. TNSA protons in figure 7.19a2) are affected significantly less by

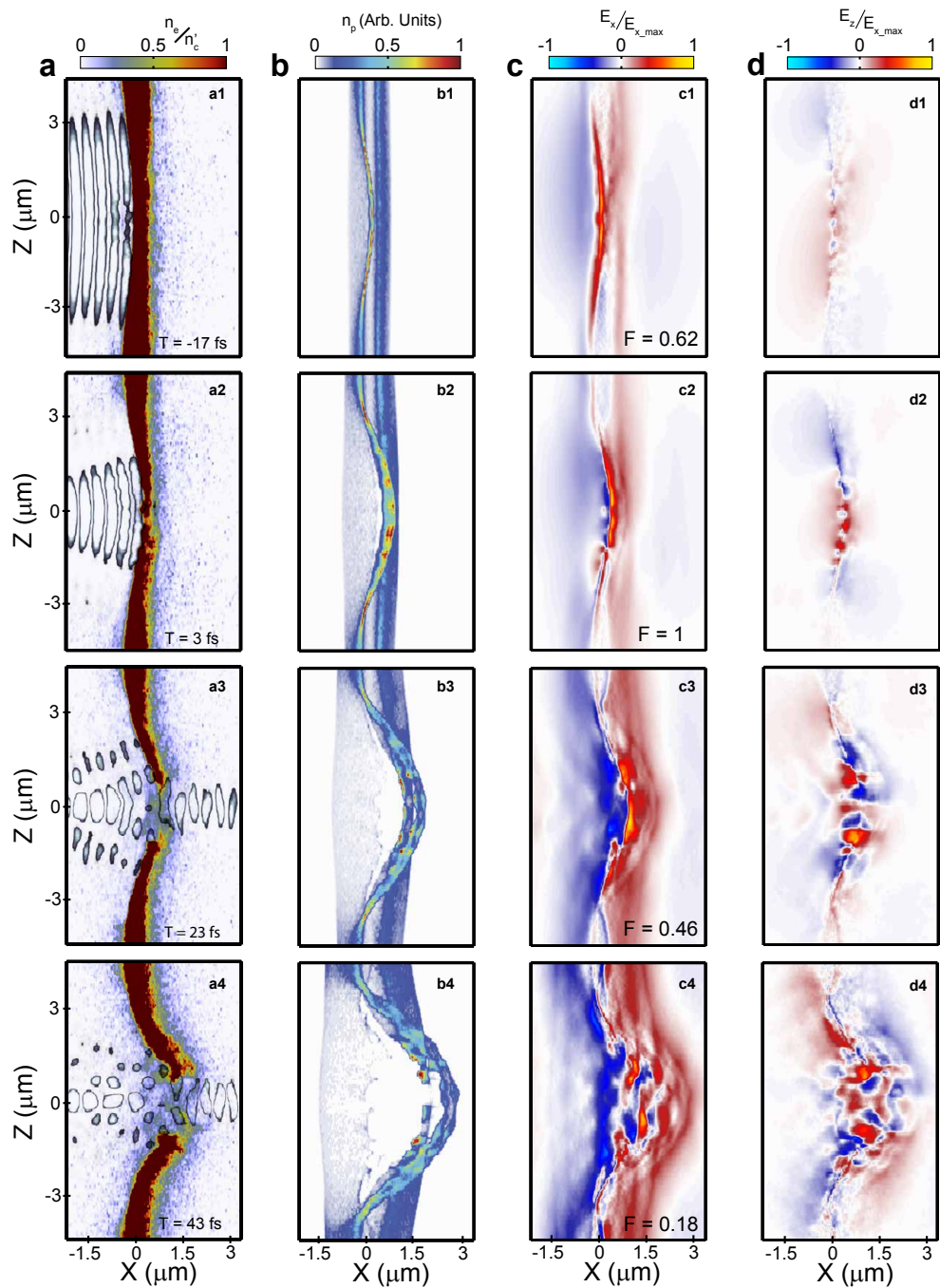


Figure 7.18: Electrostatic field and particle density evolution with protons on both surfaces. Same as figure 7.14 but for circularly polarised laser. **a**, Laser intensity contours and electron density in a plane rotated 45° (same as figure 6.13a-d) at: **a1** $T=-17$ fs; **a2** $T=3$ fs; **a3** $T=23$ fs; and, **a4** $T=43$ fs; The onset of transparency and laser diffraction is observed. **b**, Same for proton density, showing the front surface protons being accelerated into the rear surface population. **c,d**, Same for the longitudinal and transverse electrostatic field components, resulting from charge separation. The simulation time sampled is stated in **a** and is the same in all four sub-plots.

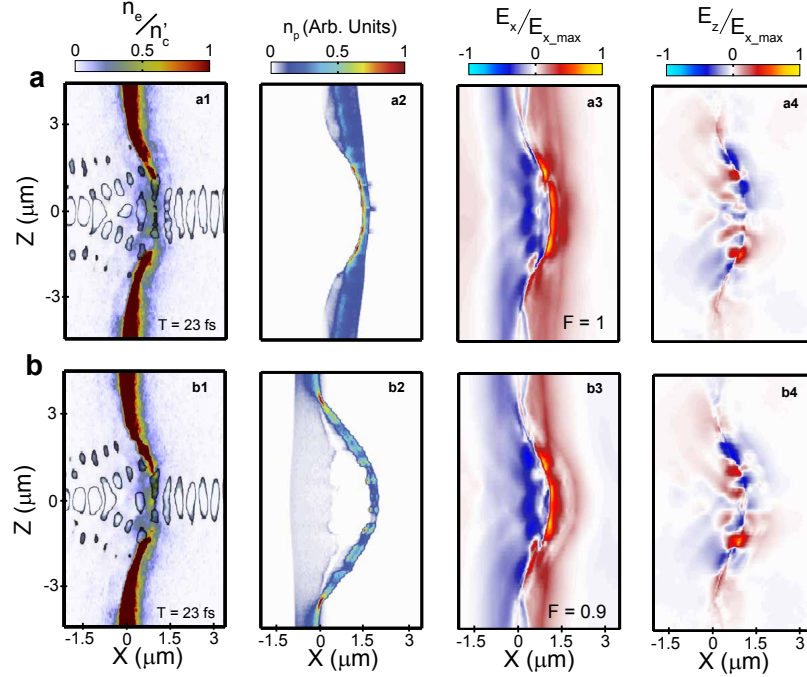


Figure 7.19: Comparison of electrostatic field and particle density distributions for front-only and rear-only proton sources with circularly polarised laser. **a-b**, From left to right (as in figure 7.18): laser intensity contours and electron density; proton density; and longitudinal and transverse electrostatic field components, in a plane rotated 45° for hydrocarbon layer on the target **a**, rear surface and **b**, front surface. $T=23$ fs in both cases.

the instabilities. Besides this, a closer investigation of the electron dynamics for all the cases with double (figure 7.18a), only rear (figure 7.19a1) and only front (figure 7.19b1) hydrocarbon layers show that the accelerated electron distribution does not exhibit this kind of instability in any of these cases. This absence of electron instabilities was obtained in the investigation of the previous chapter, presented in figure 6.15 and 6.20c, and for the experimental results displayed in figure 6.5c. This form of instability is only found in the low density electrons trapped inside the relativistic plasma aperture, which are not accelerated during the laser interaction. This suggests that additionally to pure Rayleigh-Taylor instabilities, protons are affected by some additional processes, as they propagate through a medium. Future numerical and analytical work could shed light on the underlying physics behind this particular proton response.

Investigation of the temporal proton energy evolution

In this section the temporal evolution of the energy of protons, sourced in each particular hydrocarbon layer, for different degree of ellipticity in the laser polarisation is investigated. These results are shown in figure 7.20. They display the maximum proton energy as a function of time (solid lines), plus the maximum proton energy acceleration, i.e. the rate of increase of the proton energy over time (MeV/fs) (dashed line), for linear (figure 7.20a), elliptical (figure 7.20b) and circular polarisation (figure 7.20c).

It is interesting to note that in these simulation results for all three polarisation cases, the highest energy protons are produced due to radiation pressure at the target front, but maximum proton energies are obtained when hydrocarbon layers are present on both surfaces. Several conclusions can be drawn from this. For the linear polarisation case (figure 7.20a), firstly, although the acceleration time is slightly longer for the rear surface protons, the radiation pressure accelerated front surface protons reach higher energies because the magnitude of the acceleration is almost a factor of two higher. Secondly, the overall higher proton energies in the case of the dual proton layer results from a combination of the high magnitude of acceleration of the front surface layer and the longer acceleration time, due to RIT occurring slightly later in the laser-foil interaction (because of the aforementioned $\sim 38\%$ increase in the overall target thickness). The distinctive proton energy and its acceleration can be explained by analysing the maximum longitudinal electrostatic field for the three hydrocarbon layer configurations. Figure 7.21a shows the time evolution of the maximum longitudinal electrostatic field normalised to the field with dual hydrocarbon layers. It clearly shows that the peak value of the electrostatic field with dual layers is significantly higher than the case with hydrocarbon layer only on the rear surface. Additionally, comparing this figure with figure 7.20a, it is demonstrated that the highest proton energy accelerations correspond, in time, with the maximum longitudinal electrostatic

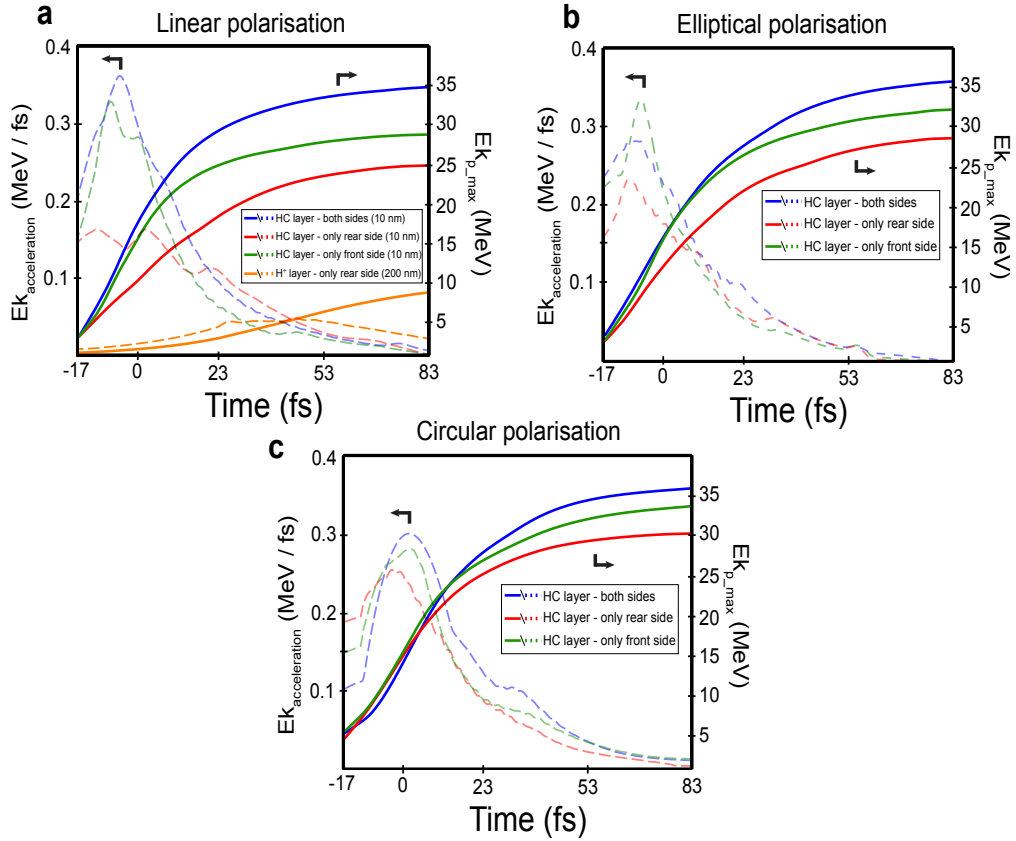


Figure 7.20: **a**, Evolution of the maximum proton energy (solid lines) and rate of change in kinetic energy (dashed lines) for three cases, corresponding to hydrocarbon layers on both surfaces (blue), only on the rear surface (red) and only on the front surface (green). The result using a thicker target (200 nm), orange solid and dashed lines, with a proton layer in the rear surface is included for comparison. In all cases the laser is linearly polarised along the Y-axis. **b**, Same as **a** but for elliptical polarisation. **c**, Same as **a** but for circular polarisation

fields generated, which in turn, coincides with the time when the laser peak reaches the target.

For the elliptical polarisation case (figure 7.20b), a similar behaviour is obtained. However, in this case the maximum proton energy measured for the three hydrocarbon layer configurations are closer than those found for the linear polarisation case. Besides this, the peak acceleration with only a front hydrocarbon layer exhibits higher values than for layers on both surfaces. As in the linear case, the highest values in the maximum proton energy for the dual proton layer results then from longer acceleration time due to RIT occurring later in the interaction. The longitudinal electrostatic field evolution, presented in figure 7.21b (for elliptical polarisation), shows that the field is also higher when

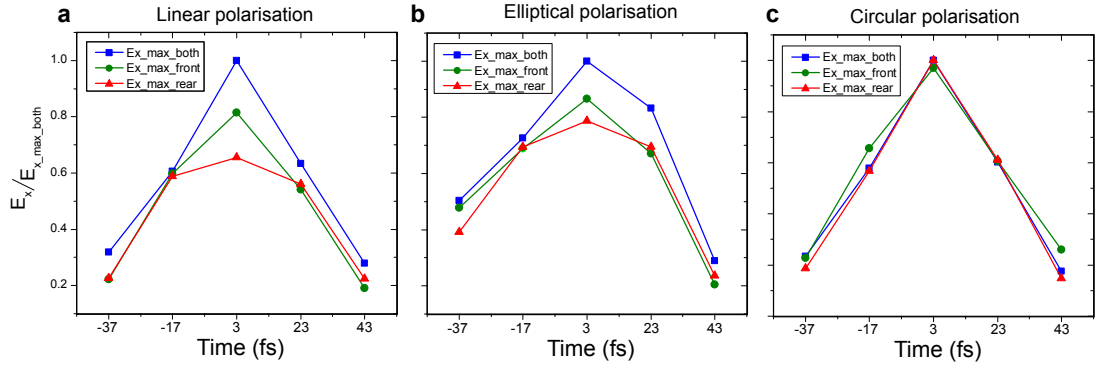


Figure 7.21: **a**, Evolution of the maximum longitudinal electrostatic field for three cases, corresponding to hydrocarbon layers on both surfaces (blue), only on the rear surface (red) and only on the front surface (green), normalised to the maximum longitudinal electrostatic field from the case with hydrocarbon layers on both surfaces. In all cases the laser is linearly polarised along the Y-axis. **b**, Same as **a** but for elliptical polarisation. **c**, Same as **a** but for circular polarisation. $T = 0$ corresponds to the time at which the laser peak interacts with the plasma.

double hydrocarbon layers are used. However, the relative maximum values are much closer to each other between the three configurations than in the linear polarisation case.

Using circularly polarised light the maximum proton energy for all configurations are very similar. However, the maximum values is again obtained with the dual proton layer configuration, as shown in figure 7.20c. Analysing the proton energy acceleration reveals that not only is the peak acceleration higher for the double hydrocarbon layers, but it also exhibits a longer acceleration time compared to single hydrocarbon layer cases. This is consistent with a more efficient/longer duration of radiation pressure accelerating due to RIT occurring later in the interaction. The longitudinal electrostatic field, shown in figure 7.21c, presents a very similar evolution for the three hydrocarbon layer configurations investigated, being also maximum at times when the peak of the laser reaches the target. With this, it can be concluded that in order to achieve higher proton energies it is not only important to generate strong electrostatic fields but also to maximise the proton acceleration time.

Finally, as a comparison with the linear polarisation case, a similar analysis for a relatively thicker (200 nm) target simulation has been performed. The laser

pulse parameters are identical and thus this represents a case in which RIT does not occur. In this simulation a pure proton layer was placed only on the rear surface of the target. The results of the time evolution of the maximum proton energy and proton acceleration is shown in figure 7.20a. This target thickness produces a significantly lower maximum proton energy (~ 10 MeV) and proton acceleration in comparison to the $l = 10$ nm results. In this case the magnitude of acceleration is smaller due to the target areal density being a factor of 20 higher. The maximum ion energy produced by RPA scales inversely with the areal density [155].

7.2.5 Focal spot size effect

As in the previous chapter, where the collective electron motion was investigated, in this section the influence of the laser focal spot size on the proton dynamics response, when it is increased in size to $6 \mu\text{m}$ (FWHM) and decreased to $1.5 \mu\text{m}$ (FWHM), with a linearly polarised laser is investigated. The laser intensity of all the simulations presented in this section is the same as previous simulations and in the previous chapter, i.e. $6 \times 10^{20} \text{ Wcm}^{-2}$, adjusting the laser energy accordingly to account for changes in the laser focal spot size.

Figure 7.22a and b shown the proton spatial-density distribution for a focal spot size equal to $1.5 \mu\text{m}$ and $6 \mu\text{m}$, respectively, at a time $T = 123$ fs. The $1.5 \mu\text{m}$ focal spot size shows a small distribution with a salient double lobe structure with the axis of separation perpendicular to the laser polarisation direction. This structure is more prominent when the proton density is integrated over a specific energy range, as shown in figure 7.22c, which corresponds to the highest proton energies obtained in this simulation. On the other hand, the $6 \mu\text{m}$ focal spot size shows a larger distribution, as expected, with a ring-like structure and noticeable modulations in the form of stripes parallel to the laser polarisation direction. As in the previous case, an integration over a given energy range makes it

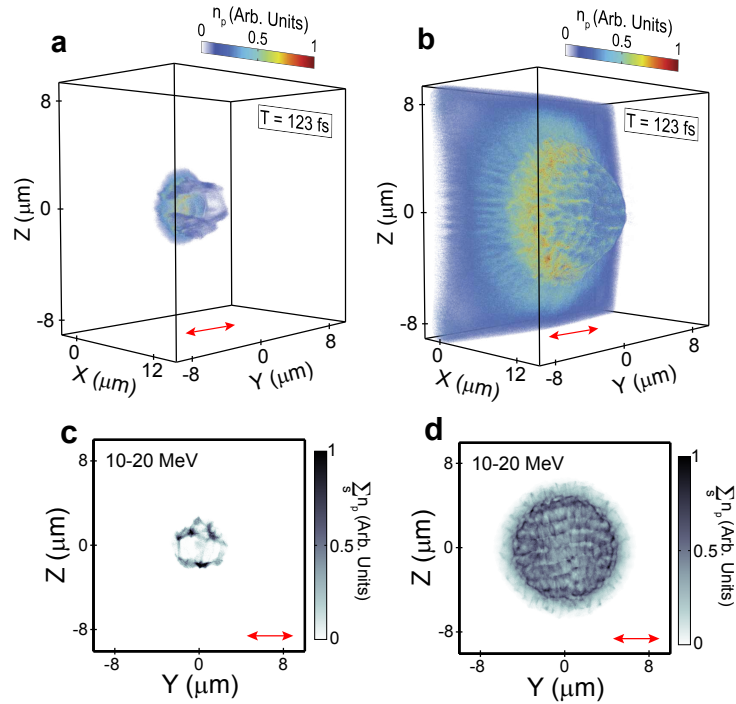


Figure 7.22: **a**, 3D-PIC simulation results showing the proton spatial-density distribution for linear polarisation and $1.5 \mu\text{m}$ focal spot size, sampled at $T = 123 \text{ fs}$. **b**, Same for $6 \mu\text{m}$ focal spot size. Protons are sourced in both surfaces of the target. **c** and **d**, proton spatial density distributions, for the stated energy range, integrated over $X=0-15 \mu\text{m}$ for $1.5 \mu\text{m}$ and $6 \mu\text{m}$ focal spot size, respectively.

evident that these stripes modulations in the proton spatial-density distribution are present, as shown in figure 7.22d. Both particular proton structures, for 1.5 and $6 \mu\text{m}$ focal spot sizes, present a very similar distribution to those found for the electron density response investigated in the previous chapter 6.2.5. This further reveals, as in the previous study with $3 \mu\text{m}$ focal spot size, that there is a direct relationship between the electron and proton dynamics.

Figure 7.23 and figure 7.24 show a time sequence of the laser intensity contours, electron and proton density and the longitudinal and transversal electrostatic field due to charges displacement, measured in a X - Z plane and $Y=0$ perpendicular to the laser polarisation direction, for both 1.5 and $6 \mu\text{m}$ focal spot sizes, respectively. The $1.5 \mu\text{m}$ case (figure 7.23) shows that before RIT occurs, the highest longitudinal electrostatic field is along the laser axis, as presented in figure 7.23a3. However, when the target becomes relativistically transparent,

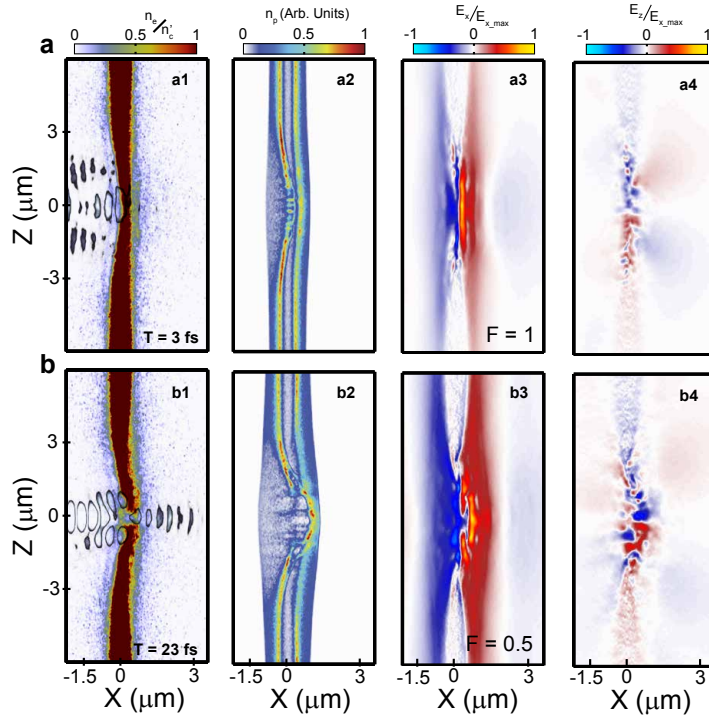


Figure 7.23: Electrostatic field and particle density evolution with protons on both surfaces and linearly polarised light. Same as figure 7.14 but for $1.5 \mu\text{m}$ focal spot size. **a-b**, From left to right: laser field contours and electron density; proton density; and longitudinal and transverse electrostatic field components, in the X-Z plane at $Y=0$, for **a** $T=3$ fs and **b** $T=23$ fs.

and the plasma aperture is formed, the laser diffraction pattern produces a locally double lobe dense electron distribution in the edges of the aperture and perpendicular to the laser polarisation. This electron displacement create an additional longitudinal electrostatic field in those areas (figure 7.23b3), which together with a noticeable transverse electrostatic field (figure 7.23b4) favours the generation of a proton structure predominantly in a double lobe structure, as shown in figure 7.22c.

On the other hand, for the larger focal spot size case, $6 \mu\text{m}$ (figure 7.24), the laser diffraction pattern presents multiple stripes (figure 7.24a1 and b1) due to a higher ration of plasma aperture size to laser wavelength when the target becomes relativistically transparent, as was discussed in the previous chapter. This particular diffraction pattern produces a striped electron distribution ponderomotively trapped between the laser near-field intensity distribution. When the electrons are displaced with respect to the charged particle background

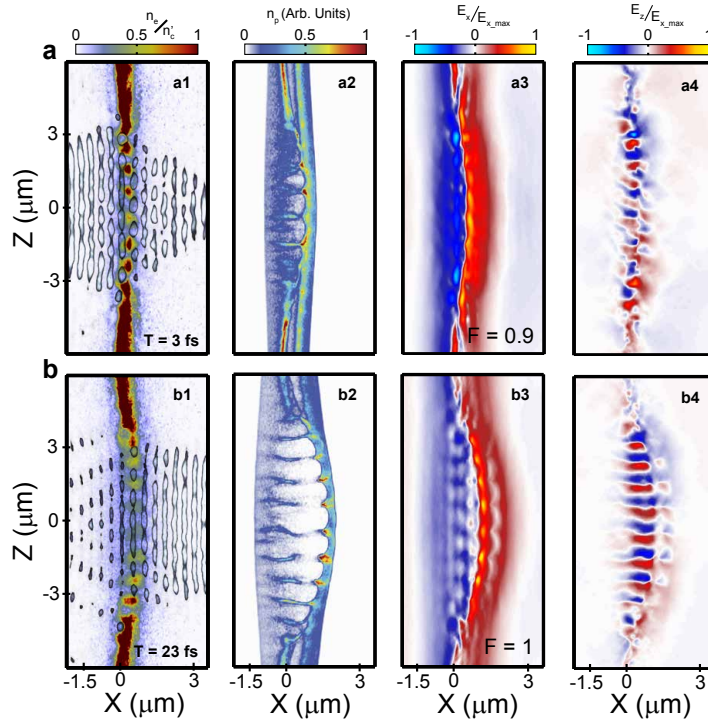


Figure 7.24: Electrostatic field and particle density evolution with protons on both surfaces and linearly polarised light. Same as figure 7.14 but for $6 \mu\text{m}$ focal spot size. **a-b**, From left to right: laser field contours and electron density; proton density; and longitudinal and transverse electrostatic field components, in the X-Z plane at $Y=0$, for **a** $T=3$ fs and **b** $T=23$ fs.

a longitudinal electrostatic field is created which is maximum where the displaced electron densities are maximum. This produces a longitudinal electrostatic field, also predominantly distributed in a striped pattern (figure 7.24a3 and b3), which in turn pulls from the protons, producing the characteristic proton pattern with a striped structure parallel to the laser polarisation, as shown in figure 7.22d.

7.3 Conclusions

Building on the results presented in Chapter 6 focusing on the collective response and control of plasma electrons via diffraction of intense laser light in ultra-thin foils, in this chapter the possibility to also control the spatial-intensity profile of the beam of accelerated protons is demonstrated. The experimental results show that distinctive structures in the proton beam, such as rings, bubbles and striped distributions, can be manipulated by variation of the degree of ellipticity

in the laser polarisation. Through EPOCH-PIC simulations it was demonstrated that the electron beam structure, in foils undergoing relativistic transparency, is mapped into the proton beam via transverse modulation of the electrostatic field that is produced by charge separation. The experimentally measured proton beam profiles resemble the modelled proton beam structures, in terms of the overall shape and the orientation of features with respect to the average polarisation axis. It is thus demonstrated that the degree of ellipticity of the laser polarisation defines the spatial-intensity distribution of the proton beam profile and can therefore be used to control it. The simulation results further show that, as in electron beams investigated in Chapter 6, the collective response of protons are also affected by the laser focal spot size.

Additionally, these simulations show that both RPA and TNSA ion populations, from hydrocarbon layers placed on the front and rear surface of the target respectively, are affected by the modulated field structures and in distinctive ways. This effect is not only displayed in the spatial-intensity distribution of proton beams but also in the maximum energy of the protons attainable. It is shown that the highest proton energies are obtained when both, front and rear, hydrocarbon layers are presented for the three laser polarisations investigated. Thus the combination of selective coating of a target foil, with variation of laser polarisation and focal spot size should enable manipulation of the collective dynamics of energetic ions produced by either acceleration mechanism. Development of this approach may enable optical control over the shape, divergence and energy profile of beams of laser-accelerated protons, without recourse to complex target or laser pulse engineering. This could enable active proton beam tailoring at high repetition rates required by many potential applications of intense laser-driven ion sources.

Understanding these processes (in which intense laser diffraction is mapped into the collective electron motion and in turn to the protons via the electrostatic

fields) is also highly important to the development of laser-driven ion acceleration, given that many of the most promising schemes involve ultra-thin foil targets [99, 156]. This demonstration of dynamic optical control of structures within the spatial-intensity distribution of the beam of laser-accelerated ions opens a new route to optimising the properties of these ion sources.

Chapter 8

Conclusions & Future Work

The research presented in this thesis focuses on experimental and numerical investigations exploring the onset of relativistic induced transparency and its influence on the collective response of the plasma electrons and ions in ultra-intense laser-foil interactions. PIC simulations have been a significant component of this investigation. Although always simulations represent a simplification (which can be more or less sophisticated and accurate) of nature, they enable properly interpretation of the experimental results and obtain a reasonable theoretical comprehension of the underpinning physics, in this case, of the ultra-intense laser pulses interacting with thin solid targets. The results of this investigation are reported in three research chapters, Chapter 5, Chapter 6 and Chapter 7 and a summary of the main conclusions is included in the following section.

8.1 Main research achievements

Onset of relativistic induced transparency

In chapter 5 experimental and numerical investigations examining the onset and fundamental physics of relativistic induced transparency is presented. This study focused on the dependency of RIT on the target areal density, laser

intensity and polarisation using optical diagnostics. The results show that the laser transmission is maximised for the thinnest targets and decreases exponentially with increasing target thickness. Moreover, it is shown that once the thinnest targets become relativistically transparent, the transmitted light fraction increases rapidly as the laser intensity increases. The increasing rate is shown to be more pronounced in the thinnest targets investigated.

Additionally, an alternative diagnostic approach, based on numerical determination of the critical surface velocity, as a function of time, for various target thickness, and comparing it with corresponding analytical models has been proposed. These results are in good agreement with the values predicted by the *hole boring* model for the thickest targets. On the contrary, the traditional *light sail* model predicts an evolution and maximum velocities significantly different to those obtained with the numerical results presented in this chapter. The main reason for this disagreement is that in the light sail model a temporal top-hat laser intensity profile is assumed. However, in the present numerical investigation a temporal Gaussian-like has been employed for a more realistic comparison to experiments. Because of this, a revised light sail model including a temporal Gaussian laser beam has been formulated. This revised model presents a better predictive capability for the time evolution and maximum critical surface velocity in the thinnest targets. The experimental results are also in good agreement with these conclusions.

The ‘Relativistic Plasma Aperture’ concept

In chapter 6 a novel concept in laser-electron interaction in relativistically transparent plasmas is formulated and described in detail. The concept introduced for the first time is that of a ‘relativistic plasma aperture’ produced in the ultra-thin foil by the ultra-intense laser. The remainder of the laser light transmitted through this self-formed aperture undergoes the fundamental

optic process of diffraction. To understand and characterise this process as well as its implication on the electron dynamics in a laser-solid interaction subjected to relativistic transparency, numerous 3D PIC simulations have been performed. They show that the collective dynamics of relativistic electron beams is determined by the resulting near-field diffraction pattern, which through suitable choice of laser drive parameters such as polarisation or focal spot size, can be distinctively modified and controlled. It is also shown that the angular rotational frequency can be varied by changing the degree of ellipticity in the laser polarisation. Beside this, the simulations included in this chapter suggest that it could potentially be used to induce orbital angular momentum states at high laser intensity. A rotating diffraction lobe structure produced with circularly polarised light results in a helical structure of intense laser light with an optical vortex at the centre, on the beam axis. All these results are not only of fundamental importance to the understanding of relativistic transparency and the interpretation of experimental results involving transparency in ultrathin foils, but could also profoundly affect the development of laser-driven particle and radiation sources involving dense laser-irradiated targets.

A double-lobe electron density structure was observed in 3D simulations of ion acceleration in relativistically transparent thin foils by Yin *et al.* [104], using linearly polarised laser light. In that work, the origin of that double-lobe structure is uncertain and attributed to the plasma response to the radially symmetric laser intensity profile, and specifically to the combination of oscillatory and non-oscillatory electron momentum components in the plane perpendicular to the laser propagation direction. By investigating the sensitivity of the electron distribution to the drive laser polarisation, numerically and experimentally, the investigation presented in this chapter reveals that the underpinning physics giving rise to the lobe features arises from diffraction. This is further confirmed by the simulations in which the relativistic plasma aperture diameter is varied.

Collective proton response to transparency and diffraction

Building on the investigation reported in chapter 6 about the collective response control of plasma electrons via diffraction of intense laser light in ultra-thin foils undergoing relativistic transparency, the collective ion response and possibility to also control the spatial-intensity profile of the beam of accelerated protons is explored in chapter 7. The experimental results show that distinctive structures in the proton beam, such as rings, bubbles and striped distributions, can be manipulated by variation of the degree of ellipticity in the laser polarisation. The PIC simulation results demonstrate that the electron beam structure is mapped into the proton beam via transverse modulation of the electrostatic field that is produced by charge displacement. The measured proton beam profiles resemble the modelled electron beam structures, in terms of the overall shape and the orientation of features with respect to the average polarisation axis. It is thus demonstrated that the degree of ellipticity of the laser polarisation defines the spatial-intensity distribution of the proton beam profile and can therefore be used to control it.

The simulation results further show that, as for electron beams, the collective response of protons is also significantly affected by the laser focal spot size. Additionally, these simulations show that protons sourced from hydrocarbon layers at the front and rear surface of the target, are affected by the modulated field structures and in different ways. This effect is not only on the spatial-intensity distribution of the beam of protons but also on the maximum attainable energy of the protons. It is shown that the highest proton energies are obtained when both front and rear hydrocarbon layers are present for the three laser polarisations investigated. This demonstration of dynamic optical control of structures within the spatial-intensity distribution of the beam of laser-accelerated protons opens a new route to optimising the properties of these promising ion sources.

8.2 Future work

The physics of the onset of relativistic induced transparency in thin foils, which is intrinsically linked to target electron heating and expansion, is complex. The new results reported in this thesis have produced new understanding of the onset of transparency and the collective response of target electrons and ions. There are a number of ways in which this study can be continued and some of these are proposed below.

- In chapter 5 a time evolution of the critical surface velocity was numerically investigated. Employing an autocorrelator system, as FROG, would enable time-resolved measurement of the critical surface velocity by evaluating the relativistic Doppler-shift of the second harmonic (or higher) from the back-reflected light. Additionally, using this autocorrelator system to measure the transmitted light, would enable not only the fraction of transmitted light in time but also determination of the duration of such a transmitted pulse.
- The experimental wavelength narrowing of the transmitted light during RIT, which, in principle, is contrary to the expected result [113], was investigated in chapter 5. As mentioned in this chapter, a possible configuration to confirm this effect on the transmitted light would be to guide all transmitted light into a spectrometer possessing an entrance slit, in order to measure the spatially-resolved transmitted spectrum along a radial direction of such a beam. This would determine whether the spectrum shows different bandwidths from the centre to the edges of the transmitted beam. Another proposed option to confirm the narrowing and broadening of the transmitted spectrum in distinct areas of the beam would be to make pin-holes in a diffuse screen placed at the rear of the target that collects the transmitted light, at strategic positions, including the centre and edges. An

optical fibre could then be attached at each pin-hole in order to characterise the spectrum of transmitted light at those positions.

- The investigation presented in chapters 6 and 7 focused on the spatial-intensity distribution of electron and proton beams in thin targets undergoing relativistic transparency. This study could be extended by investigating the energy spectrum of these charged particles by both experimentally and by employing PIC simulations for thin and in thicker targets. Moreover, a complete study of the collective dynamics of heavier ions, as carbon and aluminium, would also provide further understanding of the charged particles response in relativistically transparent plasmas.
- The investigation presented in chapters 6 and 7 has been performed using laser pulses of 40 fs (FWHM) in duration and 800 nm wavelength. Additional investigations employing longer pulses and different laser wavelengths could produce new particular electron and proton beam structures and contribute to a better understanding of the laser-plasma interaction in thin targets undergoing relativistic transparency.
- As described in chapter 7, the results of proton beam instabilities using a circularly polarised laser suggest that, additionally to pure Rayleigh-Taylor-like instabilities, protons are affected by other processes when they propagate through a medium. Future numerical and analytical work could shed light on the underlying physics behind this particular proton response in laser-foil interactions.
- At present, experimental verification of the numerical results on the collective electron and proton dynamics driven by laser focal spot sizes of $6\ \mu\text{m}$ and $1.5\ \mu\text{m}$, described in chapters 6 and 7, are not achievable. However, with future multi-petawatt laser systems such as the proposed ELI facilities [146, 147], and by employing diffraction limited focusing

optics by elliptical plasma mirrors [148], testing these predictions will be experimentally feasible.

- In chapter 6 the influence of the relativistic plasma aperture, produced by circularly polarised light, on the magnetic field strength and distribution is discussed. It is found that the field is relatively strong over a longer range and is more helical compare to an ideal simulation with a predefined aperture, suggesting that the field is modified by the induced plasma current structure. Future investigations of the underlying physics of the collective plasma effects on the magnetic field could enable, for example, the generation and a more precise understanding of laboratory analogues of astrophysical phenomena.

As a final note, the research presented in this thesis has resulted in new concepts and understanding of collective processes in laser-produced plasma undergoing relativistic induced transparency. There are many new scientific ideas and directions which can build on this work. Science is after all a collective process in which one does not always get to draw definite conclusions, but which establishes a basis upon which others, with better tools, more capacity or just luckier, can reach at the end of the issue. In the words of *Charles H. Townes* “It’s very important to recognise that science grows as a result of a community, a community of scientists and engineers who add further ideas. Science grows like a tree, as people keep adding on more and more new things”.

Bibliography

- [1] A. Fresnel. Memoire sur la diffraction de la lumiere. *Ann. Chim et Phys.*, 1:129, 1816. [pages 4, 130]
- [2] L. Piazza, T. Lummen, E. Quinonez, Y. Murooka, B. Reed, B. Barwick, and F. Carbone. Simultaneous observation of the quantization and the interference pattern of a plasmonic near-field. *Nature communications*, 6:1–7, 2015. [page 5]
- [3] A. L. Schawlow and C. H. Townes. Infrared and optical masers. *Physical Review*, 112(6):1940, 1958. [page 5]
- [4] A. M. Sessler. New particle acceleration techniques. *Physics today*, 41(1):26–34, 1988. [page 6]
- [5] S. V. Bulanov and V. S. Khoroshkov. Feasibility of using laser ion accelerators in proton therapy. *Plasma Physics Reports*, 28(5):453–456, May 2002. [page 7]
- [6] H. Daido, M. Nishiuchi, and A. S. Pirozhkov. Review of laser-driven ion sources and their applications. *Reports on Progress in Physics*, 75(5):056401, 2012. [page 7]
- [7] T. Tajima and J. Dawson. Laser electron accelerator. *Physical Review Letters*, 43(4):267, 1979. [page 7]
- [8] J. M. Dawson. On the production of plasma by giant pulse lasers. *Physics of Fluids (1958-1988)*, 7(7):981–987, 1964. [page 7]

- [9] K. Nakajima, D. Fisher, T. Kawakubo, H. Nakanishi, A. Ogata, Y. Kato, Y. Kitagawa, R. Kodama, K. Mima, H. Shiraga, et al. Observation of ultrahigh gradient electron acceleration by a self-modulated intense short laser pulse. *Physical review letters*, [74\(22\):4428](#), 1995. [page 7]
- [10] D. Strickland and G. Mourou. Compression of amplified chirped optical pulses. *Optics communications*, [56\(6\):219–221](#), 1985. [pages 7, 67]
- [11] P. Maine, D. Strickland, P. Bado, M. Pessot, and G. Mourou. Generation of ultrahigh peak power pulses by chirped pulse amplification. *IEEE Journal of Quantum Electronics*, [24\(2\):398–403](#), Feb 1988. [pages 7, 67]
- [12] P. Maine and G. Mourou. Amplification of 1-nsec pulses in nd: glass followed by compression to 1 psec. *Optics letters*, [13\(6\):467–469](#), 1988. [page 7]
- [13] H. Boot and R. Harvie. Charged particles in a non-uniform radio-frequency field. *Nature*, [180\(4596\):1187](#), 1957. [page 7]
- [14] W. L. Kruer and K. Estabrook. Jxb heating by very intense laser light. *Physics of Fluids*, [28\(1\):430–432](#), 1985. [pages 7, 46, 46]
- [15] R. Kidder. Laser-driven isentropic hollow-shell implosions: The problem of ignition. *Nuclear Fusion*, [19\(2\):223](#), 1979. [page 8]
- [16] M. Tabak, J. Hammer, M. E. Glinsky, W. L. Kruer, S. C. Wilks, J. Woodworth, E. M. Campbell, M. D. Perry, and R. J. Mason. Ignition and high gain with ultrapowerful lasers. *Physics of Plasmas (1994-present)*, [1\(5\):1626 – 1634](#), 1994. [page 8]
- [17] J. Fuchs, G. Malka, J. Adam, F. Amiranoff, S. Baton, N. Blanchot, A. Héron, G. Laval, J. Miquel, P. Mora, et al. Dynamics of subpicosecond relativistic laser pulse self-channeling in an underdense preformed plasma. *Physical review letters*, [80\(8\):1658](#), 1998. [pages 9, 66]

- [18] A. Lei, A. Pukhov, R. Kodama, T. Yabuuchi, K. Adumi, K. Endo, R. Freeman, H. Habara, Y. Kitagawa, K. Kondo, et al. Relativistic laser channeling in plasmas for fast ignition. *Physical Review E*, [76\(6\):066403](#), 2007. [pages 9, 66]
- [19] R. Kodama, P. Norreys, K. Mima, A. Dangor, R. Evans, H. Fujita, Y. Kitagawa, K. Krushelnick, T. Miyakoshi, N. Miyanaga, et al. Fast heating of ultrahigh-density plasma as a step towards laser fusion ignition. *Nature*, [412\(6849\):798–802](#), 2001. [pages 9, 65]
- [20] R. Stephens, S. Hatchett, R. Turner, K. Tanaka, and R. Kodama. Implosion of indirectly driven reentrant-cone shell target. *Physical review letters*, [91\(18\):185001](#), 2003. [pages 9, 65]
- [21] J. Honrubia and J. Meyer-ter Vehn. Three-dimensional fast electron transport for ignition-scale inertial fusion capsules. *Nuclear fusion*, [46\(11\):L25](#), 2006. [page 9]
- [22] A. Kemp, F. Fiuza, A. Debayle, T. Johzaki, W. Mori, P. Patel, Y. Sentoku, and L. Silva. Laser-plasma interactions for fast ignition. *Nuclear Fusion*, [54\(5\):054002](#), 2014. [page 9]
- [23] A. Robinson, D. Strozzi, J. Davies, L. Gremillet, J. Honrubia, T. Johzaki, R. Kingham, M. Sherlock, and A. Solodov. Theory of fast electron transport for fast ignition. *Nuclear Fusion*, [54\(5\):054003](#), 2014. [page 9]
- [24] J. Fernandez, B. Albright, F. Beg, M. Foord, B. Hegelich, J. Honrubia, M. Roth, R. Stephens, and L. Yin. Fast ignition with laser-driven proton and ion beams. *Nuclear Fusion*, [54\(5\):054006](#), 2014. [page 9, 9]
- [25] M. Temporal, J. Honrubia, and S. Atzeni. Proton-beam driven fast ignition of inertially confined fuels: Reduction of the ignition energy by the use of two proton beams with radially shaped profiles. *Physics of Plasmas (1994-present)*, [15\(5\):052702](#), 2008. [page 9]

- [26] J. Honrubia, J. Fernandez, B. Hegelich, M. Murakami, and C. Enriquez. Fast ignition driven by quasi-monoenergetic ions: Optimal ion type and reduction of ignition energies with an ion beam array. *Laser and Particle Beams*, [32:419427](#), 2014. [page 9]
- [27] C. Regan, T. Schlegel, V. Tikhonchuk, J. Honrubia, J. Feugeas, and P. Nicolai. Cone-guided fast ignition with ponderomotively accelerated carbon ions. *Plasma Physics and Controlled Fusion*, [53\(4\):045014](#), 2011. [page 9]
- [28] R. Gray, D. Carroll, X. Yuan, C. Brenner, M. Burza, M. Coury, K. Lancaster, X. Lin, Y. Li, D. Neely, et al. Laser pulse propagation and enhanced energy coupling to fast electrons in dense plasma gradients. *New Journal of Physics*, [16\(11\):113075](#), 2014. [page 9]
- [29] E. S. Weibel. Spontaneously growing transverse waves in a plasma due to an anisotropic velocity distribution. *Physical Review Letters*, [2\(3\):83](#), 1959. [page 9]
- [30] L. O. Silva, R. A. Fonseca, J. W. Tonge, W. B. Mori, and J. M. Dawson. On the role of the purely transverse weibel instability in fast ignitor scenarios. *Physics of Plasmas (1994-present)*, [9\(6\):2458–2461](#), 2002. [page 9]
- [31] A. Sgattoni, S. Sinigardi, L. Fedeli, F. Pegoraro, and A. Macchi. Laser-driven rayleigh-taylor instability: Plasmonic effects and three-dimensional structures. *Physical Review E*, [91\(1\):013106](#), 2015. [pages 9, 154, 164, 173, 183]
- [32] J. J. Thomson. Cathode rays. *Philosophical Magazine*, 44:295, 1897. [page 12]
- [33] J. C. Maxwell. On Faraday’s lines of force, volume 10. Cambridge Philosophical Society, 1855. [page 14]

- [34] J. C. Maxwell. On physical lines of force. The London, Edinburgh, and Dublin Philosophical Magazine and Journal of Science, 21 & 23(140):161, 1861. [pages 14, 15]
- [35] N. Forbes and B. Mahon. Faraday, Maxwell, and the electromagnetic field: how two men revolutionized physics. Prometheus Books, New York, NY, Mar 2014. [page 15]
- [36] O. Heaviside. On the forces, stresses, and fluxes of energy in the electromagnetic field. Proceedings of the Royal Society of London, 50(302-307):126–129, 1891. [page 15]
- [37] R. B. Feynman, R. P. Leighton and M. Sands. The Feynman Lectures on Physics, volume II. AddisonWesley, 1964. [page 16]
- [38] P. A. Ade, N. Aghanim, M. Alves, C. Armitage-Caplan, M. Arnaud, M. Ashdown, F. Atrio-Barandela, J. Aumont, H. Aussel, C. Baccigalupi, et al. Planck 2013 results. Astronomy & Astrophysics, [571:A1](#), 2014. [page 18]
- [39] I. Langmuir. Oscillations in ionized gases. Proceedings of the National Academy of Sciences of the United States of America, [14\(8\):627](#), 1928. [pages 19, 22]
- [40] Penning. Physica, 6:241, 1926. [page 19]
- [41] H. Mott-Smith. History of plasmas. Nature, [233\(5316\):219](#), 1971. [page 19]
- [42] F. F. Chen. Introduction to Plasma Physics and Controlled Fusion. Springer, 1984. [page 20]
- [43] T. J. M. Boyd and J. J. Sanderson. The physics of plasmas. Cambridge University Press, 2003. [page 20]

- [44] P. Debye and E. Huckel. The theory of electrolytes i. the lowering of the freezing point and related occurrences. *PHYSIKALISCHE ZEITSCHRIFT*, [24:185–206](#), 1923. [page 20]
- [45] L. Tonks and I. Langmuir. Oscillations in ionized gases. *Physical Review*, [33\(2\):195](#), 1929. [page 22]
- [46] E. Biémont, Y. Frémat, and P. Quinet. Ionization potentials of atoms and ions from lithium to tin ($z= 50$). *Atomic Data and Nuclear Data Tables*, [71\(1\):117–146](#), 1999. [page 24]
- [47] A. Kramida, Yu. Ralchenko, J. Reader, and NIST ASD Team. NIST Atomic Spectra Database (ver. 5.3), [Online]. Available: <http://physics.nist.gov/asd> [2016, January 18]. National Institute of Standards and Technology, Gaithersburg, MD., 2015. [page 24]
- [48] M. Göppert-Mayer. Über elementarakte mit zwei quantensprüngen. *Annalen der Physik*, [401\(3\):273–294](#), 1931. [page 24]
- [49] A. L’Huillier, L. Lompre, G. Mainfray, and C. Manus. Multiply charged ions induced by multiphoton absorption processes in rare-gas atoms at $1.064 \mu\text{m}$. *Journal of Physics B: Atomic and Molecular Physics*, [16\(8\):1363](#), 1983. [page 25]
- [50] L. Keldysh. Ionization in the field of a strong electromagnetic wave. *Sov. Phys. JETP*, [20\(5\):1307–1314](#), 1965. [page 26]
- [51] S. Braginskii. *Transport Processes in a Plasma*. 1965. [page 29]
- [52] K. L. Kruer. *The Physics of Laser Plasma Interactions*. Addison-Wesley, 1988. [page 29]
- [53] S. C. Wilks and W. L. Kruer. Absorption of ultrashort, ultra-intense laser light by solids and overdense plasmas. *IEEE Journal of Quantum Electronics*, [33\(11\):1954–1968](#), Nov 1997. [pages 29, 43, 44]

- [54] A. Macchi, T. V. Liseikina, S. Tuveri, and S. Veghini. Theory and simulation of ion acceleration with circularly polarized laser pulses. *Comptes Rendus Physique*, [10\(2\):207–215](#), 2009. [page 36]
- [55] A. Macchi. *A Superintense Laser-plasma Interaction Theory Primer*. Springer, 2013. [pages 36, 39, 41, 46, 59]
- [56] P. Mulser and D. Bauer. *High power laser-matter interaction*, volume 238. Springer, 2010. [pages 41, 44, 46]
- [57] P. Gibbon. *Short pulse laser interactions with matter*. Imperial College Press London, 2005. [pages 41, 46]
- [58] L. Schlessinger and J. Wright. Inverse-bremsstrahlung absorption rate in an intense laser field. *Physical Review A*, [20\(5\):1934](#), 1979. [page 43]
- [59] J. R. Davies. Laser absorption by overdense plasmas in the relativistic regime. *Plasma Physics and Controlled Fusion*, [51\(1\):014006](#), 2009. [page 43]
- [60] J. Freidberg, R. Mitchell, R. L. Morse, and L. Rudsinski. Resonant absorption of laser light by plasma targets. *Physical Review Letters*, [28:795–799](#), 1972. [page 44]
- [61] D. Forslund, J. Kindel, K. Lee, E. Lindman, and R. Morse. Theory and simulation of resonant absorption in a hot plasma. *Physical Review A*, [11\(2\):679](#), 1975. [page 44]
- [62] S. Eliezer. *The interaction of high-power lasers with plasmas*. Series in plasma physics. Institute of Physics Publishing, Bristol, Philadelphia, 2002. [page 44]
- [63] S. Pfalzner. *An introduction to inertial confinement fusion*. CRC Press, 2006. [page 44]
- [64] F. Brunel. Not-so-resonant, resonant absorption. *Physical Review Letters*, [59\(1\):52](#), 1987. [page 44]

- [65] S. C. Wilks, A. B. Langdon, T. E. Cowan, M. Roth, M. Singh, S. Hatchett, M. H. Key, D. Pennington, A. MacKinnon, and R. A. Snavely. Energetic proton generation in ultra-intense laser-solid interactions. *Physics of Plasmas*, [8\(2\):542–549](#), Feb 2001. [page 48]
- [66] X. Yan, C. Lin, Z.-M. Sheng, Z. Guo, B. Liu, Y. Lu, J. Fang, J. Chen, et al. Generating high-current monoenergetic proton beams by a circularly polarized laser pulse in the phase-stable acceleration regime. *Physical review letters*, [100\(13\):135003](#), 2008. [page 48]
- [67] A. Robinson, M. Zepf, S. Kar, R. Evans, and C. Bellei. Radiation pressure acceleration of thin foils with circularly polarized laser pulses. *New Journal of Physics*, [10\(1\):013021](#), 2008. [pages 48, 173]
- [68] A. Macchi, S. Veghini, T. V. Liseykina, and F. Pegoraro. Radiation pressure acceleration of ultrathin foils. *New Journal of Physics*, [12:045013](#), Apr 2010. [pages 48, 50]
- [69] A. Macchi and C. Benedetti. Ion acceleration by radiation pressure in thin and thick targets. *Nuclear Instruments & Methods in Physics Research Section a-Accelerators Spectrometers Detectors and Associated Equipment*, [620\(1\):41–45](#), Aug 2010. [page 48]
- [70] S. C. Wilks, W. L. Kruer, M. Tabak, and A. B. Langdon. Absorption of ultra-intense laser pulses. *Physical Review Letters*, [69\(9\):1383–1386](#), 1992. [page 49]
- [71] A. P. L. Robinson, P. Gibbon, M. Zepf, S. Kar, R. G. Evans, and C. Bellei. Relativistically correct hole-boring and ion acceleration by circularly polarized laser pulses. *Plasma Physics and Controlled Fusion*, [51\(2\):024004](#), Feb 2009. [page 50]
- [72] T. Schlegel, N. Naumova, V. T. Tikhonchuk, C. Labaune, I. V. Sokolov, and G. Mourou. Relativistic laser piston model: Ponderomotive ion acceleration

- in dense plasmas using ultraintense laser pulses. *Physics of Plasmas*, [16\(8\):083103](#), 2009. [page 50]
- [73] A. Macchi, S. Veghini, and F. Pegoraro. Light sail acceleration reexamined. *Phys. Rev. Lett.*, [103:085003](#), Aug 2009. [pages 50, 59]
- [74] G. Marx. Interstellar vehicle propelled by terrestrial laser beam. *Nature*, [211:22–23](#), 1966. [page 50]
- [75] J. Simmons and C. McInnes. Was marx right? or how efficient are laser driven interstellar spacecraft? *American journal of physics*, [61\(3\):205–207](#), 1993. [page 50]
- [76] A. Einstein. Zur elektrodynamik bewegter körper. *Annalen der physik*, [322\(10\):891–921](#), 1905. [page 50]
- [77] P. Kaw and J. Dawson. Relativistic nonlinear propagation of laser beams in cold overdense plasmas. *Physics of Fluids*, [13:472](#), 1970. [pages 52, 53, 57, 57]
- [78] C. Max and F. Perkins. Strong electromagnetic waves in overdense plasmas. *Physical Review Letters*, [27\(20\):1342](#), 1971. [pages 52, 53]
- [79] A. Akhiezer and R. Polovin. Theory of wave motion of an electron plasma. *Soviet Phys. JETP*, [3:696–705](#), 1956. [page 52]
- [80] J. Fuchs, J. Adam, F. Amiranoff, S. Baton, P. Gallant, L. Gremillet, A. Héron, J. Kieffer, G. Laval, G. Malka, et al. Transmission through highly overdense plasma slabs with a subpicosecond relativistic laser pulse. *Physical review letters*, [80\(11\):2326–2329](#), 1998. [page 53]
- [81] J. Fuchs, J. Adam, F. Amiranoff, S. Baton, N. Blanchot, P. Gallant, L. Gremillet, A. Héron, J. Kieffer, G. Laval, et al. Experimental study of laser penetration in overdense plasmas at relativistic intensities. ii: Explosion of thin foils by laser driven fast electrons. *Physics of Plasmas* (1994-present), [6\(6\):2569–2578](#), 1999. [page 53]

- [82] E. Lefebvre and G. Bonnaud. Transparency/opacity of a solid target illuminated by an ultrahigh-intensity laser pulse. *Physical review letters*, [74\(11\):2002](#), 1995. [page 53]
- [83] H. Sakagami and K. Mima. Anomalous penetration mechanisms of very intense laser pulses into overdense plasmas. *Physical Review E*, [54\(2\):1870](#), 1996. [pages 53, 57]
- [84] B. Shen and Z. Xu. Transparency of an overdense plasma layer. *Physical Review E*, [64\(5\):056406](#), 2001. [page 53]
- [85] M. Tushentsov, A. Kim, F. Cattani, D. Anderson, and M. Lisak. Electromagnetic energy penetration in the self-induced transparency regime of relativistic laser-plasma interactions. *Physical Review Letters*, [87\(27\):275002](#), 2001. [page 53]
- [86] F. Cattani, A. Kim, D. Anderson, and M. Lisak. Threshold of induced transparency in the relativistic interaction of an electromagnetic wave with overdense plasmas. *Physical Review E*, [62\(1\):1234–1237](#), 2000. [page 53]
- [87] P. Kaw, A. Sen, and T. Katsouleas. Nonlinear 1d laser pulse solitons in a plasma. *Physical Review Letters*, [68\(21\):3172](#), 1992. [page 53]
- [88] J. H. Marburger and R. F. Tooper. Nonlinear optical standing waves in overdense plasmas. *Physical Review Letters*, [35\(15\):1001](#), 1975. [page 53]
- [89] S. Guerin, P. Mora, J. Adam, A. Héron, and G. Laval. Propagation of ultraintense laser pulses through overdense plasma layers. *Physics of Plasmas*, [3\(7\):2693–2701](#), 1996. [pages 53, 57, 57]
- [90] J. Fuchs, P. Antici, E. d’Humières, E. Lefebvre, M. Borghesi, E. Brambrink, C. Cecchetti, T. Toncian, H. Pépin, and P. Audebert. Ion acceleration using high-contrast ultra-intense lasers. [133:1151–1153](#), 2006. [pages 53, 54, 61]
- [91] J. Fuchs, P. Antici, E. d’umières, E. Lefebvre, M. Borghesi, E. Brambrink, C. Cecchetti, M. Kaluza, V. Malka, M. Manclossi, et al. Laser-driven

- proton scaling laws and new paths towards energy increase. *Nature physics*, [2\(1\):48–54](#), 2006. [pages 53, 54, 61]
- [92] M. Borghesi, P. Audebert, S. Bulanov, T. Cowan, J. Fuchs, J. Gauthier, A. Mackinnon, P. Patel, G. Pretzler, L. Romagnani, et al. High-intensity laser-plasma interaction studies employing laser-driven proton probes. *Laser and Particle Beams*, [23\(03\):291–295](#), 2005. [page 53]
- [93] A. Maksimchuk, S. Gu, K. Flippo, D. Umstadter, and V. Y. Bychenkov. Forward ion acceleration in thin films driven by a high-intensity laser. *Physical Review Letters*, [84\(18\):4108](#), 2000. [page 53]
- [94] L. Yin, B. Albright, B. Hegelich, and J. Fernández. GeV laser ion acceleration from ultrathin targets: The laser break-out afterburner. *Laser and Particle Beams*, [24\(2\):291](#), 2006. [pages 54, 61]
- [95] S. M. Weng, P. Mulser, and Z. M. Sheng. Relativistic critical density increase and relaxation and high-power pulse propagation. *Physics of Plasmas*, [19\(2\):022705](#), 2012. [page 57, 57]
- [96] S. Weng, M. Murakami, P. Mulser, and Z. Sheng. Ultra-intense laser pulse propagation in plasmas: from classic hole-boring to incomplete hole-boring with relativistic transparency. *New Journal of Physics*, [14\(6\):063026](#), 2012. [page 57, 57]
- [97] V. A. Vshivkov, N. M. Naumova, F. Pegoraro, and S. Bulanov. Nonlinear electrodynamics of the interaction of ultra-intense laser pulses with a thin foil. *Physics of Plasmas*, [5\(7\):2727–2741](#), 1998. [pages 58, 59]
- [98] S. Bulanov, C. Schroeder, E. Esarey, and W. Leemans. Optimized laser pulse profile for efficient radiation pressure acceleration of ions. *Physics of Plasmas (1994-present)*, [19\(9\):093112](#), 2012. [page 59]
- [99] A. Henig, D. Kiefer, K. Markey, D. Gautier, K. Flippo, S. Letzring, R. Johnson, T. Shimada, L. Yin, B. Albright, et al. Enhanced laser-driven

- ion acceleration in the relativistic transparency regime. *Physical review letters*, [103\(4\):045002](#), 2009. [pages 61, 194]
- [100] Q. Dong, Z.-M. Sheng, M. Yu, and J. Zhang. Optimization of ion acceleration in the interaction of intense femtosecond laser pulses with ultrathin foils. *Physical Review E*, [68\(2\):026408](#), 2003. [page 61]
- [101] E. dHumières, E. Lefebvre, L. Gremillet, and V. Malka. Proton acceleration mechanisms in high-intensity laser interaction with thin foils. *Physics of Plasmas (1994-present)*, [12\(6\):062704](#), 2005. [page 61]
- [102] T. Esirkepov, M. Yamagiwa, and T. Tajima. Laser ion-acceleration scaling laws seen in multiparametric particle-in-cell simulations. *Physical review letters*, [96\(10\):105001](#), 2006. [page 61]
- [103] L. Yin, B. Albright, B. Hegelich, K. J. Bowers, K. Flippo, T. Kwan, and J. Fernández. Monoenergetic and gev ion acceleration from the laser breakout afterburner using ultrathin targets. *Physics of Plasmas*, [14:056706](#), 2007. [page 61]
- [104] L. Yin, B. J. Albright, K. J. Bowers, D. Jung, J. C. Fernandez, and B. M. Hegelich. Three-dimensional dynamics of breakout afterburner ion acceleration using high-contrast short-pulse laser and nanoscale targets. *Physical Review Letters*, [107\(4\):045003](#), Jul 2011. [pages 61, 197]
- [105] O. Buneman. Instability, turbulence, and conductivity in current-carrying plasma. *Physical Review Letters*, [1\(1\):8](#), 1958. [page 62]
- [106] D. Jung, B. Albright, L. Yin, D. Gautier, R. Shah, S. Palaniyappan, S. Letzring, B. Dromey, H. Wu, T. Shimada, et al. Beam profiles of proton and carbon ions in the relativistic transparency regime. *New Journal of Physics*, [15\(12\):123035](#), 2013. [page 62]
- [107] H. Powell, M. King, R. Gray, D. MacLellan, B. Gonzalez-Izquierdo, L. Stockhausen, G. Hicks, N. Dover, D. Rusby, D. Carroll, et al. Proton acceleration enhanced by a plasma jet in expanding foils undergoing

- relativistic transparency. *New Journal of Physics*, [17\(10\):103033](#), 2015. [page 62, 62]
- [108] S. Palaniyappan, C. Huang, D. C. Gautier, C. E. Hamilton, M. A. Santiago, C. Kreuzer, A. B. Sefkow, R. C. Shah, and J. C. Fernández. Efficient quasi-monoenergetic ion beams from laser-driven relativistic plasmas. *Nature communications*, [6](#), 2015. [page 62]
- [109] A. A. Sahai, F. S. Tsung, A. R. Tableman, W. B. Mori, and T. C. Katsouleas. Relativistically induced transparency acceleration of light ions by an ultrashort laser pulse interacting with a heavy-ion-plasma density gradient. *Physical Review E*, [88\(4\):043105](#), 2013. [page 63, 63]
- [110] S. A. Reed, T. Matsuoka, S. Bulanov, M. Tampo, V. Chvykov, G. Kalintchenko, P. Rousseau, V. Yanovsky, R. Kodama, D. W. Litzenberg, et al. Relativistic plasma shutter for ultraintense laser pulses. *Applied physics letters*, [94\(20\):201117](#), 2009. [page 64]
- [111] B. Dromey, S. Kar, M. Zepf, and P. Foster. The plasma mirror - subpicosecond optical switch for ultrahigh power lasers. *Review of Scientific Instruments*, [75\(3\):645–649](#), 2004. [pages 64, 70]
- [112] L. Ji, B. Shen, X. Zhang, F. Wang, Z. Jin, C. Xia, M. Wen, W. Wang, J. Xu, and M. Yu. Generating quasi-single-cycle relativistic laser pulses by laser-foil interaction. *Physical Review Letters*, [103\(21\):215005](#), 2009. [page 65]
- [113] S. Palaniyappan, B. M. Hegelich, H.-C. Wu, D. Jung, D. C. Gautier, L. Yin, B. J. Albright, R. P. Johnson, T. Shimada, S. Letzring, D. T. Offermann, J. Ren, C. Huang, R. Hrlein, B. Dromey, J. C. Fernandez, and R. C. Shah. Dynamics of relativistic transparency and optical shuttering in expanding overdense plasmas. *Nature Physics*, [8\(10\):763–769](#), 2012. [pages 65, 94, 199]

- [114] R. Kodama, K. Takahashi, K. A. Tanaka, M. Tsukamoto, H. Hashimoto, Y. Kato, and K. Mima. Study of laser-hole boring into overdense plasmas. *Physical Review Letters*, [77\(24\):4906–4909](#), Dec 1996. [page 66]
- [115] A. Pukhov and J. Meyer-ter Vehn. Laser hole boring into overdense plasma and relativistic electron currents for fast ignition of icf targets. *Physical review letters*, [79\(14\):2686](#), 1997. [page 66, 66]
- [116] M. Streeter, P. Foster, F. Cameron, R. Bickerton, S. Blake, P. Brummit, B. Costello, E. Divall, C. Hooker, P. Holligan, et al. Astra gemini compact plasma mirror system. *Central Laser Facility Annual Report*, [pages 225–227](#), 2009. [page 70]
- [117] B. N. Azzam R.M.A. *Ellipsometry and Polarized Light*. North Holland, 1977. [page 82]
- [118] M. Sonoda, M. Takano, J. Miyahara, and H. Kato. Computed radiography utilizing scanning laser stimulated luminescence. *Radiology*, [148\(3\):833–838](#), 1983. [page 84]
- [119] S. Gales and C. Bentley. Image plates as x-ray detectors in plasma physics experiments. *Review of scientific instruments*, [75\(10\):4001–4003](#), 2004. [page 84]
- [120] K. Zeil, S. Kraft, A. Jochmann, F. Kroll, W. Jahr, U. Schramm, L. Karsch, J. Pawelke, B. Hidding, and G. Pretzler. Absolute response of fuji imaging plate detectors to picosecond-electron bunches. *Review of Scientific Instruments*, [81\(1\):013307](#), 2010. [page 84]
- [121] K. Takahashi, K. Kohda, J. Miyahara, Y. Kanemitsu, K. Amitani, and S. Shionoya. Mechanism of photostimulated luminescence in BaFX:Eu²⁺ (X= Cl,Br) phosphors. *Journal of Luminescence*, [31:266–268](#), 1984. [page 85]

- [122] Y. Iwabuchi, N. Mori, K. Takahashi, T. Matsuda, and S. Shionoya. Mechanism of photostimulated luminescence process in BaFBr:Eu²⁺ Phosphors. *Japanes Journal of Applied Physics*, **33:178**, 1994. [page 85]
- [123] F. Nurnberg, M. Schollmeier, E. Brambrink, A. Blazevic, D. Carroll, K. Flippo, D. Gautier, M. Geibel, K. Harres, B. Hegelich, et al. Radiochromic film imaging spectroscopy of laser-accelerated proton beams. *Review of Scientific Instruments*, **80(3):033301**, 2009. [page 85]
- [124] P. Bolton, M. Borghesi, C. Brenner, D. Carroll, C. De Martinis, A. Flacco, V. Floquet, J. Fuchs, P. Gallegos, D. Giove, et al. Instrumentation for diagnostics and control of laser-accelerated proton (ion) beams. *Physica Medica*, **30(3):255–270**, 2014. [page 85]
- [125] D. Kirby, S. Green, H. Palmans, R. Hugtenburg, C. Wojnecki, and D. Parker. Let dependence of gafchromic films and an ion chamber in low-energy proton dosimetry. *Physics in medicine and biology*, **55(2):417–433**, 2009. [page 86]
- [126] D. Kirby, S. Green, F. Fiorini, D. Parker, L. Romagnani, D. Doria, S. Kar, C. Lewis, M. Borghesi, and H. Palmans. Radiochromic film spectroscopy of laser-accelerated proton beams using the fluka code and dosimetry traceable to primary standards. *Laser and Particle Beams*, **29(02):231–239**, 2011. [page 86]
- [127] A. Pukhov. Particle-in-cell codes for plasma-based particle acceleration. arXiv, , 2015. [page 88]
- [128] <https://ccpforge.cse.rl.ac.uk/gf/project/epoch/>. [page 89]
- [129] T. D. Arber, K. Bennett, C. S. Brady, A. Lawrence-Douglas, M. G. Ramsay, N. J. Sircombe, P. Gillies, R. G. Evans, H. Schmitz, A. R. Bell, and C. P. Ridgers. Contemporary particle-in-cell approach to laser-plasma modelling. *Plasma Physics and Controlled Fusion*, **57(11):1–26**, November 2015. [pages 89, 129]

- [130] J. Bin, W. Ma, H. Wang, M. Streeter, C. Kreuzer, D. Kiefer, M. Yeung, S. Cousens, P. Foster, B. Dromey, et al. Ion acceleration using relativistic pulse shaping in near-critical-density plasmas. *Physical review letters*, [115\(6\):064801](#), 2015. [page 94]
- [131] P. Gibbon. Harmonic generation by femtosecond laser-solid interaction: A coherent water-window light source? *Phys. Rev. Lett.*, [76:50–53](#), Jan 1996. [page 103]
- [132] C. Thaury and F. Quere. High-order harmonic and attosecond pulse generation on plasma mirrors: basic mechanisms. *Journal of Physics B: Atomic, Molecular and Optical Physics*, [43\(21\):213001](#), 2010. [page 103]
- [133] J. Stratton and L. Chu. Diffraction theory of electromagnetic waves. *Physical Review*, [56\(1\):99](#), 1939. [page 130]
- [134] M. A. Bandres, J. C. Gutiérrez-Vega, et al. Ince-gaussian modes of the paraxial wave equation and stable resonators. *Journal of the Optical Society of America A*, [21\(5\):873–880](#), 2004. [page 131]
- [135] S. Guha and G. Gillen. Description of light propagation through a circular aperture using nonparaxial vector diffraction theory. *Optics express*, [13\(5\):1424–1447](#), 2005. [pages 131, 132]
- [136] L. Rayleigh. On the passage of waves through apertures in plane screens, and allied problems. *The London, Edinburgh, and Dublin Philosophical Magazine and Journal of Science*, [43\(263\):259–272](#), 1897. [page 131]
- [137] G. Kirchhoff. Zur theorie der lichtstrahlen. *Annalen der Physik*, [254\(4\):663–695](#), 1883. [page 131]
- [138] K. Asada, M. Inoue, Y. Uchida, S. Kamenno, K. Fujisawa, S. Iguchi, and M. Mutoh. A helical magnetic field in the jet of 3c 273. *Publications of the Astronomical Society of Japan*, [54\(3\):L39–L43](#), 2002. [pages 142, 143]

- [139] G. Ghisellini, F. Tavecchio, and M. Chiaberge. Structured jets in TeV bl lac objects and radiogalaxies-implications for the observed properties. *Astronomy & Astrophysics*, [432\(2\):401–410](#), 2005. [page 142]
- [140] M. Zamaninasab, E. Clausen-Brown, T. Savolainen, and A. Tchekhovskoy. Dynamically important magnetic fields near accreting supermassive black holes. *Nature*, [510\(7503\):126–128](#), 2014. [page 142]
- [141] S. Bouquet, E. Falize, C. Michaut, C. Gregory, B. Loupias, T. Vinci, and M. Koenig. From lasers to the universe: Scaling laws in laboratory astrophysics. *High Energy Density Physics*, [6\(4\):368–380](#), 2010. [page 143]
- [142] I. Martí-Vidal, S. Müller, W. Vlemmings, C. Horellou, and S. Aalto. A strong magnetic field in the jet base of a supermassive black hole. *Science*, [348\(6232\):311–314](#), 2015. [page 143]
- [143] J.-L. Gómez, A. P. Marscher, A. Alberdi, S. G. Jorstad, and C. García Miró. Flashing superluminal components in the jet of the radio galaxy 3c120. *Science*, [289\(5488\):2317–2320](#), 2000. [page 143]
- [144] M. Tamburini, T. Liseykina, F. Pegoraro, and A. Macchi. Radiation-pressure-dominant acceleration: Polarization and radiation reaction effects and energy increase in three-dimensional simulations. *Physical Review E*, [85\(1\):016407](#), 2012. [page 154]
- [145] D. Stark, C. Bhattacharjee, A. Arefiev, T. Toncian, R. Hazeltine, and S. M. Mahajan. Relativistic plasma polarizer: Impact of temperature anisotropy on relativistic transparency. *Physical Review Letters*, [115:025002](#), 2015. [pages 154, 164]
- [146] G. Korn, B. LeGarrec, and B. Rus. Eli extreme light infrastructure science and technology with ultra-intense lasers. In *CLEO: Science and Innovations*, pages CTu2D–7. Optical Society of America, 2013. [pages 157, 200]

- [147] G. Mourou and T. Tajima. The extreme light infrastructure: Optics' next horizon. *Optics and Photonics News*, [22\(7\):47–51](#), 2011. [pages 157, 200]
- [148] R. Wilson, M. King, R. Gray, D. Carroll, R. Dance, C. Armstrong, S. Hawkes, R. Clarke, D. Robertson, D. Neely, et al. Ellipsoidal plasma mirror focusing of high power laser pulses to ultra-high intensities. *Physics of Plasmas (1994-present)*, [23\(3\):033106](#), 2016. [pages 157, 201]
- [149] S. Corde, E. Adli, J. Allen, W. An, C. Clarke, C. Clayton, J. Delahaye, J. Frederico, S. Gessner, S. Green, et al. Multi-gigaelectronvolt acceleration of positrons in a self-loaded plasma wakefield. *Nature*, [524\(7566\):442–445](#), 2015. [page 158]
- [150] D. Carroll, P. McKenna, O. Lundh, F. Lindau, C.-G. Wahlström, S. Bandyopadhyay, D. Pepler, D. Neely, S. Kar, P. Simpson, et al. Active manipulation of the spatial energy distribution of laser-accelerated proton beams. *Physical Review E*, [76\(6\):065401](#), 2007. [page 161]
- [151] C. Palmer, J. Schreiber, S. Nagel, N. Dover, C. Bellei, F. Beg, S. Bott, R. Clarke, A. Dangor, S. Hassan, et al. Rayleigh-taylor instability of an ultrathin foil accelerated by the radiation pressure of an intense laser. *Physical review letters*, [108\(22\):225002](#), 2012. [page 164, 164]
- [152] L. Seidel. *Abh. bayer. akad. wiss. math. Naturwiss. Kl.*, 11:81108, 1874. [page 167]
- [153] D. M. Young. Iterative methods for solving partial difference equations of elliptical type. PhD thesis, Harvard University, 1950. [page 167]
- [154] C. Jacobi. Ueber eine neue auflösungsart der bei der methode der kleinsten quadraten vorkommenden lineare gleichungen. *Astr. Nachr.*, [22\(523\):297306](#), 1845. [page 167]
- [155] S. Kar, K. Kakolee, B. Qiao, A. Macchi, M. Cerchez, D. Doria, M. Geissler, P. McKenna, D. Neely, J. Osterholz, et al. Ion acceleration in multispecies

targets driven by intense laser radiation pressure. *Physical Review Letters*, [109\(18\):185006](#), 2012. [page 189]

- [156] A. Macchi, M. Borghesi, and M. Passoni. Ion acceleration by superintense laser-plasma interaction. *Reviews of Modern Physics*, [85\(2\):751–793](#), May 2013. [page 194]